Ab initio approaches to nuclear structure, scattering and tests of fundamental symmetries

by

Michael Gennari

B.Sc., University of Waterloo, 2019

A THESIS SUBMITTED TO THE FACULTY OF GRADUATE STUDIES

IN PARTIAL FULFILLMENT OF THE REQUIREMENTS FOR THE DEGREE OF

Master of Science

in the Department of Physics and Astronomy

University of Victoria, Victoria

Supervisory Committee

Ab initio approaches to nuclear structure, scattering and tests of fundamental symmetries

by

Michael Gennari

B.Sc., University of Waterloo, 2019

Supervisory Committee

Dr. Petr Navrátil, Co–Supervisor
Department of Physics and Astronomy

Dr. Robert Kowalewski, Co–Supervisor
Department of Physics and Astronomy

Dr. Falk Herwig, Department Member
Department of Physics and Astronomy

Abstract

In recent decades, the accessibility of nuclear physics has been greatly improved due to the advent of modern supercomputers, as well as theoretical developments in effective field theory and *ab initio* (first–principles) nuclear approaches. As a result, in modern nuclear theory it is possible to perform realistic quantum many–body calculations of nuclear systems, beginning solely from underlying Standard Model symmetries.

A fundamental object of interest in nuclear structure are the nuclear densities, which may be abundantly used in calculation of other nuclear observables. Utilizing the *ab initio* no–core shell model, a rigorous theoretical approach for calculations involving light–nuclei, we study the coordinate space densities of various nuclear systems and discuss the importance of nonlocality and translation invariance in the densities. In particular, this property is investigated at length in the context of scattering theory, in which optical potentials are constructed from the *ab initio* no–core shell model densities. We explore the impacts of nonlocality and translation invariance in proton and antiproton scattering, and in the latter we review the first fully microscopic optical potential for antiproton–nucleus scattering. In addition, while the full problem is intractable at present, we assess the potential impact of many–nucleon dynamics on scattering observables. We additionally present an analytic computation of the nuclear kinetic density distribution, derived from the nonlocal nuclear densities.

While the nuclear problem has become increasingly tractable, the computational barrier is still ever present, with nuclear calculations pushing the frontier of modern supercomputing. Many approaches have been developed to quell the computational demand, e.g. the similarity renormalization group approach. We introduce and discuss another approach, namely the natural orbitals unitary transformation, which has been shown increase the convergence rate of quantum many–body calculations.

Lastly, in the past three years there has revitalized interest in reevaluation of particular Standard Model symmetries. Notably, the Cabibbo–Kobayashi–Maskawa quark mixing matrix has been established as a high–precision test of the Standard Model, capable of pointing to novel physics. Recent theoretical advances in corrections needed to evaluate unitarity of the Cabibbo–Kobayashi–Maskawa matrix have indicated a statistical discrepancy with the Standard Model expectation. In light of this development, using the *ab initio* no–core shell model with continuum, we pursue a high–precision calculation of the isospin symmetry breaking correction, δ_C. This correction is one of two nuclear structure dependent corrections needed to shed light on this discrepancy, and potentially identify physics beyond the Standard Model.

Contents

List of Figures

List of Tables

Declaration

This thesis comprises the original work of the author, M. Gennari, under superversion of Dr. Petr Navrátil. Though, several of the discussed works were obtained in collaborations with remarkable researchers at TRIUMF, most notably Dr. Matteo Vorabbi, Dr. Mack Atkinson and Dr. Angelo Calci. This thesis was completed with the support of all these individuals. The results discussed in this dissertation have been published in the following references:

M. Gennari, M. Vorabbi, A. Calci, and P. Navrátil, "Microscopic optical potentials derived from ab initio translationally invariant nonlocal one-body densities," *Phys. Rev. C*, vol. 97, p. 034619, Mar 2018

M. Gennari and P. Navrátil, "Nuclear kinetic density from ab initio theory," *Physical Review C*, vol. 99, p. 024305, Feb 2019

M. Vorabbi, M. Gennari, P. Finelli, C. Giusti, and P. Navrátil, "Elastic antiproton-nucleus scattering from chiral forces," *Physical Review Letters*, vol. 124, p. 162501, Apr 2020

M. Vorabbi, M. Gennari, P. Finelli, C. Giusti, P. Navrátil, and R. Machleidt, "Impact of three-body forces on elastic nucleon-nucleus scattering observables," *Physical Review C*, vol. 103, p. 024604, Feb 2021

Acknowledgments

Of greatest importance, I would like to thank my research supervisor, Dr. Petr Navrátil, for taking me on as an M.Sc. student and guiding me throughout this arduous work. The multi–disciplinary field of nuclear theory is vast and complicated, yet Dr. Navrátil consistently supported my education in the field. I wish to thank Dr. Matteo Vorabbi, a friendly post–doctoral collaborator whom I first met during my time as an undergraduate at TRIUMF. Dr. Vorabbi has been tremendously helpful throughout my degree, and his efforts on optical potential theory have proved to be a fantastic theoretical application for the nonlocal densities discussed in this work. I further thank Dr. Angelo Calci, who initially supported the work on nonlocal densities. Lastly, I wish to thank Dr. Mack Atkinson, with whom we are presently collaborating on a challenging project to test fundamental symmetries of the Standard Model. I look forward to our future collaborations.

I thank Dr. Robert Kowalewski and Dr. Falk Herwig for being members of my committee, and the former I thank for his continuous support during a rather stressful time this past year and a half. I abundantly thank the whole of TRIUMF, including its facilities, staff, and students, with a special thanks paid to the theory department. The community of TRIUMF is unique and kind, and I am grateful to be one part of a much larger whole.

Dedication

I dedicate this thesis to my entire family, all of whom have provided unwavering support in my pursuit of theoretical physics. A special thanks goes to my father, Marino Gennari, my mother, Silvia Gennari, and my brother, Alex Gennari. They have continually encouraged my progress throughout the most difficult moments, and without them I know my education, and furthermore this thesis, would not have been possible.

I owe a great deal to my grandparents on both sides of my family, who perilously journeyed across the Atlantic. Salvatore and Antonietta Marzilli, who worked as humble *contadini* in Italy, moved every obstacle to raise their children in Canada. Giovanni and Norma Gennari laboured hard their entire lives, both in Italy and in Canada, and to provide them opportunity raised a family here in Canada. It is because of the collective efforts of these people that I was able to pursue my studies.

Chapter 1

Introduction

Nuclear theory is the study of the atomic nucleus, a fundamental quantum structure observed in nature, which gives rise to all other matter structures, such as stars, molecules, cells, etc. In particular, nuclear physics is concerned with the questions of why these bound quantum systems can be formed, and more generally, how these systems interact and undergo reactions. These systems are non–trivial to describe, and hence nuclear theory is a complicated field of quantum many–body physics, often requiring advanced mathematical techniques and extensive knowledge of computer science.

Particularly relevant for nuclear structure physics is the low–energy regime of Quantum Chromo–dynamics (QCD), the quantum field theory pertaining to the strong interaction. QCD, one of the three interactions successfully incorporated into the Standard Model of Particle Physics (SM), is the source of the effective interactions experienced by protons and neutrons and is ultimately what binds the atomic nucleus. It is then natural to study nuclei as a system of nucleons (protons and neutrons) interacting via inter–nucleon forces, which has been a long–standing goal in nuclear theory. In fact, this general procedure for describing nuclei is known as *ab initio* nuclear theory. This process is part of a large–scale effort in the nuclear physics community to transition from phenomenological descriptions of nuclei to nuclear models employing realistic inter–nucleon interactions, rooted in the underlying QCD symmetries.

The motivations for a fully predictive *ab initio* nuclear structure and reaction theory are numerous and have far–reaching implications for other fields of physics. For one, investigations of nuclear properties have significant impact on precision tests of fundamental symmetries and existsence of physics beyond the Standard Model (SM) of particle physics. By studying nuclear Fermi transitions, a special form of beta decay in nuclei (i.e. $^{10}\mathrm{C} \rightarrow ^{10}\mathrm{B}$), it is possible to probe the SM through the element V_{ud} of the Cabbibo–Kobayashi–Maskawa (CKM) matrix [25]. This parameter is significant to the fundamental symmetry test of CKM unitarity, $|V_{ud}|^2 + |V_{us}|^2 + |V_{ub}|^2 = 1$, with other parameters V_{us} and V_{ub}. Moreover, recent experimental analyses of CKM unitarity show statistical discrepancy with the SM prediction. This condition, if unsatisfied, is a key indicator of missing physics in the SM. To correctly identify this disagreement with the SM, precision calculations of nuclear structure corrections to Fermi transitions are required. Furthermore, with a predictive *ab initio* theory, it is possible to pursue other fundamental symmetry tests of the SM. For example, an experimental measurment of an electric dipole moment would strongly indicate new physics, as the SM presently predicts undetectable results for electrons, nucleons, and nuclei. With modern nuclear approaches, we may highlight nuclei of interest for future experimental studies, e.g. ^{11}Be, which has a ground state halo structure with strong electromagnetic (E1) transitions to other low–lying bound states, meaning significant enhancements to the nuclear electric dipole moment are anticipated.

Additionally, predictive nuclear theories are intrinsic to a deeper understanding of nuclear astrophysics. Relevant reactions are often not accessible through laboratory experiments, due to the low–energy nature of Cosmic processes. The usefullness of an *ab initio* theory for describing astrophysical processes cannot be understated [26, 27], as one can address the experimental and theoretical obstacles encountered in nuclear astrophysics, providing direct connections between macroscopic astrophysics and QCD. Reactions

of major theoretical interest include the $^{13}\mathrm{C}(\alpha, n)^{16}\mathrm{O}$ transfer reaction and $^{12}\mathrm{C}(\alpha, \gamma)^{16}\mathrm{O}$ radiative capture reaction, which are needed for complete understanding of the astrophysical processes (such as the s–process in stars) responsible for producing heavy elements. Of similar interest is the $^{14}\mathrm{N}(p, \gamma)^{15}\mathrm{O}$ proton capture reaction, which must be well understood for an accurate description of the famous Carbon–Nitrogen–Oxygen (CNO) cycle in stars. Another reaction of interest is the neutron-induced $^{14}\mathrm{N}(n, p)^{14}\mathrm{C}$ charge exchange reaction, which is relevant for stellar nucleosynthesis. While there exists fair amounts of experimental data, there also exists a discrepancy in the $^{14}\mathrm{N}(n, p)^{14}\mathrm{C}$ cross sections [28]. Lastly, there is great effort in attempting to understand to formation of heavy–elements from the primordial abundance of light nuclei [29]. The complicated reaction processes in the first stars are the gateway to understanding how light–nuclei clustered into their heavier counterparts. A fully predictive *ab initio* theory capable of describing clustering in nuclei could assist in shedding light on the early formation of heavy elements in our universe. As it stands, a first–principles description of nuclear structure and reaction theory would not only benefit the nuclear physics community, but would be of tremendous use to the particle theory and astrophysics communities as well.

This thesis covers many topics. We aim to discuss improvements to nuclear structure and reaction theory, as well as tests of fundamental SM symmetries: (i) we introduce a generalized nuclear density, then applied to scattering calculations (ii) we discuss natural similarity transformations capable of improving the convergence rate of nuclear calculations (iii) we discuss how SM symmetry tests may benefit from *ab initio* nuclear structure theory. The dissertation is organized as follows. The first chapter following the introduction, Chapter 2, will cover a variety of content required to understand the status of modern nuclear physics. Beginning with the SM, we pedagogically describe the extraction of relevant low–energy physics in the form of inter–nucleon interactions, and their subsequent incorporation into nuclear many–body approaches; in particular, for the no–core shell model (NCSM). In Chapter 3, we will discuss NCSM densities, which can be used as input in nuclear reaction theory methods. Specifically, we discuss the procedural removal of spurious center–of–mass contamination in NCSM eigenstates, significantly improving the physical description of light–nuclear systems. In Chapter 4, we introduce the challenges of many–body convergence with respect to our basis truncation parameter in the NCSM. We discuss the application of alternative, physically adapted single–particle bases in the many–body calculation which are shown to improve convergence rates at the same computational cost. In Chapter 5, we will discuss the modern no–core shell model with continuum (NCSMC), a unified approach to describing nuclear structure and reaction theory. We discuss the necessity of this approach in the context of consistently understanding nuclear structure as well as fundamental properties of the SM.

Chapter 2

Preliminary Material

2.1 From the Standard Model to Nucleons

In its modern form, the field of nuclear theory may be subdivided into two halves: the construction of effective nuclear interactions, which will be discussed in Sec. 2.1, and the quantum many–body approaches which use these interactions, to be discussed in Sec. 2.2. As is emphasized by this dissection, one finds that perhaps the oldest and yet still relevant obstacle to theory is the development of nuclear approaches from the underlying Standard Model (SM) physics. In investigations of nuclear physics, we are interested in the Quantum Field Theory (QFT) which governs the low–energy nuclear regime, namely Quantum Chromo–Dyanmics (QCD). As the underlying dynamics are extremely complicated, effective field theory (EFT) approaches have become a core tool in developing our understanding of nuclear physics. EFTs are theories within an energy range small compared to a particular cutoff. In this energy range, EFTs can systematically reproduce the physics of a given Lagrangian in a perturbative expansion. The Chiral Perturbation Theory (ChPT) approach was first considered by Weinberg [30] and further formalized in the subsequent works of Gasser and Leutwyler [31, 32], having now become a standard for developing nuclear interactions. In particular, the purpose of this section is to provide a technical (yet accessible) introduction to modern approaches in ChPT from a basic understanding of the SM, and is modeled after a series of review papers, Refs. [33, 5, 34, 35], to which we direct the reader for a deeper understanding of the EFT formalism. The application of the EFT formalism may be summarized by the following set of steps:

(i) Identify low– and high–energy scales and relevant degrees of freedom at low–energy

(ii) Recognize relevant symmetries and symmetry breaking patterns

(iii) Construct general effective Lagrangian consistent with broken (and unbroken) symmetries

(iv) Organize expansion in low–energy regime using powers of high–energy scale

(v) Evaluate Feynman diagrams to desired accuracy

Here, we will guide the reader through this procedure and derive the leading order (LO) contributions to the nuclear interaction.

2.1.1 Quantum Chromo–Dynamics

The Standard Model (SM) is our greatest fundamental theory of quantum interactions. In particular for our work, we are most interested in the theory of the strong interaction, QCD [36, 37], which is one of four known fundamental interactions and one of the three successfully incorporated into the SM. QCD

is a Yang–Mills gauge theory with a local gauge invariance described by the $\mathrm{SU}(3)_c$ colour group; space–time dependent colour transformations leave the QCD Lagrangian invariant. In QCD, quarks (Fermion fields with colour quantum numbers) and gluons (bosonic fields in colour superposition states) are the fundamental fields. Quark fields are represented in the fundamental representation of the colour group **3** (antiquarks are then represented in the conjugate representation of the colour group **3***), which comes solely from the fact that there exists $N_c = 3$ colour degrees of freedom [38]. The modern QCD Lagrangian for three quark generations (six flavours of quarks) may be written as

$$\mathcal{L} = \sum_q i\bar{\psi}_q^i \gamma^\mu (D_\mu)_{ij} \psi_q^j - m_q \bar{\psi}_q^i \psi_{qi} - \frac{1}{4} G_{\mu\nu}^a G^{\mu\nu a} \qquad \psi_q = \begin{bmatrix} \psi_q^R \\ \psi_q^G \\ \psi_q^B \end{bmatrix} \epsilon\, V_{RGB} \tag{2.1}$$

Let us define the components of this equation. The spinor ψ_q^i is a quark field with mass m_q, flavour $q\,\epsilon\{u, d, s, c, b, t\}$ and colour index $i\,\epsilon\{R, G, B\}$. It exists in the fundamental representation of SU(3) and is a triplet (3−vector) of fields in colour space, V_{RGB}. Note that we have used the Dirac adjoint notation, $\bar{\psi} = \psi^\dagger \gamma^0$, which guarantees that $\bar{\psi}\psi$ and $\bar{\psi}\gamma^\mu\psi$ transform covariantly. $\gamma^\mu = (\gamma^0, \gamma^1, \gamma^2, \gamma^3)$ is the usual 4–vector of Dirac gamma matrices. Further, we have the definition

$$(D^\mu)_{ij} = \delta_{ij}\partial_\mu - \frac{ig_s}{2} T_{ij}^a A_\mu^a \tag{2.2}$$

where $\{T^a\}$, $a\,\epsilon\{1, \ldots, 8\}$ are the generators of the $\mathrm{SU}(3)_c$ colour group; these generators act in the fundamental representation as linear maps, and are the Gell–Mann matrices [39]. The generators satisfy the SU(3) algebra:

$$[T^a, T^b] = i f_{abc} T^c \qquad a, b, c\,\epsilon\{1, \cdots, 8\} \tag{2.3}$$

where f_{abc} are the real and anti–symmetric algebraic structure constants. The *gluon field* is written as $A_\mu = T^a A_\mu^a$ and is a fundamental field in QCD which can change the colour quantum numbers of quarks. This field is responsible for all interactions between coloured quantum objects and is mediated by force carriers referred to as gluons. In order to understand how gluons mediate colour, we must investigate the set of possible gluon colour states.

Bosons of QCD

The gluon field describes the vector gauge bosons of QCD and tells us how quantum objects with colour charge will interact. In order to exchange arbitrary colour, gluons must be composed of a superposition of colour and anti–colour, i.e. gluons must be built from a quark and an antiquark pair. Hence, given the fundamental colour representation **3**, the defining representation for gluons in colour space will be given by the product representation $\mathbf{3} \otimes \mathbf{3^*}$. Using the Young–Tableaux method, we can decompose this product representation into $\mathbf{3} \otimes \mathbf{3^*} = \mathbf{8} \oplus \mathbf{1}$, indicating that there are eight possible gluon states which dynamically influence the colour sector.

Remark. One gluon state is unique and occupies the singlet representation **1**. This state occupies the singlet because it is incapable of colour changing processes; it cannot change the colour of quarks, and so it is trivial. Notably, the state in colour space is given by $|G_9\rangle = \frac{1}{\sqrt{3}}(|r\bar{r}\rangle + |g\bar{g}\rangle + |b\bar{b}\rangle)$.

Confinement

One of the most interesting properties of the QCD Lagrangian is that it produces a 'confining' theory. The direct implication of this is simply that the quark and gluon fields are not individually observable in nature. In fact, only *gauge invariant* objects are observable; any detectable field constructed from quarks and gluons must be colourless! The gauge invariant many–quark bound states which we observe in nature

are known as hadrons. Through thorough analysis using hadron spectroscopy, there is a strong indication that there are six quark flavours with different masses but similar dynamical properties with respect to the gluon field; each quark interacts identically with coloured objects.

Notably, the gluon field strength tensor has a uniquely different structure compared to other physical theories. Specifically, we mention the term $gf_{abc}A_{\mu b}A_{\nu c}$ of the QCD Lagrangian, which is different from, for example, the electromagnetic field strength tensor $F_{\mu\nu} = \partial_\mu A_\nu - \partial_\nu A_\mu$ in Quantum Electro–Dyanmics (QED). In fact, the existence of this term in the gluon field strength tensor is a result of the non–abelian nature of the QCD algebra, and gives rise to the colour self–interaction of gluons. This creates a highly non–linear structure in QCD, and is the reason the theory is mathematically challenging to understand.

Flavour symmetry with equal mass quarks

One feature of QCD is the approximate flavour symmetry of the (u, d, s) quarks, which is due to their light masses with respect to the other three quarks (c, b, t). In fact, if all the quarks had equal masses, we would see the emergence of an SU(6) flavour symmetry in $\mathcal{L}_{QCD}$. Let us see the emergence of the approximate flavour symmetry in detail. Considering the case of equal mass quarks with arbitrary number of flavours N_f, the quark part of the QCD Lagrangian is written as:

$$\mathcal{L}_q = \sum_q^{N_f} \bar{\psi}_q^i (i\gamma_\mu [D^\mu]_{ij} - m)\bar{\psi}_q^j \ . \tag{2.4}$$

If we now apply infinitesimal global flavour transformations of the form $\psi \to e^{i\delta\alpha^a T^a}\psi$, expanding $e^{i\delta\alpha^a T^a} = 1 + i\delta\alpha^a T^a + O(\alpha^2)$ we may write the variation in the fields to first order as

$$\delta\psi^i = -i\delta\alpha^a (T^a)^i{}_j \psi^j \qquad \delta\bar{\psi}_i = i\delta\alpha^a \bar{\psi}_j (T^a)^j_i \qquad \delta A_\mu = 0 \tag{2.5}$$

We now introduce Noether's theorem, one of the most important theorems in modern theoretical physics.

Theorem 1 (Noether's Theorem)**.** *If a Lagrangian has a continuous symmetry (global or local), then there exists a Noether current associated with the symmetry that is conserved when the equations of motion are satisfied* [40]*. Consider a Lagrangian invariant to a continuous infinitesimal transformation described by the variation $\delta\alpha$, then the total variation in the Lagrangian may be expressed as:*

$$\frac{\delta\mathcal{L}}{\delta\alpha} = \sum_n \left\{ \left[\frac{\partial\mathcal{L}}{\partial\phi_n} - \partial_\mu \frac{\partial L}{\partial(\partial_\mu\phi_n)} \right] \frac{\delta\phi_n}{\delta\alpha} + \partial_\mu \left[\frac{\partial\mathcal{L}}{\partial(\partial_\mu\phi_n)} \frac{\delta\phi_n}{\delta\alpha} \right] \right\} = 0 \tag{2.6}$$

The first term is the usual Euler–Lagrange equations that define our equations of motion, and if they are satisfied, this term is zero. Hence, we are left with the result of Noether's theorem,

$$\partial_\mu J^\mu = \partial_\mu \left[\frac{\partial\mathcal{L}}{\partial(\partial_\mu\phi_n)} \frac{\delta\phi_n}{\delta\alpha} \right] = 0 \tag{2.7}$$

where J^μ is the aforementioned Noether current.

Let us apply Noether's theorem to the quark Lagrangian, which yields the conserved currents:

$$j^a_\mu(x^\nu) = -i\frac{\partial\mathcal{L}_q}{\partial(\partial^\mu\psi^i)}(T^a)^i{}_j\psi^j = \bar{\psi}_i\gamma_\mu(T^a)^i{}_j\psi^j \qquad \partial^\mu j^a_\mu(x^\nu) = 0 \ . \tag{2.8}$$

Utilizing the currents, we may now compute the associated generators of our group transformations. We perform spatial integration over the 0^{th} component of the j_μ current as follows:

$$Q^a = \int d^3x \ j^a_0(x^\mu) = \int d^3x \ \bar{\psi}_i\gamma_0(T^a)^i{}_j\psi^j \ . \tag{2.9}$$

The current conservation result of Noether's theorem implies that the generators Q^a are time–independent and so they commute with the corresponding Hamiltonian H. In particular, $[H, Q^a] = 0$ and the Q^a operators satisfy the SU(N_f) algebra:

$$[Q^a, Q^b] = i f_{abc} Q^c \qquad a, b, c \, \epsilon \{1, \ldots, N_f^2 - 1\} \ . \tag{2.10}$$

The N_f quark fields $\{\psi^i\}$ create N_f one-particle quark states $\{|pi\rangle\}$ which change under the action of a generator of flavour transformations as

$$Q^a \, |pi\rangle = -(T^a)_{ij} \, |pj\rangle \ . \tag{2.11}$$

The realization of a symmetry in this way, i.e. with the appearance of a multiplet of identical mass particles, is known as the Wigner–Weyl mode. Unfortunately, we know from experiment that there does not exist a multiplet of identical massive particles. As we will learn, the Wigner–Weyl mode is not the only possible way to realize a symmetry of the Lagrangian; in fact, it is not the way in which SU(3)$_c$ is realized.

Flavour symmetry in quarks with non–equal masses

Let us now introduce non–equal masses for the quarks, in the form of $m_a = m + (\Delta m)_a$. In this case, if we work out the variation under the previously considered infinitesimal flavour transformation, we arrive at the following Noether current:

$$\partial^\mu j^a_\mu = -i \sum_{a,b=1}^{N_f} (m_a - m_b) \bar{\psi}_i (T^a)^i_j \psi^b \neq 0 \ , \tag{2.12}$$

which is non–zero and directly proportional to the differences in the quark masses. Hence, the flavour symmetry of the quarks is explicitly broken due to their non–equal masses. While this symmetry is explicitly broken, there are a subset of quarks for which the mass differences are small enough to be considered perturbative effects, i.e. the symmetry is approximately preserved.

Visualized in nature, the approximate flavour symmetry of quarks can be seen in the properties of hadrons, the bound states of quarks. In the case of identical quark masses, we would expect the hadrons to be organized in SU(N_f) multiplets with degenerate mass. This is obviously not the case for the entire spectrum of quarks, however a subset of quarks do exhibit this behaviour. The flavour symmetry of the u and d quarks can be expressed as SU(2) isospin symmetry. Nature produces strong evidence for this, particularly through the approximate equality of the proton and neutron masses, as well as through the approximate equality of the charged and neutral pion masses. As we will see, it is convenient to place nucleons in the isospin $\frac{1}{2}$ doublet representation **2** of SU(2) (and antinucleons in the conjugate representation **2***) while the pions are placed in the isospin 1 adjoint representation **3** of SO(3) $\sim$ SU(2). Pions being formed from quark and antiquark pairs gives rise to the triplet representation by the Young–Tableaux decomposition of the product group $\mathbf{2} \otimes \mathbf{2^*} = \mathbf{3} \oplus \mathbf{1}$.

2.1.2 Chiral symmetry

The first step in the construction of an effective field theory is to identify the relevant symmetries to the theory, as these symmetries provide crucial constraints on the possible interactions. Hence, a discussion on the fundamental symmetries of QCD is necessary in order to understand nuclear physics. We have already explored flavour transformations of fermions in Sec. 2.1.1, however it is possible to formulate other symmetry transformations. Here, we discuss the importance of chiral symmetry to low–energy QCD.

The light–quark model

Let us consider the QCD Lagrangian in the case of a light–quark model, in which we only consider the *up* and *down* quarks, i.e. the constituents of nucleons. Recall the QCD Lagrangian, albeit modified to only include the two lightest quarks:

$$\mathcal{L} = \sum_q i\bar{\psi}_q^i \gamma^\mu (D_\mu)_{ij} \psi_q^j - m_q \bar{\psi}_q^i \psi_{qi} - \frac{1}{4} G^a_{\mu\nu} G^{\mu\nu a} \qquad \psi_q = \begin{bmatrix} \psi_q^R \\ \psi_q^G \\ \psi_q^B \end{bmatrix} \epsilon V_{RGB} \tag{2.13}$$

Recalling the objects in the Lagrangian, ψ_q represents a quark field and m_q is the corresponding quark mass. Further, we have $D_\mu = \partial_\mu - \frac{ig}{2} T^a A^a_\mu$, where the set $\{T^a\}$ corresponds to the generators of the SU(2) symmetry group; in this representation these are the Pauli matrices. By defining the chiral projectors $P_L = \frac{1}{2}(1-\gamma_5)$ and $P_R = \frac{1}{2}(1+\gamma_5)$, which project quark fields onto their respective left– and right–handed components, we may rewrite the Lagrangian in a chiral projected basis. Projecting onto chirality and expanding the QCD Lagrangian in quark fields yields:

$$\mathcal{L}_{QCD} = i\bar{\psi}_{qL}\gamma_\mu D^\mu \psi_{qL} + i\bar{\psi}_{qR}\gamma_\mu D^\mu \psi_{qR} - i\bar{\psi}_{qL} M \psi_{qR} - i\bar{\psi}_{qR} M \psi_{qL} - \frac{1}{4} G^a_{\mu\nu} G^{a\mu\nu} \ , \tag{2.14}$$

in which we can explicitly see the two chirality mixing (CM) terms, notably $\mathcal{L}_{CM} = -i(\bar{\psi}_{qL} M \psi_{qR} + \bar{\psi}_{qR} M \psi_{qL})$. It appears that left– and right–chirality are connected solely by the quark mass matrix. Let us now analyze this in the context of chiral transformations.

Chiral rotations may be expressed in a similar way as flavour rotations, albeit with the inclusion of a γ_5 factor in the transformation. The γ_5 matrix is responsible for altering the parity properties of our fundamental fields. Proceeding as with flavour rotations, we consider an infinitesimal chiral rotation parameterized by $\delta\alpha$. This results in the following variations:

$$\delta\psi^i = -i\delta\alpha^a (T^a)^i_{\ j} \gamma_5 \psi^j \qquad \delta\bar{\psi}_i = i\delta\alpha^a \bar{\psi}_j \gamma_5 (T^a)^j_{\ i} \qquad \delta A_\mu = 0 \ . \tag{2.15}$$

If we consider the special case of $m_u = m_d$, the variation in $\mathcal{L}_{QCD}$ is non–zero and may be written as

$$\delta\mathcal{L}_{QCD} = 2im\delta\alpha^a \bar{\psi}_i (T^a)^i_{\ j} \gamma_5 \psi^j \ . \tag{2.16}$$

Immediately from this expression we see that *any* non–zero quark masses break the possible chiral symmetry of the QCD Lagrangian. This is in contrast to our discussion on $\mathrm{SU}(3)_f$ rotations, in which equivalent quark masses were enough to guarantee flavour symmetry. Generalizing the above result to the case of arbitrary quark masses where $M = \mathrm{diag}(m_u, m_d)$, the variation may instead be written as:

$$\delta\mathcal{L}_{QCD} = i\delta\alpha^a \bar{\psi}_i \{M, T^a\}^i_{\ j} \gamma_5 \psi^j \ , \tag{2.17}$$

with $\{\cdots\}$ as the usual anti–commutator. Since this variation is only non–zero due to the non–zero quark masses, it is instructive to first consider the Lagrangian in the case of massless quark fields, so that we may determine the conserved currents corresponding to a completely preserved chiral symmetry.

Chiral symmetry in massless QCD

From our previous discussion, under the consideration of two–quark massless QCD, we know that $\mathcal{L}_{QCD}$ is invariant to flavour and axial–flavour (chiral) transformations. An application of Noether's theorem yields the following conserved currents:

$$\begin{aligned} j^a_\mu &= \bar{\psi}_i \gamma_\mu (T^a)^i_{\ j} \psi^j & \partial^\mu j^a_\mu &= 0 \\ j^a_{5\mu} &= \bar{\psi}_i \gamma_\mu \gamma_5 (T^a)^i_{\ j} \psi^j & \partial^\mu j^a_{5\mu} &= 0 \end{aligned} \tag{2.18}$$

From these conserved currents we obtain the generators of group transformations (charges),

$$Q^a = \int d^3x \; j_0^a \qquad\qquad Q_5^a = \int d^3x \; j_{50}^a \tag{2.19}$$

which define the complete set of chiral rotations and satisfy the following algebra SU(3):

$$[Q^a, Q^b] = if_{abc}Q^c \qquad [Q^a, Q_5^b] = if_{abc}Q_5^c \qquad [Q_5^a, Q_5^b] = if_{abc}Q^c \qquad a, b, c\,\epsilon\{1, 2, 3\} \tag{2.20}$$

Remark. It is worth pointing out that the axial charges alone do not form a complete algebra, since the subgroup of axial charges is not closed under the commutator operation. This is explicit in the third commutator relation of Eq. (2.20).

This algebra is more conveniently expressed by defining new left– and right–handed charges. Making the definitions:

$$Q_L^a = \frac{1}{2}(Q^a - Q_5^a) \qquad Q_R^a = \frac{1}{2}(Q^a + Q_5^a) \; , \tag{2.21}$$

we find the following algebraic rules:

$$[Q_L^a, Q_L^b] = if_{abc}Q_L^c \qquad [Q_R^a, Q_R^b] = if_{abc}Q_R^c \qquad [Q_L^a, Q_R^b] = 0 \; . \tag{2.22}$$

With these new definitions, we see that the left– and right–handed charges are completely decoupled from one another. Each set of chiral generators defines a set of SU(2) group transformations, hence the full chiral group is described by the decomposition $G_{chiral} = \mathrm{SU}(2)_L \times \mathrm{SU}(2)_R$ transformations. The previously considered flavour transformations form a subgroup of the chiral group, $\mathrm{SU}(2)_V \subset \mathrm{SU}(2)_L \times \mathrm{SU}(2)_R$; this is the isospin (flavour) group.

Chiral symmetry in massive QCD

It is well known that the quarks in fact do have masses, which as shown in Eq. (2.17), introduces explicit chiral symmetry breaking in $\mathcal{L}_{QCD}$. In particular, this symmetry breaking may be treated as perturbative if $m_q \ll \Lambda_{QCD} \sim 1\,\mathrm{GeV}$, which for the light quarks is a very reasonable approximation. We are then left with an approximate $\mathrm{SU}(2)_L \times \mathrm{SU}(2)_R$ chiral symmetry. The question is then how to realize such a symmetry. Let us first understand the concept of symmetry breaking in more detail.

In the Wigner–Weyl realization of chiral symmetry, the behaviour of the axial generators is characterized by:

$$Q_5^a \,|mspi+\rangle = -(T^a)_{ij} \,|mspj-\rangle \tag{2.23}$$

where m, s, p are arbitrary labels for mass, spin and momentum. There is a direct parity transformation occuring and so we would experimentally expect to find parity doublets for all massive states. Unfortunately, no parity doublets of massive particles with approximately equal masses are found in the hadrons, so the Wigner–Weyl realization must be abandoned in favour of a more realistic approach for realizing QCD symmetries. An inherent assumption of the Wigner–Weyl mode of realizing a gauge symmetry is that the QFT vacuum state $|0\rangle$ is invariant under the same symmetry group of transformations as the Lagrangian. Otherwise expressed, this means that the generators of transformations will annhilate the vacuum

$$Q^a \,|0\rangle = 0 \; . \tag{2.24}$$

Since our one–particle states are defined by the action of a field on the vacuum, the previous relation guarantees that states transform as elements of the irreducible representation of the symmetry group, i.e. the generator acting on a one–particle state gives another one–particle state of the same representation. For an exact symmetry of the Lagrangian $[Q, \mathcal{L}] = 0$, this realization results in degenerate multiplets of particles (as discussed above), conserved charges, massless chiral fermions and massless gauge bosons. However, alternative realizations exist! We introduce the following theorem in order to continue.

Theorem 2 (Goldstone's Theorem)**.** *Let the Lagrangian $\mathcal{L}$ be invariant to some symmetry group G. Let Q be a generator of a continuous symmetry transformation of $\mathcal{L} \propto V(\phi)$, where V is some field potential. Taking an infintesimal transformation of the form Q and evaluating at the field minimum $\bar{\phi}$ of the Lagrangian potential V, one can derive the following condition on the field ϕ:*

$$\left(\frac{\partial^2 V}{\partial\phi_a \partial\phi_b}\right)\Bigg|_{\phi=\bar{\phi}} Q^i_{bc}\bar{\phi}_c = 0 \ . \tag{2.25}$$

The second order partial derivative of the potential is known as the mass matrix for fluctuations of the fields about the minimum of the potential. This restriction can be satisfied in two possible ways. One such way is the aforementioned Wigner–Weyl symmerty realization, in which the product of the generator on the vacuum is identically zero. However, if the product $Q^i_{bc}\bar{\phi}_c \neq 0$, the generator Q of the corresponding symmetry transformation is said to be spontaneously broken by the vacuum. Then, the mass matrix must have zero eigenvalue in order to uphold the symmetry. Thus, for each broken generator of the symmetry, a massless fluctuation is produced, yielding a corresponding massless Nambu–Goldstone boson upon quantization. The number of Nambu–Goldstone bosons produced is equivalent to $dim(G) - dim(G_{res.})$, where $G_{res.}$ is the residual symmetry group unbroken by $\bar{\phi}$.

As stated in the remarkable Theorem 2, in fact, the vacuum may not be invariant to a particular symmetry group even if the Lagrangian is. In this case of an exact symmetry of the Lagrangian $[Q, \mathcal{L}] = 0$, it is admissable that:

$$Q^a \left|0\right\rangle \neq 0 \ . \tag{2.26}$$

This phenomenon is known as *spontaneous symmetry breaking*, and implies that our generators no longer annhilate the vacuum. In the context of chiral symmetry, the axial generators are known to be spontaneously broken since the ordinary flavour symmetry is still intact. This symmetry breaking pattern is represented by the breaking of the chiral group $\mathrm{SU}(2)_L \times \mathrm{SU}(2)_R \to \mathrm{SU}(2)_V$ down to the isospin subgroup . This particular realization of a symmetry is known as the Nambu–Goldstone realization. The fantastic consequence of this theorem is the production of the Nambu–Goldstone bosons for each of the broken generators; the three pions. Though, Theorem 2 states that the fluctuations are massless, however we know that pions are in fact massive. This can be understood directly as a result of the additional explicit symmetry breaking $[Q, \mathcal{L}] \neq 0$ caused by non–zero quark masses, made explicit in Eq. (2.17). While in the case of only spontaneuous breaking the Nambu–Goldstone bosons are created as massless fluctuations, the addition of explicit symmetry breaking assigns mass to the pions.

In summary, utilizing the Nambu–Goldstone realization for chiral symmetry, it can be shown that due to spontaneous breaking chiral fermions directly acquire mass and Nambu–Goldstone bosons are produced from the broken symmetry generators. Further, the explicit symmetry breaking in the Lagrangian leads to the acquisition of mass by the Nambu–Goldstone bosons. This completes our understanding of the low–energy properties of QCD, and provides us the foundation for constructing an effective field theory for low–energy QCD based on the chiral symmetry breaking pattern.

2.1.3 Effective Lagrangians

The next step in the process of constructing an effective field theory for QCD is to write down the most general Lagrangian consistent with the broken (and unbroken) QCD symmetries [41, 42]. Before this can be accomplished, however, we must clarify a few details. First, we must quantitatively identify the energy scale of low–energy nuclear physics, which we have only spoken about ambiguously prior to this. As we are interested in nuclear dynamics, we wish to eliminate the complexity of considering nucleons as composite systems of quarks. Hence, the degrees of freedom that are relevant to nuclear theory are nucleons and pions. Nucleons are treated as fundamental objects in this scheme, despite physically being built from

quark constituents, with pions serving the role of Goldstone bosons corresponding to the spontaneously broken chiral symmetry of QCD.

Energy scale and perturbation theory

In order to tractably use Feynman's diagramatic approach for interactions in a QFT, we require a perturbative scheme. Yet, the strong coupling of gluon fields in the QCD Lagrangian makes the interaction highly non–perturbative, and hence the diagramtic approach will fail for finite sums of terms. For QCD, we must be more clever with constructing a perturbative expansion in the desired energy regime. In nuclear physics, we identify that the relevant degrees of freedom (fundamental fields) are nucleons and pions. In principle, this is analogous to setting the energy scale of the theory.

Qualitatively, we can determine the hard–scale at which this perturbation theory will be invalid. This scale can be motivated in a few different ways. For one, we have chosen to restrict ourselves to light–QCD, in which we only need to describe the u and d quarks. The mass difference between the light quarks (u, d, s) and the heavier quarks (c, b, t) is approximately 1 GeV, and the mass difference between the u and d quarks and the s quark is ~ 100 MeV. Furthermore, a large gap in the masses of the pions ($m_{\pi^\pm} \approx 140$, $m_{\pi^0} \approx 135$) and the vector mesons (i.e. $M_\rho \approx 775\,\text{MeV} \sim 1\,\text{GeV}$) provides additional motivation to describe the hard chiral symmetry breaking scale as $\Lambda_\chi \sim 1\,\text{GeV}$. Doing so, one is setting the energy scale above which the physics is neglected, which corresponds to the 'freezing out' of higher energy quark–gluon processes.

Remark. Of course, it is important to wonder about the value of the physics neglected above Λ_χ to nuclear processes. As we will learn, the high–energy physics is captured in constants that emerge naturally at each chiral order in ChPT. These are known as low–energy constants and they are fundamental parameters of the theory which may be determined empirically or, more recently, from sophisticated lattice QCD calculations [43, 44, 45].

On the other hand, the pion mass $m_\pi \approx 135\,\text{MeV}$ represents the scale of interaction processes as pions are the force carrying boson in this theory. With this in mind, the pion mass is understood to be representative of the soft scale Q of theory. Hence, in this scheme, one way in which we intuitively count perturbative contributions is in terms of the order of the pion masses.

To summarize, we have identified the high– and low–energy scales of the problem, and we have learned that the ChPT expansion will be organized in terms of orders of $\frac{Q}{\Lambda_\chi}$, where for now one may assume that Q is of the order m_π. We will elaborate on the soft scale more when discussing the power counting scheme in Sec. 2.1.4.

Pion transformation properties

First, let us take the energy to be so small that only pions must be considered. We proceed in this way to construct the most general Lagrangian for pion–pion ($\pi\pi$) interactions. Let us further restrict ourselves to QCD in the chiral limit (massless QCD), so chiral symmetry is exact. To build a chiral invariant Lagrangian, we must ascertain how pion fields transform under chiral rotations.

We know that pions are formed as quark–antiquark pairs, and so in consideration of light-QCD, we gather that three types of pions may be formed using u and d quarks: $|\pi^+\rangle = |u\bar{d}\rangle$, $|\pi^-\rangle = |d\bar{u}\rangle$, and $|\pi^0\rangle = |u\bar{u}\rangle = |d\bar{d}\rangle$. In particular, we know the following:

1. The pion fields form an isospin triplet and will transform linearly under $\text{SU}(2)_V \subset \text{SU}(2)_L \times \text{SU}(2)_R$ global isospin transformations in the chosen representation

2. The chiral group must be realized non–linearly as we only have three pion fields, yet $\text{SU}(2)_L \times \text{SU}(2)_R \sim \text{SO}(4)$ group requires four coordinates to construct the fundamental representation

We must then explore the transformation properties of the isospin triplet of pion fields in the SO(4) representation. First, we begin with the naive linear transformation of a vector $(\vec{\pi}, \sigma)$ under an infinitesimal SO(4) rotation, which is completely parameterized by six angles $\{\theta_i^{V,A}\}$ $i\,\epsilon\{1,2,3\}$. The (V, A) labels correspond to vector and axial–vector transformations. Considering a linear SO(4) transformation, we have

$$\begin{bmatrix}\vec{\pi}\\ \sigma\end{bmatrix} \to \begin{bmatrix}\vec{\pi}\,'\\ \sigma'\end{bmatrix} = \Big[\mathbb{1} + \sum_{i=1}^{3}\theta_i^V V_i + \sum_{i=1}^{3}\theta_i^A A_i\Big]\begin{bmatrix}\vec{\pi}\\ \sigma\end{bmatrix}\ , \tag{2.27}$$

where

$$\sum_{i=1}^{3}\theta_i^V V_i = \begin{bmatrix}0 & -\theta_3^V & \theta_2^V & 0\\ \theta_3^V & 0 & -\theta_1^V & 0\\ -\theta_2^V & \theta_1^V & 0 & 0\\ 0 & 0 & 0 & 0\end{bmatrix} \qquad \sum_{i=1}^{3}\theta_i^A A_i = \begin{bmatrix}0 & 0 & 0 & \theta_1^A\\ 0 & 0 & 0 & \theta_2^A\\ 0 & 0 & 0 & \theta_3^A\\ -\theta_1^A & -\theta_2^A & -\theta_3^A & 0\end{bmatrix}\ . \tag{2.28}$$

The form of these matrices is important as the V_i matrices have a one–to–one correspondance with the generators of the fundamental representation of SO(3) $\sim$ SU(2) $\subset$ SO(4); the V_i generate all possible SO(3) rotations in the SO(4) group. Furthermore, in our efforts to realize SO(4) non–linearly, we must make note of the fact that the normalization of the pion fields (and the corresponding fourth component σ) is relativistically constrained in the following way: $\vec{\pi}^2+\sigma^2 = F_\pi^2$, where F_π is a constant of dimension mass. Hence, the pion fields, with σ, geometrically represent points on a four dimensional sphere. Substituting this constraint in the linear transformation defined in Eq. (2.27), we have that the following transformation properties for pions emerge:

$$\begin{aligned}\vec{\pi} &\xrightarrow{\vec{\theta}^V} \vec{\pi'} = \vec{\pi} + \vec{\theta}^V \times \vec{\pi}\ ,\\ \vec{\pi} &\xrightarrow{\vec{\theta}^A} \vec{\pi'} = \vec{\pi} + \vec{\theta}^A\sqrt{F_\pi^2 - \vec{\pi}^2}\ ,\end{aligned} \tag{2.29}$$

where we have $\vec{\theta}^{A,V} = [\theta_1^{A,V}, \theta_2^{A,V}, \theta_3^{A,V}]^T$. This is exactly the desired non–linear realization of the chiral group $\mathrm{SU}(2)_L \times \mathrm{SU}(2)_R \simeq \mathrm{SO}(4)$ [1] with the triplet of pion fields. In this manner, we have maintained the requirement that pion fields transform linearly under $\mathrm{SU}(2)_V \simeq \mathrm{SO}(3)$ isospin rotations, which are fully parameterized by the set $\{\theta_i^V\}$. As noted in Ref. [5], we may conveniently write linear transformations in SO(4) as

$$U = \frac{1}{F_\pi}(\sigma\mathbb{1}_{2\times 2} + i\vec{\pi}\cdot\vec{\tau})\ , \tag{2.30}$$

which, under the non–linear realization of SO(4) where pions are the sole degrees of freedom, becomes

$$U = \frac{1}{F_\pi}(\sqrt{F_\pi^2 - \vec{\pi}^2}\mathbb{1}_{2\times 2} + i\vec{\pi}\cdot\vec{\tau})\ . \tag{2.31}$$

Here $\vec{\tau}$ is the vector of usual 2×2 Pauli matrices. Additionally, we demand that

$$U \to U' = LUR^\dagger = RUL^\dagger \qquad L, R\,\epsilon\,\mathrm{SU}(2)_L \times \mathrm{SU}(2)_R \tag{2.32}$$

where L and R are global flavour rotations acting in the left– and right–handed chiral spaces, respectively. In particular, the condition $\vec{\pi}^2 + \sigma^2 = F_\pi^2$ enforces the unitarity of the matrix U.

[1] It is neccessary to note that the notation $\approx$ refers to a local isomorphism between the groups shown. Two topological groups are said to be locally isomorphic if there exists open neighbourhoods around the respective unity elements which may be connected by a homeomorphism. This information is not intrinsically important to this thesis, but is mentioned for notational purposes.

Leading order pion Lagrangian

With our understanding of pion field transformation properties complete, we may now construct the most general chiral invariant Lagrangian for pions in massless QCD. Before continuing, we further wish to emphasize that only global chiral rotations are considered, and so the transformation matrices L and R are independent of space–time coordinates x^μ. This implies that derivatives of U – objects such as $\partial_\mu U$ or $\partial_\nu \partial_\mu U$ – transform in precisely the same way as U. We may then proceed as in Ref. [5] and construct all terms of the effective Lagrangian using flavour space trace operations $\langle \cdots \rangle_f$ of products of U and $U^\dagger$, as well as derivatives of these quantities. The constraint of Lorentz covariance further restricts the types of terms which can be written to those with an even number of derivatives. Recalling that we expand our pion Lagrangian as $\mathcal{L}_\pi = \mathcal{L}_\pi^{(0)} + \mathcal{L}_\pi^{(2)} + \cdots$ and noting that $\mathcal{L}_\pi^{(0)} = UU^\dagger = \mathbb{1}$ may be neglected in the Lagrangian, we write the LO Lagrangian for pion interactions as:

$$\mathcal{L}_\pi^{(2)} = \frac{F_\pi^2}{4} \langle \partial_\mu U \partial^\mu U^\dagger \rangle_f \ . \tag{2.33}$$

The constant F_π is chosen to match the usual Lagrangian for a massless scalar field, i.e. the usual pion Lagrangian to second order is written as $\mathcal{L}_\pi^{(2)} = \frac{1}{2}\partial_\mu \vec{\pi} \cdot \partial^\mu \vec{\pi} + \frac{1}{2F_\pi^2}(\partial_\mu \vec{\pi} \cdot \vec{\pi})^2 + O(\vec{\pi}^6)$.

In the end, we have created a non–linear realization of the chiral group $\mathrm{SU}(2)_L \times \mathrm{SU}(2)_R$ in terms of the triplet of pion fields and determined the corresponding representation of the $\mathrm{SU}(2)_V \simeq \mathrm{SO}(3)$ isospin group embedded in the chiral group. This allowed us to then construct the most general effective Lagrangian for pions to leading order. As a final point, we notice that in the limit of $\vec{\pi} \to \vec{0}$, the ground-state of theory will be characterized by the vacuum expectation value $(\vec{0}, F_\pi)$, and so the theory is not $\mathrm{SU}(2)_L \times \mathrm{SU}(2)_R \simeq \mathrm{SO}(4)$ chiral invariant, however it still retains SO(3) gauge invariance. This is exactly what is expected in accordance with the spontaneous breaking of chiral symmetry. In particular, the intact symmetry $\mathrm{SO}(3) \simeq \mathrm{SU}(2)_V$ corresponds to the global isospin symmetry in the Lagrangian.

Remark. There is a particular subtlety in this approach, notably, the choice of representation for the chiral group is not unique. In fact, there are an arbitrary number of realizations possible for the chiral group, and as a result the definition of U is similarly arbitrary. One is tempted to ask how this affects the physics described by the chiral group. However, as discussed in Refs. [41, 42], every representation of the chiral group is equivalent under non–linear field redefinitions; they all provide the same group structures. Furthermore, Haag remarkably showed that such field redefinitions have no effect on the resultant $S-$matrix elements [46].

Pions in a massive QCD

The natural way to extend the previous description of massless QCD to that of light–QCD, in which we assign masses to the u and d quarks, is to consider the presence of an arbitrary external field H interacting with the quarks. This is done by including a term of the form $\mathcal{L}_{ext.} = -\bar{\psi}_q H \psi_q$ in the massless QCD Lagrangian, $\mathcal{L}_0$. If the external field H transforms in precisely the same was as U, that is $U \to U' = LUR^\dagger$, then the resulting Lagrangian would be similarly chiral invariant. Hence, to recover massive QCD and account for explicit chiral symmetry breaking in the Lagrangian, we must include all chiral invariant terms constructed from the external field H and U and $U^\dagger$ (as well as derivatives of these quantities), and then make the final substitution $H \to M$, where $M = \mathrm{diag}(m_u, m_d)$ is the quark mass matrix. Since we treat the quark masses as perturbative effects in QCD, the LO terms which contribute to the Lagrangian should only contain a single insertion of the external field H and no derivatives of the pion fields. Thus, making the substitution $H \to M$, only a single symmetry breaking term is possible at LO, and it is given by:

$$\mathcal{L}_{ext.} = \frac{F_\pi^2 B}{2} \langle MU + MU^\dagger \rangle_f \ . \tag{2.34}$$

This term may be expanded in pion fields as

$$\begin{aligned}\mathcal{L}_{ext.} &= F_\pi^2 B(m_u + m_d) - \frac{B}{2}(m_u + m_d)\vec{\pi}^2 + O(\vec{\pi}^4) \\ &= M^2 F_\pi^2 - \frac{1}{2}M^2\vec{\pi}^2 + O(\vec{\pi}^4)\ .\end{aligned} \tag{2.35}$$

The first term is constant and hence does not impact the physics of the Lagrangian. The second term in this expression describes the pion mass term which results from the inclusion of non–zero quark masses. Notably, the theory predicts that all pions $\{|\pi^+\rangle, |\pi^-\rangle, |\pi^0\rangle\}$ have equivalent masses, $M_\pi^2 = B(m_u + m_d)$. Of course, when one includes the full flavour spectrum of quarks, this will not be the case.

The question remains of how to count these effective Lagrangian terms with pion masses in a consistent way with the derivatives of pion fields. Thankfully, an intuitive solution exists. A derivative acting on pion fields $\partial_\mu\vec{\pi}$ creates pion momenta $\vec{p}_\pi$ with the same order as the number of derivatives. These pion momenta are generally assumed to be low for nuclear physics processes, in fact, they are generally of the order of the pion mass M_π. It is therefore natural to consider terms with explicit pion mass insertions as being equivalent in contribution to those with applications of derivatives on pion fields, so long as they are kept to the same order.

The inclusion of all possible chiral invariant and symmetry breaking terms means that we have constructed the most general effective Lagrangian consistent with the (broken and unbroken) QCD Lagrangian symmetries. Hence, we have the major result of this section:

$$\mathcal{L}_\pi^{(2)} = \frac{F_\pi^2}{4}\langle\partial_\mu U\partial^\mu U^\dagger + 2B(MU + MU^\dagger)\rangle_f\ , \tag{2.36}$$

the pion Lagrangian to LO.

The nucleon–nucleon (NN), three–nucleon (NNN) and nucleon–pion (Nπ) interactions are all derived in a similar spirit, and are discussed at length in Refs. [33, 5, 34, 35].

2.1.4 Chiral power counting

In the last step of the previous section, we implied the idea that the effective Lagrangian terms can be counted in a consistent manner. Moreover, we are interested in an exact method for determining all possible diagrams which will contribute at a given order in ChPT. The effective Lagrangian has an infinite number of terms, which implies that we are required to evaluate an infinite number of Feynman diagrams in order to produce an exact result. However, as discussed earlier, we have established a perturbative scheme that can be used to analyze the importance of graphs appearing in the diagramatic approach. We choose to organize the expansion in terms of powers of $\frac{Q}{\Lambda_\chi}$, where Q is representative of the pion 4–momentum, nucleon 3–momentum or m_π, and Λ_χ represents the hard chiral symmetry breaking scale above which the effective theory breaks down. We represent the powers of this expansion by ν, and we require a counting procedure for determining the power ν to assign to a particular Feynman graph. This procedure is known as power counting, and doing so allows us to determine the effective "strength" of a diagram's contribution in the low–energy expansion.

The following rules are a summary of the important *Feynman rules for covariant perturbation theory* in application to ChPT.

1. Nucleonic propagators are proportional to Q^{-1}
2. Pionic propagators are proportional to Q^{-2}
3. Derivative operators are proportional to Q
4. Four–momentum integrations are proportional to Q^4

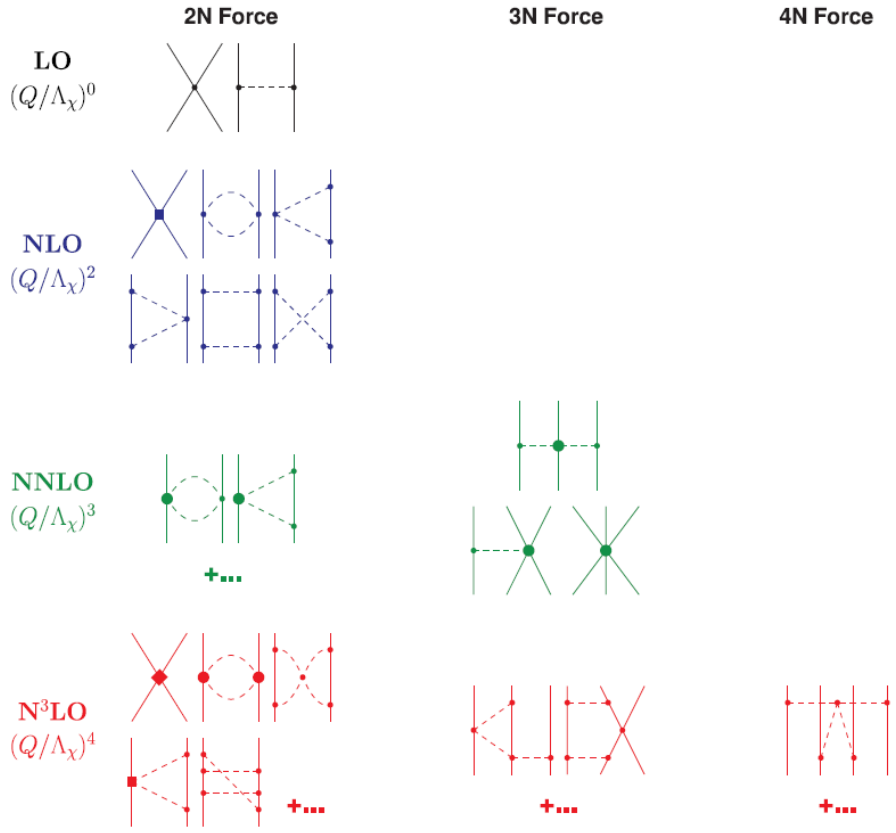

Figure 2.1: ChPT interaction diagrams for two– and many–nucleon interactions. Nucleon field are represented by solid lines, and pion fields by dashed lines. Dots, filled circles and filled squares represent contributions from $\Delta_i = 0, 1, 2$, respectively (see Eq. (2.37)). Many–nucleon forces are created in a hierarchical fashion, with two–body being the dominant interaction. Figure originally presented as **Fig. 1** in Ref. [5].

Utilizing this ruleset, it is possible to derive the powers of irreducible diagrams involving A–nucleons, as was originally done by Weinberg in Refs. [47, 48, 49]. However, the original power counting scheme is insufficient for describing three–nucleon dynamics, as the power ν can take on negative values (which leads to a breakdown of the expansion) as discussed in Ref. [5]. We are then required to adopt a more suitable power counting scheme consistent with Ref. [50]:

$$\nu = -2 + 2A - 2C + 2L + \sum_{i=1}^{n} \Delta_i \qquad \Delta_i = d_i + \frac{n_i}{2} - 2 \ , \tag{2.37}$$

where A is the number of nucleons, C is the number of "separately connected" pieces of the diagram and L refers to the number of loops in a given diagram. Δ_i is defined for the i–th vertex, and the sum runs over all vertices in the diagram. Further, d_i is counted as the number of derivatives (or corresponding pion mass insertions) and n_i refers to the number of nucleon legs. In this power counting scheme, all powers ν are bounded from below ($\nu \geq 0$) which is absolutely necessary for guaranteeing convergence of the low–energy ChPT expansion. Furthermore, at any particular order ν, one may use this scheme to estimate the error of the theory by understanding the following terms in the low–energy expansion are suppressed by a factor of $\left(\frac{Q}{\Lambda_\chi}\right)^{\nu+1}$. In this ordering at a particular chiral order ν there will be a finite number of Feynman graphs, ensuring that the effective theory is now tractable!

In fact, what is particularly special about this expansion is the manner in which the many–nucleon interactions naturally emerge with increasing chiral order. Referring to Fig. 2.1.4, Feynman interaction diagrams from ChPT are presented. Interaction diagrams are presented for the two–nucleon interaction in the first column, the three–nucleon interaction in the second column and the four–nucleon interaction in the last column. Consider the leading order (LO) diagrams for which $\nu = 0$; they only appear at the two–body level and are simple contact and one–pion exchange terms. At next–to–leading–order (NLO), for which $\nu = 2$ (all terms vanish at order $\nu = 1$ due to parity and time–reversal invariance), we still have only the two–nucleon interaction. However, we see the emergence of the more complicated two–pion exchange diagrams. At next–to–next–to–leading–order ($\mathrm{N^2LO}$), we finally have non–vanishing three–nucleon forces. Since they are suppressed by $\left(\frac{Q}{\Lambda_\chi}\right)^3$, the ChPT expansion naturally captures why 2N $\gg$ 3N. Higher orders of the expansion contain more complicated two–pion exchange diagrams with increasing numbers of loops as well as three–pion exchange diagrams, though the three–pion exchange diagrams have been shown to be negligible [51, 52]. With the technique of chiral power counting, the low–energy ChPT expansion establishes a nuclear force hierarchy, with increasingly complex pion exchange processes and naturally emerging many–nucleon interactions.

Power counting is the last tool required to develop the two– and three–nucleon interactions. With the development of ChPT, the nuclear Hamiltonian may be constructed in a realistic way from the underlying symmetries of low–energy QCD and solved utilizing *ab initio* nuclear many–body approaches.

2.2 From Nucleons to the Nucleus

With the development of the nuclear interactions complete, we now guide the reader through the quantum many–body problem and the modern approaches utilized to solve for the intrinsic wave functions of nuclear systems. In this section we present various topics from quantum theory relevant for understanding the nuclear many–body problem. In particular, we will provide a discussion on the fundamentals of the no–core shell model, an *ab initio* theory for the description of nuclei which utilizes solely the aforementioned nuclear interactions as input for calculations.

2.2.1 Review of angular momentum coupling and tensors

In general, the total angular momentum of a quantum system (including many–body systems) is conserved. Let us consider the simplest case of two particles with momenta $\vec{J}_1$ and $\vec{J}_2$ corresponding to states $|J_1 M_1\rangle$ and $|J_2 M_2\rangle$. Under the standard tensor operation between Hilbert spaces, these states may be combined by the standard tensor product as $|J_1 M_1 J_2 M_2\rangle = |J_1 M_1\rangle \otimes |J_2 M_2\rangle$. However, a more convenient prescription exists for multi–particle systems.

As already stated, the total $\vec{J} = \vec{J}_1 + \vec{J}_2$ is conserved. The allowed values of J are given by the triangle condition, $\Delta(J_1 J_2 J)$, which constrains $J \,\epsilon \{|J_1 - J_2|, \ldots, J_1 + J_2\}$. It is then possible to write states of total J momentum $|J_1 J_2 J M\rangle$ as linear combinations of the uncoupled two–particle states,

$$|J_1 J_2 J M\rangle = \sum_{M_1 M_2} \langle J_1 M_1 J_2 M_2 | J_1 J_2 J M\rangle \, |J_1 M_1 J_2 M_2\rangle \;\; : \;\; M_1 + M_2 = M \tag{2.38}$$

where (under specific normalization and phase–conventions) the coefficients of this expansion are equivalent to the Clebsch–Gordan coefficients:

$$\langle J_1 M_1 J_2 M_2 | J_1 J_2 J M\rangle = \langle J_1 M_1 J_2 M_2 | J M\rangle \;\epsilon \mathbb{R} \tag{2.39}$$

As the coefficients are real, they are guaranteed to be Hermitian. More detailed descriptions of angular momentum coupling, as well as three particle coupling procedures, may be found in Refs. [53, 54]. These procedures can be applied to couple to an arbitrary number of momenta.

Tensors and tensor products

Here we introduce the basic properties (relevant for our work) of a rank–λ tensor T^λ_μ, which is a set of $2\lambda+1$ operators with $\mu\,\epsilon\{-\lambda,\ldots,\lambda\}$. One may specify the transformation properties of a tensor operator by requiring commutation with the $J_\pm$ and J_z operators, which leads to some remarkable results in quantum theory. In particular, the use of tensors allows for the reduction M–state dependence by Wignar–Eckart theorem:

$$\langle JM|\,T^\lambda_\mu\,|J'M'\rangle = (-1)^{2\lambda}\frac{(J'M'\lambda\mu|JM)}{\sqrt{2J+1}}\langle J||T^\lambda||J'\rangle\ , \tag{2.40}$$

where $\langle J||T^\lambda||J'\rangle$ is a J–reduced matrix element.

Further, arbitrary tensors $T^{\lambda_1}_{\mu_1}$ and $U^{\lambda_2}_{\mu_2}$ may be combined into the tensor S^λ_μ with the angular momentum coupling techniques introduced prior as:

$$S^\lambda_\mu = [T^{\lambda_1}\otimes U^{\lambda_2}]^\lambda_\mu = \sum_{\mu_1\mu_2}\langle\lambda_1\mu_1\lambda_2\mu_2|\lambda\mu\rangle\,T^{\lambda_1}_{\mu_1}U^{\lambda_2}_{\mu_2}\ . \tag{2.41}$$

One can derive relations for the reduced matrix elements of the tensor product operator; in general one must derive separate results for when T^{λ_1} and U^{λ_2} act in the same or different vector spaces.

2.2.2 General many–body problem for Fermions

The basic construct of the general many–Fermion problem is the Schrödinger equation for n Fermions of mass m in a central potential U and interacting through a two–body potential V:

$$H\,|\psi\rangle = \left\{H^{(0)}+W\right\}|\psi\rangle = \left\{\sum_{i=1}^{n}(T_i+U_i)+\sum_{i<j}^{n}V_{ij}\right\}|\psi\rangle = E_\psi\,|\psi\rangle\ \ , \tag{2.42}$$

where $T_k=\frac{P_k^2}{2m}$ is the kinetic term, U_k is a central potential (generally taken to be zero in vacuum) and V_{ij} is the two–nucleon interaction term.

It is convenient to first address the simpler problem $H^{(0)}\,|\phi_\alpha\rangle = E^{(0)}_\alpha\,|\phi_\alpha\rangle$, for which the solution may be formulated as

$$\langle\vec{r}_1\cdots\vec{r}_n|\phi_\alpha\rangle = \prod_{i=1}^{n}\langle\vec{r}_i|a_i\rangle = \phi(\vec{r})_{a_i}\cdots\phi(\vec{r})_{a_n} \tag{2.43}$$

and

$$E^{(0)}_\alpha = \sum_{i=1}^{n}\mathcal{E}_{a_i}\ . \tag{2.44}$$

Here $\alpha=\{a_1,\cdots,a_n\}$ is one set of possible single–particle configurations, and the a_i correspond to the single–particle quantum numbers of solutions to the equation

$$(T+U)\,|a_i\rangle = \mathcal{E}_{a_i}\,|a_i\rangle\ \ . \tag{2.45}$$

The set of solutions $\{|a_i\rangle\}$ must be chosen such that they form a complete orthonormal single–particle basis, hence $\langle a_i|a_j\rangle=\delta_{ij}$. With this, we may reformulate the many–body problem in terms of the $\{|\phi_\alpha\rangle\}$ basis, which is assumed to be complete and orthonormal. Then,

$$|\psi\rangle = \sum_\alpha c_\alpha\,|\phi_\alpha\rangle \qquad\rightarrow\qquad \sum_\alpha c^*_\beta c_\alpha\,\langle\phi_\beta|\,H\,|\phi_\alpha\rangle = E_\psi \tag{2.46}$$

In general, this characterizes the approach to solving the many–body Schrödinger equation for nuclear states. The main ingredients are one– and two–body operator matrix elements (at least as far as we have considered).

Fermions

As we are studying systems of identical Fermions, we must ensure that the systems obey the correct Fermionic statistics; the *spin–statistics theorem* was first derived by Pauli from the simple postulates of (i) positive energy (ii) commutation of observables with no causal connection (locality) [55].

Definition 2.2.1 (Spin–Statistics Theorem)**.** The spin–statistics theorem states the following:

(i) Particles with half–integer spin are restricted by the Pauli exclusion principle, i.e. only one Fermion may occupy a given quantum state

(ii) Particles with integer spin are not restricted, i.e. an arbitrary number of bosons may occupy the same quantum state

---

Making use of this beautiful theorem, when working with identical Fermions we must ensure that our states are completely antisymmetric with respect to the coordinate exchange operator P_{ij} (swaps the coordinate vectors of nucleons i and j). In particular, this may be achieved through use of the Cartesian coordinate Slater determinant (SD) basis [56]. In general for a many–body state $|\psi_\alpha\rangle$, we write the following:

$$\langle \vec{r}_1 \cdots \vec{r}_n | \psi_\alpha \rangle = \langle \vec{r}_1 \cdots \vec{r}_n | a_1 \cdots a_n \rangle_{\mathcal{A}} = \frac{1}{\sqrt{n!}} \begin{vmatrix} \phi_{a_1}(\vec{r}_1) & \cdots & \phi_{a_1}(\vec{r}_n) \\ \vdots & \ddots & \vdots \\ \phi_{a_n}(\vec{r}_1) & \cdots & \phi_{a_n}(\vec{r}_n) \end{vmatrix} \tag{2.47}$$

where $\phi_{a_i}(r_j)$ is a single–particle wave function with quantum numbers a_i and coordinate $\vec{r}_j$. The subscript $\mathcal{A}$ refers to the antisymmetrized quantum state, and differs from the usual direct tensor product representation of a many–body state $|a_1 \cdots a_n\rangle = |a_1\rangle \otimes \cdots \otimes |a_n\rangle$. The operation $|\cdots|$ is a symbolic determinant of the matrix composed of all single–particle quantum states and possible coordinate arguments. Notice that by the properties of determinants, if we have $a_i = a_j$ for arbitrary $i, j \, \epsilon \{1, \ldots, n\}$, then the result of the determinant operation will be null. Hence, Pauli exclusion is explicitly enforced by SD antisymmetrization.

Conserved quantum numbers

In order to further characterize the features of our many–body basis states $|\psi\rangle = |a_1 \cdots a_n\rangle$, we must identify the conserved quantum numbers of the Hamiltonian system introduced prior. Consider the Schrödinger equation $H|\psi\rangle = E|\psi\rangle$ where H is given by Eq. 2.42.

Angular Momentum: The angular momentum operator is defined as $\vec{J} = \vec{L} + \vec{S}$, with

$$\vec{J} = \sum_{i=1}^{n} \vec{J}_i \qquad\qquad J_z^{(i)} = \sum_{i=1}^{n} J_z^{(i)} \tag{2.48}$$

where i denotes one of the n particles. Since the Hamiltonian is a scalar quantity in spatial (i.e. Cartesian) coordinates and is spherically symmetric, the expectation value is invariant to the orientation of the system. This invariance is expressed through commutation of the Hamiltonian H and the total angular momentum operator $\vec{J}^2$.

$$[H, J^2] = 0 \qquad\qquad [H, J_z] = 0 \tag{2.49}$$

Since the commutator with the Hamiltonian is zero, there exists a basis in which the operators are simultaneously diagonalizable. Hence we choose our many–body states $|\psi\rangle$ to have definite values of J and J_z.

Parity: The parity of an n particle state is given by:

$$\pi = \prod_{i=1}^{n} \pi_{int.}^{(i)} \pi_{orb.}^{(i)} = \prod_{i=1}^{n} (-1)^{l_i} \qquad \pi \in \{-1, 1\} \ , \tag{2.50}$$

where $\pi_{int.} = 1$ is the intrinsic parity of the nucleon and $\pi_{orb.}$ is the parity contribution from the orbital angular momentum of the nucleon. The strong and electromagnetic Hamiltonians conserve parity, i.e. $\langle \psi_{\pi_1} | H | \psi_{\pi_2} \rangle = E_{\pi_2} \delta_{\pi_1 \pi_2}$. In this case, the eigenstates may be separated into two independent equivalence classes according to their transformation under parity. As parity is a valuable quantum number for classifying states, we choose to construct eigenstates with definite parity:

$$P |\psi^{\pm}\rangle = \pm 1 |\psi^{\pm}\rangle \ . \tag{2.51}$$

Remark. The weak interaction Hamiltonian does not conserve parity. However, effects of the weak interaction are very small and are often neglected, unless one is directly investigating weak physics, i.e. anapole moments [57, 58, 59]. Due to the relative size of the weak interaction effects, these calculations may be performed within a perturbation theory framework.

Isospin: Isospin is a quantum number used to identify that the proton ($t_z = \frac{1}{2}$) and the neutron ($t_z = -\frac{1}{2}$) may be seen as two different isospin states of the nucleon. The isospin operator is defined as

$$\vec{\mathcal{T}} = \sum_{i=1}^{n} \vec{t}^{(i)} \qquad\qquad \mathcal{T}_z = \sum_{i=1}^{n} t_z^{(i)} \tag{2.52}$$

and obeys the same algebraic rules as spin (though it is not a form of momentum). Further, isospin is conserved by the Hamiltonian. Thus, we choose to construct eigenstates with definite isospin, and so the action of the isospin operator on our many–body eigenstate may then be characterized by:

$$\mathcal{T}^2 |\psi\rangle = T(T+1) |\psi\rangle \qquad\qquad \mathcal{T}_z |\psi\rangle = T_z |\psi\rangle \ . \tag{2.53}$$

For an arbitrary nucleus with N_p protons and N_n neutrons, we have $T_z = \frac{N_p - N_n}{2}$.

Remark. A particular consequence of an exact isospin symmetry would be mirror symmetry; nuclei with opposite numbers of protons and neutrons would have identical spectra. However, the strong interaction weakly breaks isospin. More importantly, any major deviation from mirror symmetry is largely due to the Coulomb interaction, which strongly breaks isospin.

2.2.3 Creation and annhilation operator method

In this section we introduce the formalism of the creation and annhiliation operator approach, frequently referred to as the technique of second quantization [60]. This method is useful for describing systems of many identical particles and is heavily used in the following chapters.

A Fock state is defined as a state with well–defined (integer) particle number. For the case of A indistinguishable Fermionic particles, the space $\mathcal{F}^A$ is spanned by a basis of antisymmetric many–body states. These states are constructed from the standard product representation of single–particle Hilbert spaces, $\mathcal{H}^A = \mathcal{H} \otimes \cdots \otimes \mathcal{H}$. The Fock space is then given by the direct sum of all possible antisymmetrized Fermion spaces (from zero particles to A particles):

$$\mathcal{F}(\mathcal{H}) = \bigoplus_{A} (\mathcal{H}_{\mathcal{A}})^{\otimes A} = \mathbb{1} \oplus [\mathcal{H} \otimes \mathcal{H}]_{\mathcal{A}} \oplus [\mathcal{H} \otimes \mathcal{H} \otimes \mathcal{H}]_{\mathcal{A}} \oplus \cdots \ , \tag{2.54}$$

where the ellipses denote Fermion spaces with more than three particles. The general states of a Fock space are created from the vacuum state $|0\rangle$ through the use of creation operators $c^\dagger$. These operators act as maps between the n–particle subspaces of $\mathcal{F}$; they change the number of particles in a given state, mapping n–particle states to $(n+1)$–particle states. Furthermore, by use of the annihilation operators c, a particular state may be annihilated to an $(n-1)$–particle state (minimally to the vacuum state). We define the operators and their algebraic properties as follows:

$$\begin{aligned} c_a^\dagger |0\rangle &= |a\rangle & c_a^\dagger |a\rangle &= 0 \\ c_a |a\rangle &= |0\rangle & c_a |0\rangle &= 0 \end{aligned} \tag{2.55}$$

with

$$\{c_i, c_j\} = 0 \qquad \{c_i^\dagger, c_j^\dagger\} = 0 \qquad \{c_i, c_j^\dagger\} = \delta_{ij} \quad . \tag{2.56}$$

Notably, these last algebraic relations precisely capture the Fermi–Dirac statistics of the nucleons (anti–commutators for Fermions). A given n–particle state is then formed as

$$|a_1 \cdots a_n\rangle_{SD} = a_{a_n}^\dagger \cdots a_{a_1}^\dagger |0\rangle \tag{2.57}$$

and is inherently antisymmetrized due to the properties of the creation and annihilation operators. It can be shown that this is equivalent to the SD antisymmetrization.

This formalism is extremely convenient, and the second quantization approach is utilized to discretize and calculate operators in nuclear structure theory. Though, special attention must be paid to the annihilation operator c. While the creation operator $c^\dagger$ is a rank–j tensor, the same is not true for the operator c (see appendix of Ref. [61]). However, an operator which does obey the correct tensor transformation properties, and is hence a rank–j tensor, is written in terms of the standard annihilation operator as:

$$\tilde{c}_{jm} = (-1)^{j-m} (c^\dagger)_{j-m}^\dagger = (-1)^{j-m} c_{j-m} \quad . \tag{2.58}$$

2.2.4 No–core shell model

In this section we introduce the *ab initio* no–core shell model (NCSM), the computational many–body approach to solving the A–body Schroedinger equation, discussed at great length in Ref. [62]. *Ab initio* refers to the fact that the NCSM is a first–principles approach, taking solely the two– and three–nucleon interactions as input, to diagonalizing the intrinsic nuclear Hamiltonian:

$$H_{nuc.} = T_{rel.} + V = \frac{1}{A} \sum_{i<j}^{A} \frac{(\vec{p}_i - \vec{p}_j)^2}{2m_N} + \sum_{i<j}^{A} V_{NN}^{(ij)} + \sum_{i<j<k}^{A} V_{NNN}^{(ijk)} \tag{2.59}$$

where m_N denotes the nuclear mass. Notably, this Hamiltonian differs from Eq. (2.42) in the manner of preserving translation invariance; more attention will be paid to this fact shortly. The NCSM describes the nucleus as a system of A interacting non–relativistic, point-like particles interacting via inter–nucleonic forces, i.e. those derived from chiral EFT described in Sec. 2.1. At the present time, it is generally only possible to include the two– and three–nucleon interactions, depicted in Eq. (2.59), though there remains interest in calculating and testing the impact of four–nucleon interactions [63, 64]. In principle, one can include up to A–body interaction terms, however the contribution of higher–body terms (greater than the three–body level) is generally small. In fact, *ab initio* calculations of larger nuclear systems have shown that the few–body physics captured by the two– and three–nucleon interactions are sufficient for describing nuclear properties [65, 66]. In the NCSM, all A nucleons are considered to be active degrees of freedom. This makes the diagonalization procedure computationally quite expensive; a discussion on the general size of the *ab initio* nuclear problem and the scalability of Many–Fermion Dynamics nuclear (MFDn) codes is provided in Ref. [67].

In general, the NCSM makes use of a large but finite expansion in a set of antisymmetrized harmonic oscillator (HO) many-body basis states represented in the Jacobi basis (see Sec. 2.2.4 for the definition of relative coordinates):

$$\langle \vec{\xi}_1 \cdots \vec{\xi}_{A-1} | \Psi^A \rangle = \sum_{N=0}^{N_{max}} \sum_{\alpha} c_{N\alpha} \langle \vec{\xi}_1 \cdots \vec{\xi}_{A-1} | \Phi^A_{N\alpha} \rangle \tag{2.60}$$

Relative coordinates encode the fact that the nuclear Hamiltonian is translation invariant, and it is hence the natural coordinate basis in which to represent nuclear wave functions. Here α refers to one possible configuration of the $\{a_1, \ldots, a_A\}$ quantum numbers. The nuclear many–body states satisfy the symmetry properties described in the previous section; that is, they are chosen to be eigenstates of total angular momentum and projection, parity, and isospin. This expansion is characterized by two parameters, $\hbar\Omega$ and N_{max}, which correspond to the HO frequency and the total number of oscillator excitation quanta considered. In order to understand the many–body truncation scheme, we refer to Fig. 2.2. In this diagram, we begin with the nucleons distributed according to the lowest Pauli configuration (minimal excitation), the contribution of which to the total oscillator quanta is called N_{pauli}. For a value of N_{max}, we consider the possible excitations of all nucleons to other energy levels, provided the total sum of the quanta associated with the nucleons does not exceed the sum of $N_{pauli} + N_{max}$. Hence, the possible many–body states for a given N_{max} are described by the total number of oscillator quanta

$$N = \sum_{i=1}^{A} N_i = \sum_{i=1}^{A} 2n_i + l_i \leq N_{pauli} + N_{max} \ . \tag{2.61}$$

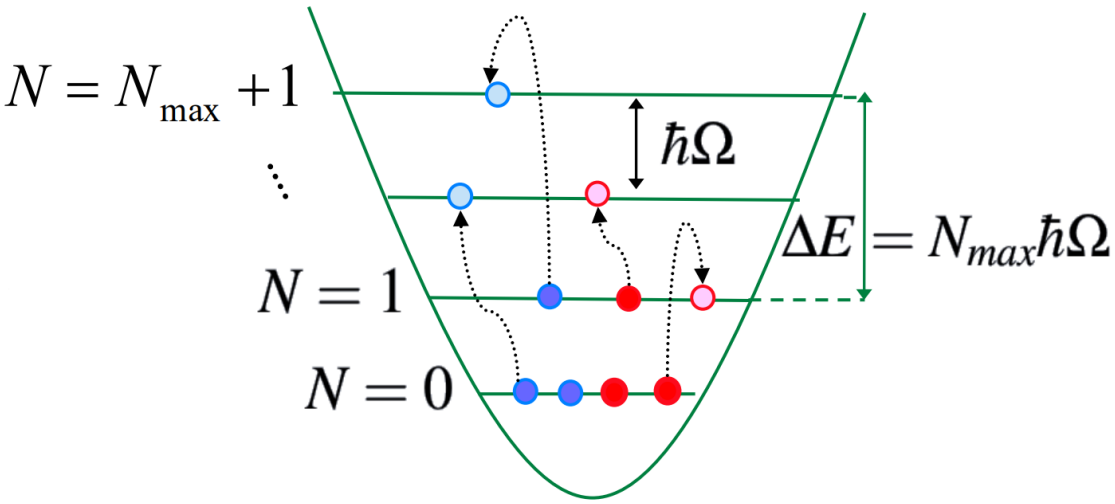

Figure 2.2: Truncation diagram for the NCSM HO many–body expansion. For a given value of the parameter N_{max}, the NCSM considers all possible nucleon excitations from the lowest Pauli configuration such that the sum of oscillator quanta N is less than $N_{pauli} + N_{max}$.

However, the necessary procedure of antisymmetrization when working with the Jacobi basis becomes increasingly complicated in larger A nucleon systems, whereas we discussed earlier in Sec. 2.2.2, in the Cartesian coordinate SD basis the antisymmetrization is trivial. Due to this complexity, computationally the HO many–body basis states are defined using single–nucleon coordinates $\{\vec{r}_1, \ldots, \vec{r}_A\}$, and so each nucleon has a coordinate $\vec{r}_i$ defined with respect to an arbitrary origin. This is where we first encounter the idea of center–of–mass (c.m.) contamination in the NCSM. Moreover one is relegated to working

with the full Cartesian coordinate SD basis which includes c.m. motion. Since we are interested in the purely *physical*, intrinsic motion of the nucleons, not the total motion relative to the origin, this c.m. contamination must be procedurally dealt with. While this is not ideal, remarkably, the HO basis allows for an exact factorization of the c.m. and intrinsic degrees of freedom when combined with the N_{max} truncation scheme [68]. The HO many–body expansion in the SD basis is given as:

$$\langle \vec{r}_1 \cdots \vec{r}_A | \Psi^A \rangle_{SD} = \sum_{N=0}^{N_{max}} \sum_{\beta} c_{N\beta}^{(SD)} \langle \vec{r}_1 \cdots \vec{r}_A | \Phi_{N\beta}^A \rangle_{SD} = \langle \vec{\xi}_1 \cdots \vec{\xi}_{A-1} | \Psi^A \rangle \phi_{000}(\vec{R}_{c.m.}) \ . \tag{2.62}$$

Much of the contamination caused by the c.m. motion may be remedied by modifying the intrinsic Hamiltonian of Eq. (2.59). In the NCSM, one further adds the Lawson projection term to the nuclear Hamiltonian, where:

$$H_{Law.} = \beta(H_{c.m.} - \frac{3}{2}\hbar\Omega) \tag{2.63}$$

and

$$H_{c.m.} = T_{c.m.} + V_{c.m.} = \frac{\vec{P}^2}{2M} + \frac{1}{2}Am\Omega^2\vec{R}^2 \qquad \vec{R} = \frac{1}{A}\sum_{i=1}^{A}\vec{r}_i \ . \tag{2.64}$$

The purpose of the Lawson term is to project out higher–energy excitations of the spurious c.m. motion, which leads to the same eigenstates as would be given by the intrinsic Hamiltonian [69]. The projection is controlled by the parameter β which is set for a given NCSM run. The eigenenergies of physical states are unaffected by the parameter β, and so the addition of the Lawson term does not impact the physics of the nuclear system under consideration. While this removes excitations of the HO c.m. motion, it in general does not remove contamination from the ground state c.m. motion, which continues to contaminate the NCSM eigenstates. The technical procedure for treating this, namely the Talmi–Moshinsky transformation, will be described below.

Basis

The single–particle HO wave function is generated as a solution to the HO central potential problem (same Hamiltonian form as in Eq. (2.64)) and is given as:

$$\psi_{nlm}(r;b) = \frac{1}{r}R_{nl}(r;b)Y_{lm}(\hat{r}) \qquad E_{nlm} = \big(N + \frac{3}{2}\big)\hbar\Omega \tag{2.65}$$

where $R_{nl}(r;b)$ is the radial HO function (RHO) and $Y_{lm}(\hat{r})$ are the usual spherical harmonics. The HO length parameter $b = \sqrt{\frac{(\hbar c)^2}{(m_N c^2)\hbar\Omega}}$ sets the scale for the RHO functions. The eigenenergies for a given state are specified by the total number of oscillator quanta $N = 2n + l$. There are two core benefits to expansion over a complete set of antisymmetrized HO states. These may be summarized as follows:

1. Using the Cartesian coordinate SD basis constructed from single–nucleon HO states gives eigenstates of the translation invariant Hamiltonian which factorize as products of a wave function depending on the relative coordinates and the wave function depending on the c.m. coordinate. Hence, we have complete separation of intrinsic and c.m. motion provided an N_{max} truncation scheme is utilized.

2. The Talmi–Moshinksy transformation greatly simplifies the calculation of operators dependent on relative coordinates.

In particular, this factorization of the relative and SD eigenstates is made explicit in the following expression:

$$\langle \vec{r}_1 \cdots \vec{r}_A \vec{\sigma}_1 \cdots \vec{\sigma}_A \vec{\tau}_1 \cdots \vec{\tau}_A | A\lambda JMTM_T \rangle_{SD} = \langle \vec{\xi}_1 \cdots \vec{\xi}_{A-1} \vec{\sigma}_1 \cdots \vec{\sigma}_A \vec{\tau}_1 \cdots \vec{\tau}_A | A\lambda JMTM_T \rangle \phi_{000}(\vec{\xi}_0) \ . \tag{2.66}$$

The physical eigenstates of H have c.m. motion, but only in the $0\hbar\Omega$ ground state. Use of any basis except for the HO basis results in the mixing of c.m. and internal motion, making it much more difficult to remove the contamination. Greater detail on the HO basis may be found in the Refs. [60, 70, 71].

Jacobi (relative) coordinates

Jacobi coordinates (relative coordinates) may be defined in a variety of ways; this particular convention is consistent with the NCSM nuclear theory codes of Dr. Petr Navrátil.

Consider a system of A nucleons, each nucleon having the same mass m. We neglect the difference between the proton and the neutron masses. We then define:

$$\vec{R} = \sqrt{\frac{1}{A}}\vec{\xi}_0 = \sqrt{\frac{1}{A}}\big[\vec{r}_1 + \cdots + \vec{r}_A\big] \ , \tag{2.67}$$

and so we see $\vec{\xi}_0$ is directly proportional to the c.m. coordinate of the A–nucleon system, $\vec{R}$. We further define the remaining $A-1$ coordinates, denoted with the index i as $\vec{\xi}_i$, as being relative coordinates between the $(i+1)$–th nucleon with respect to the c.m. position of the i–nucleon system. Mathematically we may write these coordinates as:

$$\begin{aligned}
\vec{\xi}_1 &= \sqrt{\frac{1}{2}}\big[\vec{r}_1 - \vec{r}_2\big] \\
\vec{\xi}_2 &= \sqrt{\frac{2}{3}}\left[\frac{1}{2}\big(\vec{r}_1 + \vec{r}_2\big) - \vec{r}_3\right] \\
&\ \ \vdots \\
\vec{\xi}_{A-2} &= \sqrt{\frac{A-2}{A-1}}\left[\frac{1}{A-2}\big(\vec{r}_1 + \cdots + \vec{r}_{A-2}\big) - \vec{r}_{A-1}\right] \\
\vec{\xi}_{A-1} &= \sqrt{\frac{A-1}{A}}\left[\frac{1}{A-1}\big(\vec{r}_1 + \cdots + \vec{r}_{A-1}\big) - \vec{r}_A\right] \ .
\end{aligned} \tag{2.68}$$

Using the definition $\vec{R}^{(A-1)}_{c.m.} = \sqrt{\frac{1}{A-1}}\big[\vec{r}_1 + \cdots + \vec{r}_{A-1}\big]$, it is possible to write $\vec{\xi}_0$ and $\vec{\xi}_{A-1}$ respectively as

$$\begin{aligned}
\vec{\xi}_0 &= \sqrt{\frac{A-1}{A}}\vec{R}^{A-1}_{c.m.} + \sqrt{\frac{1}{A}}\vec{r}_A \\
\vec{\xi}_{A-1} &= \sqrt{\frac{1}{A}}\vec{R}^{A-1}_{c.m.} - \sqrt{\frac{A-1}{A}}\vec{r}_A \ .
\end{aligned} \tag{2.69}$$

These are an important set of relations for understanding the Talmi–Moshinsky transformation, a fundamental transformation on HO functions which allows for the exact separation of intrinsic and c.m. motion in many–particle systems.

Talmi–Moshinsky transformation

Let us consider a two–particle system in an external HO potential, with mass m and with Cartesian position vectors $\vec{r}_1$ and $\vec{r}_2$. The Hamiltonian for this system is then written as:

$$H = \frac{\vec{p}_1^{\,2} + \vec{p}_2^{\,2}}{2m} + \frac{1}{2}m\Omega^2(\vec{r}_1^{\,2} + \vec{r}_2^{\,2}) \ . \tag{2.70}$$

We may describe the eigenstates as being two–particle SD states by utilizing an expansion in the HO single–particle basis. Yet, the SD basis contains the unphysical motion of the c.m., and so we must isolate the intrinsic motion of the nucleons. We may then transform to new coordinates, i.e. relative coordinates

$$\vec{r} = \frac{1}{\sqrt{2}}(\vec{r}_1 - \vec{r}_2) \qquad\qquad \vec{R} = \frac{1}{\sqrt{2}}(\vec{r}_1 + \vec{r}_2) \ . \tag{2.71}$$

In this new coordinate system, the Hamiltonian is then written as

$$H = \frac{\vec{p}_1^2 + \vec{p}_2^2}{2m} + \frac{1}{2}m\Omega^2(\vec{r}^2 + \vec{R}^2) \ , \tag{2.72}$$

which may be described similarly as a product wave function. As these Hamiltonians are equivalent modulo a coordinate change, the eigenenergies are the same, and this hence implies relations between the quantum numbers of the relative and SD basis states. Further, this means we may express the eigenstates of the respective Hamiltonians in terms of one another,

$$|N_1 L_1 n_1 l_1 Q\rangle = \sum_{nlNL} \langle nlNLQ|N_1 L_1 n_1 l_1 Q\rangle \ |nlNLQ\rangle \ . \tag{2.73}$$

This expansion may be further generalized to the case of unequal mass particles, for which the product of HO wave functions depending on $\vec{R}$ and $\vec{r}$ transform elegantly as:

$$\begin{aligned} &\sum_{M_1 m_1} (L_1 M_1 l_1 m_1|Qq)\, \varphi_{N_1 L_1 M_1}(\vec{R})\, \varphi_{n_1 l_1 m_1}(\vec{r}) \\ &\qquad = \sum_{NLMnlm} \langle nlNLQ|N_1 L_1 n_1 l_1 Q\rangle_{\frac{1}{A-1}} (lmLM|Qq)\, \varphi_{nlm}(\vec{\xi}_1)\, \varphi_{NLM}(\vec{\xi}_0) \ , \end{aligned} \tag{2.74}$$

where $\langle nlNLQ|N_1 L_1 n_1 l_1 Q\rangle_d$ is a generalized Talmi–Moshinsky HO bracket for a two particle system with mass ratio $d = \frac{1}{A-1}$ [72, 73, 74, 75, 76]. Using this transformation, it is possible to express our operators in a translation invariant way by analytically removing c.m. contamination from the ground state HO wave function. Now, all that is left is to diagonalize the Hamiltonian matrix in the Cartesian coordinate SD HO basis.

Many-body calculations

Made possible by the introduction of the second quantization framework, we may discretize the nuclear Hamiltonian. Relevant for the many–body calculation are the matrix elements of the Hamiltonian between the set of HO many–body basis states, $H_{nm} = \langle\Phi_n| H |\Phi_m\rangle$. The nuclear Hamiltonian matrix is then discretely represented as:

$$H = \begin{pmatrix} \langle\Phi_1| H |\Phi_1\rangle & \cdots & \langle\Phi_1| H |\Phi_d\rangle \\ \vdots & \ddots & \vdots \\ \langle\Phi_d| H |\Phi_1\rangle & \cdots & \langle\Phi_d| H |\Phi_d\rangle \end{pmatrix} \tag{2.75}$$

where d is the dimension of the many–body basis $\{|\Phi_\alpha\rangle\}$. Diagonalization of the Hamiltonian then gives the solution of the nuclear states in terms of the many–body HO basis expansion. The diagonalization procedure is non–trivial given that H is usually a large, sparse matrix. The iterative Lanczos algorithm is applied [77, 78], with the number of iterations being determined based on calculation parameters such as the number of desired states, the size of the nucleus, the N_{max} basis size, etc.. The Lanczos algorithm is utilized to determine the m largest eigenvalues and eigenvectors of the $n \times n$ Hamiltonian matrix. Application of the algorithm brings the Hamiltonian into a tri–diagonal form. Then, the small block matrix $H_{m\times m}$ is diagonalized using a suitable algorithm for a tri–diagonal Hermitian matrix, and the low–lying nuclear eigenstates are extracted.

The many–body code which is used to compute the nuclear wave functions discussed in this work is known as the `ncsd.f`, the no-core Slater determinant (NCSD) code, of Dr. Petr Navrátil. Generally speaking, the size of these calculations (as discussed in Ref. [67]) is quite significant and requires large–scale parallelization techniques and access to massive computers.

Importance truncation

An important method worth mentioning is the importance truncation (IT) approach to reducing the number of required model space configurations based on the importance of their contributions. This approach is referred to as the IT–NCSM and is discussed at length in Refs. [79, 80], and the general idea is summarized here.

We introduce the parameter κ which will control the size of the N_{max} HO many–body basis. We wish to calculate the first–order effects from inclusion of a larger basis, using a perturbation theory (PT) framework. The expansion of the many–body state with an $N_{max}+2$ basis size in PT is then given by:

$$|\Psi^{(\mathrm{IT})}(N_{max}+2)\rangle = \sum_{\nu\,\epsilon N_{max}+2} \frac{\langle\phi_\nu|\,W\,|\Psi(N_{max})\rangle}{\mathcal{E}_\nu - \mathcal{E}_{un.}}\;|\phi_\nu\rangle \tag{2.76}$$

where $W = H - H_0$ is the interaction Hamiltonian (perturbation operator). The state $|\Psi(N_{max})\rangle$ is the reference state, calculated from the N_{max} truncated Hamiltonian. The state $|\phi_\nu\rangle$ is the set of $N_{max}+2$ HO many–body basis states which would naturally be used to initialize the $N_{max}+2$ truncated Hamiltonian. The $\mathcal{E}_{un.}$ corresponds to the lowest unperturbed energy configuration of the nucleus in the N_{max} space. Using this first–order result from PT, we define a metric of importance κ_ν given by:

$$\kappa_\nu = \frac{|\,\langle\phi_\nu|\,H\,|\Psi(N_{max})\rangle\,|}{\mathcal{E}_\nu - \mathcal{E}_{un.}} \tag{2.77}$$

and restrict $\kappa_\nu > \kappa$. Essentially, we are discarding all many–body basis states with contributions smaller than the parameter κ, and so it directly controls the size of the $N_{max}+2$ many–body basis.

Similarity Renormalization Group

In general, the bare chiral interactions discussed in Sec. 2.1 are hard interactions. These interactions are capable of reproducing NN elastic scattering phase shifts with high quality, however, they typically exhibit strong short–range repulsion and tensor forces [81]. These features unfortunately produce strong correlations in the many–body wave function, making the diagonalization procedure sensitive to high–momentum information and convergence of calculations slow (with respect to some basis truncation parameter). As a result, additional transformations to further soften the Hamiltonian are often necessary in order to produce converged many–body results, i.e. unitary correlation operator method [82], the $V_{low\,k}$ renormalization group method [83, 84, 85] and the Okubo–Lee–Suzuki similarity transformation [86, 87]. The similarity renormalization group (SRG) [88, 81, 89] is one such approach, which has been the most successfully applied transformation method in nuclear theory. The application of SRG weakens the short–range repulsion in chiral interactions, allowing for reduced correlations in the many–body calculation and hence an improved convergence rate. Furthermore, SRG preserves the symmetries of interactions and allows for the consistent transformation of two– and many–nucleon interactions (i.e. $3N$).

The SRG method is defined by the continuous unitary transformation of the free–space Hamiltonian $H_A \equiv H_{\lambda=\infty}$, where λ is denoted as the wave–flow parameter. The transformation equation is:

$$H_\lambda = U_\lambda H_{\lambda=\infty} U_\lambda^\dagger \qquad\qquad \lambda\,\epsilon(\infty, 0)\;, \tag{2.78}$$

and the evolution is defined by the first–order differential operator flow equation

$$\frac{dH_\lambda}{d\lambda} = [\eta_\lambda, H_\lambda]\;. \tag{2.79}$$

In this equation $\eta_\lambda = (\frac{2\mu}{\hbar^2})^2[T_{int}, H_\lambda]$. By utilizing the commutator of H_λ and the intrinsic kinetic energy operator to define the anti–Hermitian dynamic generator η_λ, the high– and low–momentum contributions of the interaction become decoupled. This particular flow equation guarantees the unitary equivalence

of the spectrum of H_λ operators. General operators evaluated with the SRG transformed interactions must be similarly transformed in a consistent way [90, 91]. If we decompose the SRG Hamiltonian (rather crudely and without sum notation) into creation and annihilation operators as:

$$H_\lambda \propto \langle T \rangle a^\dagger a + \langle V_\lambda^{(2)} \rangle a^\dagger a^\dagger a a + \langle V_\lambda^{(3)} \rangle a^\dagger a^\dagger a^\dagger a a a + \cdots \ , \tag{2.80}$$

it is apparent from Eq. (2.79) that continued multiplication of this operator will lead to increasingly relevant many–body contributions. In practice, this constitutes the largest challenge with SRG as many–nucleon interactions are difficult to generate, and may only be included up to the three–body level at present.

Procedurally, the operator equation is represented in a finite basis and solved numerically; the preferred basis is the Jacobi HO representation [92, 93]. This basis provides an efficient formulation and allows connection to the SD particle representation used by the NCSM through the Talmi–Moshinsky transformation [94]. In the discrete HO basis, it is possible to directly identify many–body forces and treat them consistently with the two–nucleon interaction.

2.2.5 Fermi transitions in nuclei

Allowed beta decays in nuclear physics are classified based on the angular momentum information of the outgoing electron and neutrino pair. The possible transitions are those with no change in the orbital angular momentum, $\Delta l = 0$, which is the corresponding selection rule for "allowed" decay. This gives rise to two different manifestations of beta decay, namely the Fermi (isospin) and Gamow–Teller (spin) transitions. The former, Fermi transitions, are transitions in which the spins of the outgoing particles are anti–parallel; the operator couples to $S = 0$ spin (implies $\Delta J = 0$). Hence, Fermi decays only connect isobaric analogue states in the nuclei experiencing the transition. This makes Fermi transitions an excellent test of isospin conservation in nuclei, since the result would be exact if isospin symmetry was respected between the analogue states. On the other hand, Gamow–Teller transitions are dependent on the nuclear spin operator $\vec{S}$, implying decay paths to a variety of states since S is not a good quantum number (only J) of the many–body system.

Focusing specifically on Fermi transitions, the Fermi beta decay operator is given by

$$O(F) = T_\pm = \sum_{i=1}^{A} t_\pm^{(i)} \ , \tag{2.81}$$

where the sum is over all nucleons. The $t_\pm$ operator is defined such that the action of the raising operator will change a neutron into a proton or annihilate a proton, and the action of the lowering operator will change a proton into a neutron or annihilate a neutron. The transition probability for this operator between an initial and final state is given by $B(F) = |\langle \Psi_f | T_\pm | \Psi_i \rangle|^2$. For a system with exact isospin conservation, this matrix element may be analytically determined to be:

$$|\langle \Psi_f | T_\pm | \Psi_i \rangle|^2 = T_i(T_i+1) - T_{zi}(T_{zi} \pm 1) \ . \tag{2.82}$$

Notably, one can derive several conditions on the nuclei based solely on the operator structure, i.e. $\Delta J = 0$ and $\pi_i \pi_f = 1$.

Chapter 3

Nonlocal densities in the NCSM

Nuclear density matrices are fundamental quantities in the study of nuclear physics. In particular, they can be used in a second–quantization framework to drastically simplify the calculation of N–body operators. Using the properties of the creation and annihilation operators, one may derive an expansion of N–body operators in terms of single–particle states multiplied by the density matrix elements. Explicitly, for an N–body operator we may write in a tensor coupled form as:

$$O^{(\lambda)} = -\sum_{\alpha\beta}\langle a||O^{(\lambda)}||b\rangle \ \frac{\left(a_a^\dagger \tilde{a}_b\right)^{(\lambda)}_\mu}{\sqrt{2\lambda+1}} \ , \tag{3.1}$$

where α and β represent a particular configuration of single–particle quantum numbers for the N–body system. The creation and annihilation operators are as defined in Eq. (2.55) and Eq. (2.58). Then a general many–body matrix element of the operator is written in a J–coupled form as:

$$\langle \Psi_f||O^{(\lambda)}||\Psi_i\rangle = -\sum_{\alpha\beta}\langle a||O^{(\lambda)}||b\rangle \ \frac{\langle \Psi_f||\left(a_a^\dagger \tilde{a}_b\right)^{(\lambda)}||\Psi_i\rangle}{\sqrt{2\lambda+1}} \ . \tag{3.2}$$

Remarkably, in order to calculate the many–body matrix elements of any arbitrary operator, one must simply calculate the single–particle matrix elements of the operator and sum them in conjunction with the N–body density matrix elements, which can be computed directly from the many–body eigenstates. In particular, the numerator $\langle \Psi_f||\left(a_a^\dagger \tilde{a}_b\right)^{(\lambda)}||\Psi_i\rangle$ is referred to as the one–body transition density (OBTD) matrix. We will use these results in calculation of coordinate forms of one–body density matrices (OBDMs). As outlined in Sec. 2.2.4, the construction of translation invariance is necessary for describing the intrinsic nuclear wave function, and as such, the focus of this work is on the construction and analysis of translation invariance in coordinate OBDMs.

The OBDMs are fundamental objects in many nuclear structure calculations. Consider, for example, nucleon–nucleus (NA) scattering calculations. Historically, the optical potential method for scattering has been a powerful tool in the calculation of nuclear observables such as cross sections and spin polarizations, for a wide range of energies and nuclei [95, 96]. While there has been great success in the application of phenomenological optical potentials to regions of the nuclear chart with available experimental data [97, 98, 99], they may also be obtained from microscopic approaches. We pursue this approach using *ab initio* theory, which gives a robustness and predictivity in foreign regions of the nuclear chart where experimental data is not accessible. In particular, in application of Watson multiple scattering theory (WMST), one needs solely the nucleon–nucleon t–matrix and the matter distribution of the nucleus [100, 101, 102, 103, 104, 105] in order to compute various scattering observables. Using the WMST approach, it is possible to develop microscopic optical potentials constructed from the one–body density matrices of the *ab initio* NCSM, the results of which are discussed in Sec. 3.2. These methods are further extended to the case of antiproton–nucleus scattering in Sec. 3.2.2 and an analysis of the effects of $3N$ force inclusion in Sec. 3.2.3.

Additionally, there are a variety of operators expressible with dependence on coordinate OBDMs. One such operator is the nuclear kinetic density, a fundamental input of density functional theory (DFT). DFT is an alternative many–body method used in the study of nuclear properties, though there has recently been an effort to bridge *ab initio* theory with DFT [106, 107, 108]. With the advent of nonlocal densities [1], it is possible to analytically compute the kinetic density from NCSM wave functions, and hence to compare *ab initio* predictions for the kinetic functional to DFT models. Using the translation invariant coordinate OBDMs, we compute the physically realistic nuclear kinetic density, the results of which are discussed in Sec. 3.3.

The theory work on densities presented in this section is a generalized form of the procedure presented in Ref. [109], and has been discussed at length in Refs. [1, 2, 3, 4]. This work has been implemented in the `trdens.f` code of Dr. Petr Navrátil.

3.1 Nonlocal one-body densities

With the knowledge of the A–nucleon eigenstates discussed in Sec. 2.2.4, we may construct the one-body density matrix from a second quantization approach. In Cartesian coordinate representation, the nonlocal density operator for an A-nucleon system is given by:

$$\rho_{op}(\vec{r},\vec{r}\,') = \sum_{i=1}^{A} \left(|\vec{r}\rangle \langle \vec{r}\,'| \right)^{(i)} = \sum_{i=1}^{A} \delta(\vec{r}-\vec{r}_i)\,\delta(\vec{r}\,'-\vec{r}\,'_i)\ . \tag{3.3}$$

In the Cartesian coordinate single-particle SD basis, the matrix element between an initial and final NCSM state is given by:

$$\begin{aligned} {}_{SD}\langle A\lambda_f J_f M_f|\,\rho_{op}(\vec{r},\vec{r}\,')\,|A\lambda_i J_i M_i\rangle_{\,SD} = \frac{1}{\hat{J}_f}\sum_{K\bar{s}} (J_i M_i K k|J_f M_f)\,\hat{j}_1\hat{j}_2\hat{K}(-1)^{j_2+\frac{1}{2}+l_1+l_2+K} \begin{Bmatrix} j_2 & l_2 & \frac{1}{2} \\ l_1 & j_1 & K \end{Bmatrix} \\ \times R_{n_1 l_1}(r)\,R_{n_2 l_2}(r') \left[\frac{-1}{\hat{K}} {}_{SD}\langle A\lambda_f J_f||(a^{\dagger}_{n_1 l_1 j_1}\widetilde{a}_{n_2 l_2 j_2})^{(K)}||A\lambda_i J_i\rangle_{SD} \right] \left(Y^*_{l_1}(\hat{r})\,Y^*_{l_2}(\hat{r}\,') \right)^{(K)}_{k}\ , \end{aligned} \tag{3.4}$$

where $\bar{s} = \{n_1, l_1, j_1, n_2, l_2, j_2\}$ in the sum, as $k = M_i - M_f$ is restricted. Both $\vec{r}$ and $\vec{r}\,'$ are measured from the centre of the HO potential well. Note the convention $\hat{J} = \sqrt{2J+1}$. The $R_{nl}(r)$ functions are the RHO functions introduced prior. The one-body density matrix elements ${}_{SD}\langle A\lambda_f J_f||(a^{\dagger}_{n_1 l_1 j_1}\widetilde{a}_{n_2 l_2 j_2})^{(K)}||A\lambda_i J_i\rangle_{SD}$ have been introduced using the second–quantization approach. As discussed earlier, there is an inherent spurious contamination from the HO c.m. when using the single–particle SD basis [110]. As the nuclear Hamiltonian is translationally invariant, the use of the SD basis effects calculations of observables in the NCSM by including the unphysical motion of the c.m.. Hence, we require the explicit removal of the c.m. degrees of freedom from the density operator of Eq. 3.3, or more generally, from **any** coordinate dependent observable in the NCSM.

There exists a clean algebraic solution to the problem of c.m. removal in the NCSM. In particular, we recall the exact factorization between the Jacobi and SD eigenstates in Eq. (2.66). The c.m. component has been labelled as $\phi_{000}(\vec{\xi}_0)$ and corresponds to the $N = 0$ ground state of the HO, with $\vec{\xi}_0 \propto \vec{R}$, the A–nucleon c.m. coordinate. This is discussed in more detail in Sec. 2.2.4. By explicitly measuring each coordinate from the c.m. of the A–nucleon system $\vec{R}$, the translationally invariant density operator may be represented in Cartesian coordinates as:

$$\rho_{op}(\vec{r}-\vec{R},\vec{r}\,'-\vec{R}) = \sum_{i=1}^{A} \delta([\vec{r}-\vec{R}]-[\vec{r}_i-\vec{R}])\,\delta([\vec{r}\,'-\vec{R}]-[\vec{r}\,'_i-\vec{R}])\ . \tag{3.5}$$

The calculation of the translationally invariant density in the Jacobi basis is a more complicated calculation, the derivation of which is shown in Appendix A.2. Further, there exists alternative techniques for c.m. removal, such as the one discussed in Ref. [111] which makes use of the transformation properties of oscillator wave functions into momentum space to decouple the intrinsic and c.m. motion.

Features of the derivation worth noting include the fact that the calculation of the one-body density matrix in the Jacobi basis is computationally costly; it is much more reasonable to calculate these matrix elements in the SD HO basis due to the trivial antisymmetrization procedure. Hence a core goal of the derivation is to relate the relative Jacobi matrix elements to the SD basis matrix elements. The derivation begins in the Jacobi basis and is transformed using the Talmi–Moshinksy transformation brackets to bring it into the SD HO basis, with the spurious c.m. motion analytically removed. The resultant matrix element of the translation invariant density operator between an initial and final state in the SD HO basis is given by:

$$\rho_{fiK}(\vec{\xi},\vec{\xi}\,') = \sum_{k\bar{s}} \frac{1}{\hat{J}_f}(J_i M_i K k|J_f M_f)\Big(Y_l^*(\hat{\xi})Y_{l'}^*(\hat{\xi}\,')\Big)_k^{(K)} R_{nl}(\xi)R_{n'l'}(\xi\,')\,(-1)^{l_1+l_2+K+j_2+\frac{1}{2}} \\ \times\ \hat{j}_1\hat{j}_2\hat{K}\begin{Bmatrix} j_1 & j_2 & K \\ l_2 & l_1 & \frac{1}{2}\end{Bmatrix}(M^K)^{-1}_{n_1l_1n_2l_2nln'l'}\left[\frac{-1}{\hat{K}}{}_{SD}\langle A\lambda_f J_f||(a^\dagger_{n_1l_1j_1}\widetilde{a}_{n_2l_2j_2})^{(K)}||A\lambda_i J_i\rangle_{SD}\right], \tag{3.6}$$

where $\bar{s} = \{n_1, l_1, j_1, n_2, l_2, j_2, n, l, n', l'\}$ and we have the matrix definition

$$(M^K)_{n_1l_1n_2l_2nln'l'} = \sum_{N_1L_1}(-1)^{l+l'+K+L_1}\hat{l}\hat{l}'\begin{Bmatrix} l_1 & L_1 & l \\ l' & K & l_2\end{Bmatrix}\langle nl00l|\,N_1L_1n_1l_1l\rangle_{\frac{1}{A-1}}\langle n'l'00l'|\,N_1L_1n_2l_2l'\rangle_{\frac{1}{A-1}}\ . \tag{3.7}$$

3.1.1 Ground state density results

In this section we discuss predictions for the distributions of the c.m. contaminated and translation invariant nuclear densities. We provide a direct comparison between the distributions and gauge the effects of c.m. removal on density dependent quantities. Figure plots will be labeled with *wiCOM* for the c.m. contaminated density and with *trinv* for the translational invariant density. In particular, we study a range of light-nuclear systems from ^{4,6,8}He to larger systems such as ^{12}C and ^{16}O, which allows us to determine the importance of c.m. removal with increasing nucleon number A. Ground state densities are plotted with the angular dependence factorized out:

$$\rho_{fiK}(\vec{\xi},\vec{\xi}\,') = \rho_{fiK}(\xi,\xi\,')\big[Y_l^*(\hat{\xi})Y_{l'}^*(\hat{\xi}\,')\big]_k^{(K)}\ , \tag{3.8}$$

where only the radial component $\rho_{fik}(\xi,\xi\,')$ of this equation is plotted. As well, in this section we will only show the $(K,l,l\,') = (0,0,0)$ partial waves as these tend to be the most significant partial wave contribution to the density. Further, other than for ^{4}He, we only plot the neutron densities for these systems as the proton densities are almost identical; any small differences in structure predictions are due to the charged nature of the proton. Lastly, for these calculations the SRG–evolved NN–N^{4}LO(500)+3N$_{\rm lnl}$ interaction has been used. First we discuss the two–body interaction of Ref. [112], for which there are several motivating factors (i) fifth order in ChPT is the highest meaningful expansion order available (ii) at N^{4}LO, nucleon–nucleon scattering data below the pion–production threshold has been reproduced with the highest ever precision, with a χ^2/datum = 1.15 (iii) the interaction softness achieved in the Entem–Machleidt–Nosyk approach allows for smaller three–body contributions to the nuclear interactions. For a discussion on SRG evolution, see Sec. 2.2.4. While the NN interaction is certainly of high–quality, it has been extensively shown that solely two–body physics is insufficient to reproduce most nuclear observables, particularly with the induction of many–nucleon terms from the SRG procedure. Now, we mention the

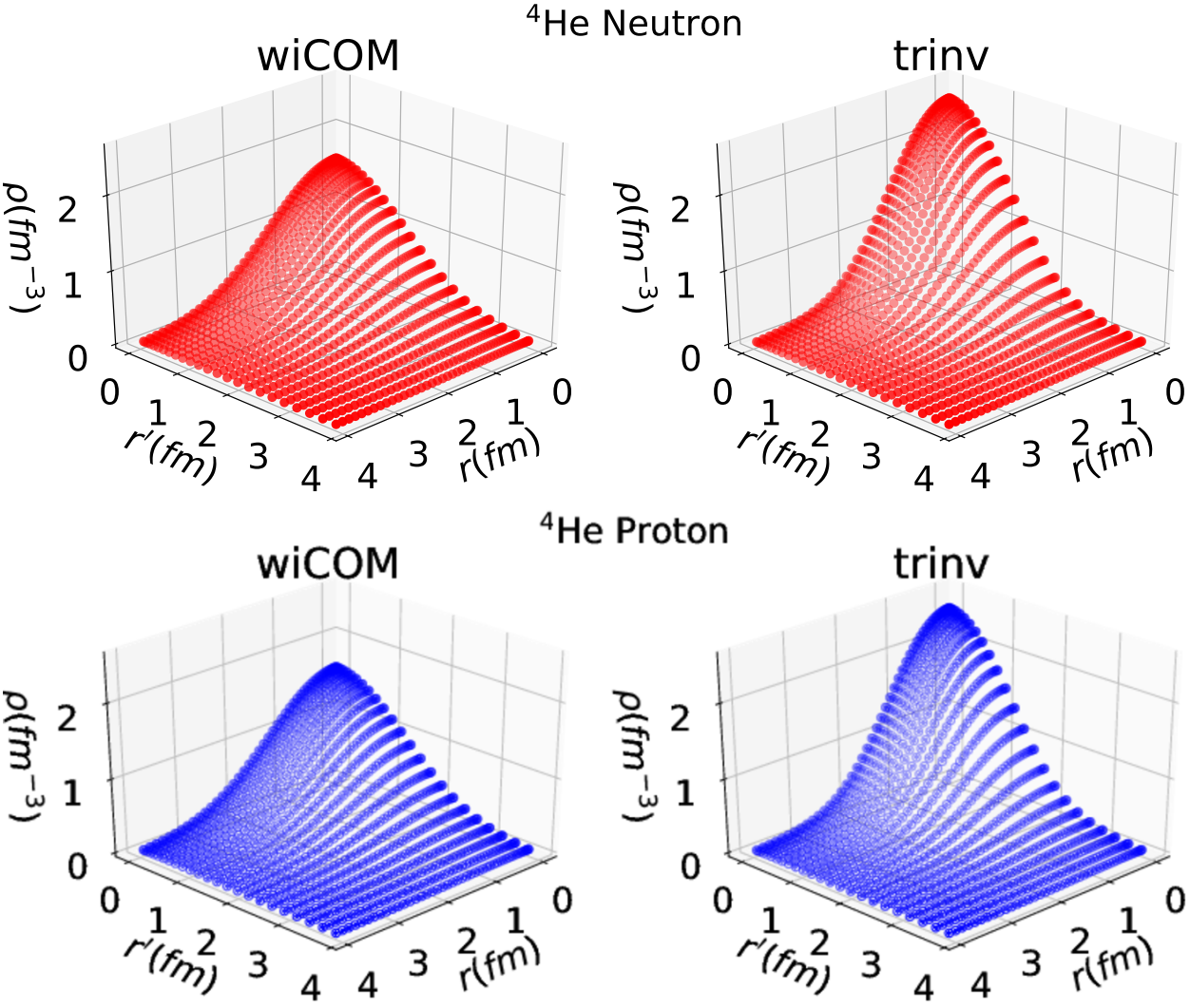

Figure 3.1: Ground-state ^{4}He nonlocal proton (blue) and neutron (red) densities calculated with an $N_{\max} = 14$ basis space, an oscillator frequency of $\hbar\Omega = 20$ MeV, and a flow parameter of $\lambda_{\mathrm{SRG}} = 2.0$ fm^{-1}. These results were published in Ref. [1].

three–body component to this interaction, denoted $3\mathrm{N}_{\mathrm{lnl}}$, computed at N^{2}LO in the ChPT expansion and first systematically studied in Ref. [113]. This interaction is an extension of the one presented in Ref. [114]; the core reason for additional developments being the unsatisfactory performance in medium–mass nuclei. While the older 3N interaction utilized only local regulators, the novel $3\mathrm{N}_{\mathrm{lnl}}$ interaction is obtained with local and nonlocal regulators simultaneously applied, and as discussed in Ref. [113], this appears to be a crucial feature in the description of experimental energies from light– to medium–mass nuclei. Beyond this, the $3\mathrm{N}_{\mathrm{lnl}}$ interaction behaves well under SRG transformations, allowing for consistent evolution of NN and 3N interactions. As a final note, while the Hamiltonian construction is the same as in the aforementioned works, the low–energy constants used in the present work are consistent with Ref. [115].

The maximal effect of c.m. removal is seen in the lightest nuclear systems, and so we first show the comparison of *wiCOM* and *trinv* proton and neutron densities of the ^{4}He system in Fig. 3.1. There is quite a difference in the predicted nuclear structure given by Eq. (3.4) and Eq. (3.6). One notices that these effects are pronounced at small r and r' (~ 1 fm), i.e. closer to the centre of the nuclear system. For example, the maximum value of the respective densities is different, with the *trinv* density having a

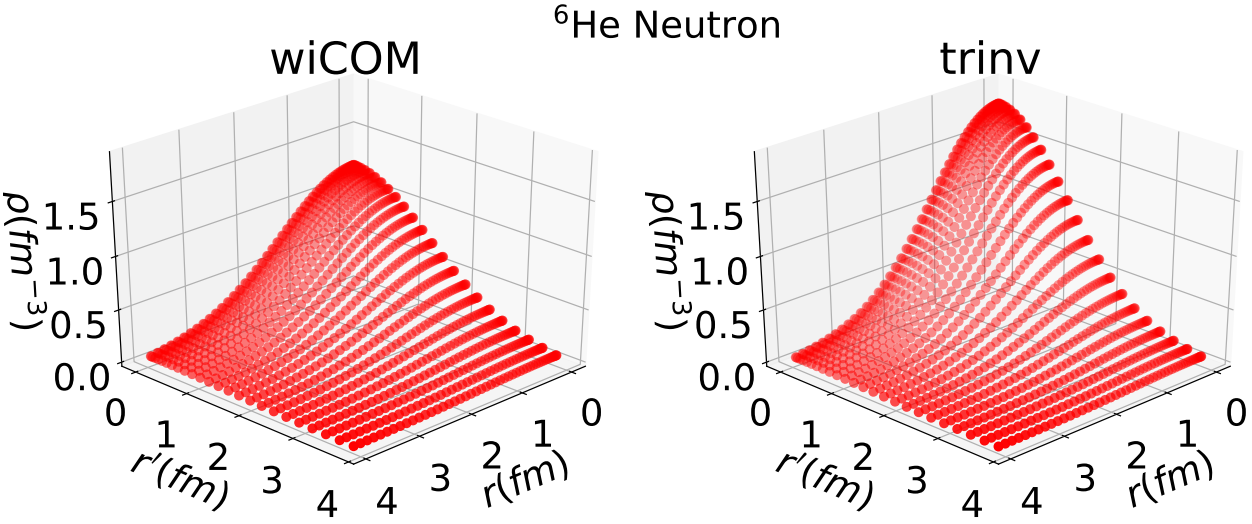

Figure 3.2: Ground-state ^{6}He nonlocal neutron density calculated with an $N_{\max} = 12$ basis space, an oscillator frequency of $\hbar\Omega = 20$ MeV, and a flow parameter of $\lambda_{\mathrm{SRG}} = 2.0$ fm^{-1}. These results were published in Ref. [1].

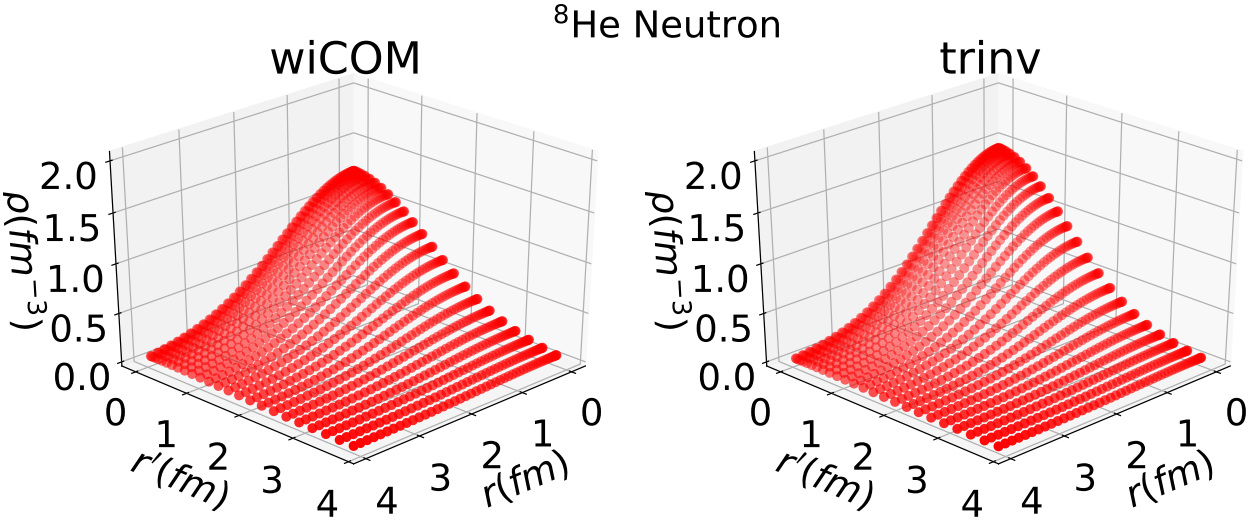

Figure 3.3: Ground-state ^{8}He nonlocal neutron density calculated with an $N_{\max} = 10$ basis space, an oscillator frequency of $\hbar\Omega = 20$ MeV, and a flow parameter of $\lambda_{\mathrm{SRG}} = 2.0$ fm^{-1}. These results were published in Ref. [1].

higher global maximum and much sharper features moving away from it. These sharper features of the *trinv* density matrix imply that the matrix elements fall to zero more rapidly than in the case of the standard shell model density. Based purely on this qualitative information, in light nuclei such as ^{4}He, it is sensible to expect that operators which explore the rate of change of the density will be quite sensitive to the effects of c.m. removal.

In general, we can see that the *trinv* density provides a drastically different physical picture of the short– and medium–range physics, while both densities are certainly unphysical in their long–range behaviour (this is due to the expansion in HO basis which has unphysical asymptotic behaviour for nuclear systems). We may further look at the ^{6,8}He systems, in Fig. 3.2 and Fig. 3.3 respectively, which exhibit a similar change in structure predictions. As observed in all three systems, ^{4,6,8}He, the spurious c.m. contamination caused by the HO potential creates a smoothing effect in the density, obscuring the intrinsic

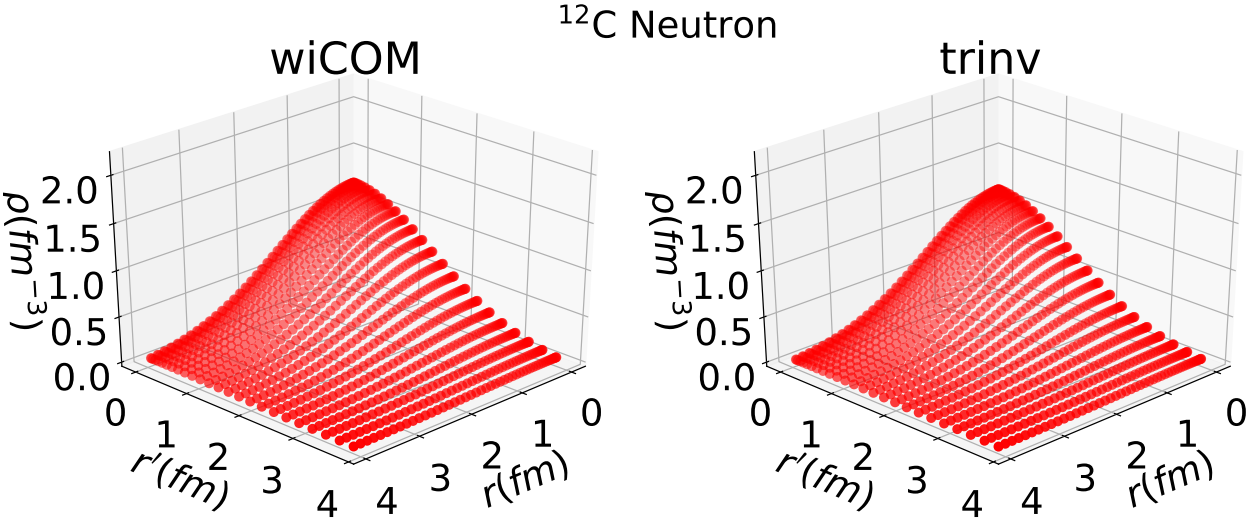

Figure 3.4: Ground-state ^{12}C nonlocal neutron density calculated with an $N_{\max} = 10$ basis space, an oscillator frequency of $\hbar\Omega = 20$ MeV, and a flow parameter of $\lambda_{\mathrm{SRG}} = 2.0$ fm^{-1}. These results were published in Ref. [1].

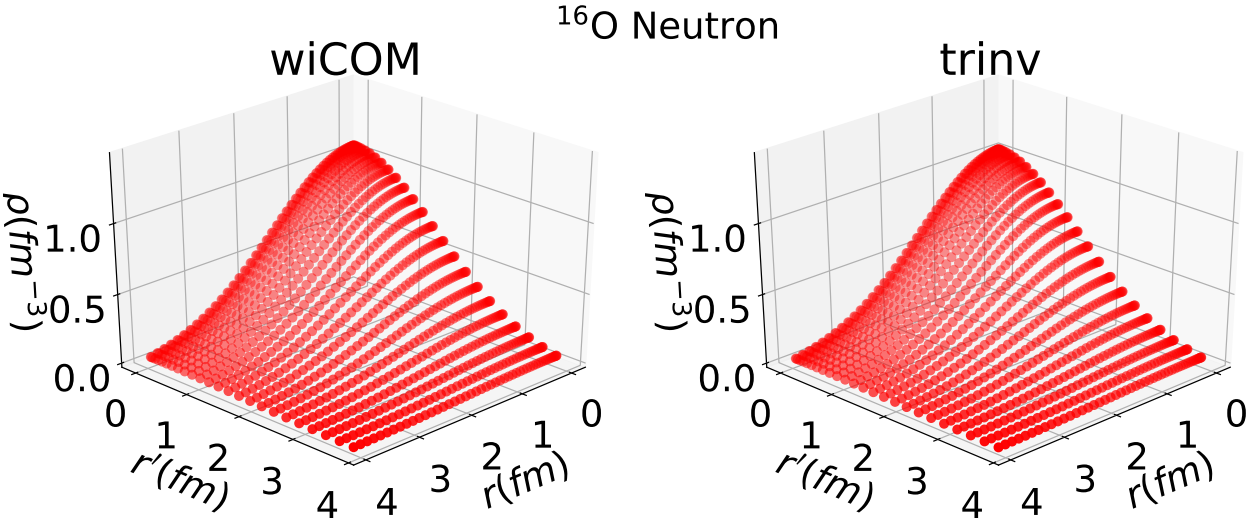

Figure 3.5: Ground-state ^{16}O nonlocal neutron density calculated with an $N_{\max} = 8$ importance truncated basis space, an oscillator frequency of $\hbar\Omega = 20$ MeV, and a flow parameter of $\lambda_{\mathrm{SRG}} = 2.0$ fm^{-1}. These results were published in Ref. [1].

structure and spreading the density distribution over larger r and r' values. Effectively, the suppression of the density due to c.m. effects near $r = 0$ is a kind of "blurring" of the physical structure.

Another item worth noting is the overall difference in c.m. removal effects as observed in the ^{4,6,8}He nuclei. The contribution from the c.m. in the total density diminishes as $\frac{1}{A}$, and so while in ^{4}He effects of translation invariance are on the order of 25%, as we move to larger systems such as ^{8}He we see a reduction in the size of the correction ($\sim 10\%$ reduction). This is further emphasized in the comparison plots of the larger nuclei ^{12}C and ^{16}O, shown in Fig. 3.4 and Fig. 3.5, respectively. In these figures, it is hard to discern the differences between the *wiCOM* and *trinv* densities, which is of course due to the significant suppression of the c.m. motion in these nuclei. However, while the effects seem small they are certainly non-negligible, and this can be seen by studying the local form of the coordinate densities. The procedure

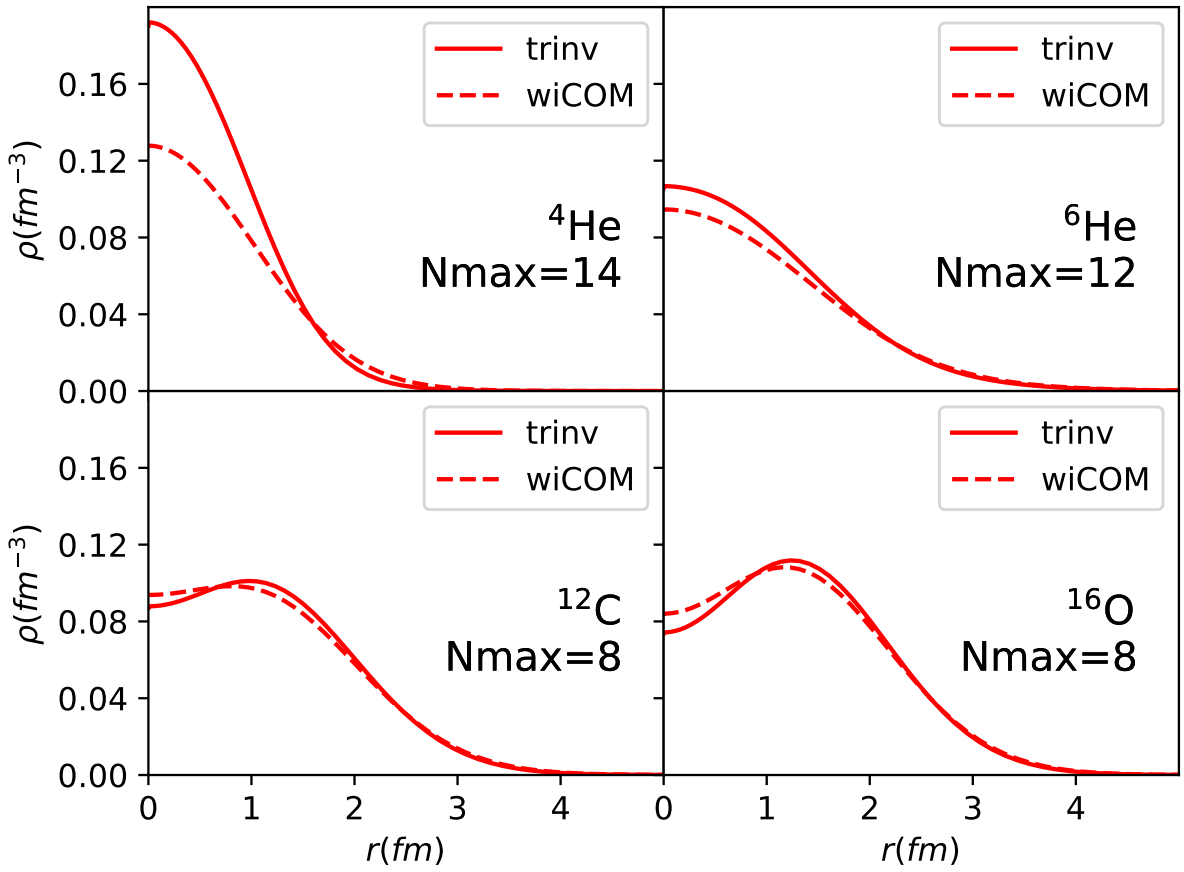

Figure 3.6: Comparison of the *trinv* (solid) and *wiCOM* (dashed) ground state densities of the nuclei: ^{4}He in the top left panel, ^{6}He in the top right panel, ^{12}C in the bottom left panel and ^{16}O in the bottom right panel. These results were published in Ref. [1].

for obtaining the local density from the nonlocal density is trivial and is described in Appendix A, and the local *trinv* density is given in Eq. (A.35). Essentially, the local density is proportional to the diagonal elements ($r = r'$) of the nonlocal density matrix.

We refer to Fig. 3.6. Here the differences between the *trinv* and *wiCOM* densities are most apparent; the structure below $r \sim 2\,\text{fm}$ is where the most substantial changes in the distribution occur, with the most pronounced effects occurring in the light–nuclei. This is not to say that the effects are not sizable in ^{16}O. In fact, even in the larger nuclei where the c.m. motion is suppressed, the short–range structure predictions up to $\sim 1\,\text{fm}$ are considerably different for the *trinv* density.

The sizeable differences between the translation invariant and c.m. contaminated density matrices ensure that the construction of translation invariant densities is of great importance for high–precision nuclear structure calculations, and operators which probe the short–range physics of the nonlocal one–body density are certain to be affected. Furthermore, these effects of c.m. removal are sure to amplified in any density dependent quantities which are more sensitive to the distribution features, i.e. gradients acting on the coordinate density.

Convergence results

In Fig. 3.7 and Fig. 3.8, we show convergence plots labelled by the parameter N_{max}, the HO many–body truncation parameter. These plots illustrate the strong convergence trends of the ground state density with respect to the parameter N_{max}. Referring to Fig. 3.7, it is evidenced by the overlapping curves of the final three N_{max} iterations that for $N_{max} \geq 10$ the system has reached a well-converged status. In fact, referring to Fig. 3.8, even ^{16}O – which presently exists near the border of NCSM applicability – enjoys rapid convergence in the parameter N_{max}. The closeness of the $N_{max} = 6$ calculation and $N_{max} = 8$ importance truncated calculation across the domain indicate that the $N_{max} = 8$ basis space is of reasonable size to obtain a good structural description of ^{16}O.

As a final note, we investigated the convergence of the long–range structure of the density by calculating the logarithm $\log_{10}(\rho_{fik}(r))$. In the logarithmic plot, panel (b) of Fig. 3.8, we can see that there is no visible convergence trend in the density at long–range. In fact, this is not a surprise. A result of the HO basis expansion is that the densities exhibit Gaussian long–range behaviour; they have an asymptotic behaviour which is unphysical for the nuclear wave functions (naturally it should be exponential). While a relatively great description of the structure is achieved, in general, operators sensitive to the tail of the distribution will likely not exhibit a convergence pattern in N_{max}.

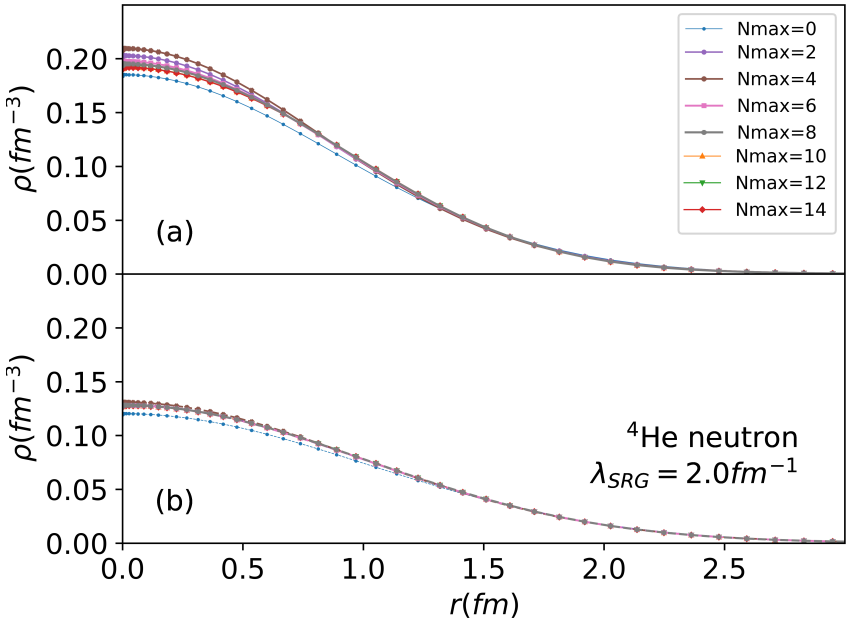

Figure 3.7: Comparison of the ^{4}He ground state local neutron density for each iteration of $N_{max} \epsilon \{0, 2, \ldots, 14\}$. In panel **(a)** we show the *trinv* density and in panel **(b)** we have the *wiCOM* density. These results were published in Ref. [1].

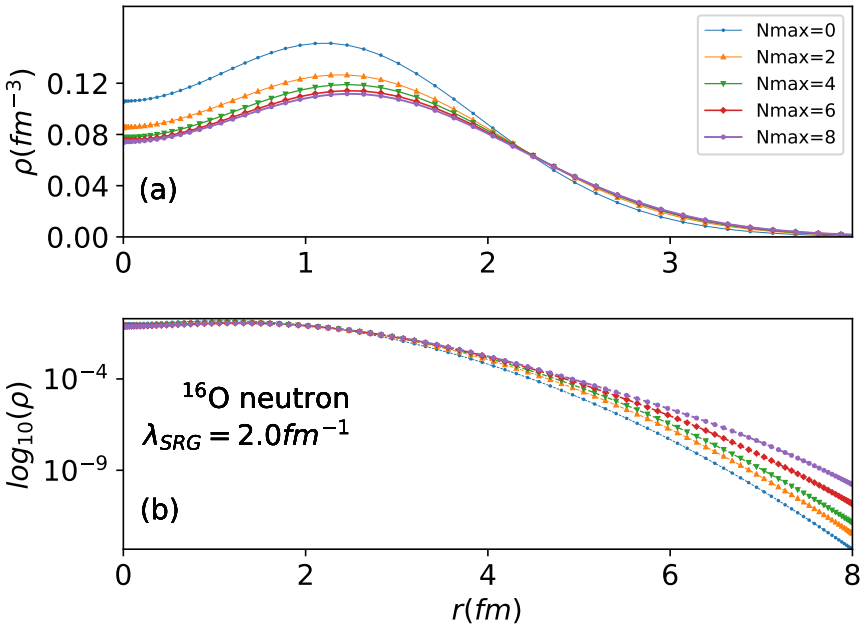

Figure 3.8: Comparison of the ^{16}O ground state local *trinv* neutron density for each iteration of $N_{max} \epsilon \{0, 2, \ldots, 8\}$. In panel **(a)** we show the usual *trinv* neutron density while in panel **(b)** we show the comparison of the *trinv* density at long–range by plotting the logarithmic distribution, $\log_{10}(\rho)$. These results were published in Ref. [1].

3.2 Applications to scattering

As briefly discussed earlier, one of the primary applications of the one–body density matrices is in calculations of optical potentials for describing nuclear scattering processes. The results discussed in this section have been obtained through collaboration with Dr. Matteo Vorabbi. A brief summary of the formalism is provided here.

Nucleon–nucleus elastic scattering in momentum space is defined by the (non–solvable) operator equation:

$$T = V + VG_0(E)T \ , \tag{3.9}$$

where T is known as the transition operator, V refers to the external interaction of the proton and the nucleus and $G_0(E)$ is the free propagator for the $(A+1)$–nucleon system. As there is presently no way in which to incorporate the three–body interactions in optical potential approaches, we only take V to the two–body level and so $V = \sum_{i=1}^{A} v_{0i}$, where v_{0i} is the two–body interaction between the projectile and the i–th nucleon. The free propagator for the $(A+1)$ system is defined by

$$G_0(E) = \frac{1}{E - h_0 - H_a + i\epsilon} \ , \tag{3.10}$$

where h_0 corresponds to the projectile energy. While this equation is unsolvable in its current form, by defining the operators P and Q which satisfy the condition $P + Q = \mathbb{1}$, we may cast this problem into an approachable form. In particular, P is taken to be a projector onto the elastic channel:

$$P = \frac{|\Psi_A\rangle \langle \Psi_A|}{\langle \Psi_A | \Psi_A \rangle} \ , \tag{3.11}$$

where $|\Psi_A\rangle$ is the ground state of the target nucleus. Utilizing these new operators, we may split Eq. 3.9 into two separate equations:

$$\begin{aligned} T &= U + UG_0(E)PT \\ U &= V + VG_0(E)QU \end{aligned} \tag{3.12}$$

where U is known as the optical potential operator. These two equations will need to be solved simultaneously. By left– and right–multiplying by P, we arrive at the expression for the elastic transition operator

$$T_{el} = PTP = PUP + PUG_0(E)PTP \ . \tag{3.13}$$

In practice, once PUP is known, this one–body equation is easily solvable. Hence the problem has been reduced to finding a suitable form for the operator U. While this is in general a non–trivial task, we make use of a few suitable approximations which allow us to continue.

First, we adopt the spectator expansion, discussed in Ref. [116]. Further, we introduce the single–scattering approximation, which assumes that the projectile nucleon only scatters off a single nucleon of the target nucleus. Lastly, we work under the impulse approximation, in which the momentum of the projectile is assumed to be large enough such that we can neglect the binding forces between the projectile and target nucleons during the collision [117]. Under these approximations, we may take the optical potential operator to be of the form:

$$U = \sum_{i=1}^{A} t_{0i} = \sum_{i=1}^{A} v_{0i} + v_{0i} g_i t_{0i} \ , \tag{3.14}$$

where t_{0i} is the free two–nucleon t–matrix and $g_i = (E - h_0 - h_i + i\epsilon)$ corresponds to the free two–nucleon propagator. The quantities h_0 and h_i are the kinetic energies of the projectile i–th nucleon, respectively.

By acting on U with the projector P (and with some significant algebra), we arrive at the expression for the optical potential operator for proton elastic scattering:

$$U(\vec{q},\vec{K};\omega) = \sum_{t_z=-\frac{1}{2},\frac{1}{2}} \int d^3\vec{P}\ \eta(\vec{q},\vec{K},\vec{P})\ t_{\frac{1}{2}t_z}\left(\vec{q},\frac{1}{2}\left[\frac{A+1}{A}\vec{K}+\sqrt{\frac{A-1}{A}}\vec{P}\right];E\right) \times \rho_{t_z}\left(\vec{P}+\sqrt{\frac{A-1}{A}}\frac{\vec{q}}{2},\vec{P}-\sqrt{\frac{A-1}{A}}\frac{\vec{q}}{2}\right)\ . \tag{3.15}$$

In this equation, $\vec{q}$ is the momentum transfer between the nucleons, $\vec{K}$ is the total momentum and $\vec{P}$ is simply a momentum integration variable introduced by resolving identity. E is the energy at which the t–matrix is evaluated. Also, $t_{\frac{1}{2}t_z}(\cdots)$ is the proton–nucleon t–matrix, $\rho_{t_z}(\cdots)$ is the nuclear density profile obtained from the one–body nuclear densities, and $\eta(\cdots)$ is the Møller factor responsible for imposing Lorentz invariance on the flux when passing from the nucleon–nucleus frame to the nucleon–nucleon frame for t–matrix evaluation. Lastly, $\omega = \frac{1}{2}h_0$ (half the kinetic energy of the projectile) in the laboratory frame. The Coulomb interaction is included as described in Refs. [118, 119].

Hence with the determination of U complete, it is then possible to solve for T_{el} in Eq. 3.13 and by studying the on–shell dynamics one can obtain scattering observables [120].

3.2.1 Proton–nucleus scattering results

Here we present scattering cross section results for proton–nucleus (pA) elastic scattering, computed from Eq. (3.15). All angles shown are measured in the laboratory frame. The nuclear density matrices which serve as input for the optical potential calculations were computed as described in Sec. 3.1. In particular, we used the NN–N^{4}LO(500)+3N$_{\rm lnl}$ interaction derived from chiral EFT for all calculations of the density quantities. However, while it is possible to include 3N forces in the NCSM and hence the densities, it is not yet possible to include the three–body interaction in optical potential approaches. Thus, the bare (no SRG evolution) two–body interaction NN–N^{4}LO(500) has been used in calculation of the free NN t–matrix introduced in Eq. (3.14). This of course leads to inconsistencies in the calculation, and essentially means that full consistency is only possible using the bare two–body interaction to compute the density matrices as well. In practice, however, the bare interaction may only be used for light–nuclei such as ^{4}He, where it is feasible to reach many–body convergence in N_{max}. Hence, in determination of the NCSM density matrices, the use of SRG and inclusion of three–body terms is necessary to study larger nuclear systems. At present, this is the highest possible level of consistency we can currently achieve with the optical potential methods.

The nonlocality of the NCSM density matrices signifies an important step forward in imporing optical potential scattering methods. Prior to computing these nonlocal densities, it was standard procedure to employ various approximations in calculation of U. First, we introduce the exact relation between the density profiles $\tilde{\rho}_{t_z}(q)$ and the one–body density matrices $\rho_{t_z}(\xi,\xi')$:

$$\tilde{\rho}_{t_z}(q) = \int d^3\vec{P}\ \rho_{t_z}\left(\vec{P}+\sqrt{\frac{A-1}{A}}\frac{\vec{q}}{2},\vec{P}-\sqrt{\frac{A-1}{A}}\frac{\vec{q}}{2}\right)\ . \tag{3.16}$$

As this relation involves the nonlocal density matrix, there have historically been approximations used to compute the profiles from the local density matrices as:

$$\tilde{\rho}_{t_z}(q) = 4\pi\int_0^\infty dr\ r^2 j_0(qr)\rho_{t_z}(r)\ . \tag{3.17}$$

This is the first approximation that has been eliminated in our approach. Secondly, the folding integral of the t–matrix with the nonlocal densities in Eq. (3.15) is frequently approximated by the factorized optical

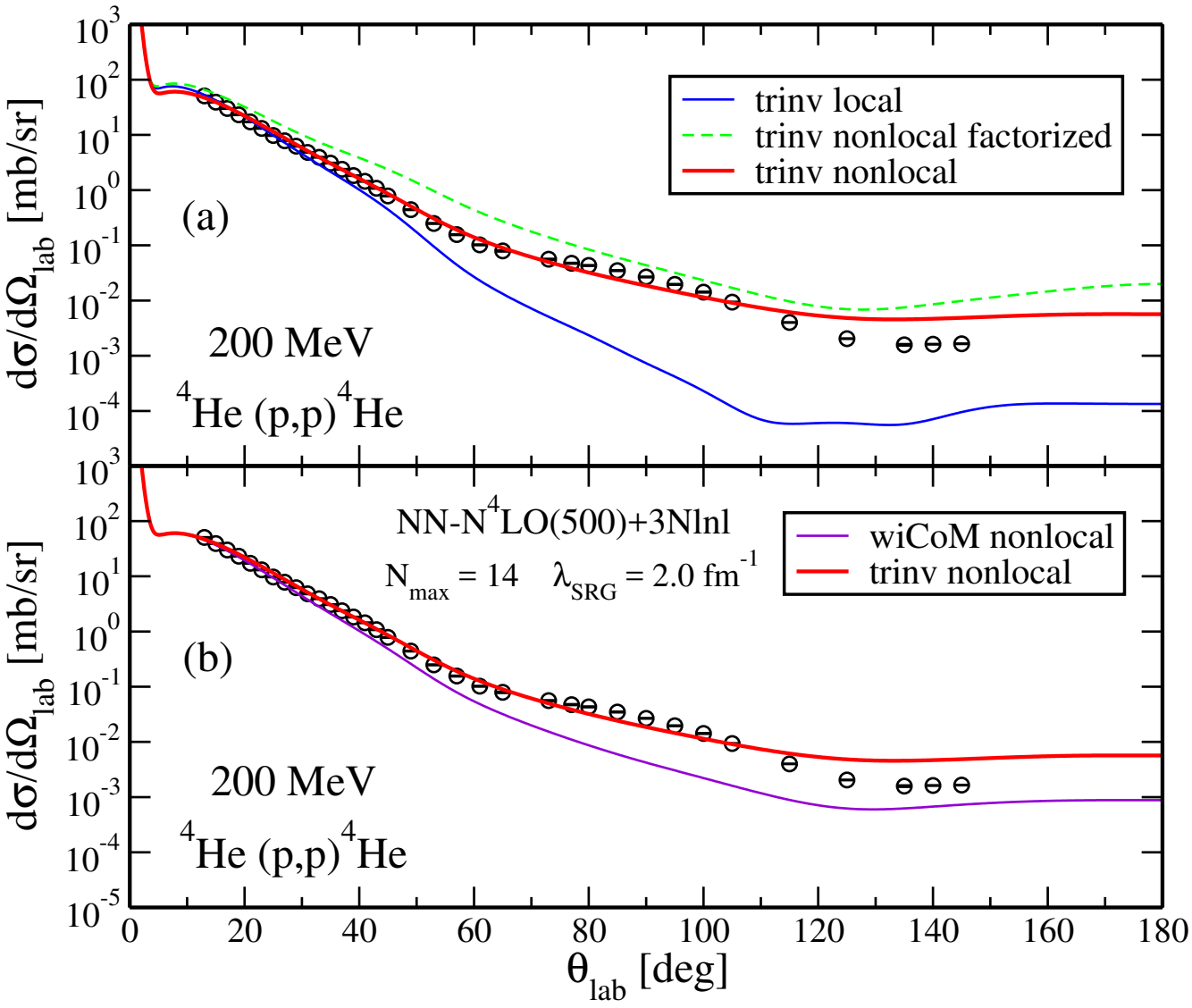

Figure 3.9: We present results for ^{4}He$(p,p)^4$He calculated as described in the previous sections. All results are computed at a laboratory energy of 200 MeV. ^{4}He densities were computed with an $N_{max} = 14$ basis space, an oscillator frequency of $\hbar\Omega = 20$ MeV and a waveflow parameter of $\lambda_{SRG} = 2.0\,\mathrm{fm}^{-1}$. In panel **(a)** are differential cross sections computed from *trinv* local and nonlocal density matrices. The dashed curve corresponds to the approximate treatment of U given in Eq. (3.18). In panel **(b)** is a comparison of differential cross sections computed from the *trinv* and *wiCOM* nonlocal densities. These results were published in Ref. [1]. Experimental data are taken from Ref. [6].

potential:

$$U(\vec{q},\vec{K};\omega) = \eta(\vec{q},\vec{K}) \sum_{t_z=-\frac{1}{2},\frac{1}{2}} t_{\frac{1}{2}t_z}\left(\vec{q},\frac{A+1}{2A}\vec{K};\omega\right)\,\tilde{\rho}_{t_z}(q)\ . \tag{3.18}$$

The density profile $\tilde{\rho}_{t_z}$ in the above equation may be computed from either the nonlocal or local densities. In summary, this means we can study the effects related to including the nonlocal densities in addition to the effects from performing the full folding integral (as opposed to using the factorized model). These results are discussed below.

We refer to Fig. 3.9. In panel **(a)**, the ^{4}He$(p,p)^4$He elastic scattering results for the differential cross section are presented. The *trinv nonlocal* curve was determined from the full solution to the optical

potential problem of Eq. (3.15), where the folding integral has been performed correctly and the nonlocal translation invariant one–body density matrices are used. This is the most consistent possible calculation which we can perform at present. The *trinv nonlocal factorized* curve was obtained from using the translation invariant nonlocal densities to compute the density profile of Eq. (3.16), and then using the factorized approach to compute the operator U with Eq. (3.18). Lastly, the *trinv local* curve utilized the translation invariant local densities to determine the density profile of Eq. (3.17), and then the factorized approach was used to compute the operator U with Eq. (3.18). From this first panel, the benefit of including nonlocality in the densities is clear. While the results are relatively similar for $\theta_{lab} < 40^\circ$, above this angle threshold the curves quickly diverge; for angles of $\theta_{lab} > 100^\circ$ the difference between the calculations is around two orders of magnitude. The jump from the *trinv local* curve (blue) to the *trinv nonlocal* curve (red) constitues a significant step in the description of reactions for light–nuclei using optical potentials.

Comparing the local (blue) and nonlocal factorized (dashed green) approaches, it is evident that nonlocality in the density produces the correct order of magnitude for the differential cross section, as opposed to the local density. However, we see that the introduction of nonlocality itself is not sufficient in order to reproduce the data. As shown by the difference between the nonlocal factorized curve and the full nonlocal optical potential calculation, it is necessary to include the densities in a consistent way and perform the folding integral when calculating the operator U.

In panel **(b)**, we show comparisons of the differential cross sections computed with c.m. contaminated (*wiCOM*) and translation invariant (*trinv*) density matrices. It cannot be overstated how important c.m. removal is in the density. The disagreement with data caused by spurious c.m. motion is significant, reaching up to an order of magnitude. This tends to be in the medium–range of angles ($\theta_{lab} \sim 40^\circ - 120^\circ$), and is a result of the more rapidly decaying *trinv* density (see Figs. 3.1, 3.6). The remarkable differences in scattering cross sections shown in these plots fully indicate the need for density matrices with translation invariant and nonlocal properties.

In Fig. 3.10, we present results for the same reaction with calculations performed as before, except with laboratory energies of 72 MeV in panel **(a)** and 156 MeV in panel **(b)**. Similarly at these energies, the nonlocal density provides an optical potential that has better agreement with the experimental data. At 72 MeV the description is poor outside of the $\theta_{lab} \lesssim 60^\circ$ domain, a result of the impulse approximation adopted in the current approach. This neglects the coupling of the target nucleon (which is struck) and the residual $(A-1)$–nucleus, an effect which becomes increasingly important at lower energies. In general, the impulse approximation is valid for energies at and beyond 200 MeV.

In Fig. 3.11, we show results for $^{12}\mathrm{C}(p,p)^{12}\mathrm{C}$ differential cross sections calculated at laboratory energies of 122 MeV in panel **(a)**, 160 MeV in panel **(b)** and 200 MeV in panel **(c)**. We again make note of the fact that this optical potential model is most accurate at higher energies ~ 200 MeV. Notably, the differences between the factorized local and nonlocal optical potentials are reduced in this system, with the greater deviation occuring in the lower energy calculations (see panel **(a)**). In these cases, the momentum of the incoming projectile is smaller and so the scattering process is more sensitive to the nuclear structure. Presumably, if one were to construct optical potentials at even lower energies, the effects of nonlocality would become increasingly important. However, in general the curves are in great agreement with the experimental data obtained, particularly at the laboratory energy of 200 MeV shown in panel **(c)**. Similar behaviour is seen in Fig. 3.12 for $^{16}\mathrm{O}(p,p)^{16}\mathrm{O}$ differential cross sections, where we perform calculations at laboratory energies of 100 MeV in panel **(a)**, 135 MeV in panel **(b)** and 200 MeV in panel **(c)**. The general form of the data is very well reproduced by our nonlocal densities and optical potential approach, albeit even at 200 MeV the data is slightly overestimated for angles $\theta_{lab} > 30^\circ$, after the first minimum.

Lastly, in Fig. 3.13, we show results for proton elastic scattering off the halo nuclei ^{6,8}He. These systems are characterized by an α cluster surrounded by a neutron halo cluster, providing an interesting long–range structure to the nuclei not observed in well bound systems such as ^{4}He, ^{12}C and ^{16}O. This makes them particularly difficult to describe in the NCSM, given the expansion in the many–body HO basis which provides a poorer description of wave function asymptotics. We use the same interaction as was

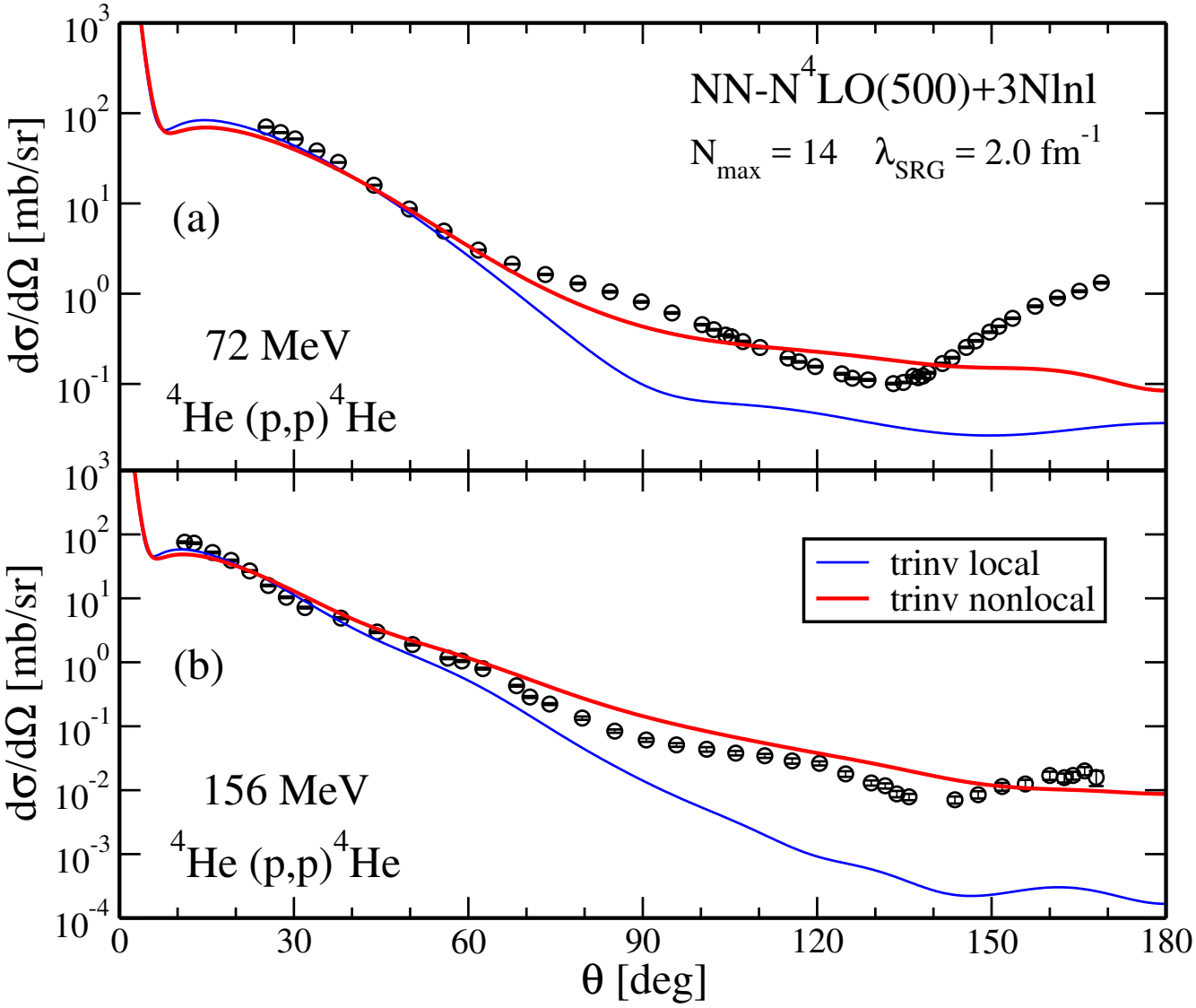

Figure 3.10: We present results for ^{4}He$(p,p)^4$He calculated with local *trinv* (blue) and nonlocal *trinv* densities (red), as described in the previous sections. The differential cross section results in panel **(a)** are computed at a laboratory energy of 72 MeV, and in panel **(b)** at 100 MeV. ^{4}He densities were computed with an $N_{max} = 14$ basis space, an oscillator frequency of $\hbar\Omega = 20$ MeV and a waveflow parameter of $\lambda_{SRG} = 2.0\,\mathrm{fm}^{-1}$. These results were published in Ref. [1]. Experimental data are taken from Ref. [7, 8].

used for the stable nuclei, namely the NN–N^{4}LO(500)+3N$_{\mathrm{lnl}}$ interaction. The laboratory energy used in calculation is 71 MeV, which is certainly out of the range of applicability of the impulse approximation. It should not be a complete surprise that the nonlocal curves somewhat miss the data, however, surprisingly the local density calculation appears to match quite well with experiment despite this fact. Regardless, in order to produce better agreement with the experimental data for halo nuclei, a more sophisticated nuclear structure and optical potential approach is required.

By the development of translation invariant nonlocal one–body nuclear density matrices, we have achieved a step forward in producing consistent microscopic optical potentials, derived solely from chiral EFT interactions. While the local density approach can work, we have seen that the more general nonlocality in the density is a desired property in the description of reactions involving light–nuclei. Furthermore, by introducing the property of translation invariance in the density, we have shown the

tremendous impact that spurious c.m. motion has on nuclear observables. In order to produce physically realistic results from NCSM eigenstates, one must always properly treat the c.m. motion, especially in the case of quantities which might amplify these structure differences.

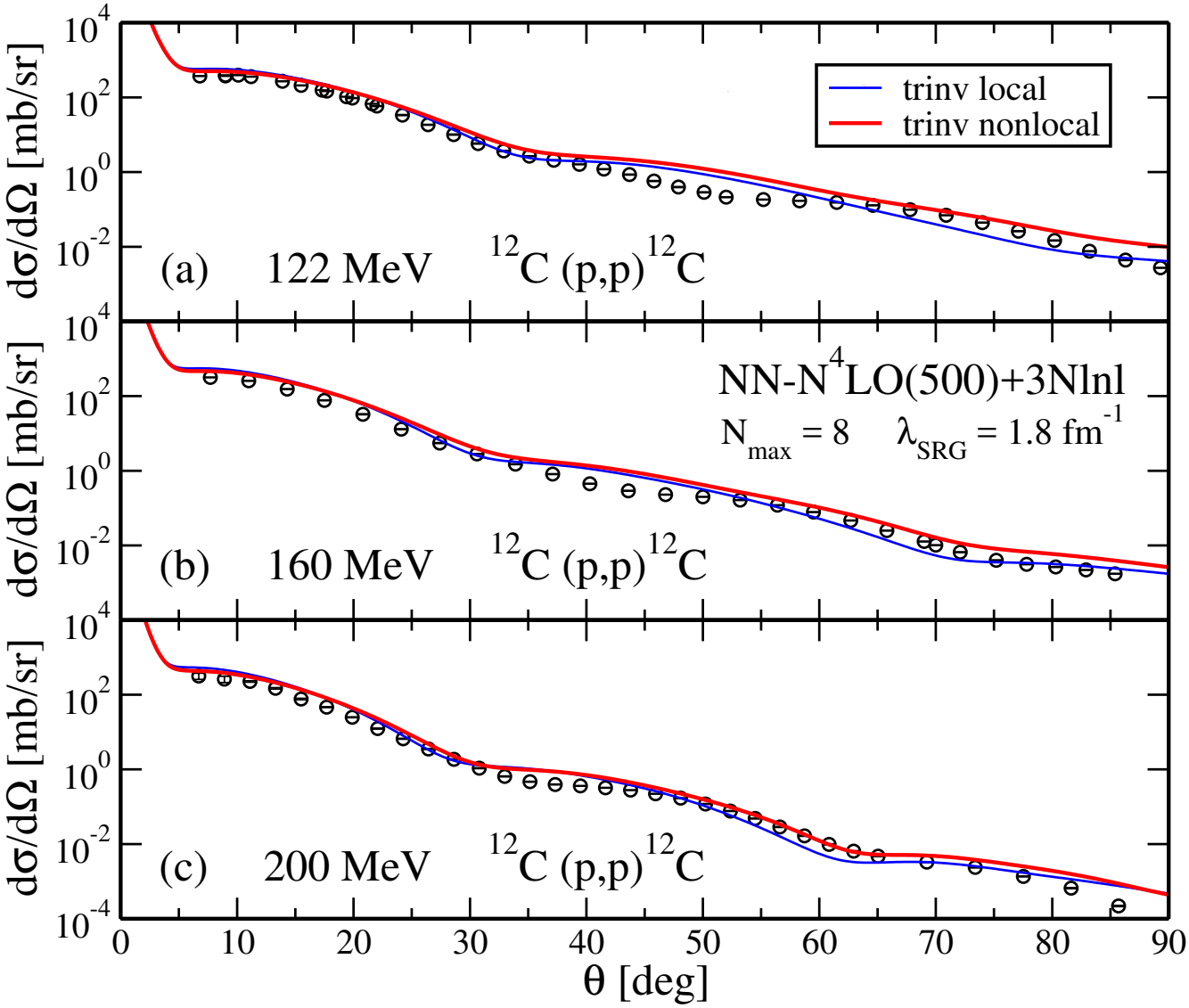

Figure 3.11: We present results for ^{12}C$(p,p)^{12}$C calculated with local *trinv* (blue) and nonlocal *trinv* densities (red), as described in the previous sections. The differential cross section results in panel **(a)** are computed at a laboratory energy of 122 MeV, in panel **(b)** at 160 MeV and in panel **(c)** at 200 MeV. ^{12}C densities were computed with an $N_{max} = 8$ basis space, an oscillator frequency of $\hbar\Omega = 20$ MeV and a waveflow parameter of $\lambda_{SRG} = 1.8\,\mathrm{fm}^{-1}$. These results were published in Ref. [1]. Experimental data are taken from Ref. [9].

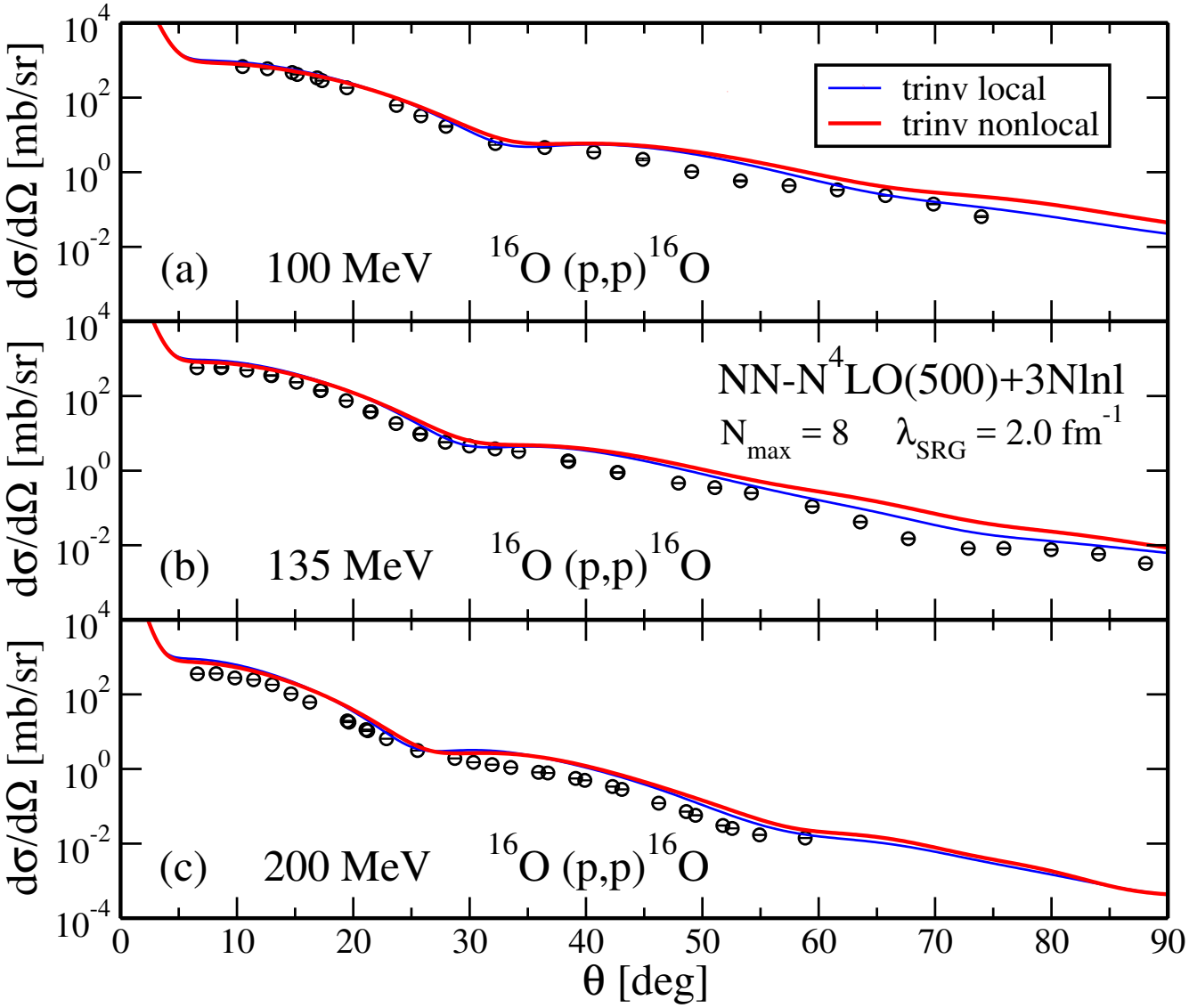

Figure 3.12: We present results for $^{16}\mathrm{O}(p,p)^{16}\mathrm{O}$ calculated with local *trinv* (blue) and nonlocal *trinv* densities (red), as described in the previous sections. The differential cross section results in panel **(a)** are computed at a laboratory energy of 100 MeV, in panel **(b)** at 135 MeV and in panel **(c)** at 200 MeV. ^{16}O densities were computed with an $N_{max} = 8$ basis space, an oscillator frequency of $\hbar\Omega = 20$ MeV and a waveflow parameter of $\lambda_{SRG} = 1.8\,\mathrm{fm}^{-1}$. These results were published in Ref. [1]. Experimental data are taken from Ref. [10].

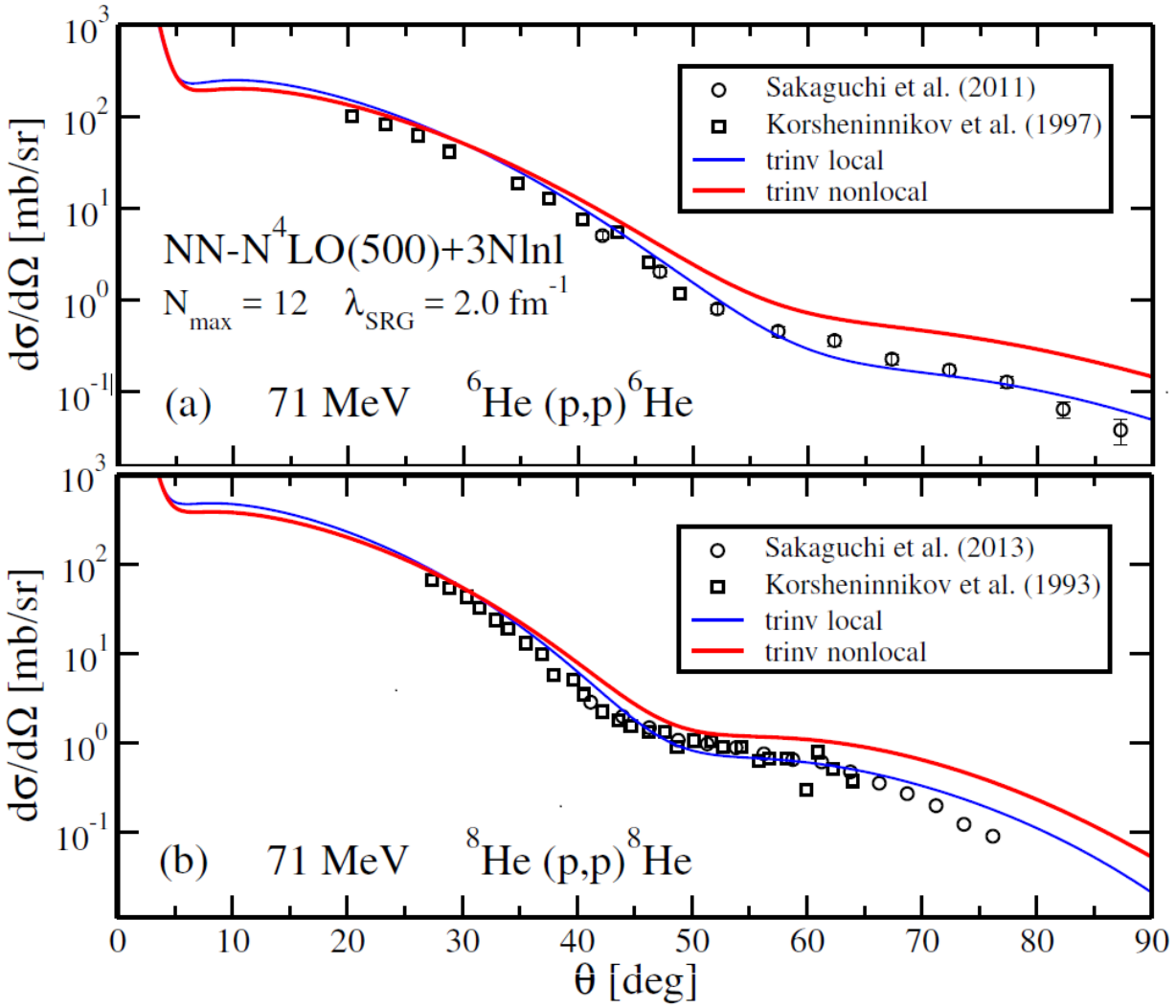

Figure 3.13: We show results for ^{6}He$(p,p)^6$He in panel **(a)** and ^{8}He$(p,p)^8$He in panel **(b)**, calculated with local *trinv* (blue) and nonlocal *trinv* densities (red). The differential cross section results are computed at a laboratory energy of 71 MeV. ^{6,8}He densities were computed with an $N_{max} = 12$ and $N_{max} = 10$ basis space, respectively, an oscillator frequency of $\hbar\Omega = 20$ MeV and a waveflow parameter of $\lambda_{SRG} = 2.0\,\mathrm{fm}^{-1}$. These results were published in Ref. [1]. Experimental data are taken from Ref. [11, 12, 13, 14].

3.2.2 Antiproton–nucleus scattering

In recent years, there has been an increasing interest in the experimental physics of antiproton scattering off nuclear targets [121]; with novel experiments proposed or underway, a revolution in our understanding of antimatter physics is likely [122, 123]. At the theoretical level, antiproton scattering provides an excellent test of nuclear structure. A core difference in the treatment of antinucleon–nucleon scattering ($\bar{N}N$) is the availability of the annihilation channel, since the total baryon number of the two–nucleon system is zero. Given that at low–energies the antiproton scattering process is dominated by the annihilation process, the probability of multi–scattering events is significantly reduced, and so the first–order calculation in WMST is more accurate than in the standard case of proton elastic scattering. This absorptive process is surface–dominated and tends to be sensitive to nuclear radii [124, 125, 126]. These simple scattering dynamics make antiproton scattering a clean method for analyzing nuclear structure.

With the advent of chiral antiproton–nucleon ($\bar{p}N$) interactions derived in the same spirit as the

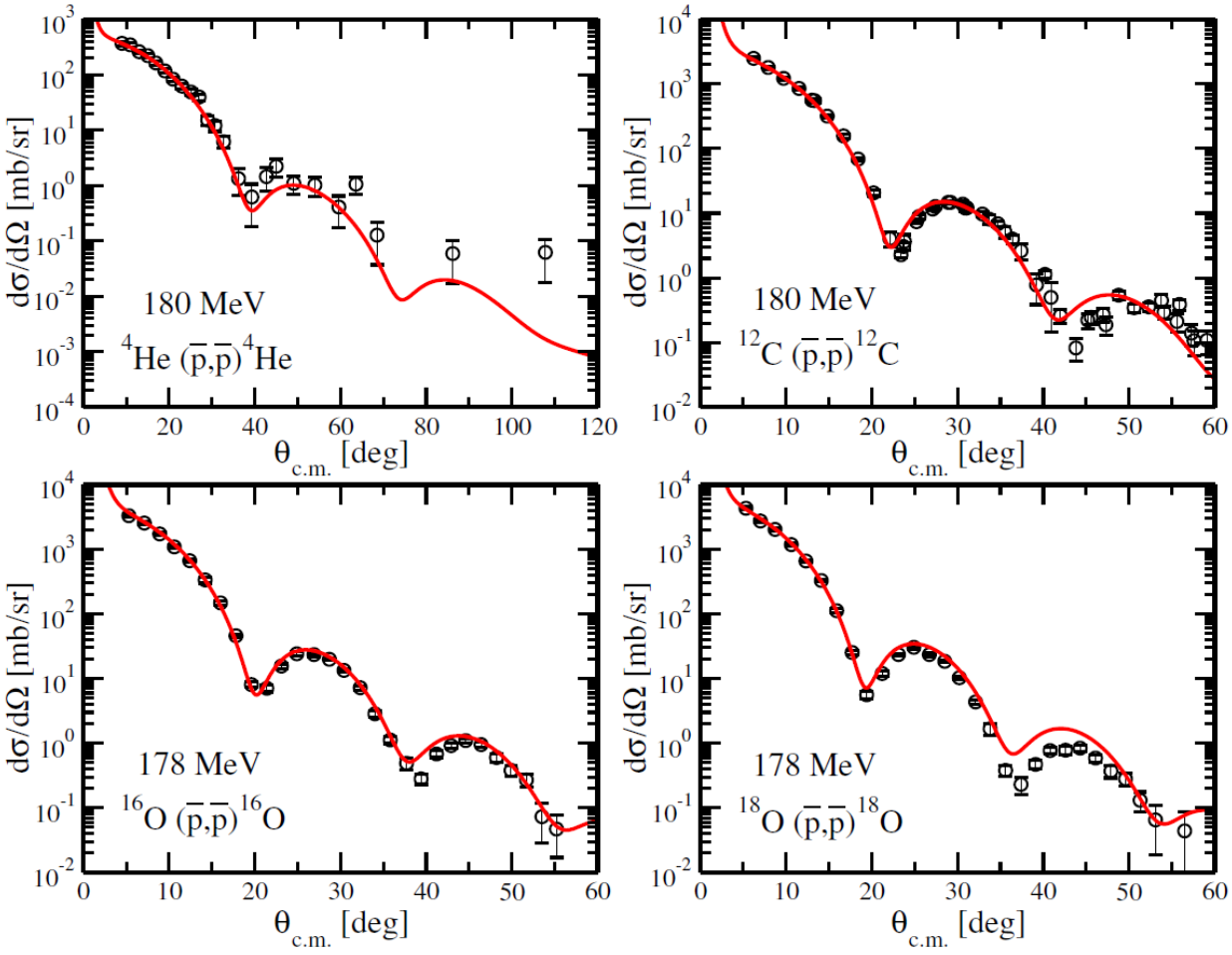

Figure 3.14: Results for the differential cross sections as a function of c.m. scattering angle for elastic antiproton scattering off ^{4}He (top left), ^{12}C (top right), ^{16}O (bottom left) and ^{18}O (bottom right). Only nonlocal translation invariant densities are used. This figure was published in Ref. [3]. Experimental data are taken from Ref. [15, 16].

previously discussed ChPT interactions, it is possible to treat the problem in a fully microscopic formalism. In fact, majority of the formalism is identical to that presented above, with the optical potential given by Eq. (3.15), albeit with slight modification. The key difference lies in the determination of the t–matrix. Whereas prior the t–matrix was computed using the same interaction as the one used to perform the nuclear structure calculations in the NCSM, it is not possible to compute the $\bar{p}N$ consistently with the NN interaction. We utilize the $\bar{p}N$ interaction derived to N^{3}LO in ChPT, kindly provided by the authors of Ref. [127], and the same NN–N^{4}LO(500)+3N$_{\rm lnl}$ interaction for computing the nonlocal translation invariant one–body densities in the NCSM, as before. For a technical description of relating the NN interaction to its corresponding $\bar{N}N$ interaction, see Ref. [127]. The first fully microscopic optical potential for elastic antiproton scattering was presented in Ref. [3].

In Fig. 3.14, we present results for antiproton scattering off various nuclear targets; in particular, we examine the ^{4}He$(\bar{p},\bar{p})^4$He, ^{12}C$(\bar{p},\bar{p})^{12}$C, ^{16}O$(\bar{p},\bar{p})^{16}$O and ^{18}O$(\bar{p},\bar{p})^{18}$O reactions. The first two systems were computed at an antiproton laboratory energy of 180 MeV, while the latter systems were computed at 178 MeV. The optical potential model provides remarkable agreement with the first diffraction minima, in terms of location and depth, particularly for ^{12}C and ^{16,18}O. Given the sensitivity of diffraction minima to nuclear radii, this tells us that our description of the radii with ChPT interactions and NCSM is strong.

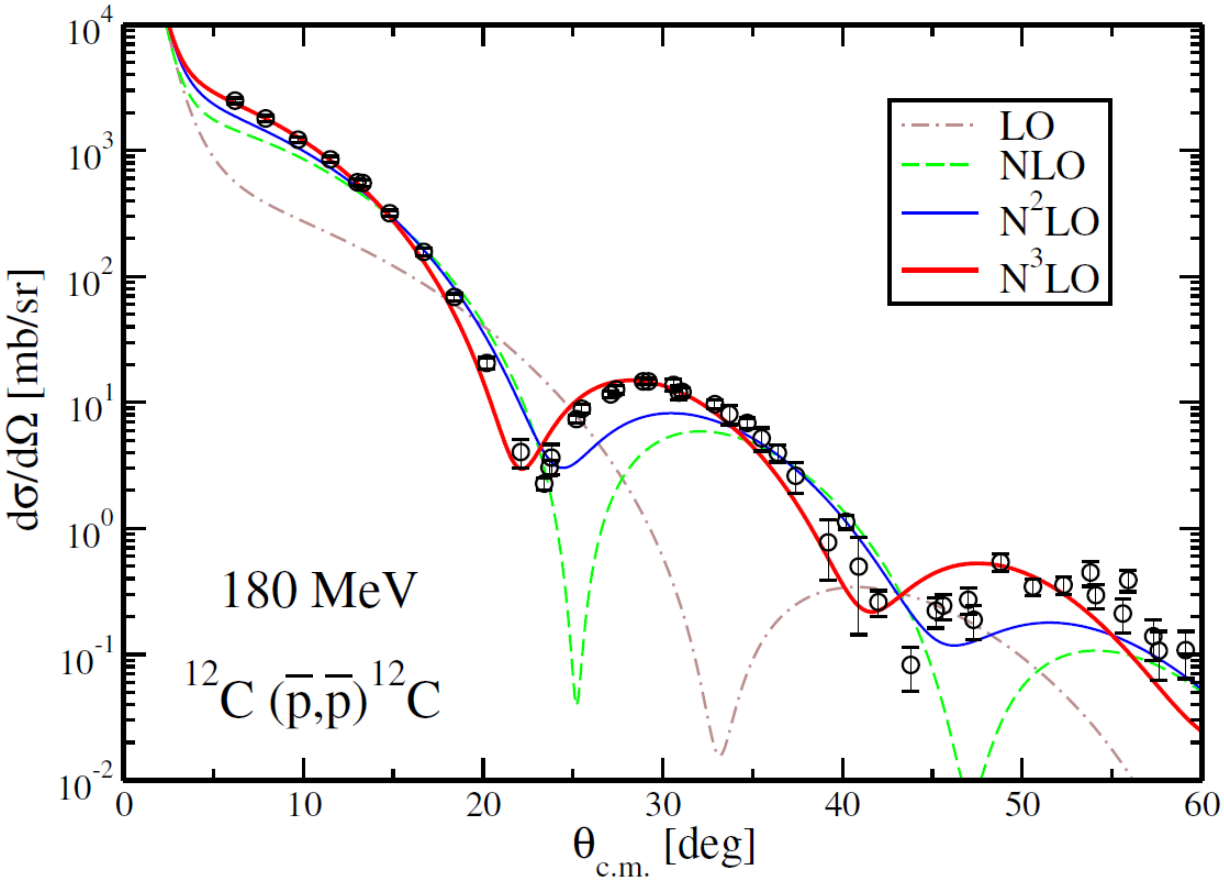

Figure 3.15: Results for the differential cross sections as a function of c.m. scattering angle for elastic antiproton scattering off ^{12}C. The cross sections are reported using the NN–N^{4}LO(500)+3N$_{\rm lnl}$ interaction computed at leading order (LO), and all the way to next–to–next–to–next–to–leading order (N^{3}LO) in the ChPT expansion. Only nonlocal translation invariant densities are used. This figure was published in Ref. [3]. Experimental data are taken from Ref. [15, 16].

In the latter nucleus, ^{18}O, this agreement is most surprising given that it is an *sd*–shell nucleus and is hence on the borderline of applicability of the NCSM at present.

In the previous sections we have discussed the convergence of NCSM densities with respect to the chiral order, which allows for some estimation of the theoretical uncertainty entering from chiral interactions. In Fig. 3.15, we show the convergence trends of our calculations with respect to the chiral order of the $\bar{p}N$ interaction. Recall that this interaction is used in calculating the dynamic part of the optical potential (t–matrix), whereas the structure part has already been shown to be convergent at N^{4}LO. Referring to the figure, we see that proceeding from the leading order (LO) calculation to the next–to–next–to–next–to–leading (N^{3}LO) calculation there are drastic changes in the predicted cross sections. Most notably, the general behaviour of the distribution is captured at third order (N^{2}LO), however, it isn't until the fourth order calculation (N^{3}LO) that the first diffraction minima is produced with a reasonably high degree of precision. We observe a fairly large shift in the N^{3}LO minima position relative to the LO minima position, with successive chiral orders coming closer to reproducing the correct location. The minima positions are highly sensitive to nuclear radii, and so a good structural description is needed in order to correctly reproduce the scattering minima. A reasonable description of the radii is only reached at N^{2}LO, and is largely due to the inclusion of more complicated two–pion exchange diagrams in the ChPT expansion. This is the first order at which a reasonable description of the short–range nuclear physics

is achieved, so the radii are more aptly captured and hence the scattering minima locations are better reproduced. In fact, this pattern confirms the expected convergence trends of the ChPT expansion, with higher chiral order contributions providing smaller and smaller refinements to the calculation.

By the development of the translation invariant one–body density matrices in the NCSM and the utilization of novel antiproton–nucleon chiral interactions developed in the same spirit as the usual NN interactions, we have successfully produced the first fully microscopic optical potential for antiproton–nucleus ($\bar{p}A$) scattering.

3.2.3 Inclusion of 3N forces

As mentioned in Sec. 3.2, it is not yet feasible to directly include the three–nucleon interaction in the dynamic part of the optical potential. Hence, while the nuclear densities may be obtained using SRG–evolved $NN + 3N$ interactions, we are limited solely to the bare NN interaction in generation of the t–matrix. While it is not possible to provide an exact treatment, a variety of medium corrections to account for higher–order effects have been proposed [116, 128, 129, 130, 131]. The value in introducing medium corrections to the dynamic part of the optical potential lies in the analysis of $3N$ effects on scattering observables. Here we investigate the impact of *genuine* (see Ref. [132]) three–body interactions, which enter at the level of the nuclear Hamiltonian. The approach here is presented in greater detail in Ref. [4].

The methodology is largely the same as before and begins from wanting to solve the $(A+1)$–body Lippmann–Schwinger equation of Eq. 3.9. However, instead we will take $V = V_{NN} + V_{3N}$ where $V_{NN} = \sum_{i=1}^{A} v_{0i}$ and the three–body piece is written as:

$$V_{3N} = \frac{1}{2}\sum_{i=1}^{A}\sum_{j=1,j\neq i}^{A} w_{0ij} \ , \tag{3.19}$$

where these interactions occur between the projectile (index 0) and arbitrary spectator nucleons. Using this form of the potential, we may then write the many–body optical potential operator as:

$$U = (V_{NN} + V_{3N}) + (V_{NN} + V_{3N})G_0(E)QU \ , \tag{3.20}$$

where the other operators are defined as before. Since this equation is not exactly solvable with the $3N$ interaction, it is here where we must introduce some approximate form in the limit of a dominant NN force (reasonable as the NN is always expected to provide more sizeable contributions than many–body forces). We then introduce an averaging over the Fermi sphere, which allows us to write

$$\sum_{j=1,j\neq i}^{A} w_{0ij} \approx \langle w_{0i} \rangle \ , \tag{3.21}$$

where $\langle w_{0i} \rangle$ is a two–body operator. Essentially, we are averaging over the dynamics of the third nucleon. As described in Ref. [4], this then allows for the optical potential operator to be written in the form

$$U = \sum_{i=1}^{A} t_{0i} \qquad\qquad t_{0i} = v_{0i}^{(1)} + v_{0i}^{(2)} g_i t_{0i} \tag{3.22}$$

where $v_{0i}^{(1)} = v_{0i} + \frac{1}{2}\langle w_{0i} \rangle$ and $v_{0i}^{(2)} = v_{0i} + \langle w_{0i} \rangle$. In this approach of averaging the third nucleon momenta over the Fermi sphere, we are functionally approximating the $3N$ interaction with a density–dependent NN interaction. This allows for a three–body medium correction to the usual NN dynamics, and hence allows us to gauge the impact of three–nucleon dynamics on scattering observables. In calculating $\langle w_{0i} \rangle$, we follow the authors of Ref. [133] which present a method for constructing the density–dependent NN

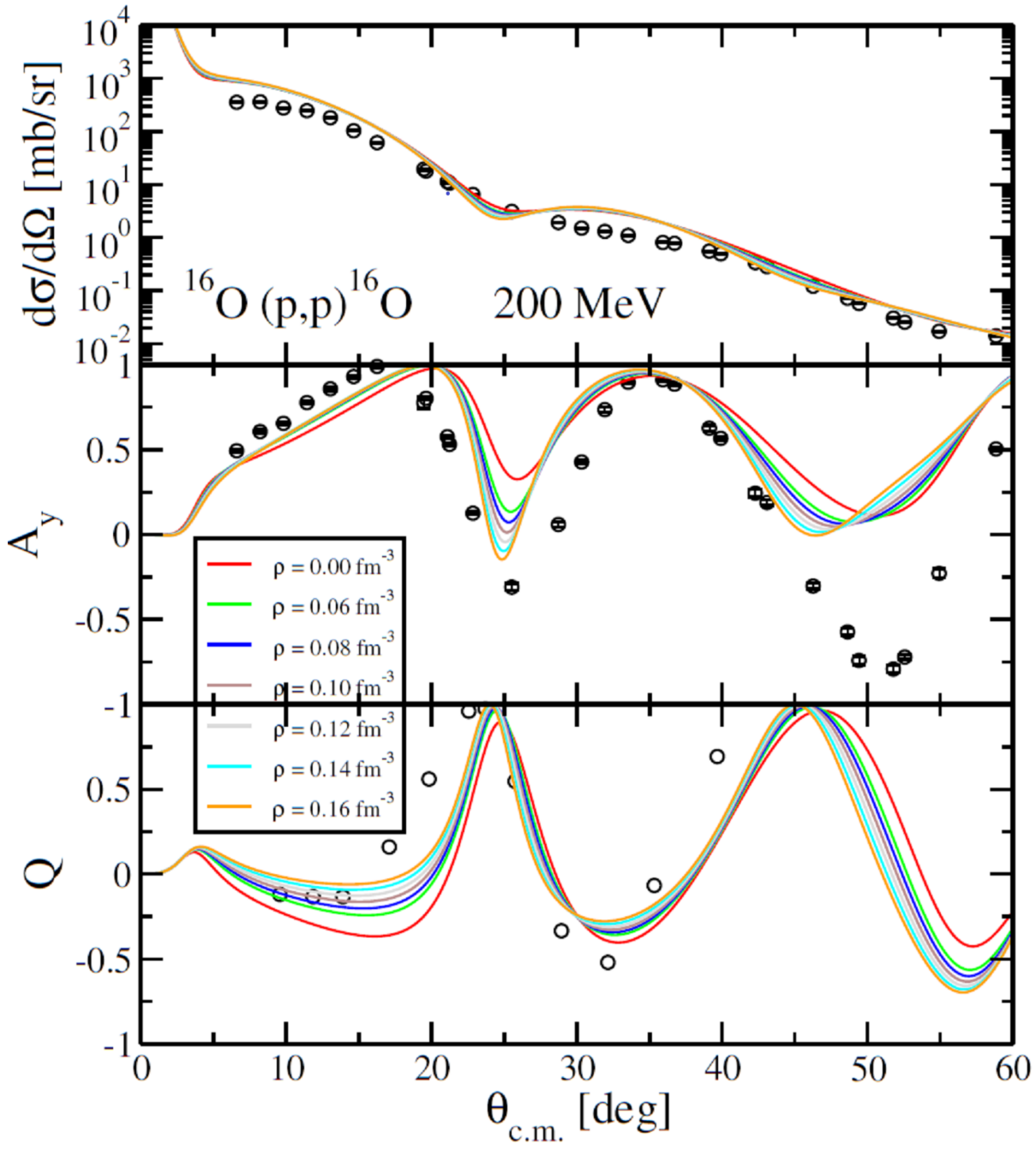

Figure 3.16: Scattering observables for $^{16}\mathrm{O}(p,p)^{16}\mathrm{O}$ reaction are plotted as functions of $\theta_{c.m.}$; in the top panel $\frac{d\sigma}{d\Omega}$, in the middle panel the analyzing power A_y, and in the bottom panel the spin rotation Q. The results are shown at a laboratory energy of 200 MeV. The baryon density is varied as $0.0\,\mathrm{fm}^{-3} \leq \rho \leq 0.16\,\mathrm{fm}^{-3}$. The nonlocal translation invariant density is computed in the NCSM. This figure was published in Ref. [4]. Experimental data are taken from Ref. [17, 18].

medium corrections from $3N$ interactions. We vary the baryon density model parameter ρ from surface–like to bulk–like densities in order to gain a broad understanding of how $3N$ interactions might effect observables.

In Fig. 3.16, we present results for the $^{16}\mathrm{O}(p,p)^{16}\mathrm{O}$ at a laboratory energy of 200 MeV. In particular, we show distributions for the differential cross sections $\frac{d\sigma}{d\Omega}$ (top panel), the analyzing power A_y (middle panel) and the spin rotation Q, as functions of the c.m. scattering angle $\theta_{c.m.}$. We introduce medium effects from *genuine* three–body interactions as first presented in Ref. [133], and vary the baryon density parameter ρ from $0.0\,\mathrm{fm}^{-3}$ to $1.6\,\mathrm{fm}^{-3}$. The minimum value of $0.0\,\mathrm{fm}^{-3}$ corresponds to no inclusion of the $3N$ medium effects, and so the optical potential equation reduces to the usual form with the two–body interaction, Eq. 3.14. We see that for the differential cross section, the medium effects of the $3N$ interaction are minimal, with vary little variation between the curves with different baryon density. However, in the middle panel we see that with the inclusion of $3N$ medium effects, there is a large shift in the description of the analyzing power and spin rotation. These polarization observables are seemingly sensitive to three–body effects, and in general the medium effects improve the agreement between the optical potential and experiment. In particular, the first minima of the analyzing power is tremendously improved in location, especially with the higher baryon densities.

As the polarization observables appear more sensitive to the inclusion of the $3N$ medium effects, it is natural to investigate these further. In Fig. 3.17, we show the analyzing power A_y for $^{16}\mathrm{O}(p,p)^{16}\mathrm{O}$ at laboratory energies of 100 MeV (top panel), 135 MeV (middle panel) and 318 MeV (bottom panel). The red band corresponds to a family of curves represented by the constraints $0.08\,\mathrm{fm}^{-3} \leq \rho \leq 0.13\,\mathrm{fm}^{-3}$, and corresponds to various baryon densities ranging from surface–like to bulk–like. For comparison, the thin blue curve corresponds to a baryon density of $0.0\,\mathrm{fm}^{-3}$, a calculation in which no three–nucleon force medium effects are considered. We see that the medium effects in general contribute at the lower reaction energies, whereas at the higher energy of 318 MeV there is little change in the A_y distribution. In particular at 135 MeV, we see that the description of the first minima is significantly improved, and the overall shape of the analyzing power is in better agreement with the data. It is hard to gauge whether or not the $3N$ medium effects improve the lowest energy calculation at 100 MeV, but this is primarily due to the breakdown of the impulse approximation which prevents this optical potential model from accurately describing low–energy dynamics.

Referring to Fig. 3.18, we similarly show results for the analyzing power A_y for $^{12}\mathrm{C}(p,p)^{12}\mathrm{C}$ at laboratory energies of 122 MeV (top panel), 160 MeV (middle panel) and 200 MeV (bottom panel). The red band corresponds to same constraints on ρ as before, and the blue curve represents a calculation with no $3N$ medium effects. This range of energies is better suited to description by the optical model with an impulse approximation, and as such, we see that in general the $3N$ medium effects greatly improve the shape of A_y. In fact, for all three panels, it is clear that the description of the first minima is positively affected by inclusion of three–body interaction effects.

By averaging one of the nucleon momenta over a Fermi sphere, we have sought to include some effects of the three–nucleon interaction in the dynamic part of the optical potential, a full treatment of which is not presently feasible. This was done in approximation by producing a density dependent three–nucleon interaction, which could then be included at the two–body level in the t–matrix. We found in general that effects of the $3N$ interaction on differential cross sections were relatively minor, whereas polarization observables were highly sensitive to the three–body contributions. This is likely due to the higher–sensitivity of A_y and Q to nuclear radii, which are more accurately reproduced with inclusion of three–nucleon interactions.

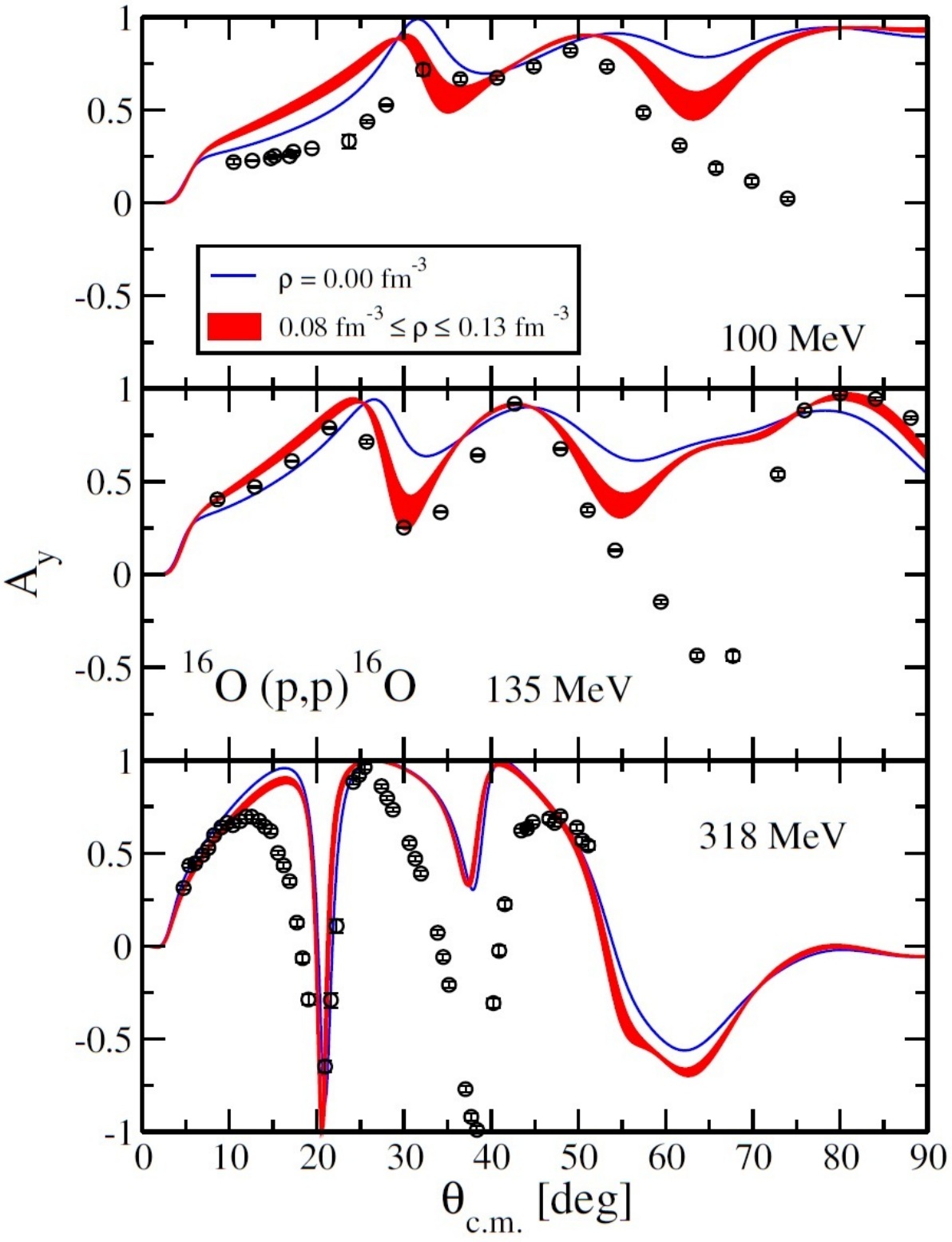

Figure 3.17: The analyzing power A_y for $^{16}\mathrm{O}(p,p)^{16}\mathrm{O}$ reaction is plotted as a function of $\theta_{c.m.}$. The laboratory energy used in the top panel is 100 MeV, in the middle panel is 135 MeV, and in the bottom panel is 318 MeV. The baryon density is varied as $0.08\,\mathrm{fm}^{-3} \leq \rho \leq 0.13\,\mathrm{fm}^{-3}$ (red band), with the $\rho = 0.0\,\mathrm{fm}^{-3}$ calculation also shown (blue curve). The nonlocal translation invariant density is computed in the NCSM. This figure was published in Ref. [4]. Experimental data are taken from Ref. [17, 18].

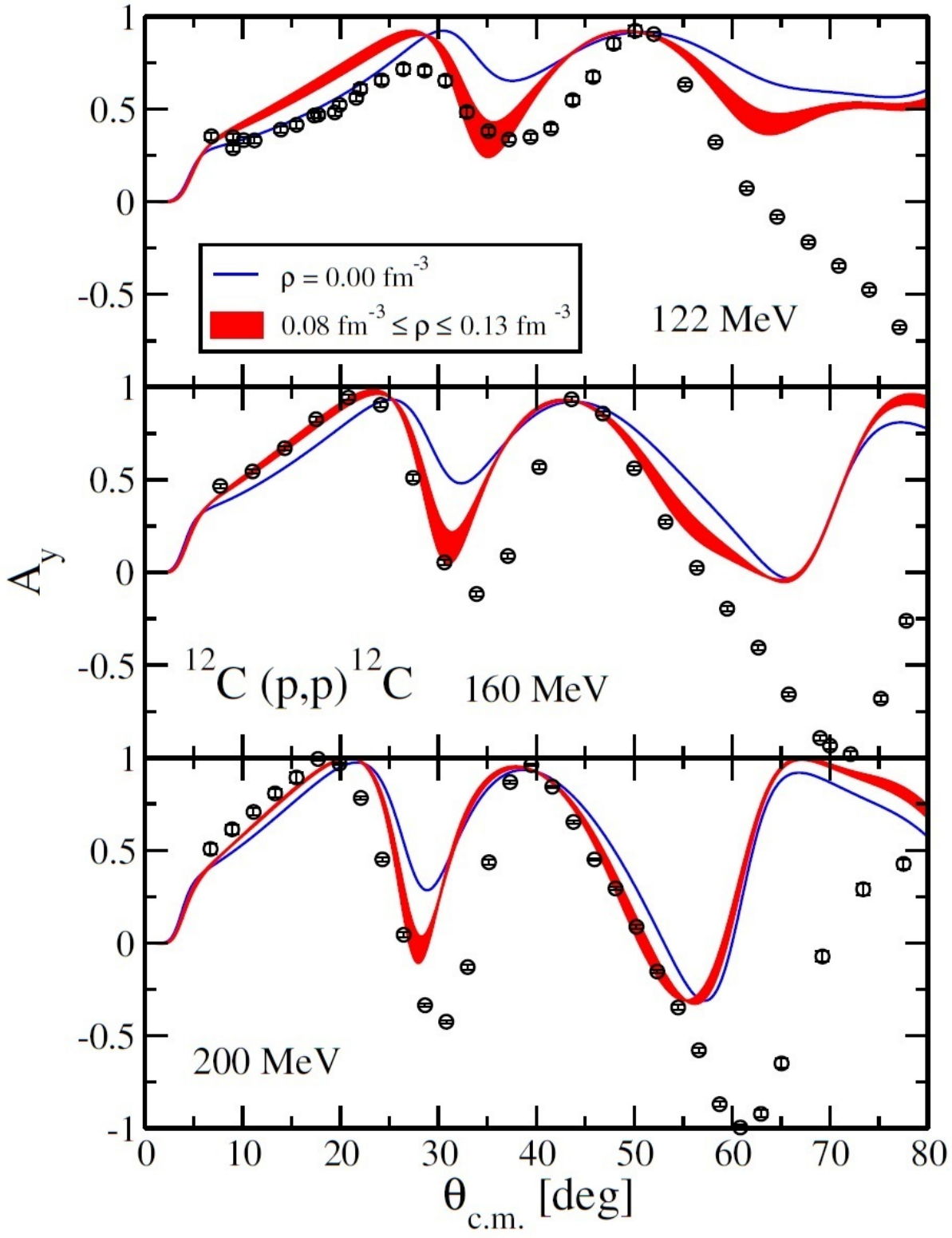

Figure 3.18: The analyzing power A_y for $^{12}\mathrm{C}(p,p)^{12}\mathrm{C}$ reaction is plotted as a function of $\theta_{c.m.}$. The laboratory energy used in the top panel is 122 MeV, in the middle panel is 160 MeV, and in the bottom panel is 200 MeV. The baryon density is varied as $0.08\,\mathrm{fm}^{-3} \leq \rho \leq 0.13\,\mathrm{fm}^{-3}$ (red band), with the $\rho = 0.0\,\mathrm{fm}^{-3}$ calculation also shown (blue curve). The nonlocal translation invariant density is computed in the NCSM. This figure was published in Ref. [4]. Experimental data are taken from Ref. [17, 18].

3.3 Kinetic density from nonlocal one–body density

The overall goal of *ab initio* theory is to accurately describe the physics of nuclei from first principles. However, this can limit one's reach in the nuclear chart for a variety of reasons, i.e. in the case of the NCSM, computational complexity. Alternative many–body methods, such as DFT, approach the problem of describing nuclei using functionals [134, 135, 136, 137, 138, 139, 140]. A local energy density functional (EDF) $\mathcal{H}(r)$ may be constructed from various system densities,

$$\mathcal{H} = \mathcal{H}_{kin.} + \mathcal{H}_{spin} + \mathcal{H}_{iso.} + \mathcal{H}_{other} \ , \tag{3.23}$$

where we include sample terms of the kinetic, spin and isospin density functionals; it is then minimized with respect to energy to provide ground state properties of nuclear systems. This field has achieved great success in the description of medium– to heavy–mass nuclei [141, 142, 143, 144, 145], systems in which the effects of nonlocality and c.m. motion are greatly suppressed. If DFT is to extend it's reach to the light–nuclei and provide valuable comparisons as a unique many–body method, we must quantitatively understand the extent to which c.m. motion affects the density functionals. Further, approaches in DFT often make use of phenomenology to improve the quality of the input functionals, though recently there has been an effort dedicated to connecting the functional inputs in DFT to *ab initio* theory, and hence to the underlying QCD structure [106, 107, 108]. With the development of nonlocal one–body densities in the NCSM, we may exactly compute fundamental inputs in the EDF; one such quantity is the kinetic density. With the development of translation invariant nonlocal one–body nuclear densities, we may compute the nuclear kinetic density from *ab initio* theory with and without c.m. contamination, allowing for a direct comparison to c.m. removal techniques in DFT. While approaches like the NCSM and DFT often explore different mass regimes, they both have the ability to study the group of Oxygen isotopes, making this particular set of nuclei an excellent comparison ground for the two methods.

The kinetic energy functional is defined as

$$\mathcal{H}_{kinetic}(\vec{r}) = \frac{\hbar^2}{2m}\tau_0(\vec{r}) \, , \tag{3.24}$$

where m is the nucleon mass and $\tau_0 = \sum_{\mathcal{N}} \tau_{\mathcal{N}} = \tau_p + \tau_n$ is the total kinetic density. The nucleon kinetic density is dependent on a Laplacian–like operation applied to the nonlocal nuclear density,

$$\tau_{\mathcal{N}}(\vec{r}) = \left[\vec{\nabla} \cdot \vec{\nabla}' \rho_{\mathcal{N}}(\vec{r}, \vec{r}') \right]_{\vec{r}=\vec{r}'} \ , \tag{3.25}$$

where $\mathcal{N}$ denotes the nucleon type for protons (p) and neutrons (n). Making use of various angular momentum relations [54],

$$\begin{aligned} \nabla_0 R_{nl}(r) Y^*_{lm_l}(\hat{r}) = & \sqrt{\frac{(l+1)^2 - m_l^2}{(2l+1)(2l+3)}} \left(\frac{dR_{nl}(r)}{dr} - \frac{l}{r} R_{nl}(r) \right) Y^*_{l+1,m_l}(\hat{r}) \\ & + \sqrt{\frac{l^2 - m_l^2}{(2l-1)(2l+1)}} \left(\frac{dR_{nl}(r)}{dr} + \frac{l+1}{r} R_{nl}(r) \right) Y^*_{l-1,m_l}(\hat{r}) \ , \end{aligned} \tag{3.26}$$

$$\begin{aligned} \nabla_{\pm 1} R_{n,l}(r) Y^*_{l,m_l}(\hat{r}) = & \sqrt{\frac{(l \pm m_l + 1)(l \pm + m_l + 2)}{2(2l+1)(2l+3)}} \left(\frac{dR_{nl}(r)}{dr} - \frac{l}{r} R_{nl}(r) \right) Y^*_{l+1,m_l \pm 1}(\hat{r}) \\ & - \sqrt{\frac{(l \mp m - 1)(l \mp m)}{2(2l-1)(2l+1)}} \left(\frac{dR_{nl}(r)}{dr} + \frac{l+1}{r} R_{nl}(r) \right) Y^*_{l-1,m_l \pm 1}(\hat{r}) \ , \end{aligned}$$

and calculating the derivative of the radial harmonic oscillator (RHO) function,

$$\frac{dR_{nl}}{dr} = \frac{l}{r}R_{nl} - \frac{1}{b}\left[\sqrt{n+l+\frac{3}{2}}\,R_{nl+1}(r) + \sqrt{n}\,R_{n-1l+1}(r)\right] , \tag{3.27}$$

it is possible to compute the kinetic density analytically from NCSM densities. The derivation of the kinetic density is shown in Appendix A.3.1. This then leads to the general form for each term in the kinetic density sum

$$\tau_{\mathcal{N}}^{(u)}(\vec{r}) = \nabla_u \nabla'_{-u} \rho_{\mathcal{N}}(\vec{r},\vec{r}')|_{\vec{r}=\vec{r}'} = \sum_{nln'l'Kkm_lm_{l'}} \alpha^{K,i,f}_{nln'l'}\,(lm_l l' m_{l'}|LM)\mathcal{K}_{nln'l'}(r)\,Y^*_{LM}(\hat{r}) . \tag{3.28}$$

where $u\,\epsilon\{\pm 1, 0\}$ and

$$\begin{aligned}
\mathcal{K}_{nln'l'}(r) = {} & c_{u0}\left(\frac{dR_{nl}(r)}{dr} - \frac{l}{r}R_{nl}(r)\right)\left(\frac{dR_{n'l'}(r)}{dr} - \frac{l'}{r}R_{n'l'}(r)\right) \\
& + c_{u1}\left(\frac{dR_{nl}(r)}{dr} - \frac{l}{r}R_{nl}(r)\right)\left(\frac{dR_{n'l'}(r)}{dr} + \frac{l'+1}{r}R_{n'l'}(r)\right) \\
& + c_{u2}\left(\frac{dR_{nl}(r)}{dr} + \frac{l+1}{r}R_{nl}(r)\right)\left(\frac{dR_{n'l'}(r)}{dr} - \frac{l'}{r}R_{n'l'}(r)\right) \\
& + c_{u3}\left(\frac{dR_{nl}(r)}{dr} + \frac{l+1}{r}R_{nl}(r)\right)\left(\frac{dR_{n'l'}(r)}{dr} + \frac{l'+1}{r}R_{n'l'}(r)\right) .
\end{aligned} \tag{3.29}$$

In Eq. 3.28, $\alpha^{Kif}_{nln'l'}$ is given by Eq. (A.39) and contains the information related to the reduced one–body density matrix elements. The c_{uj} coefficients contain the angular momentum algebra related to the kinetic density operator, while the remaining radial and angular terms are the result of gradient application. Note that we group all spherical harmonics under the collective index L and projection M. In this way, the kinetic density is analytically computed from the *ab initio* nonlocal densities [2].

The kinetic density also provides a more robust test of the c.m. removal procedure applied in the NCSM. From the nuclear kinetic densities, it is possible to exactly recover the mean value intrinsic kinetic energy of the nucleus. This may be independently calculated from the two–body density matrix elements introduced in second quantization:

$$\begin{aligned}
\langle T_{int}\rangle &= \frac{1}{4}\sum_{abcd}\langle ab|\,T_{int}\,|cd\rangle_{\,SD}\,\langle A\lambda JT|\,a_a^\dagger a_b^\dagger a_d a_c\,|A\lambda JT\rangle_{\,SD} \\
&= {}_{SD}\langle A\lambda JT|\left(\frac{\hbar^2}{2m}\tau_0^{trinv}\right)|A\lambda JT\rangle_{\,SD} \\
&= \frac{\hbar^2}{2m}\int_0^\infty dr\,r^2\tau_0^{trinv}(r) .
\end{aligned} \tag{3.30}$$

In particular, it is possible to verify that we have precisely removed the c.m. contamination present in the NCSM eigenstates as we know the c.m. contribution to the kinetic energy of the nucleus:

$$\begin{aligned}
\langle T_{wiCOM}\rangle &= {}_{SD}\langle A\lambda JT|\left(\frac{\hbar^2}{2m}\tau_0^{wiCOM}\right)|A\lambda JT\rangle_{\,SD} \\
&= \frac{\hbar^2}{2m}\int_0^\infty r^2\tau_0^{wiCOM}(r)\,dr \\
&= {}_{SD}\langle A\lambda JT|\,\frac{\hbar^2}{2m}\left(\tau_0^{int}+\tau_0^{COM}\right)|A\lambda JT\rangle_{\,SD} \\
&= \langle T_{int}\rangle + \frac{3}{4}\hbar\Omega .
\end{aligned} \tag{3.31}$$

Nucleus	$N_{\max}$	$\langle T_{int} \rangle$	$\langle T_{wiCOM} \rangle$
^{4}He	14	51.91	66.91
^{6}He	12	78.26	93.26
^{8}He	10	116.30	131.30
^{12}C	8 IT	219.84	234.84
^{16}O	8 IT	301.69	316.69

Table 3.1: Ground state mean kinetic energy values using *trinv* and *wiCOM* kinetic densities for all aforementioned nuclei, calculated with the NN–N^{4}LO(500)+3N$_{\rm lnl}$ interaction. All $\langle T \rangle$ values are recorded in MeV. Note *IT* refers to an importance truncated basis space, as described in Sec. 2.2.4. The values of $\langle T_{int} \rangle$ and $\langle T_{wiCOM} \rangle$ differ as expected, by $\langle T_{c.m.} \rangle = \frac{3}{4}\hbar\Omega$, see Eq. (3.31). These results were published in Ref. [2].

Results

In this section we discuss predictions for the distributions of the c.m. contaminated and translation invariant nuclear kinetic densities. Figure plots will be labeled with *wiCOM* for the c.m. contaminated density and with *trinv* for the translational invariant density. We study a similar range of systems as in the density section, however we emphasize that meaningful comparisons to DFT can only be performed in some of the heavier systems, i.e. ^{12}C and ^{16}O. These systems are large enough to be explored by DFT methods, and also light enough to experience non–negligible effects from c.m. motion, hence making them the optimal nuclei for studying c.m. contamination in EDFs. Kinetic densities (calculated only for the ground state) are plotted with the angular dependence factorized out:

$$\tau_{\rm N}(\vec{r}) = \tau_{\rm N}(r)\, Y^*_{LM}(\hat{r}) \tag{3.32}$$

where only the radial component $\tau_{\rm N}(r)$ of this equation is plotted. All densities have been computed as discussed in the previous sections, and so for these calculations the SRG–evolved NN–N^{4}LO(500)+3N$_{\rm lnl}$ interaction has been used.

In Table 3.1, we provide NCSM calculations of the ground state mean kinetic energy $\langle T \rangle$ using the derived kinetic densities. This table provides numerical confirmation of Eq. (3.31), a non–trivial test which confirms the separation, and successful removal, of the intrinsic and c.m. motion in the NCSM.

Now we will analyze the kinetic distribution and attempt to understand the effects of c.m. removal. We present the NCSM predictions for the kinetic density of ^{4,6,8}He in Figs. 3.19, 3.20 and 3.21, respectively. Looking at the kinetic densities depicted in the Fig. 3.19, we see that the *trinv* and *wiCOM* densities predict remarkably different distributions, with the latter looking more symmetric about the maximum and the former having a significant asymmetry. In particular, the *trinv* kinetic density is generally a narrower distribution, peaking higher in the short–range and tending toward zero more rapidly in the medium–range. What is seen in the kinetic densities is the expected amplification of c.m. removal effects in the density. Application of the gradient operators on the density has made the apparent structure differences more pronounced, in particular those features corresponding to the short– and medium–range behaviour. As was clear in the densities, c.m. motion can largely suppress the intrinsic structure of the nuclear wave function in these operators.

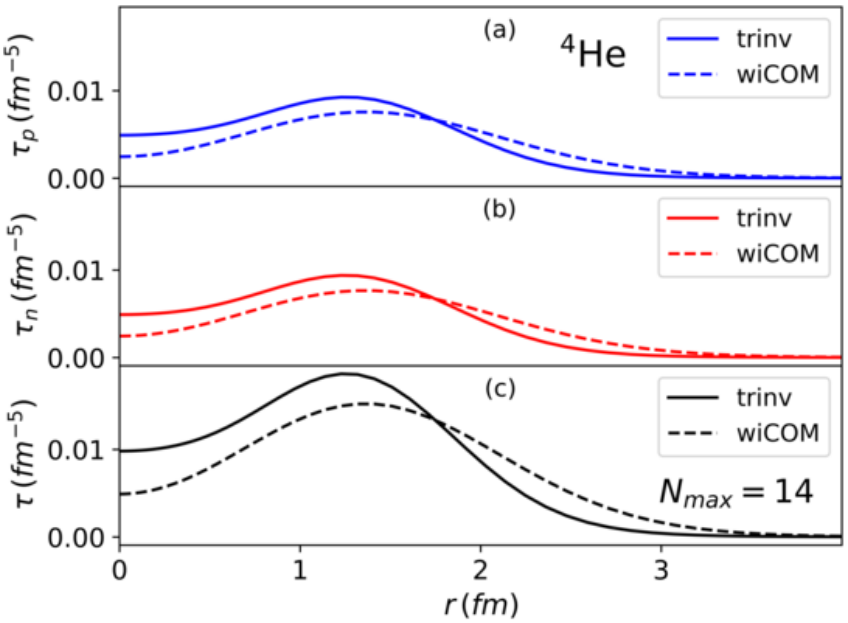

Figure 3.19: Comparison of the *trinv* and *wiCOM* kinetic densities for the nucleus ^{4}He. The proton, neutron and total kinetic densities are plotted in panels (a), (b), and (c), respectively. The ground state nonlocal density was computed as described in Sec. 3.1. These results were published in Ref. [2].

Drawing our attention to Figs. 3.20 and 3.21, we similarly see the amplified effects of c.m. removal. Referring to Fig. 3.20, we see quite drastic changes in the distributions shape, particularly in the short–range ~ 1 fm. While this is the case, the distribution is still noticeably modified in the longer–range regions, and we notice the tail does not as rapidly fall to zero as was the case in ^{4}He. This is emphasized to a greater degree in Fig. 3.21 with ^{8}He. This is most definitely due to the long–range dynamics that are observed in halo nuclei, which often have nucleon clusters extending into regions beyond the central collection of nucleons.

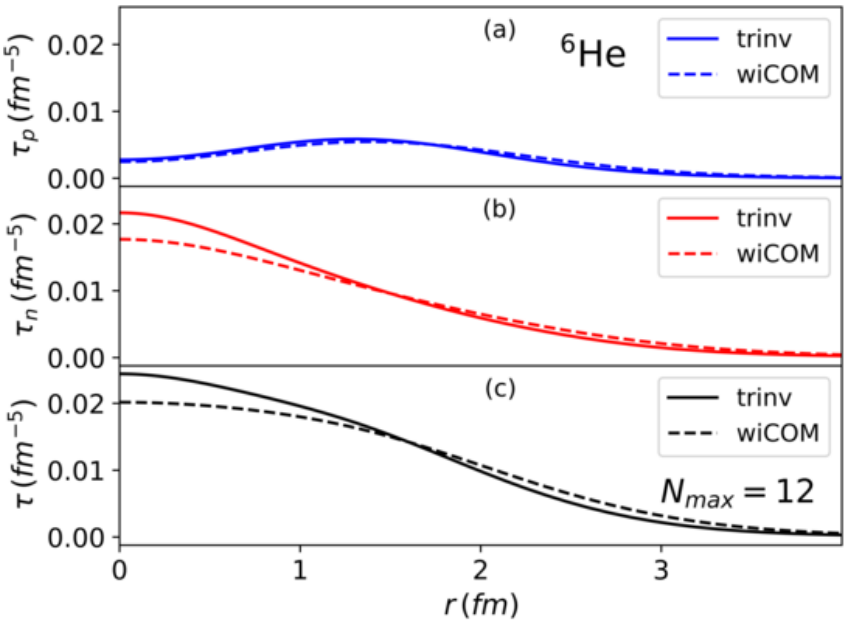

Figure 3.20: Comparison of the *trinv* and *wiCOM* kinetic densities for the nucleus ^{6}He. The proton, neutron and total kinetic densities are plotted in panels (a), (b), and (c), respectively. The ground state nonlocal density was computed as described in Sec. 3.1. These results were published in Ref. [2].

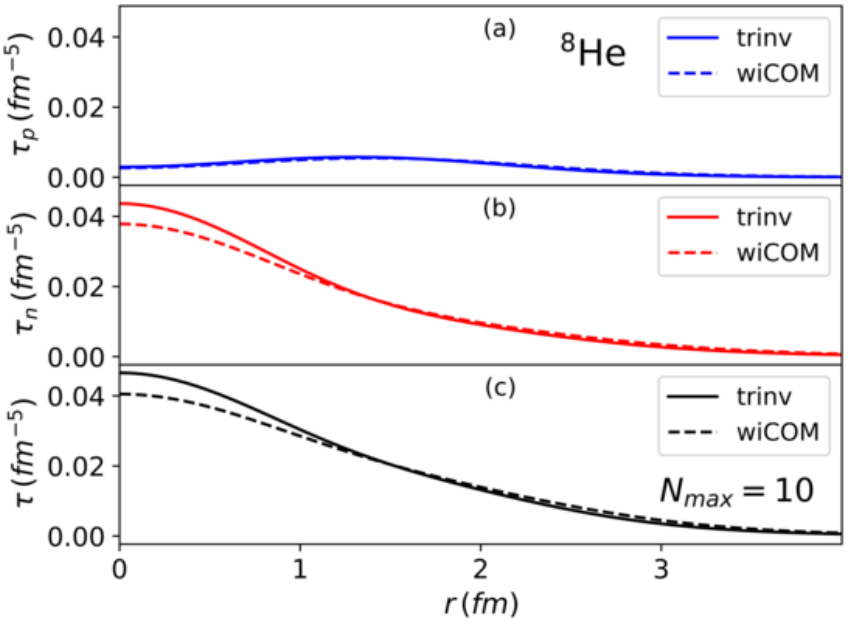

Figure 3.21: Comparison of the *trinv* and *wiCOM* kinetic densities for the nucleus ^{8}He. The proton, neutron and total kinetic densities are plotted in panels (a), (b), and (c), respectively. The ground state nonlocal density was computed as described in Sec. 3.1. These results were published in Ref. [2].

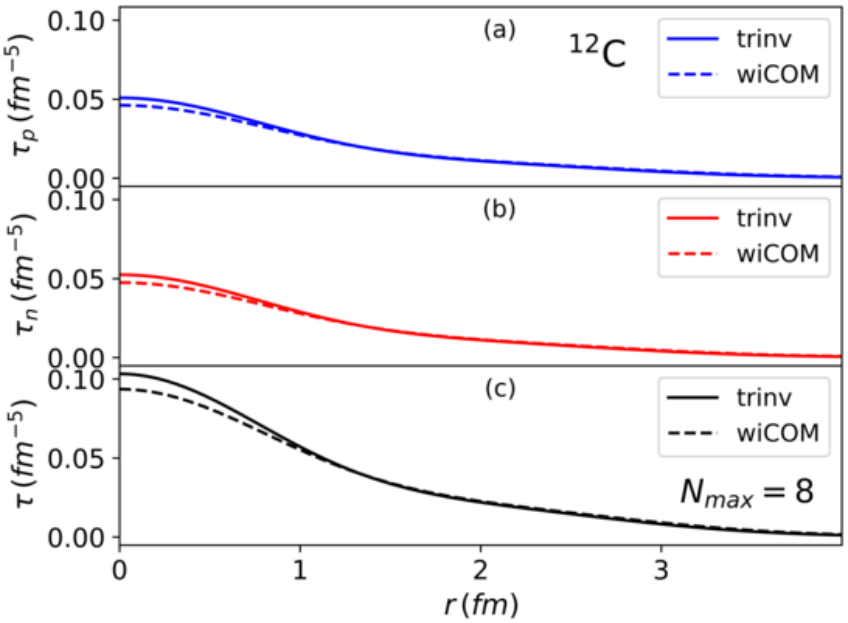

Figure 3.22: Comparison of the *trinv* and *wiCOM* kinetic densities for the nucleus ^{12}C. The proton, neutron and total kinetic densities are plotted in panels (*a*), (*b*), and (*c*), respectively. The ground state nonlocal density was computed as described in Sec. 3.1. These results were published in Ref. [2].

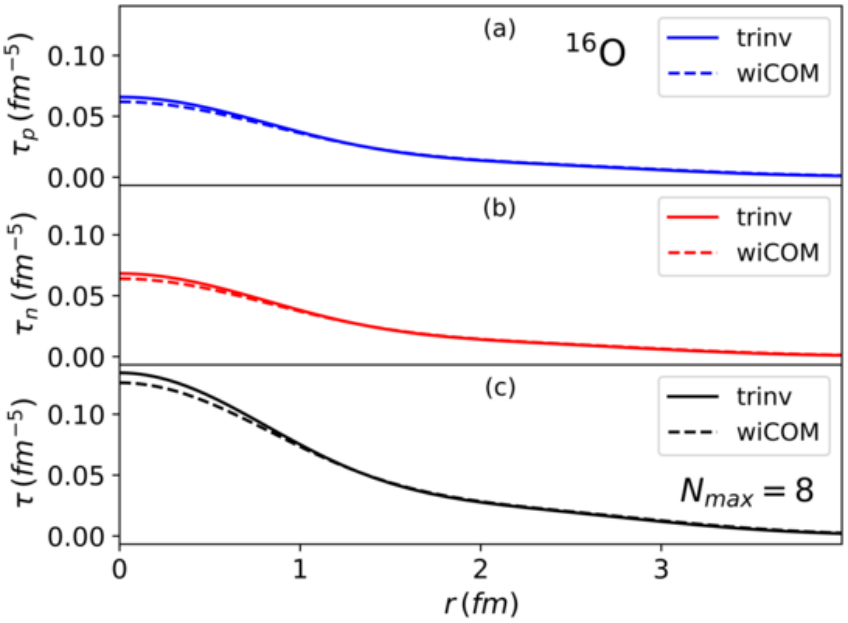

Figure 3.23: Comparison of the *trinv* and *wiCOM* kinetic densities for the nucleus ^{16}O. The proton, neutron and total kinetic densities are plotted in panels (*a*), (*b*), and (*c*), respectively. The ground state nonlocal density was computed as described in Sec. 3.1. These results were published in Ref. [2].

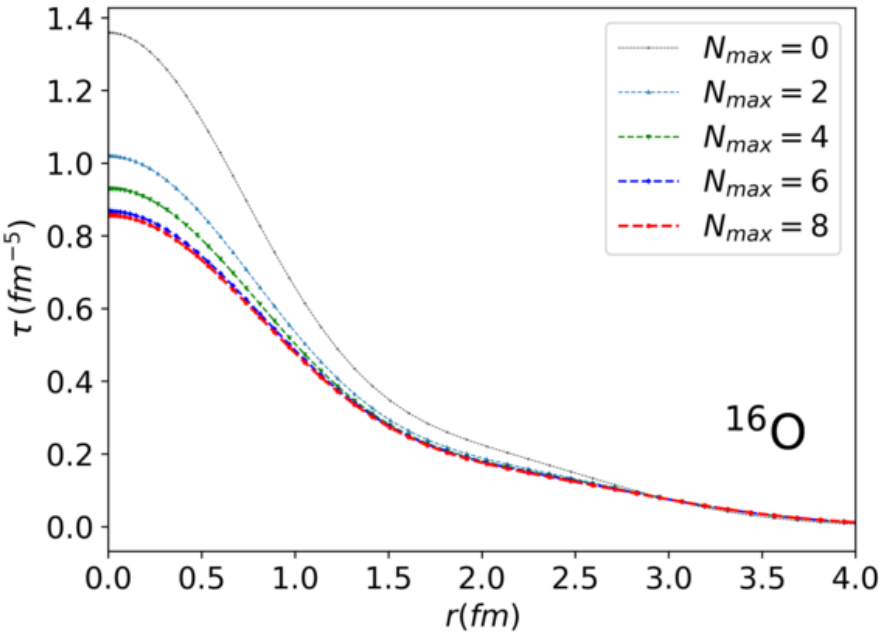

Figure 3.24: Convergence comparison of the ground state ^{16}O *trinv* kinetic densities computed in the NCSM approach. The ground state nonlocal density was computed as described in Sec. 3.1. These results were published in Ref. [2].

Any valuable comparisons to DFT require the study of larger nuclei, so we present the kinetic densities for the heavier nuclear systems ^{12}C and ^{16}O in Fig. 3.22 and Fig. 3.23. In these nuclei, the most significant differences occur in the short–range structure, though the effects are certainly not as pronounced as in the lighter nuclear systems. This is to be expected, as discussed in Sec. 3.1, due to the scaling of the c.m. potential term proportional to $\frac{1}{A}$. Nevertheless, while the effects of translational invariance are reduced in these larger nuclear systems, the kinetic density operator still exacerbates these effects and produces distributions with meaningful differences. Moreover, the non–negligible differences introduced by translational invariance in the density operator must be considered in order to probe these nuclear systems with high–precision.

As a final comment, we briefly mention the convergence of our kinetic density calculations with respect to the HO expansion parameter N_{max} shown in Fig. 3.24. As was the case with the density, even in the system ^{16}O we achieve rapid convergence when utilizing the NN–N^{4}LO(500)+3N$_{\text{lnl}}$ interaction, with the $N_{max} = 6$ and $N_{max} = 8$ importance truncated curves nearly overlapping.

Comparison to basic c.m. treatment in DFT

Recalling the form of the kinetic EDF in Eq. (3.33), without the translational invariance explicitly constructed in the NCSM nonlocal one-body densities, there is no direct avenue for treating c.m. contamination in this quantity. However, a simple approximation may be used to explicitly treat the c.m. motion in the kinetic density [146, 147, 148]. It has been motivated that by modifying the kinetic EDF with a term inversely proportional to the number of nucleons in the system,

$$\mathcal{H}_{kinetic}(\vec{r}) = \frac{\hbar^2}{2m}\left(1 - \frac{1}{A}\right)\tau_0(\vec{r}) \ , \tag{3.33}$$

Nucleus	$N_{\max}$	$\langle T_{int} \rangle$	$\langle T_{wiCOM} \rangle$	$\langle T_{DFT} \rangle$
^{4}He	14	51.91	66.91	50.18
^{6}He	12	78.26	93.26	77.72
^{8}He	10	116.30	131.30	114.89
^{12}C	8 IT	219.84	234.84	215.27
^{16}O	8 IT	301.69	316.69	296.90

Table 3.2: Ground state mean kinetic energy values using *trinv* and *wiCOM* kinetic densities for all aforementioned nuclei, calculated with the NN–N^{4}LO(500)+3N$_{\text{lnl}}$ interaction. All $\langle T \rangle$ values are recorded in MeV. Note *IT* refers to an importance truncated basis space, as described in Sec. 2.2.4. The values of $\langle T_{int} \rangle$ and $\langle T_{wiCOM} \rangle$ differ as expected, by $\langle T_{c.m.} \rangle = \frac{3}{4}\hbar\Omega$, see Eq. (3.31). The $\langle T_{DFT} \rangle$ is calculated using Eq. (3.34). These results were published in Ref. [2].

it is possible to efficiently treat some of the contamination from spurious c.m. motion. In our calculations, τ_0 would correspond to the *wiCOM* kinetic density, and so we make the definition

$$\tau_{DFT}(\vec{r}) = \left(1 - \frac{1}{A}\right)\tau_{wiCOM}(\vec{r}) \ . \tag{3.34}$$

We stress that the curve τ_{DFT} is not representative of a calculation performed in the DFT framework, but is referred to as such due to the c.m. removal procedure applied. The idea is to compare the exact construction of translational invariance in the kinetic density versus the approximate introduction of it via the DFT approximation. In Table 3.2, we present results for the mean value kinetic energy corresponding to the various kinetic density distributions. In particular, it is instructive to compare the $\langle T_{int} \rangle$ and $\langle T_{DFT} \rangle$ columns. In fact, we see that the values are quite similar and that the approximation does a reasonable job of reproducing the mean kinetic energy computed from solely the intrinsic motion, though the τ_{DFT} distribution consistently underestimates the exact result. As well, with increasing nucleon number we see that the c.m. removal approximation becomes less valid with a greater spread in the values, so there is some unphysical trend in A.

While the integral of the kinetic distributions appear to agree reasonably well, the same cannot be said for the predicted functionals from each approach. We refer to Fig. 3.25. Taking the *wiCOM* as a sort of "starting" point for both of the c.m. removal procedures, it is most important to compare the deviation of the resultant *trinv* and DFT curves. In particular, we notice that the density profiles corresponding to each c.m. removal procedure are shifted in the **opposite** directions; this can be seen easily in the lighter nuclei where the effects are more apparent. While the effects are reduced in the larger nuclear systems, they are certainly non–negligible. In fact, the approximate c.m. treatment used to compute the DFT curve only furthers the gap between the DFT curve and the true, intrinsic structure predictions from the NCSM. The inclusion of the $\frac{1}{A}$ term in the calculation of the kinetic EDF reduces the importance of the short–range physics, instead putting greater emphasis on the long–range structure.

We have identified that the basic c.m. removal procedure utilized in DFT is not valid, and in fact only worsens the description of the intrinsic nuclear physics. Despite the relatively few efforts for quantifying the effects of c.m. removal techniques with respect to *ab initio* calculations, these comparisons show precisely what many have suggested as a potential source of error in the technique [147, 148]. As was

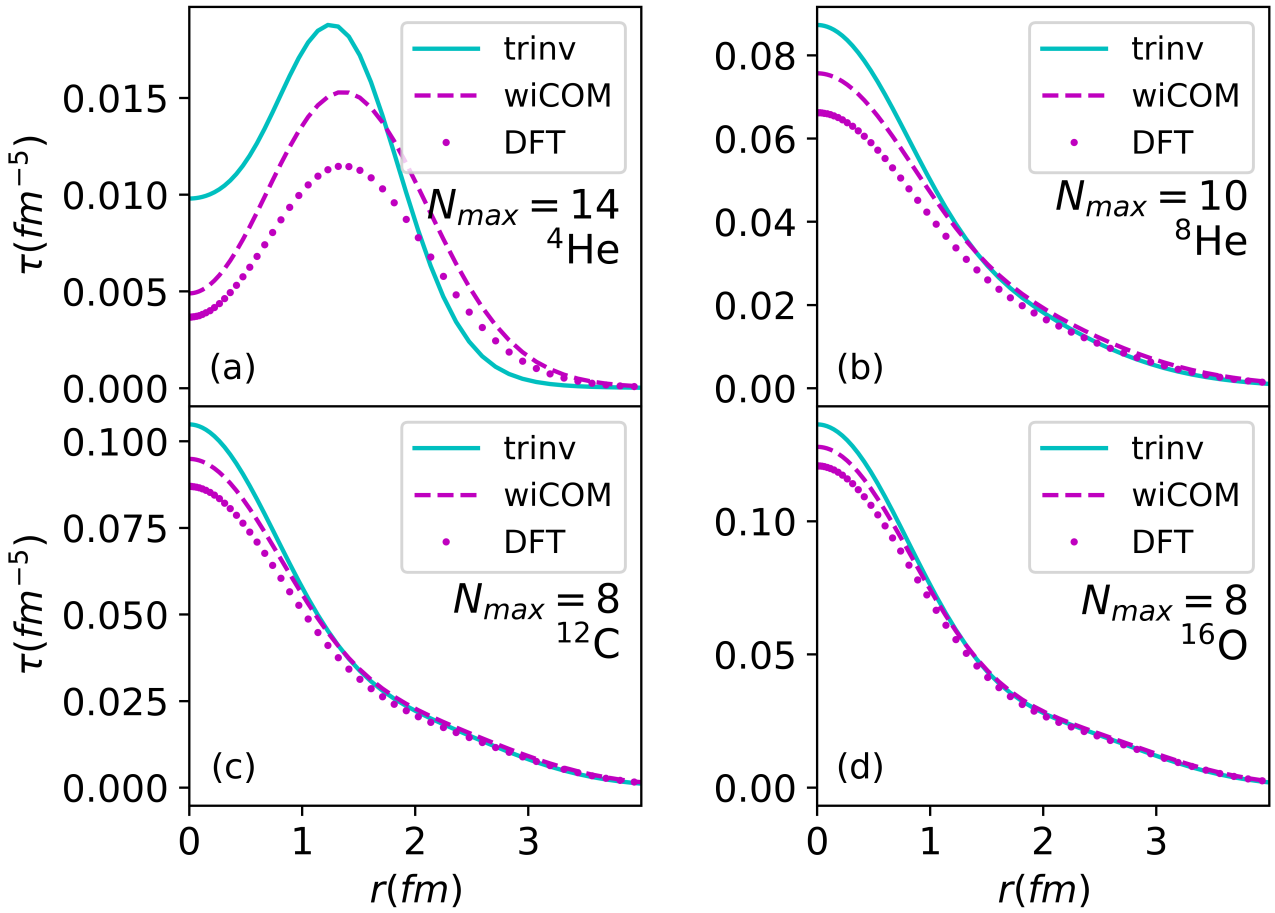

Figure 3.25: Comparison of the *trinv*, *wiCOM* and *DFT* kinetic densities for the nuclei: ^{4}He in panel **(a)**, ^{8}He in panel **(b)**, ^{12}C in panel **(c)**, and ^{16}O in panel **(d)**. The proton, neutron and total kinetic densities are plotted in panels (a), (b), and (c), respectively. The ground state nonlocal density was computed as described in Sec. 3.1. These results were published in Ref. [2].

the purpose of this section, we have made a direct link between the theory of density functionals and *ab initio* approaches like the NCSM. This procedure and analysis is generalizable to various quantities that enter the total EDF in DFT. By constructing the EDF completely from *ab initio* theory, one may then study the structural changes in the functionals and the effects that this will have on minimization of the EDF, which we anticipate will be on the order of fine structure corrections.

Chapter 4

Natural orbitals in the NCSM

As has been emphasized in Sec. 2.2.4, one of the largest obstacles of *ab initio* nuclear theory is to describe complicated quantum many–body systems using realistic inter–nucleon potentials while maintaining reasonable computation time and power. In general, the atomic nucleus encompasses physics at various scales; an accurate description of long– and short–range physics is necessary for a complete understanding of nuclear structure and dynamics. While various algorithmic approaches to solving the nuclear many–body problem exist and have been shown to be successful in their respective regimes, such as the lengthily discussed NCSM, many techniques (especially those which employ direct diagonalization approaches) suffer from the same computational limits of exponential basis space growth with respect to the truncation parameter N_{max}. Furthermore, we have seen that while the HO basis expansion provides a variety of convenient properties, the convergence pattern is in general slow. Methods such as SRG and importance truncation (see Sec. 2.2.4) have been utilized to dramatically improve the situation, however the convergence rate of larger systems, halo nuclei and observables dependent on long–range characteristics of the many–body wave function (i.e. radius) still constitute a problem in the HO expansion. As discussed in Sec. 3, the unphysical long–range behaviour of the HO expansion $\propto e^{-br^2}$ is significantly different from the natural asymptotics of the nuclear wave function $\propto e^{-br}$. Hence, we cannot expect to achieve a rapid convergence pattern in observables sensitive to the long–range structure of nuclei.

Moreover, these computational limitations are not new problems and, in fact, there exists many techniques for improving many–body convergence behaviour with respect to N_{max}. The natural orbitals basis was initially proposed in atomic physics to assist with the many–electron problem, and was shown to provide a greater convergence rate of observables with inclusion of only a small number of Slater determinants [149, 150, 151, 152, 153, 154]. Given the similarity of SD basis techniques used in nuclear many–body methods, this pioneering work has since been adopted in the nuclear physics community to enhance our description of a variety of systems and observables, i.e. closed shell nuclei [155, 156], nuclear charge distributions [157] and most recently halo nuclei [158, 159]. In essence, this approach consists of utilizing an alternative single–particle basis, the natural orbitals basis, as opposed to the traditionally used HO single–particle basis.

In this section we present the approach for constructing and utilizing the natural orbitals (NO) basis in a nuclear many–body calculation.

4.1 Proton–neutron formalism

In general, it is possible for the proton and neutron to be described by different orbital structures. Such is the case for the NO basis, however, this is not the case when using the HO basis, which assumes the same radial distribution for both the proton and the neutron. Hence we must introduce the isospin uncoupled proton–neutron (pn) formalism for describing the single–particle orbitals that we will use. We make the following definitions. When referring to a proton orbital, we will denote the single–particle states as $|a_\pi\rangle$,

whereas for describing neutron orbitals we will denote the single–particle states as $|a_\nu\rangle$.

While the formalism is different, it is certainly possible to relate the pn matrix elements to the isospin coupled matrix elements. Assigning the nucleons their isospin labels of $t_z = \frac{1}{2}$ for proton and $t_z = -\frac{1}{2}$ for neutron, and using Wigner–Eckart theorem in Eq. (2.40) to couple the nucleons in isospin space, one can convert back and forth between isospin coupled and uncoupled matrix elements easily.

4.2 Natural orbitals unitary transformation

The core idea of exploiting some natural single–particle basis stems from wanting to emphasize the physical structure of the nucleus. The NO basis minimizes the mean occupancies of single–particle states above the Fermi surface, defined by the Fermi energy E_F. Using the Pauli exclusion principle to construct the lowest Pauli configuration of a A–nucleon system, one defines the Fermi surface as the energy level below which all states have been occupied by the A nucleons. E_F is the separation between occupied and unoccupied states. Through this minimization, there is a reduction in the contributions to many–body structure from high–lying oscillator shells; a greater emphasis is put on low–lying single–particle states. Since the many–body wave function is highly correlated, this use of the NO basis ensures that the low–lying SDs provide a greater contribution than in the HO basis. As a result, the many–body wave function converges more rapidly with respect to the truncation parameter N_{max}.

A traditional natural orbitals transformation utilizes the scalar OBDM to better adapt the single–particle basis of the nucleons to the structure of the many–body wave function. The transformation directly tailors the single–particle orbitals to a given A–nucleon system, and so each distinct nucleus will have a unique set of NO basis states. As we know, the NCSM Hamiltonian is computed from two– and three–nucleon matrix elements determined in the SD HO basis. By first performing the many–body calculation in the SD HO basis, we obtain a reference many–body state from which we may compute the nuclear OBDM. We label this state $|\Psi^{J^\pi T}_{HO}\rangle$. We construct the OBDM elements in a second–quantization approach as described in Sec. 3:

$$\rho_{ab} = \langle \Psi^{J^\pi T}_{HO} || (a^\dagger_b \widetilde{a}_a)^{(0)} || \Psi^{J^\pi T}_{HO} \rangle \ , \tag{4.1}$$

where $a = (n_1 l_1 j_1 t_1)$ and $b = (n_2 l_2 j_2 t_2)$ are arbitrary single–particle labels. We recall that the occupancy of a single–particle orbital a is given by:

$$\mathcal{N}_a = \sqrt{2j_a + 1}\rho^{(0)}_{aa} \ . \tag{4.2}$$

Since the many–body wave function is constructed of $|nljm\rangle_{\mathcal{A}}$ antisymmetrized SD HO states, it is necessary to maintain good l and j quantum numbers. Notably, as we have coupled to $\lambda = 0$ transition momentum, the scalar density matrix will only connect HO orbitals with the same (l, j) quantum numbers and so the transformation will be uniquely defined in each lj–subspace. We then define the block matrices $\rho^{(lj)}_{HO}$. Then, the transformation from a HO single–particle basis state, labelled $|a\rangle$, to a NO single–particle basis state, labelled $|\bar{a}\rangle$, involves purely the overlap coefficients of the radial functions in the respective bases. Explicitly,

$$|\bar{a}_t\rangle = \sum_a \langle a|\bar{a}_t\rangle \, |a\rangle = \sum_n \delta_{\bar{l}l}\delta_{\bar{j}j} \langle n|\bar{n}\rangle \, |n\rangle = |\bar{n}ljt\rangle \tag{4.3}$$

where $t \, \epsilon \{\pi, \nu\}$. Further, $\langle a|\bar{a}_t\rangle$ are the overlap coefficients between the respective radial basis functions, and are given by

$$\langle a|\bar{a}_t\rangle = \int_0^\infty dr \ R_{n_a l_a}(b_{HO}; r) S_{\bar{n}_a \bar{l}_a}(b_{NO}; r) \ . \tag{4.4}$$

These overlaps are computed through matrix calculus by diagonalizing the $\rho^{(lj)}_{HO}$ blocks, the eigenvectors of which provide the overlap coefficients of the transformation. The eigenvalues associated with a single–particle NO state represent the mean occupation of that state in the many–body wave function, and hence, it is natural to order the eigenvectors of the transformation matrix from largest to lowest mean

occupation (decreasing eigenvalues). This ordering yields a "radial" quantum number definition in the single–particle NO basis, where the lowest $\bar{n}$ value corresponds to the largest mean occupation in the many-body wave function.

Normalization of states

Before proceeding, we must understand the normalization of the two–body NO states. Consider a NO state:

$$|\bar{a}_t\rangle = \sum_a \langle a|\bar{a}_t\rangle\,|a\rangle \qquad\qquad t\,\epsilon\{\pi,\nu\}\ , \tag{4.5}$$

where π and ν represent protons and neutrons, respectively. The normalization of two–body states with one proton and one neutron is trivially unity, so the following discussion applies to proton–proton and neutron–neutron matrix elements specifically. Combining the one–particle states in the natural way to form a two–body NO state, we may write the state as:

$$\begin{aligned} |\bar{a}_t\bar{b}_t J\rangle_{\mathcal{A}} &= \sum_{ab}\langle a|\bar{a}_t\rangle\langle b|\bar{b}_t\rangle\,|abJ\rangle_{\mathcal{A}} \\ &= \sum_{ab}\langle a|\bar{a}_t\rangle\langle b|\bar{b}_t\rangle\sqrt{1+\delta_{ab}}\sum_T\left(\frac{1}{2}\frac{1}{2}\frac{1}{2}-\frac{1}{2}|T0\right)|abJT\rangle_{\mathcal{A}}\ . \end{aligned} \tag{4.6}$$

The subscript $\mathcal{A}$ refers to an antisymmetric state. In the second line, we have elected to write the HO basis state in an isospin coupled form, as is usually done in the NCSM. Calculating the overlap between un–normalized two–body NO states, we have

$$\begin{aligned} {}_{\mathcal{A}}\langle\bar{a}'_t\bar{b}'_t J|\bar{a}_t\bar{b}_t J\rangle_{\mathcal{A}} &= \sum_{aba'b'}\langle a|\bar{a}_t\rangle\langle b|\bar{b}_t\rangle\langle\bar{a}'_t|a'\rangle\langle\bar{b}'_t|b'\rangle\,\sqrt{1+\delta_{ab}}\sqrt{1+\delta_{a'b'}} \\ &\quad\times\sum_{TT'}\left(\frac{1}{2}\frac{1}{2}\frac{1}{2}-\frac{1}{2}|T0\right)\left(\frac{1}{2}\frac{1}{2}\frac{1}{2}-\frac{1}{2}|T'0\right){}_{\mathcal{A}}\langle a'b'JT'|abJT\rangle_{\mathcal{A}} \\ &= \langle\bar{a}'_t|\bar{a}_t\rangle\langle\bar{b}'_t|\bar{b}_t\rangle+(-1)^{J+T}\langle\bar{a}_t|\bar{b}'_t\rangle\langle\bar{a}'_t|\bar{b}_t\rangle \\ &= 1+\delta_{\bar{a}\bar{b}}\ . \end{aligned} \tag{4.7}$$

Hence, we have that

$$|\bar{a}_t\bar{b}_t J\rangle_{\mathcal{NA}} = \frac{1}{\sqrt{1+\delta_{\bar{a}\bar{b}}}}|\bar{a}_t\bar{b}_t J\rangle_{\mathcal{A}}\ , \tag{4.8}$$

where the new subscript $\mathcal{N}$ refers to a normalized state. In the proceeding sections, we will omit the labels $\mathcal{N}$ and $\mathcal{A}$, however, it is important to keep this subtlety in mind as devious factors of $\frac{1}{\sqrt{2}}$ arise.

Hamiltonian two–body matrix elements

With our understanding of the transformation matrix and normalization properties complete, all that remains is to apply a similarity transformation on the Hamiltonian matrix in the HO basis. In fact, as we construct the NCSM Hamiltonian from two–body matrix elements, it is sufficient to apply the transformation on the two–body interaction and kinetic matrix elements. Then, the NO matrix elements are obtained as linear combinations of the HO matrix elements. Assuming the input matrix elements are normalized and antisymmetrized as discussed, along with the definition that $a=(n_a,l_a,j_a,t_{z_a})$ represents a HO single–particle orbital and $\bar{a}=(\bar{n}_a,\bar{l}_a,\bar{j}_a,\bar{t}_{z_a})$ represents a NO single–particle orbital, we write the *pn* matrix element of a one–body operator in the NO basis as

$$\langle\bar{a}_\pi\bar{b}_\nu J|\,\hat{O}\,|\bar{c}_\pi\bar{d}_\nu J\rangle = \sum_{abcd}\langle\bar{a}_\pi|a\rangle\langle\bar{b}_\nu|b\rangle\langle c|\bar{c}_\pi\rangle\langle d|\bar{d}_\nu\rangle\,\langle abJ|\,\hat{O}\,|cdJ\rangle\ , \tag{4.9}$$

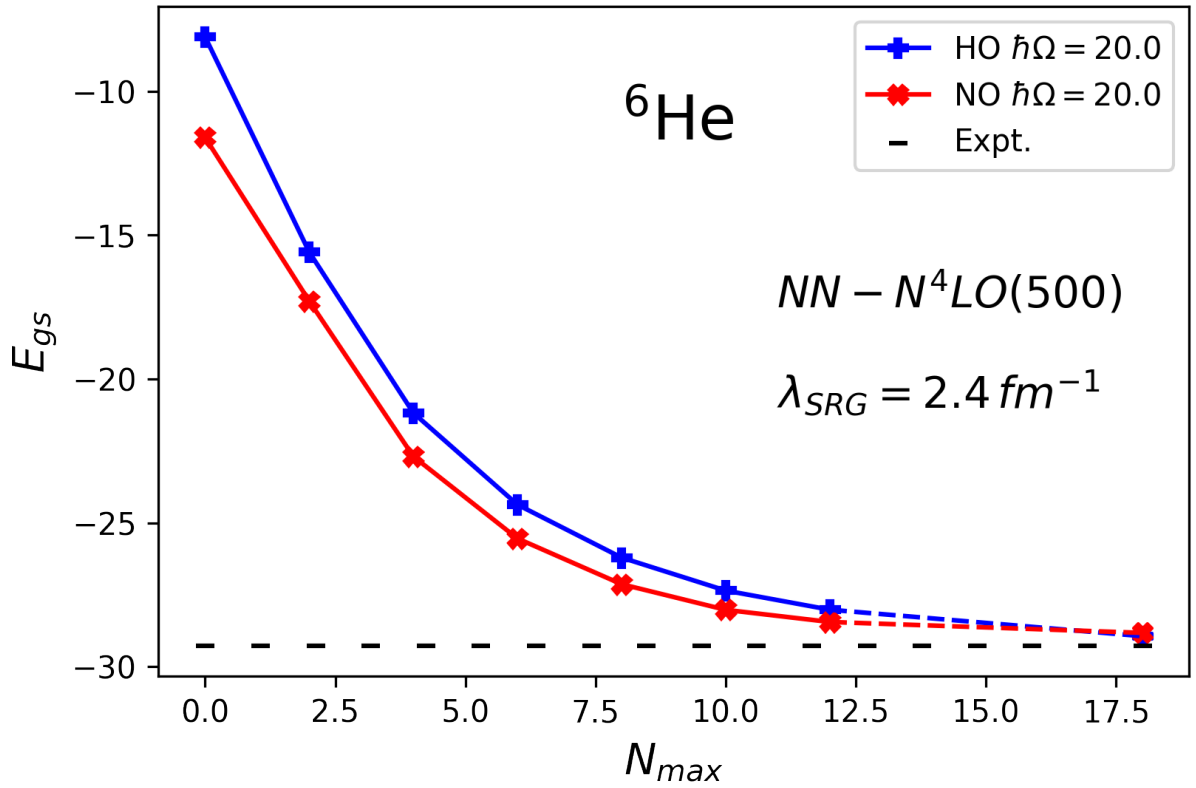

Figure 4.1: Comparison of eigenenergies for the ground state of ^{6}He calculated using different single–particle bases. Convergence curves are shown, with N_{max} ranging from 0 to 12. Natural orbital curves are shown in red and harmonic oscillator curves are shown in blue. The expected ground state energies are: $E_{\infty,HO} \approx -28.94$ MeV and $E_{\infty,NO} \approx -28.82$ MeV. The NO transformation is applied as described in Sec. 4.2. The experimental energy of ^{6}He is -29.27 MeV, as reported in the 2020 Atomic Mass Evaluation [19, 20].

where a proton π occupies the first index and a neutron ν occupies the second index. Further, for identical particles, the sum is not the same due to the normalization conditions on the states. We write the pp or nn matrix elements of a one–body operator in the NO basis as:

$$\langle \bar{a}_t \bar{b}_t J | \hat{O} | \bar{c}_t \bar{d}_t J \rangle = \frac{1}{\sqrt{1+\delta_{\bar{a}\bar{b}}}} \frac{1}{\sqrt{1+\delta_{\bar{c}\bar{d}}}} \sum_{abcd} \sqrt{1+\delta_{ab}} \sqrt{1+\delta_{cd}} \langle \bar{a}_t | a \rangle \langle \bar{b}_t | b \rangle \langle c | \bar{c}_t \rangle \langle d | \bar{d}_t \rangle \langle abJ | \hat{O} | cdJ \rangle \ , \tag{4.10}$$

where $t \epsilon \{\pi, \nu\}$. Recall that the NO transformation only connects orbitals in the same lj-subspace, hence this sum over all two–body states may be reduced to a simpler sum over solely the radial quantum numbers of the HO single–particle states.

4.3 Results

In this section, we discuss the effects of applying the natural orbitals transformation to the nuclear Hamiltonian. In particular, we analyze the difference in many–body behaviour resulting from the different single–particle bases. Simple extrapolations are also presented, assuming an *ad hoc* form for the energy

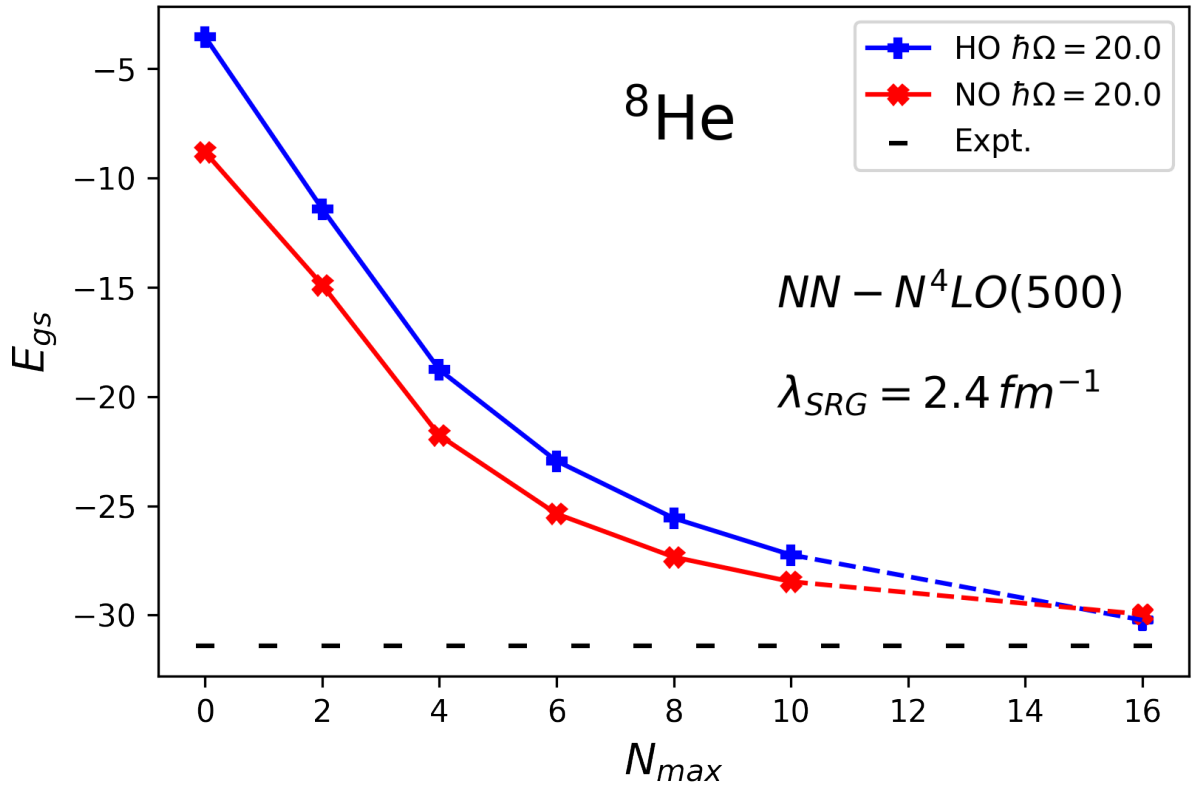

Figure 4.2: Comparison of eigenenergies for the ground state of ^{8}He calculated using different single–particle bases. Convergence curves are shown, with N_{max} ranging from 0 to 10. Natural orbital curves are shown in red and harmonic oscillator curves are shown in blue. The expected ground state energies are: $E_{\infty,HO} \approx -30.23$ MeV and $E_{\infty,NO} \approx -28.96$ MeV. The NO transformation is applied as described in Sec. 4.2. The experimental energy of ^{8}He is -31.40 MeV, as reported in the 2020 Atomic Mass Evaluation [19, 20].

convergence curve:

$$E(N_{max}) = E_\infty + Ae^{-bN_{max}} \ , \tag{4.11}$$

where we use the final three points in an N_{max} sequence to determine the parameter E_∞. This corresponds to the estimation of a complete basis calculation of the ground state energy. In general, this is not an exact treatment of the extrapolation problem and hence this *ad hoc* approach must be used with care. In less convergent systems, the extrapolation tends to be highly sensitive to these three N_{max} points and hence the quality of the result cannot be guaranteed.

As we have presented the transformation properties for only two–nucleon matrix elements, the results in this section are presented with nuclear interactions taken only to the two–body level. In particular, we choose to use two different interactions. For the halo nuclei ^{6,8}He, we use the familiar NN–N^{4}LO(500) interaction discussed in the prior sections. For the larger nuclei ^{12}C and ^{16}O, we instead utilize the NN–N^{2}LO$_{\text{opt.}}$ interaction, a lengthy discussion of which is provided in Ref. [160]. In this work, we simply treat them as two separate physical potentials.

Referring to Fig. 4.1, it is easy to see the significance of choosing the right single–particle basis for the many–body calculation. For one, at a given parameter value for N_{max}, the NO eigenenergy is always below that of the HO calculation. As these are variational calculations, the difference in curves tells us that for a fixed N_{max} using the NO basis guarantees the inclusion of more physical information in the

many–body wave function than for the HO basis. The convergence pattern is softened and as a result a more reasonable estimate can be expected for ground state energy of the system. The estimation for the ground state energy from the HO basis is $E_\infty \approx -28.94$ MeV, whereas for the NO basis the estimation is $E_\infty \approx -28.82$ MeV, which represents a shift of over 100 KeV in the expected ground state energy. Comparing the $N_{max} = 10$ and $N_{max} = 12$ calculations for both the HO and NO basis, we see that the NO basis provides greater convergence by approximately one additional step in N_{max}; an $N_{max} + 2$ calculation in the HO basis is approximately equivalent to an N_{max} calculation in the NO basis. Given the rapid nature of basis growth with respect to N_{max}, this reduction in model space size provides a significant advantage to the NO basis calculation. By similarly studying another halo nucleus ^{8}He, we see further evidence of the structural advantage that the NO basis provides. As before, the NO curve is completely below the HO curve. In fact, for ^{8}He, the softening of the energy curve is greater than the observed effect in ^{6}He. This is emphasized by the estimation for the ground state energy of ^{8}He: $E_\infty \approx -30.23$ MeV for the HO basis and $E_\infty \approx -28.96$ MeV. In this case, a difference between the ground state energy estimates of around 250 KeV is observed. As noticed in ^{6}He, it seems that the NO basis calculation is able to achieve an additional step in N_{max} convergence compared to the HO basis.

These halo nuclei confirm precisely the reasons for adopting the NO single–particle basis in many–body calculations of nuclear structure. As a result of the emphasis on the physical structure of the nucleus, the behaviour of the energy convergence curves with respect to the parameter N_{max} are improved, and we are able to gain approximately one additional step in the N_{max} model space. In a truncation scheme where increasing the N_{max} parameter exponentially increases the model space size, a technique such as this is valuable for reducing computational cost and extending the reach of *ab initio* approaches to larger nuclei.

In Fig. 4.3 and Fig. 4.4, we explore the effects of using the NO basis in larger nuclear systems. These figures further confirm the qualitative improvement in N_{max} convergence previously estimated. By examining the $N_{max} = 8$ HO basis curve and the $N_{max} = 6$ NO basis curve, we see that the eigenenergies varied over the whole range of frequencies are almost constantly overlapping. The variational minimum of the HO basis calculation for ^{12}C is -74.5013 MeV, while for the NO basis calculation it is -78.2266 MeV. The variational minimum of the HO basis calculation for ^{16}O is -109.2634 MeV, while for the NO basis calculation it is -115.9292 MeV. These differences in eigenenergies (even at the variational minimum where the curve should have the least inflection) constitute significant corrections to the ground state energy of the nuclei.

In general, the transformation to an alternative natural single–particle basis greatly improves the description of the many–body wave function. This was shown to be true in the case of the halo nuclei ^{6,8}He, which typically exhibit poor convergence patterns in the HO basis expansion. While their exotic structure certainly requires a more refined treatment, even in well–bound nuclei like ^{12}C and ^{16}O we see tremendous improvement in the convergence patterns when utilizing the NO single–particle basis. Given the great value of this similarity transformation, further studies on other observables and extensions to the natural orbitals method are suggested.

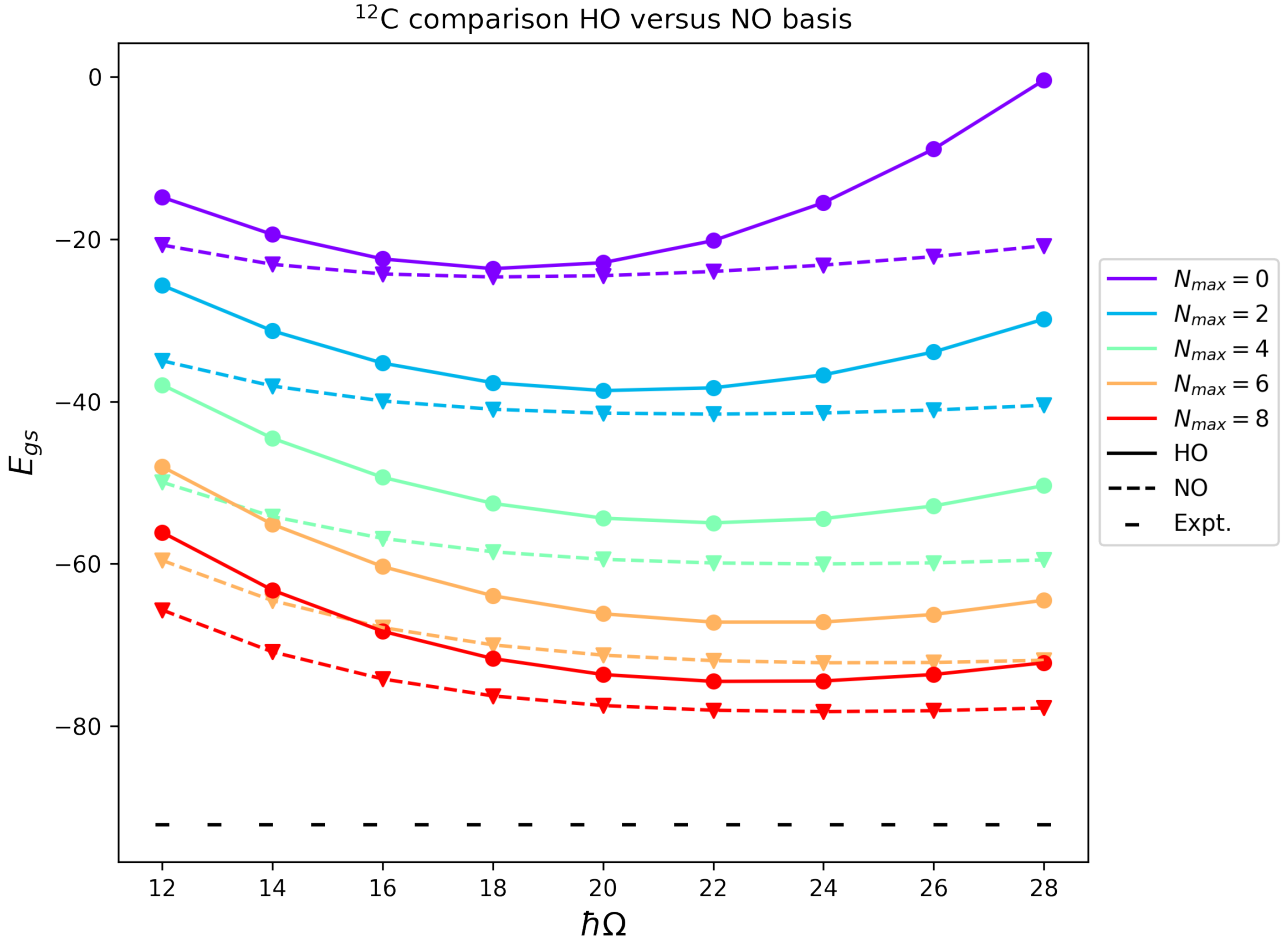

Figure 4.3: Comparison of eigenenergies for the ground state of ^{12}C calculated using different single–particle bases. For a fixed N_{max}, oscillator frequency curves are shown, with $\hbar\Omega$ varying from $12\,\hbar\Omega$ to $28\,\hbar\Omega$. N_{max} ranges from 0 to 8, and $N_{max} = 8$ results are obtained in an importance truncated model space. Natural orbital curves are shown in dashed lines and harmonic oscillator curves are shown in solid lines. The NO transformation is applied as described in Sec. 4.2. The experimental energy of ^{12}C is −92.16 MeV, as reported in the 2020 Atomic Mass Evaluation [19, 20].

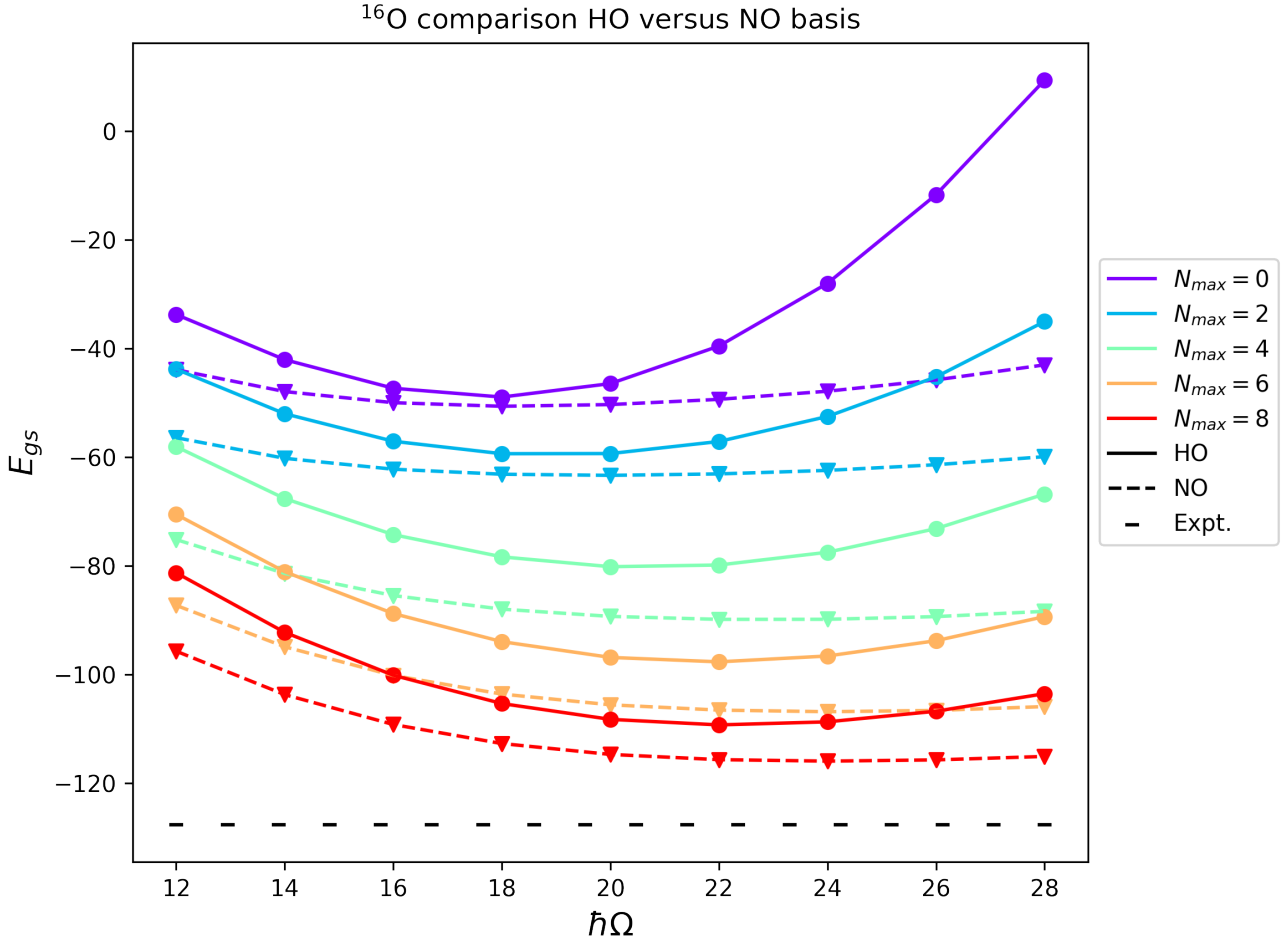

Figure 4.4: Comparison of eigenenergies for the ground state of ^{16}O calculated using different single–particle bases. For a fixed N_{max}, oscillator frequency curves are shown, with $\hbar\Omega$ varying from $12\,\hbar\Omega$ to $28\,\hbar\Omega$. N_{max} ranges from 0 to 8, and $N_{max} = 8$ results are obtained in an importance truncated model space. Natural orbital curves are shown in dashed lines and harmonic oscillator curves are shown in solid lines. The NO transformation is applied as described in Sec. 4.2. The experimental energy of ^{16}O is −127.62 MeV, as reported in the 2020 Atomic Mass Evaluation [19, 20].

Chapter 5

Beta Decay in the No–Core Shell Model with Continuum

The NCSM has contributed greatly to advancements in our understanding of nuclear structure theory over the past decades. This was furthered by the adoption of realistic two– and three–nucleon interactions derived from QCD (described in Sec. 2.1), which provide a direct connection between the quantum many–body nuclear problem and the underlying SM theory. However, fundamentally a result of the HO many–body expansions utilized, the *ab initio* NCSM is a bound state approach to describing nuclei. Moreover, while it is a rigorous many–body approach, the NCSM is incapable of describing scattering processes and nuclear reactions in a consistent framework. Hence, utilizing the NCSM as a starting point, a proper *ab initio* theory for describing scattering and reaction mechanisms requires extensions which (i) improve the wave function asymptotics of NCSM states and (ii) include the coupling of the NCSM to the continuum. The development of a unified approach for describing nuclear structure and reaction theory is a necessary step in pushing the theoretical boundaries of nuclear physics. The approach detailed in Refs. [161, 162, 26], known as the no–core shell model with continuum (NCSMC), will be described in this section.

In general, the applications of a first–principles theory are wide–ranging and so there are many reasons to produce a predictive *ab initio* theory. Unification of reaction theory with the powerful structure predictions of the NCSM open the doors to a variety of relevant calculations not feasible in the NCSM. For example, several important astrophysical reactions required as input in nuclear astrophysics are suddenly within reach [163, 164, 27]. Another such reason is the extraction of fundamental SM physics from calculations in nuclear structure and reaction theory. The Cabibbo–Kobayashi–Maskawa (CKM) matrix unitarity has been established as one of the most sensitive probes of physics Beyond the Standard Model (BSM). The largest matrix element contributing to the unitarity sum may be extracted from nuclear beta decay processes known as super–allowed Fermi transitions, allowing for a direct avenue for nuclear theory to benefit the search for BSM physics [25, 165]. Meaningful calculations of these quantities require various corrections [166, 167] that must be evaluated to high–precision, e.g. the isospin symmetry breaking correction, which may be computed from first–principles using the NCSMC.

5.1 Cabbibo–Kobayashi–Maskawa unitarity

Beta decay has been a truly remarkable probe of the SM, revealing complex information about the underlying fundamental interactions. Beta decay processes stem from the weak charged current (CC) interactions, which couple up–type quarks to a linear superposition of the down–type quarks, all with the weak coupling strength g_W. These flavour changing processes are described by the CC Lagrangian, where

the coefficients of the superposition are the matrix elements of the 3×3 unitary CKM matrix:

$$\mathcal{L}_{CC} = -\frac{g_W}{\sqrt{2}} \begin{pmatrix} \bar{u}_L & \bar{c}_L & \bar{t}_L \end{pmatrix} \gamma^\mu W_\mu^\pm V_{CKM} \begin{pmatrix} d_L \\ s_L \\ b_L \end{pmatrix} \ . \tag{5.1}$$

V_{CKM} describes the degree to which different species of quarks mix, and is approximately diagonal. As was mentioned prior, and as is discussed in Ref. [25], CKM matrix unitarity has been established as one of the most sensitive tests of Beyond Standard Model (BSM) physics. Theoretically there are several unitarity tests which can be performed, though the most common involves purely the CKM elements of the up quark u with the down–type quarks (top row of the CKM matrix), as:

$$|V_{ud}|^2 + |V_{us}|^2 + |V_{ub}|^2 = 1 \ . \tag{5.2}$$

The largest contributor to the unitarity sum is the V_{ud} matrix element, the most precise determination of which comes from nuclear Fermi transitions [37, 165, 168]. These Fermi transitions are a particular type of beta decay occuring between nuclear states of $(J^\pi; T) = (0^+; 1) \rightarrow (0^+; 1)$. The V_{ud} element can be cleanly related to nuclear physics through Fermi transitions as:

$$|V_{ud}|^2 = \frac{\hbar^2 \pi^3 \ln(2)}{G_F^2 m_e^5 c^4} \frac{1}{\mathcal{F}t(1 + \Delta_R^V)} \ , \tag{5.3}$$

where the $\mathcal{F}t$ values encapsulate all of the nuclear structure theory. Fermi transitions have been measured in nuclei as light as ^{10}C and as heavy as ^{74}Rb, constituting a wide–range of available data for comparison to theory. The modern average can be found in Ref. [37] and is given as $V_{ud} = 0.97370 \pm 0.00014$.

While this unitarity condition was initially thought to have been satisfied, recent recalculation of theoretical corrections in 2018 has indicated a discrepancy with unitarity [166] on the order of $2 - 3\sigma$. This deviation from unity is significant and justifies more thorough investigation. The unitarity sum for the top row of the CKM matrix is shown as presented in Ref. [37] below.

$$|V_{ud}|^2 + |V_{us}|^2 + |V_{ub}|^2 = 0.9985 \pm 0.0005 \tag{5.4}$$

This shift in the unitarity landscape constitutes a remarkable tension with the SM. With experimental precision of Fermi transition measurements increasing, theoretical advances in calculations of corrections to Fermi transition data play a significant role in identifying the existence and understanding the origin of this discrepancy.

5.1.1 Corrections to Fermi transitions

In general, several nuclear structure dependent and independent corrections must be taken into account in order to correctly utilize experimental data from nuclear Fermi transitions. In total there are three radiative corrections and one symmetry breaking correction, however they are better divided into nuclear structure dependent and independent contributions. The transition independent Fermi transitions may be written as:

$$\mathcal{F}t = ft(1 + \delta_R')(1 - \delta_C + \delta_{NS}) = \frac{K}{G_V^2 |M_{F0}|^2 (1 + \Delta_R^V)} \ , \tag{5.5}$$

where K contains all the constants in the previous expression for ft and $|M_{F0}|^2$ is the Fermi transition matrix element in case of exact isospin symmetry. We first mention the two nuclear structure independent corrections.

The first to discuss is the transition independent universal electro–weak radiative correction Δ_R^V, which emerges due to radiative decay processes [165]. These processes add spurious rates to the bare beta decay processes observed in nuclei and the uncertainty in this correction dominates the uncertainty in V_{ud}.

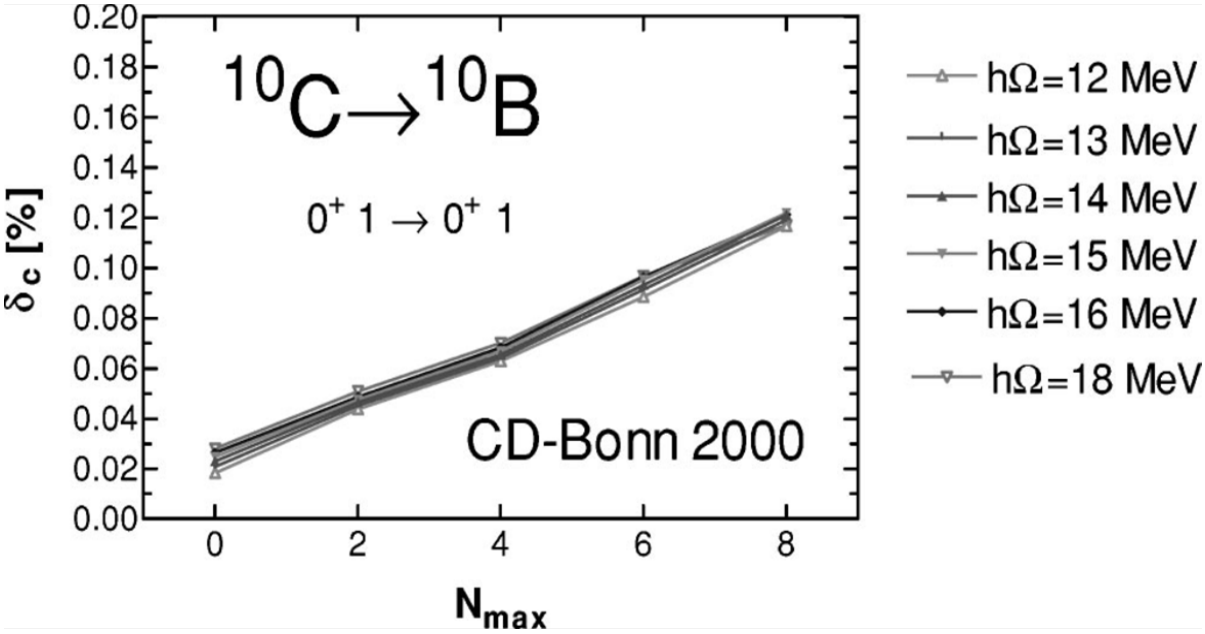

Figure 5.1: Variational calculations of the isospin symmetry breaking correction δ_C in the NCSM for oscillator frequencies of $\hbar\Omega\,\epsilon\{12,\ldots,18\}$. The Fermi transition of ^{10}C $\rightarrow$ ^{10}B is studied to determine δ_C, using the phenomenological CD–Bonn 2000 interaction. This result was originally shown as **Fig. 12** in Ref. [21].

Calculation of Δ_R^V is generally performed using free–quark Lagrangians and requires evaluating the ZW–box and the high–energy part of the γW–box diagrams. In particular, it is reevaluation of the hadronic γW–box contributions to Δ_R^V which have provided a significant reduction in uncertainties [166], and as a result have created tension with the prediction of CKM unitarity. The long–range radiative counterpart of Δ_R^V is the transition dependent correction δ_R', which requires an evaluation of the low–energy portion of the γW–box, in addition to considering radiative decay processes such as bremmsstrahlung photons [169, 170, 171, 172, 173]. This correction requires a more precise understanding of hadronic structure and is dependent on the energy of the emitted electron and the charge Z of the daughter nucleus. It has been explicitly computed to order $Z\alpha^2$, where α is the fine–structure constant.

The two remaining corrections are those which seek to benefit from an *ab initio* theory of nuclei. The first we mention is δ_{NS}, which is similarly related to the low–energy contribution from the γW–box diagram, albeit for the axial–vector weak interaction. This correction is already partially accounted for in Δ_V^R, assuming the interaction occurs withing a single nucleon. However, assuming distinct nucleons interact through this graph implies the need for a nuclear structure calculation of a two–body operator, as discussed in Ref. [174]. The last correction is the isospin symmetry breaking correction, which we now turn our attention towards.

Isospin symmetry breaking correction

In the case of an exact isospin symmetric transition of $(J^\pi;T) = (0^+;1) \rightarrow (0^+;1)$, the Fermi matrix element $|M_F|$ is given by the usual ladder–type operator matrix element:

$$|M_{F0}|^2 = T(T+1) - T_z^{(i)}T_z^{(j)} = 2\ , \tag{5.6}$$

where M_{F0} refers to the exact isospin symmetry and the T operators act on the many–body space. However, we are aware of the presence of isospin non–conserving interactions, i.e. both the Coulomb

interaction and the strong interaction. In particular, the Coulomb interaction dominates the symmetry breaking effects as the strong force only weakly breaks isospin. Due to the presence of these interactions, a renormalization of the Fermi matrix element is necessitated. This renormalization is introduced through the isospin symmetry breaking correction δ_C, and is applied as:

$$|M_F|^2 = |M_{F0}|^2(1 - \delta_C) \ , \tag{5.7}$$

where $|M_{F0}|^2$ is from Eq. (5.6) and $\delta_C = 1 - \frac{|M_{F0}|^2}{2}$. Evaluation of δ_C requires a full nuclear structure calculation of the Fermi matrix element. As such, it has been performed in the NCSM in Ref. [21], the main result of which is shown in Fig. 5.1. Here δ_C has been computed using NCSM wave functions for ^{10}C and ^{10}B, both converged systems in the NCSM. However, successive N_{max} calculations shown no general convergence for δ_C with respect to the truncation parameter, which is consistent across many variational calculations. This informs us that we require a larger basis space in order to achieve convergence with the NCSM. In particular, what we require are additional long–range correlations in the bound states of nuclei; in the ground state 0^+ of ^{10}C and in the excited 0^+ state of ^{10}B.

This is precisely where the NCSMC approach can eclipse the NCSM. By directly incorporating information from the continuum into our wave functions with a generalized ansatz, it is possible to greatly improve the description of general nuclear structure and excited nuclear states. This extension of the basis negates the immediate need to increase the N_{max} basis space, and instead increases the basis space through use of continuum basis mass partitions. The improvements to correlations from inclusion of the continuum will likely improve the convergence rate of δ_C, and hence realistic *ab initio* calculations of the isospin symmetry breaking correction are within reach. Calculation of δ_C within the NCSMC is presently underway with collaborator Dr. Mack Atkinson of TRIUMF. Here, we present the NCSMC formalism and novel nuclear structure results which provide an encouraging picture for calculation of isospin symmetry breaking correction.

5.2 NCSM with resonating group method

The resonating group method (RGM) is a nuclear cluster technique based on an A–nucleon Hamiltonian [175]. In the simplest case of a binary cluster, described in this section, the Hamiltonian is composed of the $(A-a)$–nucleon target and the a–nucleon projectile. The wave function of the Hamiltonian is fully antisymmetric.

Let us begin assuming a two–cluster description. The RGM method utilizies a description of the system in terms of the translation invariant cluster basis states, as:

$$|\Phi^{J^\pi T}_{\nu r}\rangle = \left[\Big(|\Phi^{I^{\pi_1}_1 T_1}_{A-a}\rangle \, |\Phi^{I^{\pi_2}_2 T_2}_{a}\rangle \Big)^{(sT)}_{\mathcal{A}} Y_l(\hat{r}_{A-a,a}) \right]^{(J^\pi T)} \frac{\delta(r - r_{A-a,a})}{r r_{A-a,a}} \ , \tag{5.8}$$

in which the individual nucleon clusters $|\Phi^{I^{\pi_1}_1}_{A-a} T_1\rangle$ and $|\Phi^{I^{\pi_2}_2}_{a} T_2\rangle$ are independently described within the *ab initio* NCSM by H_{A-a} and H_a Hamiltonians, respectively. Then, the internal cluster dynamics are completely microscopic. This innovation is referred to as the NCSM/RGM approach [62, 176, 177, 178]. In this equation, the state is defined by the set of quantum numbers

$$\nu = \{A-a, \alpha_1, I_1, \pi_1, T_1; a, \alpha_2, I_2, \pi_2, T_2; s, l\} \ , \tag{5.9}$$

with total momentum J, parity $\pi = \pi_1\pi_2(-1)^l$ and total isospin T. Further, s characterizes the channel spin and l the relative angular momentum. Lastly, the coordinate $\vec{r}_{A-a,a}$ describes the relative motion between the two clusters. Notably, in this form the individual NCSM states are antisymmetric with respect to internal nucleon exchange, however the cluster basis states are not completely antisymmetric

with respect to the exchange of nucleons in separate clusters. Hence, Pauli exclusion dictates the need for an inter–cluster antisymmetrizer:

$$\mathcal{A}_\nu = \sqrt{\frac{(A-a)!\,a!}{A!}}\left(1 + \sum_{P\neq id}(-1)^p P\right) , \tag{5.10}$$

which is a sum over all possible permutations P of the A nucleons different from the identity permutation; p is the number of interchanges required to permute the two nucleons. The fully antisymmetrized channel states of the NCSM/RGM approach are then obtained in a continuous basis expansion of the many–body wave function, yielding:

$$|\Psi_A^{J^\pi T}\rangle = \sum_\nu \int dr\, r^2\, \mathcal{A}_\nu\, |\Phi_{\nu r}^{J^\pi T}\rangle\, \frac{[\mathcal{N}^{-\frac{1}{2}}\chi]_\nu^{J^\pi T}(r)}{r} . \tag{5.11}$$

This expansion of the many–body wave function is over a set of continuous linear variational amplitudes, dentoed $\chi_\nu^{J^\pi T}(r)$ and obtained from solving the orthogonalized RGM equations:

$$\sum_{\nu'} \int dr'\, r'^2 \left[\mathcal{N}^{-\frac{1}{2}}\mathcal{H}\mathcal{N}^{-\frac{1}{2}}\right]_{\nu\nu'}^{J^\pi T}(r,r')\, \frac{\chi_{\nu'}^{J^\pi T}(r')}{r'} = E\, \frac{\chi_\nu^{J^\pi T}}{r} . \tag{5.12}$$

Defining the remaining quantities in the last equations, $\mathcal{N}_{\nu\nu'}^{J^\pi T}(r,r')$ and $\mathcal{H}_{\nu\nu'}^{J^\pi T}(r,r')$ are known as the norm and Hamiltonian integration kernels of the RGM equations, respectively. These kernel quantities are computed from the overlaps of the antisymmetric cluster basis states:

$$\begin{aligned} \mathcal{N}_{\nu\nu'}^{J^\pi T}(r,r') &= \langle \Phi_{\nu r}^{J^\pi T}|\, \mathcal{A}_\nu \mathcal{A}_{\nu'}\, |\Phi_{\nu' r'}^{J^\pi T}\rangle \\ \mathcal{H}_{\nu\nu'}^{J^\pi T}(r,r') &= \langle \Phi_{\nu r}^{J^\pi T}|\, \mathcal{A}_\nu H \mathcal{A}_{\nu'}\, |\Phi_{\nu' r'}^{J^\pi T}\rangle \ , \end{aligned} \tag{5.13}$$

where H corresponds to the full A–nucleon microscopic Hamiltonian, which may be decomposed as:

$$H = T_{rel.} + \bar{V}_C + \mathcal{V}_{rel.} + H_{A-a} + H_A , \tag{5.14}$$

where $\bar{V}_C = e^2 \frac{Z_{1\nu} Z_{2\nu}}{r}$ is the average Coulomb interaction between the clusters. Lastly, $\mathcal{V}_{rel.}$ is the localized relative potential

$$\mathcal{V}_{rel.} = \sum_{i=1}^{A-a}\sum_{j=A-a+1}^{A} V_{ij}^{(NN)} + \sum_{i<j}^{A-a}\sum_{k=A-a+1}^{A} V_{ijk}^{(NNN)} + \sum_{i=1}^{A-a}\sum_{j<k=A-a+1}^{A} V_{ijk}^{(NNN)} - \bar{V}_C . \tag{5.15}$$

The aforementioned integration kernel expressions are modified for evaluation within the model–space, and an expansion over a set of HO wave functions defined by $\hbar\Omega$ and N_{max} is utilized. We then introduce the SD channel states:

$$|\Phi_{\nu r}^{J^\pi T}\rangle = \left[\Big(\, |A-a\,\alpha_1\, I_1^{\pi_1} T_1\rangle_{SD}\, |a\,\alpha_2\, I_2^{\pi_1} T_2\rangle\,\Big)_{\mathcal{A}}^{(sT)} Y_l(\hat{r}_{A-a,a})\right]^{(J^\pi T)} \frac{\delta(r - r_{A-a,a})}{r r_{A-a,a}} , \tag{5.16}$$

for which $|A-a\,\alpha_1\, I_1^{\pi_1} T_1\rangle_{SD}$ is determined the SD HO basis and $|a\,\alpha_2\, I_2^{\pi_1} T_2\rangle$ is obtained in the translation invariant Jacobi basis. The use of the SD antisymmetrization for the target implies that the channel states are not translation invariant, and so calculation of physical operators requires translation invariant matrix elements to be extracted in the same spirit as in Sec. 3.

With the formalism constructed, one must then solve Eq. (5.12). This is done by using the R–matrix method [179] on a Lagrange mesh [180, 181]. The great accomplishment of the NCSM/RGM approach is the consistency with which nuclear structure and reaction theory are treated; the NCSM/RGM captures the physics of both bound and scattering eigenstates, the latter being described through the scattering matrix S.

5.3 No–core shell model with continuum

The NCSM/RGM is a great approach for extending the applicability of the NCSM from a bound state theory to one which can directly treat dynamical nuclear processes. However, it is possible to greatly enhance the NCSM/RGM by extending the cluster basis to include finite and square integrable NCSM basis, determined from the intrinsic Hamiltonian of the A–nucleon system. The inclusion of the NCSM basis provides true unity between the *ab initio* NCSM and the NCSM/RGM approaches, allowing one to treat both structure and reaction theory on equal footing. This generalized basis expansion is an augmentation of the usual ansatz used to solve the many–body Schrödinger equation, and more efficiently describes the physics of a given system. The discrete NCSM basis provides a strong description of the short– to medium–range nuclear structure, including many–nucleon correlations, while the NCSM/RGM cluster states allows for the handling of scattering processes. Hence the complete expansion is written including the usual square integrable NCSM states plus the continuous RGM cluster states introduced in the previous section. This more sophisticated approach is the aforementioned NCSMC [26, 182] and has been recently utilized to analyze unbound systems [161, 183], halo nuclei [184] and important astrophysical reactions [163, 164, 27]. The NCSMC provides a great innovation in the description of nuclear structure.

Let us consider the binary cluster expansion as before. In this case, our generalized expansion may be written as:

$$|\Psi_A^{J^\pi T}\rangle = \sum_\alpha c_\alpha \, |A\alpha J^\pi T\rangle + \sum_\nu \int dr \, r^2 \frac{\gamma_\nu^{J^\pi T}(r)}{r} \, \mathcal{A}_\nu \, |\Phi_{\nu r}^{J^\pi T}\rangle \ . \tag{5.17}$$

In this expansion, the A–nucleon NCSM eigenstate is given by $|A\alpha J^\pi T\rangle$ and the NCSM/RGM cluster basis state is given by $\mathcal{A}_\nu \, |\Phi_{\nu r}^{J^\pi T}\rangle$, where $|\Phi_{\nu r}^{J^\pi T}\rangle$ is given in Eq. (5.16). In this formalism, all states utilized are eigenstates of their respective intrinsic Hamiltonians computed in the *ab initio* NCSM. Note that the NCSM eigenstates have yet to be projected onto the N_{max} model space in this equation. The unknown variables of this generalized expansion are the discrete coefficients c_α and the continuous variational linear amplitudes $\gamma_\nu^{J^\pi T}(r)$. This ansatz should be compared to that of the NCSM in Eq. (2.60) and the NCSM/RGM in Eq. (5.11).

By projecting onto the NCSM eigenstates and binary cluster channel states, one obtains the NCSMC Hamiltonian equation formulated as a coupled equation:

$$\begin{pmatrix} \mathbb{E} & \bar{h} \\ \bar{h} & \bar{\mathcal{H}} \end{pmatrix} \begin{pmatrix} c \\ \chi \end{pmatrix} = E \begin{pmatrix} \mathbb{1} & \bar{g} \\ \bar{g} & \mathbb{I} \end{pmatrix} \begin{pmatrix} c \\ \chi \end{pmatrix} \ . \tag{5.18}$$

The first items to identify in this equation are the vector elements: c and χ. Here c corresponds to the vector of expansion coefficients in the discrete sector of the NCSMC basis, and so they describe the A–body NCSM basis expansion. On the other hand, we have that $\chi^{J^\pi T}(r)$ is the relative motion wave function previously defined in the NCSM/RGM approach and obtained from solving the orthogonalized RGM equations.

Now, let us understand the various elements of the block matrices shown in the above equation. On the left–hand side, the first item to mention is $\mathbb{E} = \mathrm{diag}(E_1, \ldots, E_n)$, which is the eigenenergy matrix of the square integrable basis elements and is the output of NCSM diagonalization of the A–body system. This corresponds to the identity matrix on the right–hand side of the equation, since this block is already diagonal. On the left–hand side in the bottom right corner, we also see $\bar{\mathcal{H}}$, which is the orthogonalized version of the Hamiltonian kernels introduced in Eq. (5.13). This is the NCSM/RGM component of the NCSMC Hamiltonian. Greater details on the importance and implementation of orthogonalized NCSMC equations may be found in Ref. [26]. This component then corresponds to $\mathbb{I}_{\nu\nu'} = \frac{\delta_{\nu\nu'}\delta(r-r')}{rr'}$ on the right–hand side of the equation.

The off–diagonal elements on each side of the equation contain all information about the coupling of the discrete and continuous bases used in the many–body expansion. First we have the coupling form

factor $\bar{h}$ on the left–hand side, which is given by:

$$\bar{h}_{\lambda\nu}(r) = \sum_{\nu'} \int dr'\, r'^2\, \mathcal{N}^{-\frac{1}{2}}_{\nu'\nu}(r', r)\, \langle A\lambda J^\pi T|\, H A_{\nu'}\, |\Phi^{J^\pi T}_{\nu' r'}\rangle \ . \tag{5.19}$$

The coupling is then represented on the right–hand side by the cluster form factor $\bar{g}$ which is given by:

$$\bar{g}_{\lambda\nu}(r) = \sum_{\nu'} \int dr'\, r'^2\, \mathcal{N}^{-\frac{1}{2}}_{\nu'\nu}(r', r)\, \langle A\lambda J^\pi T|\, A_{\nu'}\, |\Phi^{J^\pi T}_{\nu' r'}\rangle \ . \tag{5.20}$$

These form factors are computed analogously as in the NCSM/RGM, utilizing a second–quantization approach to evaluate the matrix elements.

This Hamiltonian equation is then solved for the unknown c_α and $\gamma^{J^\pi T}_\nu(r)$, which yields the NCSMC eigenstates for the desired A–body system.

5.3.1 NCSMC structure results

The ultimate goal of this work with the NCSMC is calculation of the isospin symmetry breaking correction δ_C for the ^{10}C $\rightarrow^{10}$ B super–allowed Fermi transition. However, in working towards this goal, we produce rich nuclear structure results for complicated physical systems. These results are deserving of their own analysis, which is provided in this section. All results presented in this section were obtained using the NN–N^{4}LO(500)+3N$_{\rm lnl}$ interaction with a wave flow parameter of $\lambda_{SRG} = 1.8\,\mathrm{fm}^{-1}$ and an oscillator frequency of $\hbar\Omega = 18\,\mathrm{MeV}$.

First let us understand why the nuclear structure of the systems under consideration is so interesting. In particular for ^{10}C, there is not much known from experiment regarding its exotic nuclear structure. In fact, there is a large experimental uncertainty in the measurement of its energy levels. The state of ^{10}C measurements provides an excellent opportunity for a predictive *ab initio* approach such as the NCSMC. By analyzing the structure of this system, the NCSMC can assist in guiding experimentalists in performing future precision measurements of ^{10}C structure. Furthermore, exotic systems like this serve as a challenging testing ground for *ab initio* theories given their complicated many–body physics. In the case of ^{10}B, this nucleus is structurally well understood and contains a complicated spectrum of states, hence providing a robust test of the NCSMC wave functions. In addition, ^{10}B contains the isospin analogue states ($T = 1$) to ^{10}C and so it is possible to make valuable structure comparisons between the nuclei. One particular item worth noting is that the photon energy from the ^{10}C $\rightarrow^{10}$ B Fermi transition is (by random luck of the universe) equivalent to the energy of the background electron–positron annihilation process: $e^- + e^+ \rightarrow \gamma + \gamma$. Since beta decay is a high–precision structural probe, the large background from annihilation processes is the source of the experimental challenge with ^{10}C as it greatly complicates measurement of the ground state structure. Lastly, though it is not needed in calculation of the isospin symmetry breaking correction, we also choose to study the nucleus ^{10}Be. The spectra of ^{10}Be is quite well understood, providing another suitable testing ground for the *ab initio* NCSMC. A further point of interest is that ^{10}Be is the isospin mirror of ^{10}C, and so if isospin symmetry was not violated the nuclei would have equivalent spectra; in reality ^{10}Be has a denser spectrum of states which makes it valuable for understanding the spectra of ^{10}C and the role of isospin breaking. There is also an inherent structural interest in ^{10}Be as the $J^\pi = 1^-$ and $J^\pi = 2^-$ states have an S–wave halo structure. These exotic halo states are particularly interesting to analyze in the NCSMC and studying them will further our understanding of longer–range nuclear physics. In summary, the study of these nuclei in the context of the NCSMC is in itself of great interest to the nuclear physics community.

Let us now discuss the nuclear structure results for ^{10}C. The cluster basis states chosen for this study are described by the binary mass partition $p + {}^9$B:

$$|{}^{10}\mathrm{C}\rangle = \sum_\alpha c_\alpha\, |{}^{10}\mathrm{C}, \alpha\rangle_{\rm NCSM} + \sum_\nu \int dr\, \gamma_\nu(r) \mathcal{A}_\nu\, |{}^9\mathrm{B} + p, \nu\rangle \ . \tag{5.21}$$

$J^\pi;T$	E^{3m5m}	E^{3m5m1p}	$E_{exp.}$	E_X^{3m5m}	E_X^{3m5m1p}	$E_{X,exp.}$
$0^+;1$	-3.62	-3.63	-4.006	0.0	0.0	0.0
$2^+;1$	-0.11	-0.11	-0.652	3.54	3.51	3.3536

Table 5.1: Bound state predictions from the NCSMC calculation of ^{10}C as a $p + {}^9$B mass partition, built from (i) the $J = \frac{3}{2}^-, \frac{5}{2}^-$ states, labeled 3m5m (ii) $J = \frac{3}{2}^-, \frac{5}{2}^-, \frac{1}{2}^+$ states, labeled 3m5m1p, of ^{9}B. All predicted and experimental energies are shown in MeV and E_X denotes the excitation energy with respect to the ground state. The bound state energies are determined with respect to the threshold energy of the $p + {}^9$B mass partition (4.006 MeV). These results were computed at $N_{max} = 7$ with the NN–N^{4}LO(500)+3N$_{\text{lnl}}$ interaction, using a wave flow parameter of $\lambda_{SRG} = 1.8\,\text{fm}^{-1}$ and an oscillator frequency of $\hbar\Omega = 18\,\text{MeV}$.

We further choose to study three different state configurations of ^{9}B utilized in constructing the composite nucleus ^{10}C, including the ground state and two excited states. Specifically, these configurations are (i) $J = \frac{3}{2}^-, \frac{5}{2}^-$ (ii) $J = \frac{3}{2}^-, \frac{5}{2}^-, \frac{1}{2}^-$ and (iii) $J = \frac{3}{2}^-, \frac{5}{2}^-, \frac{1}{2}^+$. We first discuss results for the predicted bound state spectra of ^{10}C, shown in Table 5.1, for the $J = \frac{3}{2}^-, \frac{5}{2}^-$ state configuration (columns 2 and 5). As shown in the table, the two known experimental bound states of ^{10}C, namely the 0^+ and 2^+, are present in the predicted NCSMC structure. The NCSMC predicts a ground state energy of -3.6251 MeV, whereas the expected energy gap with respect to $p + {}^9$B is -4.0060 MeV. In general, though slightly underbound, the 0^+ is well reproduced which is an encouraging result in preparation for the calculation of δ_C. The 2^+ is similarly underbound in the calculation. For the $J = \frac{3}{2}^-, \frac{5}{2}^-, \frac{1}{2}^-$ configuration, we do not show any results as they are identical to those for the $J = \frac{3}{2}^-, \frac{5}{2}^-$ configuration. Still referring to Table 5.1, we turn our attention to columns 3 and 6, where we present the NCSMC results for the $J = \frac{3}{2}^-, \frac{5}{2}^-, \frac{1}{2}^+$ configuration for ^{9}B. Here, the results are not significantly shifted with respect to the $J = \frac{3}{2}^-, \frac{5}{2}^-$ calculation. Utilizing the $J = \frac{1}{2}^-$ and $J = \frac{1}{2}^+$ states from ^{9}B do not impact the spectra of ^{10}C, indicating that an additional partition is also needed in order to completely capture the structure of ^{10}C, i.e. $2p + {}^8$Be.

We now present the phase shift results for the $^{10}\text{C} \to p + {}^9\text{B}$ calculation in Fig. 5.2. The phase shifts are shown in solid lines and the eigenphase shifts are shown in dashed lines. They are presented alongside the energy level diagram for ^{10}C, with states in the composite nucleus highlighted according to the colour of the corresponding curves on the phase shift plot. The black $^3\text{P}_0$ curve corresponds to the ground state 0^+ of ^{10}C. The dark blue $^5\text{P}_2$ curve corresponds to the first excited 2^+ state of ^{10}C. A direct identification between the red $^3\text{P}_2$ curve cannot be made with the experimental diagram of ^{10}C, though the resonance state is likely one of the states highlighted in the red box on the energy level diagram of Fig. 5.2. More interestingly, we see the presence of a broad 1^+ state from the yellow $^5\text{P}_1$ curve. The existence of this predicted state is supported by the existence of the analogue 1^+ in ^{10}Be, though there is no corresponding data. Though, due to the broad nature of this state this is not surprising. Referring now to the eigenphase shifts (dashed lines), we identify three important resonances: the maroon 1^- curve, the purple 2^- curve, and the cyan 3^- curve. The first two of these resonances are analogues to the 1^- and 2^- S–wave halo states of ^{10}Be, and they appear quite clearly in the NCSMC description of ^{10}C. We also see the 3^- resonance from ^{10}Be similarly appearing as a resonance in ^{10}C.

Next, we discuss the nuclear structure results for ^{10}Be. The cluster basis states chosen for this study are described by the binary mass partition $n + {}^9$Be:

$$|{}^{10}\text{Be}\rangle = \sum_\alpha c_\alpha \, |{}^{10}\text{Be}, \alpha\rangle_{\text{NCSM}} + \sum_\nu \int dr \, \gamma_\nu(r) \mathcal{A}_\nu \, |{}^9\text{Be} + n, \nu\rangle \ . \tag{5.22}$$

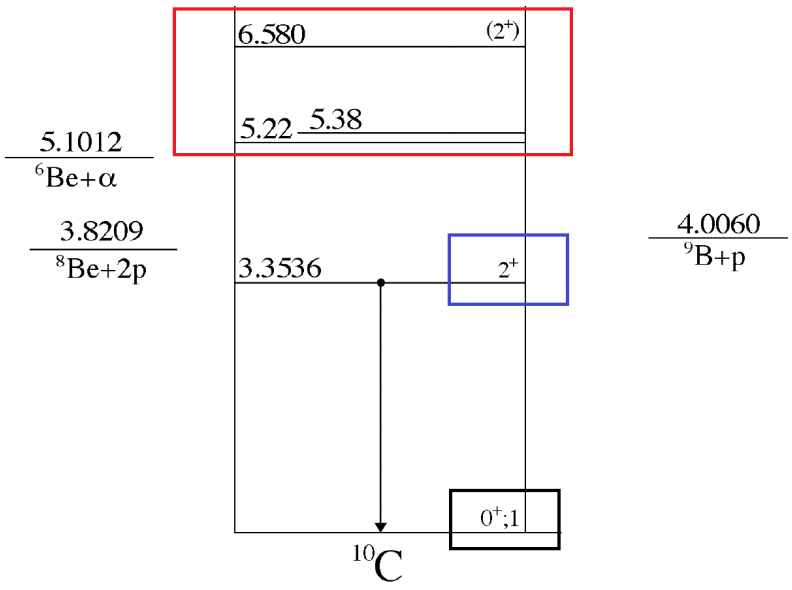

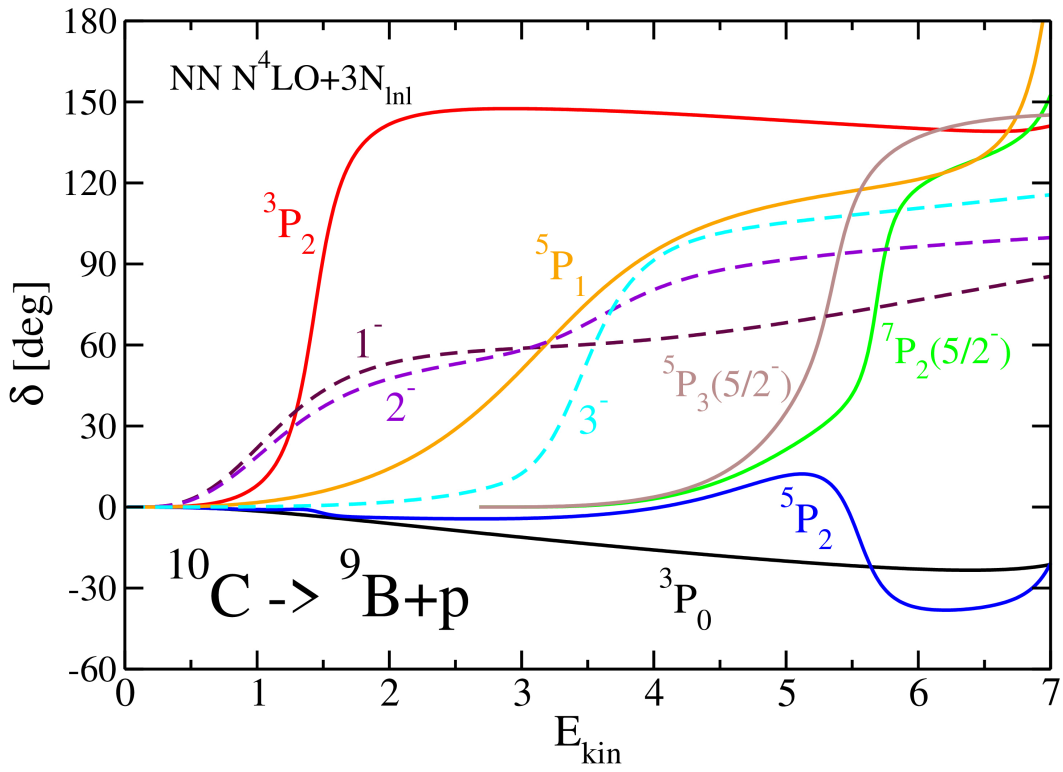

Figure 5.2: The phase shifts for $^{10}\mathrm{C} \to p + {}^{9}\mathrm{B}$ are presented alongside the experimental energy level diagram [22]. The state configuration of ^{9}B is $J = \frac{3}{2}^{-}, \frac{5}{2}^{-}, \frac{1}{2}^{-}$. Other calculation details are the same as in Table 5.1.

As before, we choose to study the same three state configurations of ^{9}Be. We present the NCSMC predictions for the bound states of ^{10}Be, shown in Table 5.2. There are six states which exist below

$J^\pi;T$	E^{3m5m}	E^{3m5m1m}	E^{3m5m1p}	$E_{exp.}$	E_X^{3m5m}	E_X^{3m5m1m}	E_X^{3m5m1p}	$E_{X,exp.}$
$0^+;1$	-6.15	-6.17	-6.15	-6.8122	0.0	0.0	0.0	0.0
$2^+;1$	-2.65	-2.65	-2.65	-3.4442	3.50	3.52	3.51	3.36803
$2^+;1$	-0.59	-0.67	-0.59	-0.8538	5.30	5.50	5.56	5.95839
$1^-;1$	-0.026	-0.029	-0.11	-0.8523	6.12	6.14	6.05	5.9599
$0^+;1$	–	–	–	-0.63	–	–	–	6.1793
$2^-;1$	-0.001	-0.001	-0.04	-0.5489	6.15	6.17	6.11	6.2633

Table 5.2: Bound state predictions from the NCSMC calculation of ^{10}Be as a $n + {}^9$Be mass partition, built from (i) the $J = \frac{3}{2}^-, \frac{5}{2}^-$ states, labeled 3m5m (ii) $J = \frac{3}{2}^-, \frac{5}{2}^-, \frac{1}{2}^-$ states, labeled 3m5m1m (iii) $J = \frac{3}{2}^-, \frac{5}{2}^-, \frac{1}{2}^+$ states, labeled 3m5m1p, of ^{9}Be. All predicted and experimental energies are shown in MeV and E_X denotes the excitation energy with respect to the ground state. The bound state energies are determined with respect to the threshold energy of the $n+{}^9$Be mass partition (6.8122 MeV). These results were computed at $N_{max} = 7$ with the NN–N^{4}LO(500)+3N$_{\rm lnl}$ interaction, using a wave flow parameter of $\lambda_{SRG} = 1.8\,\mathrm{fm}^{-1}$ and an oscillator frequency of $\hbar\Omega = 18\,\mathrm{MeV}$.

the threshold of $n + {}^9$Be, and remarkably, across all configurations five out of the six possible states are captured by the NCSMC. In fact, the ground state 0^+, the first 2^+ and the excited 2^+ states are all quite well described by the NCSMC with the $n + {}^9$Be mass partition. Though, notably the splitting of the 2^+ states is smaller than seen in experiment. In these first three states, there is no significant variation in the energies, albeit it for the slight enhancement of the second 2^+ state due to inclusion of the $J = \frac{1}{2}^-$ of ^{9}Be. The two remaining states, namely the 1^- and 2^- are quite underbound with respect to this mass partition. Yet, utilizing the $J = \frac{1}{2}^+$ state of ^{9}Be provides a greater binding effect for the halo states, indicating the importance of its inclusion. Unfortunately, as indicated in the table by a dashed line through the cell, we are missing the excited 0^+ state known by experiment yet not reproduced by the NCSMC. Lacking cluster formations such as the $\alpha + {}^6$He are likely responsible for the missing 0^+ as well as the aforementioned small separation energy of the 2^+ states.

We now present the phase shift results for the $^{10}\mathrm{Be} \to n + {}^9\mathrm{Be}$ calculation in Fig. 5.3. They are presented alongside the energy level diagram for ^{10}Be, with states in the composite nucleus highlighted according to the colour of the corresponding curves on the phase shift plot. The black $^3\mathrm{P}_0$ curve corresponds to the ground state 0^+ of ^{10}Be. The dark blue $^5\mathrm{P}_2$ curve corresponds to the first 2^+ state. The red $^3\mathrm{P}_2$ curve corresponds to the first excited 2^+ state. The brown $^3\mathrm{S}_1$ curve corresponds to the 1^- S–wave halo state, while the purple $^5\mathrm{S}_2$ channel corresponds to the other 2^- S–wave halo state. These 1^- and 2^- states of ^{10}Be were briefly mentioned earlier in the context of ^{10}C. These are the analogue states which appear as resonances in the NCSMC description of ^{10}C. We further note the presence of the anticipated 3^- resonance in ^{10}Be, which was similarly observed in ^{10}C. Lastly, we reiterate the only state below the $n + {}^9$Be threshold which is not predicted is the excited 0^+, and this problem is related to the lacking consideration of α clustering.

Lastly, let us discuss the structure results from the ^{10}B calculation. In particular for ^{10}B, a proper treatment of the problem requires that we consider multiple partitions. The cluster basis states chosen

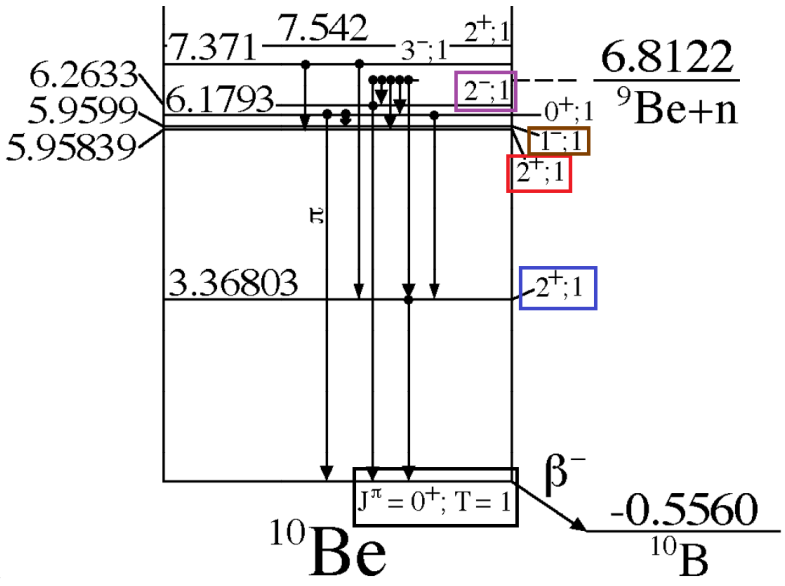

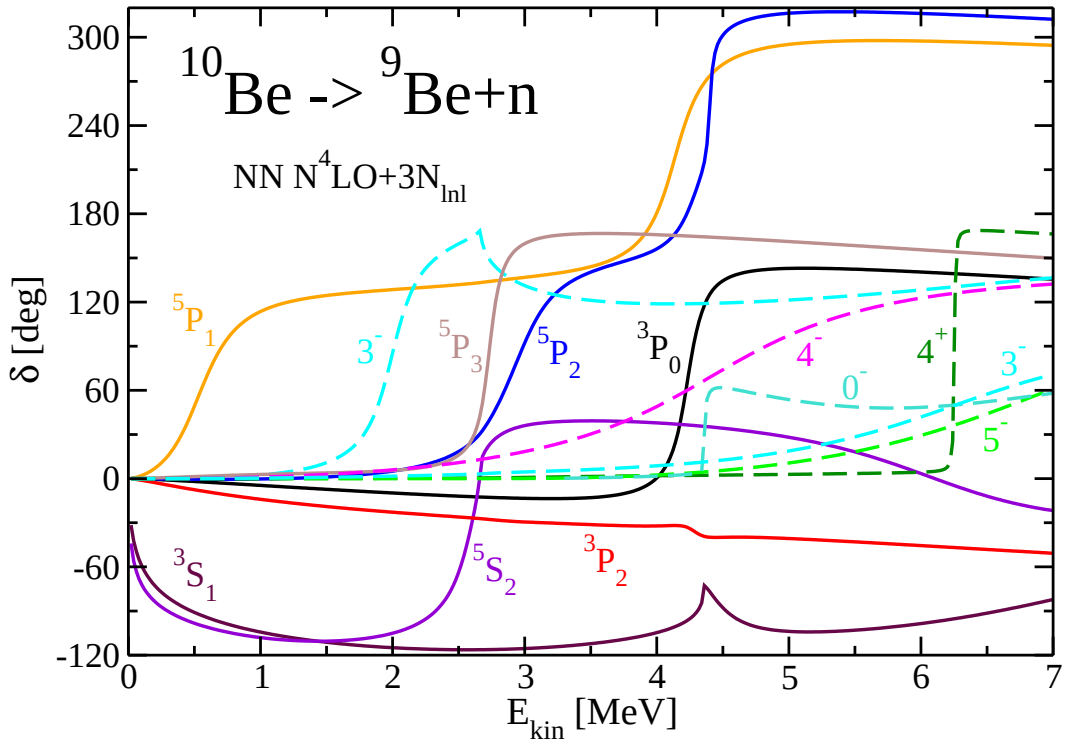

Figure 5.3: The phase shifts for ^{10}Be $\rightarrow n + {}^{9}$Be are presented alongside the experimental energy level diagram [23]. The state configuration of ^{9}Be is $J = \frac{3}{2}^{-}, \frac{5}{2}^{-}, \frac{1}{2}^{-}$. Other calculation details are the same as in Table 5.2.

for this study are described by the two mass partitions $p + {}^{9}$Be and $n + {}^{9}$B:

$$|{}^{10}\mathrm{B}\rangle = \sum_{\alpha} c_{\alpha} \, |{}^{10}\mathrm{B}, \alpha\rangle_{\mathrm{NCSM}} + \sum_{\nu} \int dr \, \gamma_{\nu}(r) \mathcal{A}_{\nu} \, |{}^{9}\mathrm{Be} + p, \nu\rangle + \sum_{\mu} \int dr \, \gamma_{\mu}(r) \mathcal{A}_{\mu} \, |{}^{9}\mathrm{B} + n, \mu\rangle \ . \quad (5.23)$$

$J^\pi;T$	E^{3m5m}	$E_{exp.}$	E_X	$E_{X,exp.}$
$3^+;0$	-5.75	-6.5859	0.0	0.0
$1^+;0$	-5.33	-5.8676	0.42	0.71835
$0^+;0$	-4.30	-4.8458	1.45	1.74015
$1^+;0$	-4.26	-4.4316	1.49	2.1543
$2^+;0$	-2.69	-2.9988	3.06	3.5871
$3^+;0$	–	-1.81	–	4.77
$2^-;0$	–	-1.48	–	5.11
$2^+;0$	-0.92	-1.4220	4.82	5.1639
$1^+;0$	–	-1.41	–	5.18
$2^+;0$	-0.70	-0.6664	5.05	5.9195
$4^+;0$	-0.19	-0.5609	5.56	6.0250
$3^-;0$	–	-0.46	–	6.13

Table 5.3: Bound state predictions from the NCSMC calculation of ^{10}B as the mass partitions $n+^9$B and $p+^9$Be, built from the $J=\frac{3}{2}^-,\frac{5}{2}^-$ states of ^{9}B and ^{9}Be (labeled 3m5m). All predicted and experimental energies are shown in MeV and E_X denotes the excitation energy with respect to the ground state. The bound state energies are determined with respect to the threshold energy of the $p+^9$Be mass partition (6.5859 MeV). Note the missing excited 3^+, first 2^-, second excited 1^+ and 3^- states. These results were computed at $N_{max}=7$ with the NN–N^{4}LO(500)+3N$_{\rm lnl}$ interaction, using a wave flow parameter of $\lambda_{SRG}=1.8\,\mathrm{fm}^{-1}$ and an oscillator frequency of $\hbar\Omega=18\,\mathrm{MeV}$.

Presently, we only show the $J=\frac{3}{2}^-,\frac{5}{2}^-$ calculation, though calculations involving a greater number of states are underway. We present the NCSMC predictions for the bound states of ^{10}B, shown in Table 5.3, to be compared to the experimental energy level diagram shown in Fig. 5.3.1. In general, ^{10}B has a high density of states compared to the other nuclei, and there are a total of twelve bound states below the respective thresholds of $p+^9$Be and $n+^9$B. With the two considered mass partitions, the *ab initio* NCSMC predicts the existence of eight of these states. The ground state 3^+ is quite well reproduced in the NCSMC, along with the first and second 1^+ states, as well as the first 2^+ state. Importantly, we have that the first 0^+ state described by the NCSMC is in the desired location, albeit slightly underbound. A good description of the 0^+ is necessary for the calculation of the isospin symmetry breaking correction, and in the cases of ^{10}C and ^{10}B the state is well described. These are encouraging preliminary results in the lead–up to the calculation of δ_C. Further confirmation of the quality of the NCSMC ^{10}B structure is the correct ordering of the ground state 3^+ and first excited state 1^+. This ordering is known to

be insufficiently described by two–body Hamiltonians [21, 185], indicating the need for multi–nucleon physics. Utilizing the three–nucleon interactions in our calculations does in fact yield the correct ordering for these states, confirming the quality of the three–body Hamiltonian. Additional ^{10}B states captured by the NCSMC are the first and second excited 2^+, as well as the high–lying 4^+ state. Unfortunately the NCSMC misses four of the twelve states, notably the excited 3^+, the first 2^-, the second excited 1^+ and the first 3^-. By including the additional $\alpha + {}^6$Li mass partition, which can be seen in Fig. 5.3.1, it is likely the situation with these four states would be improved.

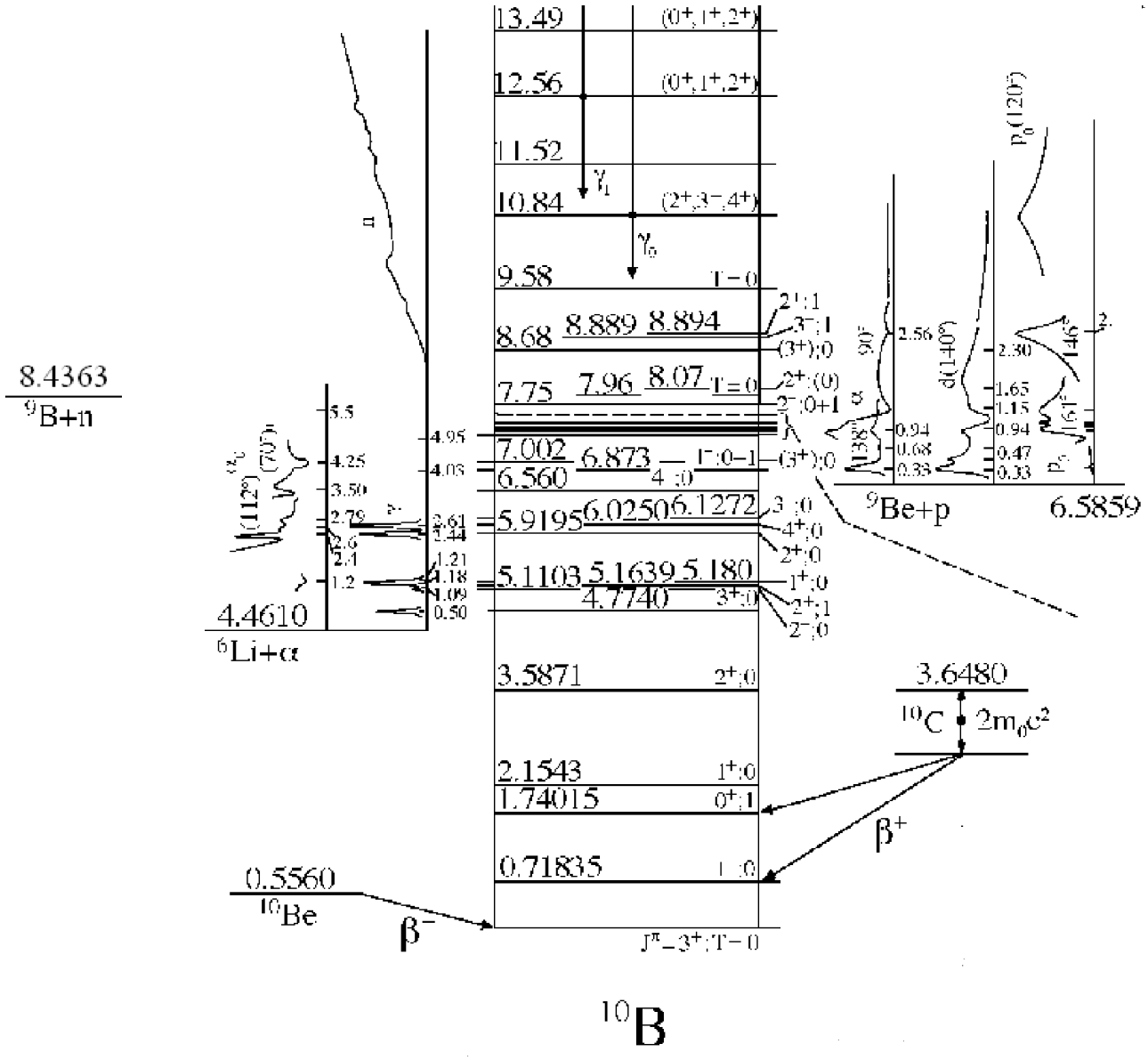

Figure 5.4: The experimental energy level diagram for ^{10}B is shown [24].

5.3.2 Outlook

As mentioned prior, the project work on beta decay in the NCSMC is still being explored. The most important development still underway is the ability to evaluate Fermi transitions in the NCSMC, which is currently under development by Dr. Mack Atkinson of TRIUMF. Once the code is successfully imple-

mented, we will be able to perform an immediate calculation of the isospin symmetry breaking correction δ_C for the $^{10}\mathrm{C} \to {}^{10}\mathrm{B}$ nuclear beta decay using NCSMC wave functions.

However, a larger study of the basis dependence in the NCSMC structure results is also required. In principle, this encapsulates three separate considerations: (i) inclusion of more states in the continuum mass partitions (ii) inclusion of α clustering partitions (iii) increasing the N_{max} basis space. We have briefly explored the variation of our results with respect to the first item, as we considered various combinations of states in ^{9}B and ^{9}Be. Notably, the $\frac{3}{2}^-$ and $\frac{5}{2}^-$ were used in all calculations, and we studied the dependence on the additional $\frac{1}{2}^-$ and $\frac{1}{2}^+$ states. In fact, we plan to include all four states in future calculations. The second item pertaining to α clustering is much more difficult to address, however, there have been recent efforts to incorporate mass partitions with α clustering in the NCSMC [186]. Lastly, while these calculations were performed at $N_{max} = 7$, by utilizing the ever increasing power of computing grids we intend to perform the calculations at $N_{max} = 9$, a significant increase in basis space size.

Chapter 6

Conclusions

As discussed in the preliminary sections, modern theoretical efforts in nuclear physics are driven by *ab initio* theories, such as the no–core shell model (NCSM) and no–core shell model with continuum (NCSMC), which utilize chiral EFT interactions as the sole input into calculations. Beginning from the underlying Standard Model physics, these interactions are derived in a low–energy expansion of the QCD Lagrangian. Chiral perturbation theory provides a consistent diagramtic expansion at increasing chiral order, and most importantly, it provides a natural hierarchy of two– and many–nucleon forces.

Utilizing the *ab initio* NCSM, in Sec. 3 we presented a generalized nonlocal one–body density matrix, which is a fundamental object in the evaluation of nuclear observables. In particular, we emphasize the importance of translation invariance in the nuclear density, which can dramatically alter the structure predictions in light–nuclei. We studied a range of nuclei, ^{4,6,8}He, ^{12}C and ^{16}O, for which we observed the highest impact of translation invariance on structure predictions to be in the lighter systems. While the effects of c.m. removal are reduced in larger A–nucleon systems, they are still non–negligible.

We first considered the applications of the coordinate densities to optical potential scattering methods, in collaboration with Dr. Matteo Vorabbi. In our case study of ^{4}He, we report the necessity of including both nonlocality and translation invariance in the density in order to achieve a reasonable description of the scattering data. The inclusion of these effects, which allows for a proper treatment of the folding integral with the t–matrix, provide corrections of approximately two orders of magnitude. This constitutes a significant step in the description of scattering processes involving light–nuclei, with agreement between theory and experiment greatly improved. We further sought application to antiproton–nucleus scattering, which provides a more robust test of our nuclear structure. Utilizing the nonlocal translation invariant densities and novel antiproton–nucleon interactions derived in the same chiral effective field theory machinery, we presented the first fully microscopic optical potential for antiproton–nucleus scattering. We computed the antiproton scattering cross sections of ^{4}He, ^{12}C, ^{16}O and ^{18}O and found remarkable agreement with available data. Given the sensitivity of antiproton scattering cross sections to nuclear radii, these results inspire confidence in the NCSM nuclear structure predictions, in particular when coupled with ChPT approaches. Lastly, we studied the impact of genuine three–body dynamics on the optical potentials, as full incorporation of the three–body interactions is not yet feasible. In general, we have determined that the impact of three–body physics on the differential cross sections is very small, whereas on other observables, e.g. the Analyzing power, the effects of $3N$ dynamics substantially alters the predicted distribution. Further efforts to incorporate three–nucleon physics are certainly required to improve the quality of optical potential approaches.

We found additional applications of the nonlocal one–body densities in development of *ab initio* functionals, such as the kinetic density functional, an essential input of DFT. While vastly different many–body approaches, by analytically computing input functionals to DFT it is possible to directly compare c.m. removal techniques as well as to gauge the quality of these functionals in light–nuclei. We presented results for the kinetic distributions of both translation invariant and c.m. contaminated densities, however the procedure is completely generalizable to other DFT quantities. It was found that

the most significant differences in the kinetic functional occur in the short–range nuclear structure, as expected from the behaviour of the translation invariant densities. Furthermore, upon comparison to an approximate treatment of c.m. contamination utilized in DFT, we identified that the kinetic density distributions obtained in both approaches were shifted in opposite directions with respect to the naive c.m. contaminated kinetic density. While description of the mean value kinetic energy was mostly preserved in this approximate treatment, the obtained distribution is shifted further from the true intrinsic structure predictions from the NCSM, and so we have concluded that this approximation is invalid.

In Sec. 4, we discussed the natural orbitals unitary transformation, an approach first utilized in atomic physics to accelerate convergence of many–body calculations. By performing a similarity transformation on the two–body matrix elements (or arbitrary Hamiltonian matrix elements) obtained in HO single–particle basis, it was shown that approximately one additional step in N_{max} convergence can be obtained for an arbitrary nuclear system. Knowing of the rapid basis growth (exponential) with respect to N_{max}, the natural orbitals provide an indispensable technique for reducing computational cost and improving the quality of nuclear structure predictions for slowly convergent systems in the NCSM.

In Sec. 5, we discussed the *ab initio* NCSMC, a generalized approach to describing nuclei by incorporating a set of continuum basis states. Utilizing this cutting edge *ab initio* theory based upon ChPT interactions, it is possible to extract important information about fundamental symmetry tests in the SM. In particular, we chose to investigate the isospin symmetry breaking correction δ_C, an essential component of high–precision CKM unitarity tests from nuclear Fermi transitions. This correction was shown to be insufficiently described in the NCSM due to lacking long–range correlations, an aspect greatly improved by the NCSMC. While the calculation of δ_C is presently underway at TRIUMF with Dr. Mack Atkinson, we presented novel nuclear structure results necessary in pursuit of δ_C. We presented novel structure results for ^{10}C, ^{10}Be and ^{10}B, though the important nuclei for calculation of δ_C are ^{10}C and ^{10}B. In the exotic ^{10}C system, we observed a strong description of the ground state 0^+, necessary for a precision calculation of δ_C. Exploring additional states in the continuum partition did not yield drastic changes in structure, and so we believe additional partitions are required to complete our understanding of ^{10}C. Similarly, in ^{10}B, the NCSMC provided a great description of the nuclear spectrum of states. This is largely due to consideration of the novel charge–exchange mass partitions, which are absolutely required for a realistic structure calculation. Even in the simplest case of utilizing two states for the partitions, the NCSMC predicted eight of the possible twelve bound states in the dense ^{10}B spectrum, in addition to predicting the correct ordering of the ground state 3^+ and first excited 1^+ state. This ordering is extremely sensitive to three–nucleon physics and is confirmation of the quality of the ChPT nuclear Hamiltonian. Importantly, we achieved a strong description of the excited 0^+ state for calculation of δ_C.

With a realistic description of ^{10}C and ^{10}B achieved, we are prepared to contribute to the analysis of fundamental symmetries in the SM by moving forward with calculation of the isospin symmetry breaking correction δ_C.

Bibliography

[1] M. Gennari, M. Vorabbi, A. Calci, and P. Navrátil, "Microscopic optical potentials derived from ab initio translationally invariant nonlocal one-body densities," *Phys. Rev. C*, vol. 97, p. 034619, Mar 2018.

[2] M. Gennari and P. Navrátil, "Nuclear kinetic density from ab initio theory," *Physical Review C*, vol. 99, p. 024305, Feb 2019.

[3] M. Vorabbi, M. Gennari, P. Finelli, C. Giusti, and P. Navrátil, "Elastic antiproton-nucleus scattering from chiral forces," *Physical Review Letters*, vol. 124, p. 162501, Apr 2020.

[4] M. Vorabbi, M. Gennari, P. Finelli, C. Giusti, P. Navrátil, and R. Machleidt, "Impact of three-body forces on elastic nucleon-nucleus scattering observables," *Physical Review C*, vol. 103, p. 024604, Feb 2021.

[5] E. Epelbaum, "Nuclear forces from chiral effective field theory: a primer," 2010.

[6] G. A. Moss, L. G. Greeniaus, J. M. Cameron, D. A. Hutcheon, R. L. Liljestrand, C. A. Miller, G. Roy, B. K. S. Koene, W. T. H. van Oers, A. W. Stetz, A. Willis, and N. Willis, "Proton-^{4}He elastic scattering at intermediate energies," *Phys. Rev. C*, vol. 21, pp. 1932–1943, May 1980.

[7] S. Burzynski, J. Campbell, M. Hammans, R. Henneck, W. Lorenzon, M. A. Pickar, and I. Sick, "p$-^4$he scattering: New data and a phase-shift analysis between 30 and 72 mev," *Phys. Rev. C*, vol. 39, pp. 56–64, Jan 1989.

[8] V. Comparat, R. Frascaria, N. Fujiwara, N. Marty, M. Morlet, P. G. Roos, and A. Willis, "Elastic proton scattering on ^{4}He at 156 mev," *Phys. Rev. C*, vol. 12, pp. 251–255, Jul 1975.

[9] "Exfor: Experimental nuclear reaction data." http://www.nndc.bnl.gov/exfor/exfor.htm.

[10] "Data tables for proton-nucleus scattering." http://www.physics.umd.edu/enp/jjkelly/ datatables.htm.

[11] T. Uesaka, S. Sakaguchi, Y. Iseri, K. Amos, N. Aoi, Y. Hashimoto, E. Hiyama, M. Ichikawa, Y. Ichikawa, S. Ishikawa, K. Itoh, M. Itoh, H. Iwasaki, S. Karataglidis, T. Kawabata, T. Kawahara, H. Kuboki, Y. Maeda, R. Matsuo, T. Nakao, H. Okamura, H. Sakai, Y. Sasamoto, M. Sasano, Y. Satou, K. Sekiguchi, M. Shinohara, K. Suda, D. Suzuki, Y. Takahashi, M. Tanifuji, A. Tamii, T. Wakui, K. Yako, Y. Yamamoto, and M. Yamaguchi, "Analyzing power for proton elastic scattering from the neutron-rich ^{6}He nucleus," *Phys. Rev. C*, vol. 82, p. 021602, Aug 2010.

[12] A. Korsheninnikov, E. Nikolskii, C. Bertulani, S. Fukuda, T. Kobayashi, E. Kuzmin, S. Momota, B. Novatskii, A. Ogloblin, A. Ozawa, V. Pribora, I. Tanihata, and K. Yoshida, "Scattering of radioactive nuclei 6he and 3h by protons: Effects of neutron skin and halo in 6he, 8he, and 11li," *Nuclear Physics A*, vol. 617, no. 1, pp. 45–56, 1997.

[13] S. Sakaguchi, T. Uesaka, N. Aoi, Y. Ichikawa, K. Itoh, M. Itoh, T. Kawabata, T. Kawahara, Y. Kondo, H. Kuboki, T. Nakamura, T. Nakao, Y. Nakayama, H. Sakai, Y. Sasamoto, K. Sekiguchi, T. Shimamura, Y. Shimizu, and T. Wakui, "Shallow and diffuse spin-orbit potential for proton elastic scattering from neutron-rich helium isotopes at 71 mev/nucleon," *Phys. Rev. C*, vol. 87, p. 021601, Feb 2013.

[14] A. Korsheninnikov, K. Yoshida, D. Aleksandrov, N. Aoi, Y. Doki, N. Inabe, M. Fujimaki, T. Kobayashi, H. Kumagai, C.-B. Moon, E. Nikolskii, M. Obuti, A. Ogloblin, A. Ozawa, S. Shimoura, T. Suzuki, I. Tanihata, Y. Watanabe, and M. Yanokura, "Experimental study of 8he + p elastic and inelastic scattering," *Physics Letters B*, vol. 316, no. 1, pp. 38–44, 1993.

[15] D. Garreta, P. Birien, G. Bruge, A. Chaumeaux, D. Drake, S. Janouin, D. Legrand, M. Lemaire, B. Mayer, J. Pain, J. Peng, M. Berrada, J. Bocquet, E. Monnand, J. Mougey, P. Perrin, E. Aslanides, O. Bing, J. Lichtenstadt, and A. Yavin, "Elastic scattering of antiprotons from carbon, calcium, and lead at 180 mev," *Physics Letters B*, vol. 149, no. 1, pp. 64–68, 1984.

[16] G. Bruge, A. Chaumeaux, P. Birien, D. Drake, D. Garreta, S. Janouin, D. Legrand, M. Lemaire, B. Mayer, J. Pain, M. Berrada, J. Bocquet, E. Monnand, J. Mougey, P. Perrin, E. Aslanides, O. Bing, J. Lichtenstadt, A. Yavin, and J. Peng, "Comparative study of the elastic scattering of 178.4 mev antiprotons by the 16o and 18o isotopes," *Physics Letters B*, vol. 169, no. 1, pp. 14–16, 1986.

[17] H. Seifert, J. J. Kelly, A. E. Feldman, B. S. Flanders, M. A. Khandaker, Q. Chen, A. D. Bacher, G. P. A. Berg, E. J. Stephenson, P. Karen, B. E. Norum, P. Welch, and A. Scott, "Effective interaction for ^{16}O(p,p') and ^{40}Ca(p,p') at e_p=200 mev," *Phys. Rev. C*, vol. 47, pp. 1615–1635, Apr 1993.

[18] C. W. Glover, P. Schwandt, H. O. Meyer, W. W. Jacobs, J. R. Hall, M. D. Kaitchuck, and R. P. DeVito, "Optical model analysis of 200 mev p$\rightarrow+^{16}$o elastic scattering data measured to large momentum transfers," *Phys. Rev. C*, vol. 31, pp. 1–11, Jan 1985.

[19] W. Huang, M. Wang, F. Kondev, G. Audi, and S. Naimi, "The AME 2020 atomic mass evaluation (i). evaluation of input data, and adjustment procedures," *Chinese Physics C*, vol. 45, p. 030002, mar 2021.

[20] M. Wang, W. Huang, F. Kondev, G. Audi, and S. Naimi, "The AME 2020 atomic mass evaluation (II). tables, graphs and references," *Chinese Physics C*, vol. 45, p. 030003, mar 2021.

[21] E. Caurier, P. Navrátil, W. E. Ormand, and J. P. Vary, "Ab initio shell model for $a = 10$ nuclei," *Phys. Rev. C*, vol. 66, p. 024314, Aug 2002.

[22] TUNL Nuclear Data Evaluation Project, "Energy level diagram, ^{10}C (2004)." `https://nucldata.tunl.duke.edu/nucldata/figures/10figs/10_06_2004.pdf`.

[23] TUNL Nuclear Data Evaluation Project, "Energy level diagram, ^{10}Be (2004)." `https://nucldata.tunl.duke.edu/nucldata/figures/10figs/10_04_2004.pdf`.

[24] TUNL Nuclear Data Evaluation Project, "Energy level diagram, ^{10}B (2004)." `https://nucldata.tunl.duke.edu/nucldata/figures/10figs/10_05_2004.pdf`.

[25] V. Cirgiliano, A. Garcia, D. Gazit, O. Naviliat-Cuncic, G. Savard, and A. Young, "Precision beta decay as a probe of new physics," *arXiv preprint arXiv:1907.02164*, 2019.

[26] P. Navrátil, S. Quaglioni, G. Hupin, C. Romero-Redondo, and A. Calci, "Unified ab initio approaches to nuclear structure and reactions," *Physica Scripta*, vol. 91, p. 053002, apr 2016.

[27] J. Dohet-Eraly, P. Navrátil, S. Quaglioni, W. Horiuchi, G. Hupin, and F. Raimondi, "^{3}He$(\alpha,\gamma)^7$Be7 and ^{3}He$(\alpha,\gamma)^7$Li astrophysical s factors from the no-core shell model with continuum," *Physics Letters B*, vol. 757, pp. 430–436, 2016.

[28] A. Wallner, K. Buczak, I. Dillmann, J. Feige, F. Kappeler, G. Korschinek, C. Lederer, A. Mengoni, U. Ott, M. Paul, and et al., "Ams applications in nuclear astrophysics: New results for 13C(n,γ)14C and 14N(n,p)14C," *Publications of the Astronomical Society of Australia*, vol. 29, no. 2, pp. 115–120, 2012.

[29] M. Wiescher, O. Clarkson, R. J. deBoer, and P. Denisenkov, "Nuclear clusters as the first stepping stones for the chemical evolution of the universe," *The European Physical Journal A*, vol. 57, no. 1, pp. 1–11, 2021.

[30] S. Weinberg, "Phenomenological lagrangians," *Physica A*, vol. 96, no. 1-2, pp. 327–340, 1979.

[31] J. Gasser and H. Leutwyler, "Chiral perturbation theory to one loop," *Annals of Physics*, vol. 158, no. 1, pp. 142–210, 1984.

[32] J. Gasser and H. Leutwyler, "Chiral perturbation theory: Expansions in the mass of the strange quark," *Nuclear Physics B*, vol. 250, no. 1, pp. 465–516, 1985.

[33] E. Epelbaum, H.-W. Hammer, and U.-G. Meißner, "Modern theory of nuclear forces," *Review of Modern Physics*, vol. 81, pp. 1773–1825, Dec 2009.

[34] R. Machleidt and D. Entem, "Chiral effective field theory and nuclear forces," *Physics Reports*, vol. 503, no. 1, pp. 1–75, 2011.

[35] R. Machleidt and F. Sammarruca, "Can chiral eft give us satisfaction?," *The European Physical Journal A*, vol. 56, Mar 2020.

[36] P. Skands, "Introduction to qcd," *Searching for New Physics at Small and Large Scales*, Sep 2013.

[37] P. Zyla *et al.*, "Review of Particle Physics," *PTEP*, vol. 2020, no. 8, p. 083C01, 2020.

[38] O. W. Greenberg, "The origin of quark color," *Physics Today*, vol. 68, no. 1, pp. 33–37, 2015.

[39] M. Gell-Mann, "Symmetries of baryons and mesons," *Physical Review*, vol. 125, pp. 1067–1084, Feb 1962.

[40] M. Schwartz, "Quantum field theory and the standard model," 02 2014.

[41] S. Coleman, J. Wess, and B. Zumino, "Structure of phenomenological lagrangians. i," *Physical Review*, vol. 177, pp. 2239–2247, Jan 1969.

[42] C. G. Callan, S. Coleman, J. Wess, and B. Zumino, "Structure of phenomenological lagrangians. ii," *Phys. Rev.*, vol. 177, pp. 2247–2250, Jan 1969.

[43] C. Aubin, C. Bernard, C. DeTar, J. Osborn, S. Gottlieb, E. B. Gregory, D. Toussaint, U. M. Heller, J. E. Hetrick, and R. Sugar, "Light pseudoscalar decay constants, quark masses, and low energy constants from three-flavor lattice qcd," *Phys. Rev. D*, vol. 70, p. 114501, Dec 2004.

[44] S. Dürr, Z. Fodor, C. Hoelbling, S. Krieg, T. Kurth, L. Lellouch, T. Lippert, R. Malak, T. Métivet, A. Portelli, A. Sastre, and K. Szabó, "Lattice qcd at the physical point meets $su(2)$ chiral perturbation theory," *Phys. Rev. D*, vol. 90, p. 114504, Dec 2014.

[45] J. Bijnens and G. Ecker, "Mesonic low-energy constants," *Annual Review of Nuclear and Particle Science*, vol. 64, no. 1, pp. 149–174, 2014.

[46] R. Haag, "Quantum field theories with composite particles and asymptotic conditions," *Phys. Rev.*, vol. 112, pp. 669–673, Oct 1958.

[47] S. Weinberg, "Nuclear forces from chiral lagrangians," *Physics Letters B*, vol. 251, no. 2, pp. 288–292, 1990.

[48] S. Weinberg, "Effective chiral lagrangians for nucleon-pion interactions and nuclear forces," *Nuclear Physics B*, vol. 363, no. 1, pp. 3–18, 1991.

[49] S. Weinberg, "Three-body interactions among nucleons and pions," *Physics Letters B*, vol. 295, no. 1, pp. 114–121, 1992.

[50] E. Epelbaum, "Few-nucleon forces and systems in chiral effective field theory," *Progress in Particle and Nuclear Physics*, vol. 57, no. 2, pp. 654–741, 2006.

[51] N. Kaiser, "Chiral 3π-exchange NN potentials: Results for representation-invariant classes of diagrams," *Physical Review C*, vol. 61, p. 014003, Dec 1999.

[52] N. Kaiser, "Chiral 3π-exchange NN potentials: Results for diagrams proportional to g_A^4 and g_A^6," *Phys. Rev. C*, vol. 62, p. 024001, Jun 2000.

[53] A. R. Edmonds, *Angular momentum in quantum mechanics*. Princeton university press, 1996.

[54] D. A. Varshalovich, A. N. Moskalev, and V. K. Khersonskii, *Quantum theory of angular momentum*. World Scientific, 1988.

[55] W. Pauli, "The connection between spin and statistics," *Physical Review*, vol. 58, no. 8, p. 716, 1940.

[56] J. C. Slater, "The theory of complex spectra," *Phys. Rev.*, vol. 34, pp. 1293–1322, Nov 1929.

[57] I. B. Zel Dovich, "Electromagnetic interaction with parity violation," *Sov. Phys. JETP*, vol. 6, no. 6, pp. 1184–1186, 1958.

[58] V. V. Flambaum and D. W. Murray, "Anapole moment and nucleon weak interactions," *Phys. Rev. C*, vol. 56, pp. 1641–1644, Sep 1997.

[59] W. C. Haxton and C. E. Wieman, "Atomic parity nonconservation and nuclear anapole moments," *Annual Review of Nuclear and Particle Science*, vol. 51, no. 1, pp. 261–293, 2001.

[60] J. Suhonen, "From nucleons to nucleus," *Berlin Heidelberg*, 2007.

[61] D. J. Rowe and J. L. Wood, *Fundamentals of nuclear models: foundational models*. World Scientific, 2010.

[62] B. R. Barrett, P. Navrátil, and J. P. Vary, "Ab initio no core shell model," *Progress in Particle and Nuclear Physics*, vol. 69, pp. 131–181, 2013.

[63] E. Epelbaum, "Four-nucleon force in chiral effective field theory," *Physics Letters B*, vol. 639, no. 5, pp. 456–461, 2006.

[64] E. Epelbaum, "Four-nucleon force using the method of unitary transformation," *The European Physical Journal A*, vol. 34, no. 2, pp. 197–214, 2007.

[65] S. Binder, J. Langhammer, A. Calci, and R. Roth, "Ab initio path to heavy nuclei," *Physics Letters B*, vol. 736, pp. 119–123, 2014.

[66] T. Miyagi, S. R. Stroberg, P. Navrátil, K. Hebeler, and J. D. Holt, "Converged ab initio calculations of heavy nuclei," 2021.

[67] P. Maris, M. Sosonkina, J. P. Vary, E. Ng, and C. Yang, "Scaling of ab-initio nuclear physics calculations on multicore computer architectures," *Procedia Computer Science*, vol. 1, no. 1, pp. 97–106, 2010. ICCS 2010.

[68] J. Elliott and T. Skyrme, "Centre-of-mass effects in the nuclear shell-model," *Proceedings of the Royal Society of London. Series A. Mathematical and Physical Sciences*, vol. 232, no. 1191, pp. 561–566, 1955.

[69] D. Gloeckner and R. Lawson, "Spurious center-of-mass motion," *Physics Letters B*, vol. 53, no. 4, pp. 313–318, 1974.

[70] M. Moshinsky and Y. Smirnov, "The harmonic oscillator in modern physics hardwood academic publishers," *The Netherlands*, pp. 289–404, 1996.

[71] E. J. Weniger, "Weakly convergent expansions of a plane wave and their use in fourier integrals," *Journal of Mathematical Physics*, vol. 26, no. 2, pp. 276–291, 1985.

[72] I. Talmi *Helvetica Physica Acta*, vol. 25, no. 185, 1952.

[73] M. Moshinsky, "Transformation brackets for harmonic oscillator functions," *Nuclear Physics*, vol. 13, no. 1, pp. 104–116, 1959.

[74] Y. Smirnov, "Talmi transformations for particles with different masses," *Nuclear Physics*, vol. 27, no. 2, pp. 177–187, 1961.

[75] Y. Smirnov, "Talmi transformation for particles with different masses (ii)," *Nuclear Physics*, vol. 39, pp. 346–352, 1962.

[76] L. Trlifaj, "Simple formula for the general oscillator brackets," *Phys. Rev. C*, vol. 5, pp. 1534–1539, May 1972.

[77] C. Lanczos, *An iteration method for the solution of the eigenvalue problem of linear differential and integral operators*. United States Governm. Press Office Los Angeles, CA, 1950.

[78] L. Komzsik, *The Lanczos method: evolution and application*. SIAM, 2003.

[79] R. Roth and P. Navrátil, "Ab initio study of ^{40}Ca with an importance-truncated no-core shell model," *Phys. Rev. Lett.*, vol. 99, p. 092501, Aug 2007.

[80] R. Roth, "Importance truncation for large-scale configuration interaction approaches," *Phys. Rev. C*, vol. 79, p. 064324, Jun 2009.

[81] S. K. Bogner, R. J. Furnstahl, and R. J. Perry, "Similarity renormalization group for nucleon-nucleon interactions," *Physical Review C*, vol. 75, p. 061001, Jun 2007.

[82] R. Roth, T. Neff, and F. Hans, "Nuclear structure in the framework of the unitary correlation operator method," *Progress in Particle and Nuclear Physics*, vol. 65, no. 1, pp. 50–93, 2010.

[83] S. Bogner, T. Kuo, and A. Schwenk, "Model-independent low momentum nucleon interaction from phase shift equivalence," *Physics Reports*, vol. 386, no. 1, pp. 1–27, 2003.

[84] S. Bogner, T. Kuo, A. Schwenk, D. Entem, and R. Machleidt, "Towards a model-independent low momentum nucleon-nucleon interaction," *Physics Letters B*, vol. 576, no. 3, pp. 265–272, 2003.

[85] S. Bogner, R. Furnstahl, P. Maris, R. Perry, A. Schwenk, and J. Vary, "Convergence in the no-core shell model with low-momentum two-nucleon interactions," *Nuclear Physics A*, vol. 801, no. 1, pp. 21–42, 2008.

[86] K. Suzuki and S. Y. Lee, "Convergent Theory for Effective Interaction in Nuclei*)," *Progress of Theoretical Physics*, vol. 64, pp. 2091–2106, 12 1980.

[87] S. Ôkubo, "Diagonalization of Hamiltonian and Tamm-Dancoff Equation," *Progress of Theoretical Physics*, vol. 12, pp. 603–622, 11 1954.

[88] F. Wegner, "Flow-equations for hamiltonians," *Annalen der Physik*, vol. 506, no. 2, pp. 77–91, 1994.

[89] S. Szpigel, R. Perry, and A. Mitra, "Quantum field theory, a 20th century profile," 2000.

[90] M. D. Schuster, S. Quaglioni, C. W. Johnson, E. D. Jurgenson, and P. Navrátil, "Operator evolution for ab initio theory of light nuclei," *Phys. Rev. C*, vol. 90, p. 011301, Jul 2014.

[91] M. D. Schuster, S. Quaglioni, C. W. Johnson, E. D. Jurgenson, and P. Navrátil, "Operator evolution for ab initio electric dipole transitions of ^{4}He," *Phys. Rev. C*, vol. 92, p. 014320, Jul 2015.

[92] E. D. Jurgenson, P. Navrátil, and R. J. Furnstahl, "Evolving nuclear many-body forces with the similarity renormalization group," *Physical Review C*, vol. 83, p. 034301, Mar 2011.

[93] R. Roth, J. Langhammer, A. Calci, S. Binder, and P. Navrátil, "Similarity-transformed chiral $nn+3n$ interactions for the ab initio description of $^{12}\mathbf{C}$ and $^{16}\mathbf{O}$," *Physical Review Letters*, vol. 107, p. 072501, Aug 2011.

[94] G. Kamuntavičius, R. Kalinauskas, B. Barrett, S. Mickevičius, and D. Germanas, "The general harmonic-oscillator brackets: compact expression, symmetries, sums and fortran code," *Nuclear Physics A*, vol. 695, no. 1, pp. 191–201, 2001.

[95] P. E. Hodgson, "Optical model of elastic scattering," 1963.

[96] W. H. Dickhoff, R. J. Charity, and M. H. Mahzoon, "Novel applications of the dispersive optical model," *Journal of Physics G: Nuclear and Particle Physics*, vol. 44, p. 033001, feb 2017.

[97] R. Varner, W. Thompson, T. McAbee, E. Ludwig, and T. Clegg, "A global nucleon optical model potential," *Physics Reports*, vol. 201, no. 2, pp. 57–119, 1991.

[98] A. Koning and J. Delaroche, "Local and global nucleon optical models from 1 kev to 200 mev," *Nuclear Physics A*, vol. 713, no. 3, pp. 231–310, 2003.

[99] S. P. Weppner, R. B. Penney, G. W. Diffendale, and G. Vittorini, "Isospin dependent global nucleon-nucleus optical model at intermediate energies," *Phys. Rev. C*, vol. 80, p. 034608, Sep 2009.

[100] G. F. Chew, "The inelastic scattering of high energy neutrons by deuterons according to the impulse approximation," *Phys. Rev.*, vol. 80, pp. 196–202, Oct 1950.

[101] K. M. Watson, "Multiple scattering and the many-body problem—applications to photomeson production in complex nuclei," *Phys. Rev.*, vol. 89, pp. 575–587, Feb 1953.

[102] N. C. Francis and K. M. Watson, "The elastic scattering of particles by atomic nuclei," *Phys. Rev.*, vol. 92, pp. 291–303, Oct 1953.

[103] C. Elster and P. C. Tandy, "Off-shell effects from meson exchange in the nuclear optical potential," *Phys. Rev. C*, vol. 40, pp. 881–886, Aug 1989.

[104] C. Elster, T. Cheon, E. F. Redish, and P. C. Tandy, "Full-folding optical potentials in elastic proton-nucleus scattering," *Phys. Rev. C*, vol. 41, pp. 814–827, Mar 1990.

[105] C. Elster and S. P. Weppner, "Energy dependence of the NN t matrix in the optical potential for elastic nucleon-nucleus scattering," *Phys. Rev. C*, vol. 57, pp. 189–195, Jan 1998.

[106] M. Grasso, "Effective density functionals beyond mean field," *Progress in Particle and Nuclear Physics*, vol. 106, pp. 256–311, 2019.

[107] D. Lacroix, A. Boulet, M. Grasso, and C.-J. Yang, "From bare interactions, low-energy constants, and unitary gas to nuclear density functionals without free parameters: Application to neutron matter," *Phys. Rev. C*, vol. 95, p. 054306, May 2017.

[108] R. Navarro Pérez, N. Schunck, A. Dyhdalo, R. J. Furnstahl, and S. K. Bogner, "Microscopically based energy density functionals for nuclei using the density matrix expansion. ii. full optimization and validation," *Phys. Rev. C*, vol. 97, p. 054304, May 2018.

[109] P. Navrátil, "Translationally invariant density," *Phys. Rev. C*, vol. 70, p. 014317, Jul 2004.

[110] P. Navrátil, G. P. Kamuntavičius, and B. R. Barrett, "Few-nucleon systems in a translationally invariant harmonic oscillator basis," *Physical Review C*, vol. 61, p. 044001, Mar 2000.

[111] M. Burrows, C. Elster, G. Popa, K. D. Launey, A. Nogga, and P. Maris, "Ab initio translationally invariant nonlocal one-body densities from no-core shell-model theory," *Physical Review C*, vol. 97, p. 024325, Feb 2018.

[112] D. R. Entem, R. Machleidt, and Y. Nosyk, "High-quality two-nucleon potentials up to fifth order of the chiral expansion," *Phys. Rev. C*, vol. 96, p. 024004, Aug 2017.

[113] V. Somà, P. Navrátil, F. Raimondi, C. Barbieri, and T. Duguet, "Novel chiral hamiltonian and observables in light and medium-mass nuclei," *Physical Review C*, vol. 101, p. 014318, Jan 2020.

[114] P. Navrátil, "Local three-nucleon interaction from chiral effective field theory," *Few-Body Systems*, vol. 41, no. 3, pp. 117–140, 2007.

[115] P. Gysbers, G. Hagen, J. Holt, G. R. Jansen, T. D. Morris, P. Navrátil, T. Papenbrock, S. Quaglioni, A. Schwenk, S. Stroberg, *et al.*, "Discrepancy between experimental and theoretical β-decay rates resolved from first principles," *Nature Physics*, vol. 15, no. 5, pp. 428–431, 2019.

[116] C. R. Chinn, C. Elster, R. M. Thaler, and S. P. Weppner, "Propagator modifications in elastic nucleon-nucleus scattering within the spectator expansion," *Phys. Rev. C*, vol. 52, pp. 1992–2003, Oct 1995.

[117] G. F. Chew and G. C. Wick, "The impulse approximation," *Physical Review*, vol. 85, pp. 636–642, Feb 1952.

[118] C. R. Chinn, C. Elster, and R. M. Thaler, "Momentum-space treatment of coulomb distortions in a multiple-scattering expansion," *Phys. Rev. C*, vol. 44, pp. 1569–1580, Oct 1991.

[119] C. Elster, L. C. Liu, and R. M. Thaler, "A practical calculational method for treating coulomb scattering in momentum space," *Journal of Physics G: Nuclear and Particle Physics*, vol. 19, pp. 2123–2134, Dec 1993.

[120] M. Vorabbi, P. Finelli, and C. Giusti, "Theoretical optical potential derived from nucleon-nucleon chiral potentials," *Physical Review C*, vol. 93, p. 034619, Mar 2016.

[121] C. Amsler and F. Myhrer, "Low energy antiproton physics," *Annual Review of Nuclear and Particle Science*, vol. 41, no. CERN-PPE-91-29, pp. 219–267, 1991.

[122] T. Aumann, W. Bartmann, A. Bouvard, O. Boine-Frankenheim, A. Broche, F. Butin, D.Calvet, J. Carbonel, P. Chiggiato, H. D. Gersem, R. D. Oliveira, T. Dobers, F. Ehm, J. F. Somoza, J. Fischer, M. Fraser, E. Friedrich, J.-L. Grenard, G. Hupin, K. Johnston, Y. Kubota, M. Gomez-Ramos, P. Indelicato, R. Lazauskas, S. Malbrunot-Ettenauer, N. Marsic, W. Müller, S. Naimi, N. Nakatsuka, R. Necca, G. Neyens, A. Obertelli, Y. Ono, S. Pasinelli, N. Paul, E. C. Pollacco, D. Rossi, H. Scheit, R. Seki, A. Schmidt, L. Schweikhard, S. Sels, E. Siesling, T. Uesaka, M. Wada, F. Wienholtz, S. Wycech, and S. Zacarias, "Puma: antiprotons and radioactive nuclei," Sep 2019.

[123] C. Amsler, D. Barna, H. Breuker, M. Fleck, A. Gligorova, H. Higaki, M. Hori, Y. Kanai, B. Kolbinger, N. Kuroda, A. Lanz, M. Leali, E. Lodi-Rizzini, V. Mäckel, C. Malbrunot, V. Mascagna, Y. Matsuda, D. J. Murtagh, Y. Nagata, A. Nanda, L. Nowak, N. Ogawa, M. C. Simon, M. Tajima, Y. Tanaka, S. Ulmer, U. Uggerhöj, L. Venturelli, E. Widmann, A. Weiser, T. Wolz, Y. Yamazaki, and J. Zmeskal, "Asacusa proposal for elena," 2019.

[124] T. Walcher, "Experiments at the low-energy antiproton ring (lear)," *Annual Review of Nuclear and Particle Science*, vol. 38, no. 1, pp. 67–95, 1988.

[125] C. Dover, T. Gutsche, M. Maruyama, and A. Faessler, "The physics of nucleon-antinucleon annihilation," *Progress in Particle and Nuclear Physics*, vol. 29, pp. 87–173, 1992.

[126] S. Adachi and H. Von Geramb, "Microscopic analysis of antiproton-nucleus elastic scattering," *Nuclear Physics A*, vol. 470, no. 3, pp. 461–476, 1987.

[127] L.-Y. Dai, J. Haidenbauer, and U.-G. Meißner, "Antinucleon-nucleon interaction at next-to-next-to-next-to-leading order in chiral effective field theory," *Journal of High Energy Physics*, vol. 2017, no. 7, pp. 1–48, 2017.

[128] H. F. Arellano, F. A. Brieva, and W. G. Love, "In-medium full-folding optical model for nucleon-nucleus elastic scattering," *Phys. Rev. C*, vol. 52, pp. 301–315, Jul 1995.

[129] M. Kohno, "Nuclear and neutron matter g-matrix calculations with a chiral effective field theory potential including effects of three-nucleon interactions," *Phys. Rev. C*, vol. 88, p. 064005, Dec 2013.

[130] M. Toyokawa, M. Yahiro, T. Matsumoto, K. Minomo, K. Ogata, and M. Kohno, "Microscopic calculations based on chiral two- and three-nucleon forces for proton- and ^{4}He-nucleus scattering," *Phys. Rev. C*, vol. 92, p. 024618, Aug 2015.

[131] M. Kohno, "Pauli rearrangement potential for a scattering state with the nucleon-nucleon interaction in chiral effective field theory," *Phys. Rev. C*, vol. 98, p. 054617, Nov 2018.

[132] P. U. Sauer, "Three-nucleon forces," *International Journal of Modern Physics E*, vol. 23, no. 09, p. 1430015, 2014.

[133] X. Guan, K. D. Launey, M. Xie, L. Bao, F. Pan, and J. P. Draayer, "Heine-stieltjes correspondence and the polynomial approach to the standard pairing problem," *Phys. Rev. C*, vol. 86, p. 024313, Aug 2012.

[134] T. Duguet, "The nuclear energy density functional formalism," in *The Euroschool on Exotic Beams, Vol. IV*, pp. 293–350, Springer, 2014.

[135] D. Vautherin and D. M. Brink, "Hartree-fock calculations with skyrme's interaction," *Physics Letters B*, vol. 32, no. 3, pp. 149–153, 1970.

[136] D. Vautherin and D. M. Brink, "Hartree-fock calculations with skyrme's interaction. i. spherical nuclei," *Physical Review C*, vol. 5, pp. 626–647, Mar 1972.

[137] D. Vautherin, "Hartree-fock calculations with skyrme's interaction. ii. axially deformed nuclei," *Physical Review C*, vol. 7, no. 1, p. 296, 1973.

[138] A. Bhattacharyya and R. Furnstahl, "The kinetic energy density in kohn–sham density functional theory," *Nuclear Physics A*, vol. 747, no. 2-4, pp. 268–294, 2005.

[139] R. Parr and Y. Weitao, *Density-Functional Theory of Atoms and Molecules*. International Series of Monographs on Chemistry, Oxford University Press, 1994.

[140] R. Dreizler, *Density Functional Theory*. Springer Berlin Heidelberg, 2013.

[141] F. Hofmann and H. Lenske, "Hartree-fock calculations in the density matrix expansion approach," *Physical Review C*, vol. 57, no. 5, p. 2281, 1998.

[142] J. Erler, N. Birge, M. Kortelainen, W. Nazarewicz, E. Olsen, A. M. Perhac, and M. Stoitsov, "The limits of the nuclear landscape," *Nature*, vol. 486, no. 7404, p. 509, 2012.

[143] M. Kortelainen, T. Lesinski, J. Moré, W. Nazarewicz, J. Sarich, N. Schunck, M. Stoitsov, and S. Wild, "Nuclear energy density optimization," *Physical Review C*, vol. 82, no. 2, p. 024313, 2010.

[144] M. Kortelainen, J. McDonnell, W. Nazarewicz, P.-G. Reinhard, J. Sarich, N. Schunck, M. Stoitsov, and S. Wild, "Nuclear energy density optimization: Large deformations," *Physical Review C*, vol. 85, no. 2, p. 024304, 2012.

[145] M. Kortelainen, J. McDonnell, W. Nazarewicz, E. Olsen, P.-G. Reinhard, J. Sarich, N. Schunck, S. Wild, D. Davesne, J. Erler, *et al.*, "Nuclear energy density optimization: Shell structure," *Physical Review C*, vol. 89, no. 5, p. 054314, 2014.

[146] J. Dobaczewski, W. Nazarewicz, and M. Stoitsov, "Nuclear ground-state properties from mean-field calculations," in *Exotic Nuclei and Atomic Masses*, pp. 55–60, Springer, 2003.

[147] M. Bender, P.-H. Heenen, and P.-G. Reinhard, "Self-consistent mean-field models for nuclear structure," *Reviews of Modern Physics*, vol. 75, no. 1, p. 121, 2003.

[148] M. Bender, K. Rutz, P.-G. Reinhard, and J. Maruhn, "Consequences of the center–of–mass correction in nuclear mean–field models," *The European Physical Journal A-Hadrons and Nuclei*, vol. 7, no. 4, pp. 467–478, 2000.

[149] P.-O. Löwdin, "Quantum theory of many-particle systems. i. physical interpretations by means of density matrices, natural spin-orbitals, and convergence problems in the method of configurational interaction," *Physical Review*, vol. 97, no. 6, p. 1474, 1955.

[150] P.-O. Löwdin, "Quantum theory of many-particle systems. ii. study of the ordinary hartree-fock approximation," *Physical Review*, vol. 97, no. 6, p. 1490, 1955.

[151] H. Shull and P.-O. Löwdin, "Natural spin orbitals for helium," *The Journal of Chemical Physics*, vol. 23, no. 8, pp. 1565–1565, 1955.

[152] P.-O. Löwdin and H. Shull, "Natural orbitals in the quantum theory of two-electron systems," *Physical Review*, vol. 101, no. 6, p. 1730, 1956.

[153] H. Shull and P.-O. Löwdin, "Superposition of configurations and natural spin orbitals. applications to the he problem," *The Journal of Chemical Physics*, vol. 30, no. 3, pp. 617–626, 1959.

[154] E. R. Davidson, "Properties and uses of natural orbitals," *Review of Modern Physics*, vol. 44, pp. 451–464, Jul 1972.

[155] M. V. Stoitsov, A. N. Antonov, and S. S. Dimitrova, "Natural orbital representation and short-range correlations in nuclei," *Physical Review C*, vol. 48, pp. 74–86, Jul 1993.

[156] M. V. Stoitsov, W. Nazarewicz, and S. Pittel, "New discrete basis for nuclear structure studies," *Physical Review C*, vol. 58, pp. 2092–2098, Oct 1998.

[157] F. Malaguti, A. Uguzzoni, E. Verondini, and P. Hodgson, "Nuclear charge distributions," *La Rivista del Nuovo Cimento*, vol. 5, no. 1, pp. 1–67, 1982.

[158] C. Constantinou, "Natural orbitals for the no-core configuration interaction approach," *arXiv preprint arXiv:1704.02363*, 2017.

[159] C. Constantinou, M. A. Caprio, J. P. Vary, and P. Maris, "Natural orbital description of the halo nucleus 6 he," *Nuclear Science and Techniques*, vol. 28, no. 12, p. 179, 2017.

[160] A. Ekström, G. Baardsen, C. Forssén, G. Hagen, M. Hjorth-Jensen, G. R. Jansen, R. Machleidt, W. Nazarewicz, T. Papenbrock, J. Sarich, and S. M. Wild, "Optimized chiral nucleon-nucleon interaction at next-to-next-to-leading order," *Phys. Rev. Lett.*, vol. 110, p. 192502, May 2013.

[161] S. Baroni, P. Navrátil, and S. Quaglioni, "Ab initio description of the exotic unbound ^{7}He nucleus," *Phys. Rev. Lett.*, vol. 110, p. 022505, Jan 2013.

[162] S. Baroni, P. Navrátil, and S. Quaglioni, "Unified ab initio approach to bound and unbound states: No-core shell model with continuum and its application to ^{7}he," *Phys. Rev. C*, vol. 87, p. 034326, Mar 2013.

[163] C. McCracken, P. Navrátil, A. McCoy, S. Quaglioni, and G. Hupin, "Microscopic investigation of the $^{8}\mathrm{Li}(n,\gamma)^{9}\mathrm{Li}$ reaction," *Physical Review C*, vol. 103, p. 035801, Mar 2021.

[164] M. Vorabbi, P. Navrátil, S. Quaglioni, and G. Hupin, "^{7}Be and ^{7}Li nuclei within the no-core shell model with continuum," *Physical Review C*, vol. 100, p. 024304, Aug 2019.

[165] J. C. Hardy and I. S. Towner, "Superallowed $0^+ \to 0^+$ nuclear β decays: 2020 critical survey, with implications for V_{ud} and ckm unitarity," *Phys. Rev. C*, vol. 102, p. 045501, Oct 2020.

[166] C.-Y. Seng, M. Gorchtein, H. H. Patel, and M. J. Ramsey-Musolf, "Reduced hadronic uncertainty in the determination of V_{ud}," *Physical Review Letters*, vol. 121, p. 241804, Dec 2018.

[167] M. Gorchtein, "γw box inside out: Nuclear polarizabilities distort the beta decay spectrum," *Physical Review Letters*, vol. 123, p. 042503, Jul 2019.

[168] J. C. Hardy and I. S. Towner, "Superallowed $0^+ \to 0^+$ nuclear β decays: 2014 critical survey, with precise results for V_{ud} and ckm unitarity," *Physical Review C*, vol. 91, p. 025501, Feb 2015.

[169] A. Sirlin, "General properties of the electromagnetic corrections to the beta decay of a physical nucleon," *Physical Review*, vol. 164, pp. 1767–1775, Dec 1967.

[170] A. Sirlin and R. Zucchini, "Accurate verification of the conserved-vector-current and standard-model predictions," *Physical Review Letters*, vol. 57, pp. 1994–1997, Oct 1986.

[171] W. Jaus and G. Rasche, "Radiative corrections to 0^+-0^+ β transitions," *Physical Review D*, vol. 35, pp. 3420–3422, Jun 1987.

[172] A. Sirlin, "Remarks concerning the o($z\alpha^2$) corrections to fermi decays, conserved-vector-current predictions, and universality," *Physical Review D*, vol. 35, pp. 3423–3427, Jun 1987.

[173] A. Czarnecki, W. J. Marciano, and A. Sirlin, "Precision measurements and ckm unitarity," *Physical Review D*, vol. 70, p. 093006, Nov 2004.

[174] I. S. Towner and J. C. Hardy, "Improved calculation of the isospin-symmetry-breaking corrections to superallowed fermi β decay," *Phys. Rev. C*, vol. 77, p. 025501, Feb 2008.

[175] K. Wildermuth and Y. Tang, "A unified theory of the nucleus," *Braunschweig, Vieweg*, 1977.

[176] S. Quaglioni and P. Navrátil, "Ab initio many-body calculations of $n-^3$H, $n-^4$He, $p-^{3,4}$He, and $n-^{10}$Be scattering," *Phys. Rev. Lett.*, vol. 101, p. 092501, Aug 2008.

[177] S. Quaglioni and P. Navrátil, "Ab initio many-body calculations of nucleon-nucleus scattering," *Phys. Rev. C*, vol. 79, p. 044606, Apr 2009.

[178] P. Navrátil and S. Quaglioni, "Ab initio many-body calculations of deuteron-^{4}He scattering and ^{6}Li states," *Phys. Rev. C*, vol. 83, p. 044609, Apr 2011.

[179] P. Descouvemont and D. Baye, "TheR-matrix theory," *Reports on Progress in Physics*, vol. 73, p. 036301, feb 2010.

[180] M. Hesse, J.-M. Sparenberg, F. Van Raemdonck, and D. Baye, "Coupled-channel r-matrix method on a lagrange mesh," *Nuclear Physics A*, vol. 640, no. 1, pp. 37–51, 1998.

[181] M. Hesse, J. Roland, and D. Baye, "Solving the resonating-group equation on a lagrange mesh," *Nuclear Physics A*, vol. 709, no. 1, pp. 184–200, 2002.

[182] P. Navrátil, S. Quaglioni, I. Stetcu, and B. R. Barrett, "Recent developments in no-core shell-model calculations," *Journal of Physics G: Nuclear and Particle Physics*, vol. 36, p. 083101, may 2009.

[183] M. Vorabbi, A. Calci, P. Navrátil, M. K. G. Kruse, S. Quaglioni, and G. Hupin, "Structure of the exotic ^{9}He nucleus from the no-core shell model with continuum," *Physical Review C*, vol. 97, p. 034314, Mar 2018.

[184] S. Quaglioni, C. Romero-Redondo, P. Navrátil, and G. Hupin, "Three-cluster dynamics within the ab initio no-core shell model with continuum: How many-body correlations and α clustering shape ^{6}He," *Physical Review C*, vol. 97, p. 034332, Mar 2018.

[185] P. Navrátil and E. Caurier, "Nuclear structure with accurate chiral perturbation theory nucleon-nucleon potential: Application to ^{6}Li and ^{10}B," *Phys. Rev. C*, vol. 69, p. 014311, Jan 2004.

[186] K. Kravvaris, S. Quaglioni, and P. Navratil, "No-core shell model with continuum approach to α clustering and α-induced reactions.," *Bulletin of the American Physical Society*, 2020.

Appendix A

Derivation of densities in the NCSM

A.1 Nonlocal c.m. contaminated one–body nuclear density

The nonlocal density operator is defined as

$$\rho_{op}(\vec{r},\vec{r}\,') = \sum_{i=1}^{A} \left(|\vec{r}\rangle \langle \vec{r}\,'| \right)^{(i)} = \sum_{i=1}^{A} \delta(\vec{r}-\vec{r}_i)\,\delta(\vec{r}\,'-\vec{r}\,'_i)\,. \tag{A.1}$$

Expanding the dirac delta distributions as $\int \delta(\vec{x}_1-\vec{x}_2)\,d\vec{x}_1 d\vec{x}_2 = \sum_{nlm}\int \varphi^*_{nlm}(\vec{x}_1)\varphi_{nlm}(\vec{x}_2)\,d\vec{x}_1 d\vec{x}_2$, we may write this operator in terms of spherical harmonics as

$$\rho_{op}(\vec{r},\vec{r}\,') = \sum_{i=1}^{A} \frac{\delta(r-r_i)}{rr_i}\,\frac{\delta(r'-r'_i)}{r'r'_i} \sum_{lm} Y_{lm}(\hat{r}_i)\,Y^*_{lm}(\hat{r}) \sum_{l'm'} Y^*_{l'm'}(\hat{r}\,'_i)\,Y_{l'm'}(\hat{r}\,')\,. \tag{A.2}$$

We may directly compute the matrix elements of this operator in the NCSM using the nuclear eigenstates, denoted $|A\lambda JM\rangle_{SD}$, in a SD HO basis. Recalling the discussion in Sec. 2.2.4 and Eq. (2.62), this implies that c.m. degrees of freedom are contained in the NCSM states, as opposed to when they are represented in the translational invariant Jacobi HO basis of Eq. (2.60). We identify that J corresponds to the angular momentum of the A–nucleon system, M the corresponding projection, and λ refers to all other distinguishing quantum numbers. Notice we may write the introduced product of spherical harmonics in the following way:

$$\begin{aligned}
\sum_{lm} Y_{lm}(\hat{r}_i)Y^*_{lm}(\hat{r}) \sum_{l'm'} Y_{l'm'}(\hat{r}\,'_i)Y^*_{l'm'}(\hat{r}\,') &= \sum_{lml'm'} Y_{lm}(\hat{r}_i)Y_{l'm'}(\hat{r}\,'_i)Y^*_{lm}(\hat{r})Y^*_{l'm'}(\hat{r}\,') \\
&= \sum_{lml'm'Kk} (lml'm'|Kk)(lm''l'm'''|Kk)\; Y_{lm}(\hat{r}_i)Y_{l'm'}(\hat{r}\,'_i)Y^*_{lm''}(\hat{r})Y^*_{l'm'''}(\hat{r}\,') \\
&= \sum_{ll'Kk} \Big(Y_l(\hat{r}_i)Y_{l'}(\hat{r}\,'_i)\Big)^{(K)}_k \; \Big(Y^*_l(\hat{r})Y^*_{l'}(\hat{r}\,')\Big)^{(K)}_k\,.
\end{aligned} \tag{A.3}$$

Then, the density operator may be written as a rank–K tensor,

$$\begin{aligned}
\rho_{op}(\vec{r},\vec{r}\,') &= \sum_{i=1}^{A} \frac{\delta(r-r_i)}{rr_i}\,\frac{\delta(r'-r'_i)}{r'r'_i} \sum_{ll'Kk} \Big(Y_l(\hat{r}_i)Y_{l'}(\hat{r}\,'_i)\Big)^{(K)}_k \; \Big(Y^*_l(\hat{r})Y^*_{l'}(\hat{r}\,')\Big)^{(K)}_k \\
&= \sum_{ll'Kk} \Big(Y^*_l(\hat{r})Y^*_{l'}(\hat{r}\,')\Big)^{(K)}_k \sum_{i=1}^{A} \Big(\rho^{(i)}_{ll'}(\vec{r},\vec{r}\,')\Big)^{(K)}_k\,.
\end{aligned} \tag{A.4}$$

Utilizing the second quantization approach, this allows for the density matrix elements to be written in terms of the one–body density matrix elements – and using Wigner–Eckart theorem for reduced matrix

elements – as

$$
\begin{aligned}
{}_{SD}\left\langle A\lambda_f J_f M_f\right|\rho_{op}(\vec{r},\vec{r}')\left|A\lambda_i J_i M_i\right\rangle_{SD} = \frac{1}{\hat{J}_f}\sum (J_i M_i K k|J_f M_f)\langle n_1 l_1 j_1 s_1||\Big(\rho^{(i)}_{ll'}(\vec{r},\vec{r}')\Big)^{(K)}||n_2 l_2 j_2 s_2\rangle \\
\times\left[\frac{-1}{\hat{K}}{}_{SD}\langle A\lambda_f J_f||(a^{\dagger}_{n_1 l_1 j_1}\tilde{a}_{n_2 l_2 j_2})^{(K)}||A\lambda_i J_i\rangle_{SD}\right]\Big(Y^*_l(\hat{r})Y^*_{l'}(\hat{r}\,')\Big)^{(K)}_k ,
\end{aligned}
\tag{A.5}
$$

where ${}_{SD}\langle A\lambda_f J_f||(a^{\dagger}_{n_1 l_1 j_1}\widetilde{a}_{n_2 l_2 j_2})^{(K)}||A\lambda_i J_i\rangle_{SD}$ are the one–body density matrix elements. Note the conventions $\hat{J}=\sqrt{2J+1}$ and $\tilde{a}_{jm}=(-1)^{j-m}a_{j-m}$. In this form, we must simply compute the reduced one–body matrix element of $(\rho^{(i)}_{ll'}(\vec{r},\vec{r}'))^{(K)}$ for the i–th nucleon shown in Eq. (A.5) and sum over all nucleon configurations. We will use the fact that $d\vec{r}_i = r_i^2 dr_i d\Omega_i$ and we will evaluate the integral over the i coordinates with the delta distributions. We further utilize Wigner–Eckart theorem and angular momentum uncoupling procedures for the spherical harmonics, as our one–body states are defined as $\langle\vec{r}|n_1 l_1 s_1 j_1\rangle = R_{n_1 l_1}(r)\big(Y_{l_1}(\hat{r})\cdot\chi_{\frac{1}{2}}\big)^{(j_1)}$, where $R_{nl}(r)$ is the RHO function. Note that the second sum is carried over the set of $\bar{m}=\{m_2,k',m_{s_1},m_{s_2},m_{l_1},m_{l_2},m,m'\}$ quantum numbers. We start witht the single–particle matrix element as:

$$
\begin{aligned}
\langle n_1 l_1 s_1 j_1||\Big(\rho^{(i)}_{op}(\vec{r},\vec{r}')\Big)^{(K)}||n_2 l_2 s_2 j_2\rangle &= \sum_{ll'm_2k'}\int d\vec{r}_i d\vec{r}_i'\ \hat{j}_1(j_2 m_2 K k'|j_1 m_1)\langle n_1 l_1 s_1 j_1 m_1|\vec{r}_i\rangle\frac{\delta(r-r_i)}{r\cdot r_i} \\
&\quad\times\frac{\delta(r'-r_i')}{r'\cdot r_i'}\langle\vec{r}_i'|n_2 l_2 s_2 j_2 m_2\rangle\Big(Y_l(\hat{r}_i)Y_{l'}(\hat{r}_i')\Big)^{(K)}_{k'} \\
&= \int d\Omega_i d\Omega_i'\sum_{ll'm_2k'}\hat{j}_1(j_2 m_2 K k'|j_1 m_1)\langle n_1 l_1 s_1 j_1 m_1|r\hat{r}_i\rangle\langle r'\hat{r}_i'|n_2 l_2 s_2 j_2 m_2\rangle\Big(Y_l(\hat{r}_i)Y_{l'}(\hat{r}_i')\Big)^{(K)}_{k'} \\
&= \int d\Omega_i d\Omega_i'\sum_{ll'}\sum_{\bar{m}}\hat{j}_1(j_2 m_2 K k'|j_1 m_1)(l_1 m_{l_1}\tfrac{1}{2}m_{s_1}|j_1 m_1)(l_2 m_{l_2}\tfrac{1}{2}m_{s_2}|j_2 m_2) \\
&\quad\times(lml'm'|Kk')\,\delta_{m_{s_1}m_{s_2}}\,\langle n_1 l_1|r\rangle\langle l_1 m_{l_1}|\hat{r}_i\rangle\langle r'|n_2 l_2\rangle\langle\hat{r}_i'|l_2 m_{l_2}\rangle\,Y_{lm}(\hat{r}_i)Y_{l'm'}(\hat{r}_i') \\
&= \int d\Omega_i d\Omega_i'\sum_{ll'}\sum_{\bar{m}}(-1)^{m_{l_2}}\hat{j}_1(j_2 m_2 K k'|j_1 m_1)(l_1 m_{l_1}\tfrac{1}{2}m_{s_1}|j_1 m_1)(l_2 m_{l_2}\tfrac{1}{2}m_{s_1}|j_2 m_2) \\
&\quad\times(lml'm'|Kk')\,R_{n_1 l_1}(r)\,R_{n_2 l_2}(r')\,Y^*_{l_1 m_{l_1}}(\hat{r}_i)\,Y_{lm}(\hat{r}_i)\,Y^*_{l_2-m_{l_2}}(\hat{r}_i')\,Y_{l'm'}(\hat{r}_i') \\
&= \sum_{ll'}\sum_{\bar{m}}(-1)^{m_{l_2}}\hat{j}_1(j_2 m_2 K k'|j_1 m_1)(l_1 m_{l_1}\tfrac{1}{2}m_s|j_1 m_1)(l_2 m_{l_2}\tfrac{1}{2}m_s|j_2 m_2) \\
&\quad\times(lml'm'|Kk')\,\delta_{l_1 l}\,\delta_{m_{l_1}m}\delta_{l_2 l'}\delta_{-m_{l_2}m'}\,R_{n_1 l_1}(r)\,R_{n_2 l_2}(r') \\
&= \sum_{\bar{m}}(-1)^{m_{l_2}}\hat{j}_1\,(j_2 m_2 K k'|j_1 m_1)(l_1 m_{l_1}\tfrac{1}{2}m_s|j_1 m_1)(l_2 m_{l_2}\tfrac{1}{2}m_s|j_2 m_2) \\
&\quad\times(l_1 m_{l_1} l_2 - m_{l_2}|Kk')\,R_{n_1 l_1}(r)\,R_{n_2 l_2}(r')\ .
\end{aligned}
\tag{A.6}
$$

In these later steps, the sum over the set $\bar{m}$ is reduced to $\bar{m}=\{m_2,k',m_s,m_{l_1},m_{l_2}\}$. Note the deltas involving l and l' quantum numbers must also be applied to the coupled spherical harmonics factor outside the single–particle matrix element, as $[Y^*_{l_1}(\hat{r})\,Y^*_{l_2}(\hat{r}\,')]^{(K)}_k$.

In particular, it is possible to analytically sum over the products of Clebsch-Gordan coefficients using

the relation labeled (8) from Ref. [54] page 291,

$$\sum_{\bar{m}}(j_{12}m_{12}j_3m_3|jm)(j_1m_1j_2m_2|j_{12}m_{12})(j_1m_1j_{23}m_{23}|j'm')(j_2m_2j_3m_3|j_{23}m_{23}) \\ = \delta_{jj'}\delta_{mm'}(-1)^{j_1+j_2+j_3+j}\hat{j}_{12}\hat{j}_{23}\begin{Bmatrix} j_1 & j_2 & j_{12} \\ j_3 & j & j_{23}\end{Bmatrix} . \tag{A.7}$$

Picking the desired form of the 6–j symbol we have

$$(-1)^{\frac{1}{2}+l_2+K+j_1}\hat{j}_2\hat{l}_1\begin{Bmatrix} \frac{1}{2} & l_2 & j_2 \\ K & j_1 & l_1\end{Bmatrix} = \sum_{\bar{m}}(j_2m_2Kk'|j_1m_1)(\frac{1}{2}m_sl_1m_{l_1}|j_1m_1)(\frac{1}{2}m_sl_2m_{l_2}|j_2m_2) \\ \times (l_2m_{l_2}Kk'|l_1m_{l_1}) , \tag{A.8}$$

and using the symmetry properties of the Clebsch–Gordan coefficients we see that

$$(\frac{1}{2}m_sl_1m_{l_1}|j_1m_1) = (-1)^{\frac{1}{2}+l_1-j_1}(l_1m_{l_1}\frac{1}{2}m_s|j_1m_1) \\ (\frac{1}{2}m_sl_2m_{l_2}|j_2m_2) = (-1)^{\frac{1}{2}+l_2-j_2}(l_2m_{l_2}\frac{1}{2}m_s|j_2m_2) \\ (l_2m_{l_2}Kk'|l_1m_{l_1}) = (-1)^{l_2-m_{l_2}}\frac{\hat{l}_1}{\hat{K}}(l_1m_{l_1}l_2m_{l_2}|Kk') . \tag{A.9}$$

Notice that $(-1)^{2j_1-\frac{1}{2}} = (-1)^{2(j_1-\frac{1}{2})+\frac{1}{2}} = (-1)^{\frac{1}{2}}$. Combining all expressions and using the column permutation symmetry of 6–j symbols, the expression reduces to

$$(-1)^{j_2+\frac{1}{2}+l_1+l_2+K}\hat{j}_2\hat{K}\begin{Bmatrix} j_2 & l_2 & \frac{1}{2} \\ l_1 & j_1 & K\end{Bmatrix} = \\ \sum_{\bar{m}}(-1)^{m_{l_1}}(j_2m_2Kk'|j_1m_1)(l_1m_{l_1}\frac{1}{2}m_s|j_1m_1)(l_2m_{l_2}\frac{1}{2}m_s|j_2m_2)(l_1m_{l_1}l_2m_{l_2}|Kk') , \tag{A.10}$$

and so our final expression for the single–particle matrix element is:

$$\langle n_1l_1s_1j_1||\left(\rho^{(i)}_{l_1l_2}(\vec{r},\vec{r}\,')\right)^{(K)}||n_2l_2s_2j_2\rangle = \hat{j}_1\hat{j}_2\hat{K}\,(-1)^{j_2+\frac{1}{2}+l_1+l_2+K}\begin{Bmatrix} j_2 & l_2 & \frac{1}{2} \\ l_1 & j_1 & K\end{Bmatrix}R_{n_1l_1}(r)R_{n_2l_2}(r') . \tag{A.11}$$

Finally, the NCSM matrix element for the nuclear density operator between an initial and final state obtained in Cartesian coordinate single–particle SD HO basis is given by

$${}_{SD}\langle A\lambda_fJ_fM_f|\,\rho_{op}(\vec{r},\vec{r}\,')\,|A\lambda_iJ_iM_i\rangle_{\,SD} = \frac{1}{\hat{J}_f}\sum_{K\bar{s}}(J_iM_iKk|J_fM_f)\,\hat{j}_1\hat{j}_2\hat{K}(-1)^{j_2+\frac{1}{2}+l_1+l_2+K}\begin{Bmatrix} j_2 & l_2 & \frac{1}{2} \\ l_1 & j_1 & K\end{Bmatrix} \\ \times R_{n_1l_1}(r)R_{n_2l_2}(r')\left[\frac{-1}{\hat{K}}{}_{SD}\langle A\lambda_fJ_f||(a^\dagger_{n_1l_1j_1}\widetilde{a}_{n_2l_2j_2})^{(K)}||A\lambda_iJ_i\rangle_{SD}\right]\left(Y^*_{l_1}(\hat{r})\,Y^*_{l_2}(\hat{r}\,')\right)^{(K)}_k , \tag{A.12}$$

where $\bar{s} = (n_1, l_1, j_1, n_2, l_2, j_2)$, as $k = M_i - M_f$ is restricted. Both $\vec{r}$ and $\vec{r}\,'$ are measured from the centre of the HO potential well. We remind the reader that this is the matrix element for the **c.m. contaminated nonlocal nuclear density**, as we have yet to treat the c.m. contamination in the SD HO eigenstates. This form is consistent with the implementation in the `trdens.f` code of Dr. Petr Navrátil.

A.2 Nonlocal translationally invariant one-body nuclear density

With the definition of Jacobi coordinates made in Sec. 2.2.4, it is now possible to construct the nonlocal translational invariant one–body density, ρ_{trinv}. This is the physically relevant form of the density derived from the intrinsic nuclear wave function, expressed in relative coordinates, with the c.m. degrees of freedom analytically removed using the Talmi–Moshinsky transformation brackets. In essence, this is accomplished by taking the reference frame of a one–body operator to be measured from the c.m. of the A–nucleon system. As noted earlier, the HO basis is the only basis which does not violate translational invariance when transforming between Jacobi coordinates and single–particle Cartesian coordinates.

We begin with the definition of the intrinisc density (normalized to the number of nucleons), which has no dependence on the c.m. coordinate $\vec{\xi}_0$, written as:

$$\begin{aligned}
\rho_{fi}(\vec{\xi},\vec{\xi}') &= A\int d\vec{\xi}_1\cdots d\vec{\xi}_{A-1}d\vec{\xi}'_{A-1}\;\psi^\dagger_f(\vec{\xi}_1,\ldots,\vec{\xi}_{A-1})\psi_i(\vec{\xi}_1,\ldots,\vec{\xi}_{A-2},\vec{\xi}'_{A-1})\,\delta(\vec{\xi}-\vec{\xi}_{A-1})\delta(\vec{\xi}'-\vec{\xi}'_{A-1}) \\
&= A\int d\vec{\xi}_1\cdots d\vec{\xi}_{A-1}d\vec{\xi}'_{A-1}\;\langle A\lambda_f J_f M_f|\vec{\xi}_1\cdots\vec{\xi}_{A-1}\rangle\langle\vec{\xi}_1\cdots\vec{\xi}'_{A-1}|A\lambda_i J_i M_i\rangle \\
&\qquad\times\delta(\vec{\xi}-\vec{\xi}_{A-1})\delta(\vec{\xi}'-\vec{\xi}'_{A-1}) \\
&= A\sum_{nlmn'l'm'}\varphi^*_{nlm}(\vec{\xi})\varphi^*_{n'l'm'}(\vec{\xi}')\int d\vec{\xi}_1\cdots d\vec{\xi}_{A-1}d\vec{\xi}'_{A-1}\;\langle A\lambda_f J_f M_f|\vec{\xi}_1\cdots\vec{\xi}_{A-1}\rangle\,\varphi_{nlm}(\vec{\xi}_{A-1}) \\
&\qquad\times\varphi_{n'l'm'}(\vec{\xi}'_{A-1})\,\langle\vec{\xi}_1\cdots\vec{\xi}'_{A-1}|A\lambda_i J_i M_i\rangle \\
&= A\sum_{nlmn'l'm'}R_{nl}(\xi)R_{n'l'}(\xi')\,(lml'm'|Kk)\big[Y^*_l(\hat{\xi})Y^*_{l'}(\hat{\xi}')\big]^{(K)}_k\int d\vec{\xi}_1\cdots d\vec{\xi}_{A-1}d\vec{\xi}'_{A-1} \\
&\qquad\times\langle A\lambda_f J_f M_f|\vec{\xi}_1\cdots\vec{\xi}_{A-1}\rangle\,\varphi_{nlm}(\vec{\xi}_{A-1})\varphi_{n'l'm'}(\vec{\xi}'_{A-1})\,\langle\vec{\xi}_1\cdots\vec{\xi}'_{A-1}|A\lambda_i J_i M_i\rangle\quad .
\end{aligned} \tag{A.13}$$

We have resolved the Dirac delta distributions as before. The central piece to evaluate in this expression is the Jacobi basis integral. First, we investigate a similar integral involving the CCSD basis. Relating this integral to the CCSD basis is a procedurally important choice as computing the Jacobi matrix elements directly is computationally intensive for systems with $A \geq 4$, due to the high degree of anti–symmetrization required. We remind the reader of the SD and Jacobi eigenstate factorization initially shown in Eq. (2.66) of Sec. 2.2.4,

$$\langle\vec{r}_1\cdots\vec{r}_A|\,A\lambda JM\rangle_{SD} = \langle\vec{\xi}_1\cdots\vec{\xi}_{A-1}|\,A\lambda JM\rangle\,\varphi_{000}(\vec{\xi}_0)\;. \tag{A.14}$$

This is an important property of the NCSM. This many–body eigenstate factorization between Jacobi and SD bases is precisely what allows for the analytic decoupling of c.m. motion, described by $\phi_{000}(\vec{\xi}_0)$,

from the intrinsic NCSM wave function. Beginning with a similar CCSD basis integral:

$$
\begin{aligned}
&\sum_{\sigma_i\tau_i m_1 m_2} (l_1 m_1 l_2 m_2|Kk) \int d\vec{r}_1 \cdots d\vec{r}_A d\vec{r}'_A \; {}_{SD}\langle A\lambda_f J_f M_f|\, \vec{r}_1 \cdots \vec{r}_A\rangle\langle \vec{r}_1 \cdots \vec{r}_{A-1}\vec{r}'_A|\, A\lambda_i J_i M_i\rangle_{SD} \\
&\quad \times \varphi_{n_1 l_1 m_1}(\vec{r}_A)\, \varphi_{n_2 l_2 m_2}(\vec{r}'_A) \\
&\quad = \sum_{\sigma_i\tau_i m_1 m_2} (l_1 m_1 l_2 m_2|Kk) \int d\vec{r}_1 \cdots d\vec{r}_A d\vec{r}'_1 \cdots d\vec{r}'_A \; {}_{SD}\langle A\lambda_f J_f M_f|\, \vec{r}_1 \cdots \vec{r}_A\rangle \\
&\qquad \times \varphi_{n_1 l_1 m_1}(\vec{r}_A)\varphi_{n_2 l_2 m_2}(\vec{r}'_A)\, \delta(\vec{r}_1 - \vec{r}'_1)\cdots\delta(\vec{r}_{A-1} - \vec{r}'_{A-1})\langle \vec{r}'_1 \cdots \vec{r}'_A|\, A\lambda_i J_i M_i\rangle_{SD} \\
&\quad = \sum_{\sigma_i\tau_i m_1 m_2} (l_1 m_1 l_2 m_2|Kk) \int d\vec{\xi}_1 \cdots d\vec{\xi}_{A-2}\, d\vec{\xi}'_1 \cdots d\vec{\xi}'_{A-2}\, d\vec{R}^{(A-1)}_{c.m.} d\vec{r}_A d\vec{R}'^{(A-1)}_{c.m.} d\vec{r}'_A \\
&\qquad \times \langle A\lambda_f J_f M_f|\, \vec{\xi}_1 \cdots \vec{\xi}_{A-1}\rangle \varphi^*_{000}(\vec{\xi}_0)\, \varphi_{000}(\vec{\xi}'_0)\langle \vec{\xi}'_1 \cdots \vec{\xi}'_{A-1}|\, A\lambda_i J_i M_i\rangle\, \varphi_{n_1 l_1 m_1}(\vec{r}_A)\varphi_{n_2 l_2 m_2}(\vec{r}'_A) \\
&\qquad \times \delta(\vec{\xi}_1 - \vec{\xi}'_1)\cdots\delta(\vec{\xi}_{A-2} - \vec{\xi}'_{A-2})\delta(\vec{R}^{(A-1)}_{c.m.} - \vec{R}'^{(A-1)}_{c.m.}) \\
&\quad = \sum_{\sigma_i\tau_i m_1 m_2} (l_1 m_1 l_2 m_2|Kk) \int d\vec{\xi}_1 \cdots d\vec{\xi}_{A-2}\, d\vec{R}^{(A-1)}_{c.m.} d\vec{r}_A d\vec{R}'^{(A-1)}_{c.m.} d\vec{r}'_A\, \langle A\lambda_f J_f M_f|\, \vec{\xi}_1 \cdots \vec{\xi}_{A-2}\vec{\xi}_{A-1}\rangle \\
&\qquad \times \varphi^*_{000}(\vec{\xi}_0)\, \varphi_{000}(\vec{\xi}'_0)\langle \vec{\xi}_1 \cdots \vec{\xi}_{A-2}\vec{\xi}'_{A-1}|\, A\lambda_i J_i M_i\rangle\, \varphi_{n_1 l_1 m_1}(\vec{r}_A)\varphi_{N_1 L_1 M_1}(\vec{R}^{(A-1)}_{c.m.}) \\
&\qquad \times (-1)^{m_2}\, \varphi^*_{n_2 l_2 -m_2}(\vec{r}'_A)\, \varphi^*_{N_1 L_1 M_1}(\vec{R}'^{(A-1)}_{c.m.}) \quad .
\end{aligned}
\tag{A.15}
$$

This is precisely the form we want, where the c.m. motion is captured by a single wave function and the remaining motion is independently described. Then, by applying the Talmi–Moshinsky transformation of Eq. (2.74) discussed in Sec. 2.2.4, we obtain (with implicit sums over new projection variables)

$$
\begin{aligned}
&\sum_{\sigma_i\tau_i m_1 m_2} (l_1 m_1 l_2 m_2|Kk) \int d\vec{r}_1 \cdots d\vec{r}_A d\vec{r}'_A \; {}_{SD}\langle A\lambda_f J_f M_f|\, \vec{r}_1 \cdots \vec{r}_A\rangle\langle \vec{r}_1 \cdots \vec{r}_{A-1}\vec{r}'_A|\, A\lambda_i J_i M_i\rangle_{SD} \\
&\quad \times \varphi_{n_1 l_1 m_1}(\vec{r}_A)\, \varphi_{n_2 l_2 m_2}(\vec{r}'_A) \\
&\quad = \sum_{\sigma_i\tau_i m_1 m_2} (-1)^{m_2} (l_1 m_1 l_2 m_2|Kk) \int d\vec{\xi}_1 \cdots d\vec{\xi}_{A-1} d\vec{\xi}'_{A-1} d\vec{\xi}_0 d\vec{\xi}'_0\, \langle A\lambda_f J_f M_f|\, \vec{\xi}_1 \cdots \vec{\xi}_{A-1}\rangle \\
&\quad \times \varphi^*_{000}(\vec{\xi}_0)\varphi_{000}(\vec{\xi}'_0)\langle \vec{\xi}_1 \cdots \vec{\xi}'_{A-1}|\, A\lambda_i J_i M_i\rangle\, \langle nlNLQ|N_1 L_1 n_1 l_1 Q\rangle_{\frac{1}{A-1}}\, (lmLM|Qq)(L_1 M_1 l_1 m_1|Qq) \\
&\quad \times \varphi_{NLM}(\vec{\xi}_0)\varphi_{nlm}(\vec{\xi}_{A-1})\, \langle n'l'N'L'Q'|N_1 L_1 n_2 l_2 Q'\rangle_{\frac{1}{A-1}}\, (l'm'L'M'|Q'q')(L_1 M_1 l_2 - m_2|Q'q') \\
&\quad \times \varphi^*_{N'L'M'}(\vec{\xi}_0)\varphi^*_{n'l'm'}(\vec{\xi}'_{A-1}) \\
&\quad = \sum_{\bar{q}} (-1)^{M_1} (L_1 M_1 l_1 m_1|lm)(L_1 M_1 l_2 - m_2|l'm')(l_1 m_1 l_2 m_2|Kk)\, \langle nl00l|N_1 L_1 n_1 l_1 l\rangle_{\frac{1}{A-1}} \\
&\quad \times \langle n'l'00l'|N_1 L_1 n_2 l_2 l'\rangle_{\frac{1}{A-1}} \int d\vec{\xi}_1 \cdots d\vec{\xi}_{A-1} d\vec{\xi}'_{A-1}\, \langle A\lambda_f J_f M_f|\, \vec{\xi}_1 \cdots \vec{\xi}_{A-1}\rangle \\
&\quad \times \langle \vec{\xi}_1 \cdots \vec{\xi}_{A-2}\vec{\xi}'_{A-1}|\, A\lambda_i J_i M_i\rangle \varphi_{nlm}(\vec{\xi}_{A-1})\varphi_{n'l'-m'}(\vec{\xi}'_{A-1}) \quad ,
\end{aligned}
\tag{A.16}
$$

where $\bar{q} = \{m_1, m_2, n, l, m, n', l', m', N_1, L_1, M_1\}$ and we have used the restriction $M_1 = m_2 + m'$. There is a meaningful subset $\bar{m} = \{m_1, m_2, m, m', M_1\}$ of the projection quantum numbers; it is in fact possible to analytically sum over the products of Clebsch–Gordan coefficients using the relation labeled (8) from Ref. [54] page 291,

$$
\begin{aligned}
&\sum_{\bar{m}} (j_{12} m_{12} j_3 m_3|jm)(j_1 m_1 j_2 m_2|j_{12} m_{12})(j_1 m_1 j_{23} m_{23}|j'm')(j_2 m_2 j_3 m_3|j_{23} m_{23}) \\
&\qquad = \delta_{jj'}\delta_{mm'}(-1)^{j_1+j_2+j_3+j}\hat{j}_{12}\hat{j}_{23} \begin{Bmatrix} j_1 & j_2 & j_{12} \\ j_3 & j & j_{23} \end{Bmatrix} \quad .
\end{aligned}
\tag{A.17}
$$

Picking the form of our 6–j symbol we have

$$(-1)^{l_1+L_1+l'+K}\hat{l}\hat{l}_2\begin{Bmatrix} l_1 & L_1 & l \\ l' & K & l_2 \end{Bmatrix} = \sum_{\bar{m}} (lml'-m'|Kk')(l_1m_1L_1M_1|lm)(l_1m_1l_2m_2|Kk') \times (L_1M_1l'-m'|l_2m_2)\ , \tag{A.18}$$

and using the symmetry properties of the Clebsch–Gordan coefficients we see

$$\begin{aligned}(l_1m_1L_1M_1|lm) &= (-1)^{l_1+L_1-l}(L_1M_1l_1m_1|lm) \\ (L_1M_1l'-m'|l_2m_2) &= (-1)^{L_1-M_1}\frac{\hat{l}_2}{\hat{l}'}(L_1M_1l_2-m_2|l'm')\ \ .\end{aligned} \tag{A.19}$$

Notably, we only have three Clebsch-Gordan coefficients in the CCSD expression. It is then necessary to resolve identity with additional sums over (K',k'), introducing the last required coefficient $(lml'm'|K'k')$. These new sums will disappear according to the $\delta_{KK'}\delta_{kk'}$ in the 6–j expression. Lastly, make note that $m_2+m'=M_1$. Hence we proceed as:

$$(-1)^{l+l'+L_1+K}\hat{l}\hat{l}'\begin{Bmatrix} l_1 & L_1 & l \\ l' & K & l_2 \end{Bmatrix} = \sum_{\bar{m}} (-1)^{M_1}(lml'-m'|K'k')(L_1M_1l_1m_1|lm)(l_1m_1l_2m_2|Kk) (L_1M_1l_2-m_2|l'm')\ . \tag{A.20}$$

By replacing the sum in the CCSD integral (and making the symmetry transformation $-m'\to m'$) we arrive at the first major result relating the Jacobi integral to the CCSD integral $(*)$ as

$$\begin{aligned}&\sum_{\sigma_i\tau_im_1m_2}(l_1m_1l_2m_2|Kk)\int d\vec{r}_1\cdots d\vec{r}_A d\vec{r}'_A\ {}_{SD}\langle A\lambda_fJ_fM_f|\,\vec{r}_1\cdots\vec{r}_A\rangle\langle\vec{r}_1\cdots\vec{r}_{A-1}\vec{r}'_A|\,A\lambda_iJ_iM_i\rangle_{SD} \\ &\qquad\times\varphi_{n_1l_1m_1}(\vec{r}_A)\varphi_{n_2l_2m_2}(\vec{r}'_A) \\ &= \sum_{\bar{s}}(lml'm'|Kk)\big(M^K\big)_{n_1l_1n_2l_2nln'l'}\int d\vec{\xi}_1\cdots d\vec{\xi}_{A-1}d\vec{\xi}'_{A-1}\,\langle A\lambda_fJ_fM_f|\,\vec{\xi}_1\cdots\vec{\xi}_{A-1}\rangle \\ &\qquad\times\langle\vec{\xi}_1\cdots\vec{\xi}_{A-2}\vec{\xi}'_{A-1}|\,A\lambda_iJ_iM_i\rangle\varphi_{nlm}(\vec{\xi}_{A-1})\varphi_{n'l'm'}(\vec{\xi}'_{A-1})\ \ .\end{aligned} \tag{A.21}$$

The sum is over the set of $\bar{s}=\{n,l,m,n',l',m',n_1,l_1,n_2,l_2\}$ quantum numbers. Further, we have made the following matrix definition:

$$(M^K)_{n_1l_1n_2l_2nln'l'} = \sum_{N_1L_1}(-1)^{l+l'+K+L_1}\hat{l}\hat{l}'\begin{Bmatrix} l_1 & L_1 & l \\ l' & K & l_2 \end{Bmatrix}\langle nl00l|\,N_1L_1n_1l_1l\rangle_{\frac{1}{A-1}}\langle n'l'00l'|\,N_1L_1n_2l_2l'\rangle_{\frac{1}{A-1}}\ . \tag{A.22}$$

We have completed the first step of relating the Jacobi integral to the CCSD integral. Next, we must relate the CCSD integral to the one–body density matrix elements; in particular we utilize the second

quantization approach:

$$
\begin{aligned}
&\sum_{\sigma_i\tau_i m_1 m_2} (l_1 m_1 l_2 m_2|Kk) \int d\vec{r}_1 \cdots d\vec{r}_A d\vec{r}'_A \; {}_{SD}\langle A\lambda_f J_f M_f|\, \vec{r}_1 \cdots \vec{r}_A\rangle\langle \vec{r}_1 \cdots \vec{r}_{A-1}\vec{r}'_A|\, A\lambda_i J_i M_i\rangle_{SD} \\
&\qquad \times \varphi_{n_1 l_1 m_1}(\vec{r}_A)\varphi_{n_2 l_2 m_2}(\vec{r}'_A) \\
&= \frac{1}{A} \sum_{\sigma_i\tau_i m_1 m_2 ab} \int d\vec{r}_1 \cdots d\vec{r}_A d\vec{r}'_A \, (l_1 m_1 l_2 m_2|Kk) \, {}_{SD}\langle A\lambda_f J_f M_f|a^\dagger_{n_a l_a j_a m_a}(\vec{r}_A)|\vec{r}_1 \cdots \vec{r}_{A-1}\rangle \\
&\quad \times \langle \vec{r}_1 \cdots \vec{r}_{A-1}|a_{n_b l_b j_b m_b}(\vec{r}'_A)|A\lambda_i J_i M_i\rangle_{SD} \, \varphi^*_{n_a l_a j_a m_a}(\vec{r}_A)\varphi_{n_1 l_1 m_1}(\vec{r}_A)\varphi_{n_b l_b j_b m_b}(\vec{r}'_A)\varphi_{n_2 l_2 m_2}(\vec{r}'_A) \\
&= \frac{1}{A} \sum_{\sigma_i\tau_i m_1 m_2 ab} \int d\vec{r}_1 \cdots d\vec{r}_A d\vec{r}'_A \, {}_{SD}\langle A\lambda_f J_f M_f|a^\dagger_{n_a l_a j_a m_a}(\vec{r}_A)|\vec{r}_1 \cdots \vec{r}_{A-1}\rangle \\
&\quad \times \langle \vec{r}_1 \cdots \vec{r}_{A-1}|a_{n_b l_b j_b m_b}(\vec{r}'_A)|A\lambda_i J_i M_i\rangle_{SD} \, (-1)^{m_{l_b}} (l_1 m_1 l_2 m_2|Kk)(l_a m_{l_a} s_a m_{s_a}|j_a m_a) \\
&\quad \times (l_b m_{l_b} s_b m_{s_b}|j_b m_b) \, \varphi^*_{n_a l_a m_{l_a}}(\vec{r}_A)\varphi_{n_1 l_1 m_1}(\vec{r}_A)\varphi^*_{n_b l_b - m_{l_b}}(\vec{r}'_A)\varphi_{n_2 l_2 m_2}(\vec{r}'_A) \\
&= \frac{1}{A} \sum_{\bar{q}} {}_{SD}\langle A\lambda_f J_f M_f|a^\dagger_{n_1 l_1 j_1 m_a} a_{n_2 l_2 j_2 m_b}|A\lambda_i J_i M_i\rangle_{SD} (-1)^{m_2} (l_1 m_1 l_2 m_2|Kk) \\
&\quad \times (l_1 m_1 \frac{1}{2} m_{s_a}|j_1 m_a)(l_2 - m_2 \frac{1}{2} m_{s_b}|j_2 m_b) \\
&= \frac{1}{A} \sum_{\bar{q}} {}_{SD}\langle A\lambda_f J_f M_f|\big(a^\dagger_{n_1 l_1 j_1} \tilde{a}_{n_2 l_2 j_2}\big)^{(K')}_{k'}|A\lambda_i J_i M_i\rangle_{SD} (-1)^{j_2 - m_{s_b}} \, (j_1 m_a j_2 - m_b|K'k') \\
&\quad \times (l_1 m_1 l_2 m_2|Kk)(l_1 m_1 \frac{1}{2} m_{s_a}|j_1 m_a)(l_2 - m_2 \frac{1}{2} m_{s_b}|j_2 m_b) \quad .
\end{aligned}
\tag{A.23}
$$

The sum is over the set of $\bar{q} = \{n_1, l_1, j_1, m_a, m_{s_a}, n_2, l_2, j_2, m_b, m_{s_b}, K', k'\}$ quantum numbers. We have used $m_2 = m_b + m_{s_b}$ with $\tilde{a}_{j_2 - m_b} = (-1)^{j_2 + m_b} a_{j_2 m_b}$. As before, we may choose the form of our 6–j symbol form and use symmetry properties of the Clebsch–Gordan coefficient to match the required expression.

$$
\begin{aligned}
(-1)^{l_1 + \frac{1}{2} + j_2 + K} \hat{j}_1 \hat{l}_2 \begin{Bmatrix} l_1 & \frac{1}{2} & j_1 \\ j_2 & K & l_2 \end{Bmatrix} = \sum_{\bar{m}} &(j_1 m_a j_2 - m_b|K'k')(l_1 m_1 \frac{1}{2} m_{s_a}|j_1 m_a)(l_1 m_1 l_2 m_2|Kk) \\
&\times (\frac{1}{2} m_{s_b} j_2 - m_b|l_2 m_2)
\end{aligned}
\tag{A.24}
$$

$$
(\frac{1}{2} m_{s_b} j_2 m_b|l_2 m_2) = (-1)^{1 + j_2 - l_2 - m_{s_b}} \frac{\hat{l}_2}{\hat{j}_2} (l_2 - m_2 \frac{1}{2} m_{s_b}|j_2 m_b) \tag{A.25}
$$

Applying these results yields

$$
\begin{aligned}
(-1)^{l_1 + l_2 + \frac{3}{2} + K} \hat{j}_1 \hat{j}_2 \begin{Bmatrix} l_1 & \frac{1}{2} & j_1 \\ j_2 & K & l_2 \end{Bmatrix} = \sum_{\bar{m}} &(-1)^{-m_{s_b}} (j_1 m_a j_2 - m_b|K'k')(l_1 m_1 \frac{1}{2} m_{s_a}|j_1 m_a)(l_1 m_1 l_2 m_2|Kk) \\
&\times (l_2 - m_2 \frac{1}{2} m_{s_b}|j_2 m_b) \; ,
\end{aligned}
\tag{A.26}
$$

and so, after using the column symmetries of the 6–j symbol, our second result $(**)$ for the CCSD integral

is given by:

$$\sum_{\sigma_i\tau_i m_1 m_2}(l_1 m_1 l_2 m_2|Kk)\int d\vec{r}_1\cdots d\vec{r}_A d\vec{r}'_A\ {}_{SD}\langle A\lambda_f J_f M_f|\,\vec{r}_1\cdots\vec{r}_A\rangle\langle\vec{r}_1\cdots\vec{r}_{A-1}\vec{r}'_A|\,A\lambda_i J_i M_i\rangle_{SD}$$
$$\times\,\varphi_{n_1 l_1 m_1}(\vec{r}_A)\varphi_{n_2 l_2 m_2}(\vec{r}'_A)$$
$$=\frac{1}{A}\sum_{\bar{q}}{}_{SD}\langle A\lambda_f J_f M_f|\,(a^\dagger_{n_1 l_1 j_1}\tilde{a}_{n_2 l_2 j_2})^{(K)}_k\,|A\lambda_i J_i M_i\rangle_{SD}\,(-1)^{l_1+l_2+K+j_2+\frac{3}{2}}\hat{j}_1\hat{j}_2\begin{Bmatrix} j_1 & j_2 & K\\ l_2 & l_1 & \frac{1}{2}\end{Bmatrix}. \tag{A.27}$$

The sum over quantum numbers is given by the set $\bar{q}=\{n_1,l_1,j_1,n_2,l_2,j_2\}$. We have succeeded in relating the CCSD basis integral to the one–body density matrices introduced in second quantization. In fact, this expression now allows us to connect the Jacobi coordinate integral $(*)$ to the one–body density matrix evaluated in the SD HO basis $(**)$, the core result of the derivation. Hence we have:

$$\begin{aligned}\sum_{\sigma_i\tau_i mm'}(lml'm'|Kk)\int d\vec{\xi}_1\cdots d\vec{\xi}_{A-1}d\vec{\xi}'_{A-1}\varphi_{nlm}(\vec{\xi}_{A-1})\varphi_{n'l'm'}(\vec{\xi}'_{A-1})\\ \times\,\langle A\lambda_f J_f M_f|\,\vec{\xi}_1\cdots\vec{\xi}_{A-1}\rangle\langle\vec{\xi}_1\cdots\vec{\xi}'_{A-1}\,|A\lambda_i J_i M_i\rangle\\ =\frac{1}{A}\sum_{\bar{q}}(-1)^{l_1+l_2+K+j_2+\frac{1}{2}}\hat{j}_1\hat{j}_2\begin{Bmatrix} j_1 & j_2 & K\\ l_2 & l_1 & \frac{1}{2}\end{Bmatrix}(M^K)^{-1}_{n_1 l_1 n_2 l_2 n l' n' l'}\\ \times\,{}_{SD}\langle A\lambda_f J_f M_f|\,(a^\dagger_{n_1 l_1 j_1}\widetilde{a}_{n_2 l_2 j_2})^{(K)}_k\,|A\lambda_i J_i M_i\rangle_{SD}\,.\end{aligned} \tag{A.28}$$

Substituting this relation into our first expression for the density in Eq. (A.13) and applying Wigner-Eckart theorem on the one–body density matrix elements, our final **translational invariant nonlocal one–body nuclear density** is given as:

$$\rho_{fiK}(\vec{\xi},\vec{\xi}')=\sum_{k\bar{s}}\frac{1}{\hat{J}_f}(J_i M_i K k|J_f M_f)\Big(Y^*_l(\hat{\xi})Y^*_{l'}(\hat{\xi}')\Big)^{(K)}_k R_{nl}(\xi)R_{n'l'}(\xi')\,(-1)^{l_1+l_2+K+j_2+\frac{1}{2}}$$
$$\times\,\hat{j}_1\hat{j}_2\hat{K}\begin{Bmatrix} j_1 & j_2 & K\\ l_2 & l_1 & \frac{1}{2}\end{Bmatrix}(M^K)^{-1}_{n_1 l_1 n_2 l_2 n l' n' l'}\left[\frac{-1}{\hat{K}}{}_{SD}\langle A\lambda_f J_f||(a^\dagger_{n_1 l_1 j_1}\widetilde{a}_{n_2 l_2 j_2})^{(K)}||A\lambda_i J_i\rangle_{SD}\right], \tag{A.29}$$

where $\bar{s}=\{n_1,l_1,j_1,n_2,l_2,j_2,n,l,n',l'\}$ and we recall the matrix definition

$$(M^K)_{n_1 l_1 n_2 l_2 n l' n' l'}=\sum_{N_1 L_1}(-1)^{l+l'+K+L_1}\hat{l}\hat{l}'\begin{Bmatrix} l_1 & L_1 & l\\ l' & K & l_2\end{Bmatrix}\langle nl00l|\,N_1 L_1 n_1 l_1 l\rangle_{\frac{1}{A-1}}\langle n'l'00l'|\,N_1 L_1 n_2 l_2 l'\rangle_{\frac{1}{A-1}}. \tag{A.30}$$

This density is consistent with the implementation in the NCSM nuclear theory code `trdens.f` of Dr. Petr Navrátil.

The normalization of the nonlocal densities is chosen such that integral of the local form,

$$\int\langle A\lambda JM|\,\rho^{(t_z)}_{iiK}(\vec{\xi},\vec{\xi})\,|A\lambda JM\rangle\,d\vec{\xi}=N_{t_z}\,, \tag{A.31}$$

returns the corresponding number of protons ($t_z=+\frac{1}{2}$) and neutrons ($t_z=-\frac{1}{2}$) in the system. The total nuclear density is simply the sum of the nucleonic densities. We may similarly compute the point–nucleon matter radius using the translational invariant local density,

$$r^2_{t_z}=\frac{1}{N_{t_z}}\int d\vec{r}\,r^2\rho^{(t_z)}_{iiK}(\vec{r}-\vec{R})=\frac{1}{N_{t_z}}\Big(\frac{A-1}{A}\Big)\int d\vec{\xi}\,\xi^2\rho^{(t_z)}_{iiK}(\xi)\,, \tag{A.32}$$

as well as the reduced EK matrix elements,

$$\begin{aligned}\int d\vec{r} r^K Y_{K,M_f-M_i}(\hat{r})\,\rho^{(t_z=+\frac{1}{2})}_{fiK}(\vec{r}-\vec{R}) &= \Big(\frac{A-1}{A}\Big)^K \int d\vec{\xi}\,\xi^K Y_{K,M_f-M_i}(\hat{\xi})\,\rho^{(t_z=+\frac{1}{2})}_{fiK}(\vec{\xi}) \\ &= \frac{1}{\hat{J}_f}(J_i M_i K M_f - M_i | J_f M_f) M(EK; J_i \to J_f)\end{aligned} \tag{A.33}$$

The c.m. contaminated density, of course, while having a consistent normalization, provides incorrect values for the radii.

Obtaining local translationally invariant one-body density

From the nonlocal densities it is possible to recover the local densities by setting $\vec{\xi} = \vec{\xi}'$, reducing the product of spherical harmonics, and by making use of the following relation,

$$\langle l_1 \frac{1}{2} j_1 || Y_K || l_2 \frac{1}{2} j_2 \rangle = \frac{1}{\sqrt{4\pi}}(-1)^{j_2+\frac{1}{2}}\,\hat{j}_1\hat{j}_2\hat{l}_1\hat{l}_2\,(l_1 0 l_2 0|K0) \begin{Bmatrix} j_1 & j_2 & K \\ l_2 & l_1 & \frac{1}{2} \end{Bmatrix} . \tag{A.34}$$

Imposing the above conditions, we arrive at the **translationally invariant local one-body density**,

$$\begin{aligned}\rho_{fiK}(\vec{\xi}) = \sum \frac{1}{\hat{J}_f}(J_i M_i K k | J_f M_f) Y^*_{Kk}(\hat{\xi}) R_{nl}(\xi) R_{nl}(\xi)\,\frac{\hat{l}\hat{l}'(l0l'0|K0)}{\hat{l}_1\hat{l}_2(l_1 0 l_2 0|K0)} \langle l_1 \frac{1}{2} j_1 || Y_K || l_2 \frac{1}{2} j_2 \rangle \\ \times (M^K)^{-1}_{n_1 l_1 n_2 l_2 n l n' l'} \left[\frac{-1}{\hat{K}} {}_{SD}\langle A\lambda_f J_f || (a^\dagger_{n_1 l_1 j_1} \widetilde{a}_{n_2 l_2 j_2})^{(K)} || A\lambda_i J_i \rangle_{SD} \right] .\end{aligned} \tag{A.35}$$

A.3 Kinetic density from nonlocal–body densities

The kinetic energy functional is defined as

$$\mathcal{H}_{kinetic}(\vec{r}) = \frac{\hbar^2}{2m}\tau_0(\vec{r}) , \tag{A.36}$$

where m is the nucleon mass and $\tau_0 = \sum_{\mathcal{N}} \tau_{\mathcal{N}} = \tau_p + \tau_n$ is the total kinetic density. The nucleon kinetic density is dependent on a Laplacian–like operation applied to the nonlocal nuclear density,

$$\tau_{\mathcal{N}}(\vec{r}) = \Big[\vec{\nabla} \cdot \vec{\nabla}\,' \rho_{\mathcal{N}}(\vec{r}, \vec{r}\,') \Big]_{\vec{r}=\vec{r}\,'} , \tag{A.37}$$

where $\mathcal{N}$ denotes the nucleon type for protons (p) and neutrons (n). Writing the kinetic density in spherical component form, we have

$$\nabla_u \nabla'_{-u} \rho(\vec{r}, \vec{r}\,') = \sum_{n l n' l' K k m_l m_{l'}} \alpha^{K,i,f}_{n l n' l'}\,(l\, m_l\, l'\, m_{l'} | L M) \Big[\nabla_u R_{n,l}(r) Y^*_{l,m_l}(\hat{r}) \Big] \Big[\nabla'_{-u} R_{n',l'}(r') Y^*_{l',m_{l'}}(\hat{r}') \Big] , \tag{A.38}$$

where $u = 0, \pm 1$ and $\alpha^{K,i,f}_{n l n' l'}$ is defined for the translationally invariant density as

$$\begin{aligned}\alpha^{K,i,f}_{n l n' l'} = \Big(\frac{A}{A-1}\Big)^{3/2} \sum_{n_1 l_1 j_1 n_2 l_2 j_2} \frac{1}{\hat{J}_f}(J_i\, M_i\, K\, k | J_f\, M_f)(-1)^{l_1+l_2+K+j_2-\frac{1}{2}}\,\hat{j}_1\hat{j}_2 \begin{Bmatrix} j_1 & j_2 & K \\ l_2 & l_1 & \frac{1}{2} \end{Bmatrix} \\ \times \big(M^K\big)^{-1}_{n l n' l' n_1 l_1 n_2 l_2} {}_{SD}\langle A\lambda_f J_f || (a^\dagger_{n_1 l_1 j_1}\, \tilde{a}_{n_2 l_2 j_2})^{(K)} || A\lambda_i J_i \rangle_{SD} .\end{aligned} \tag{A.39}$$

In this form, we must evaluate the expressions for the spherical components of $\vec{\nabla} f(\vec{r}) Y_l^m(\hat{r})$, for which analytic forms exist [54]. The relations are provided below:

$$\begin{aligned}\nabla_0 R_{nl}(r) Y^*_{lm_l}(\hat{r}) &= \sqrt{\frac{(l+1)^2 - m_l^2}{(2l+1)(2l+3)}} \left(\frac{dR_{nl}(r)}{dr} - \frac{l}{r} R_{nl}(r) \right) Y^*_{l+1,m_l}(\hat{r}) \\ &+ \sqrt{\frac{l^2 - m_l^2}{(2l-1)(2l+1)}} \left(\frac{dR_{nl}(r)}{dr} + \frac{l+1}{r} R_{nl}(r) \right) Y^*_{l-1,m_l}(\hat{r}) \ ,\end{aligned} \tag{A.40}$$

$$\begin{aligned}\nabla_{\pm 1} R_{n,l}(r) Y^*_{l,m_l}(\hat{r}) &= \sqrt{\frac{(l \pm m_l + 1)(l \pm + m_l + 2)}{2(2l+1)(2l+3)}} \left(\frac{dR_{nl}(r)}{dr} - \frac{l}{r} R_{nl}(r) \right) Y^*_{l+1,m_l \pm 1}(\hat{r}) \\ &- \sqrt{\frac{(l \mp m - 1)(l \mp m)}{2(2l-1)(2l+1)}} \left(\frac{dR_{nl}(r)}{dr} + \frac{l+1}{r} R_{nl}(r) \right) Y^*_{l-1,m_l \pm 1}(\hat{r}) \ ,\end{aligned}$$

We may then expand the product in Eq. (A.38), evaluate the functions at $\vec{r} = \vec{r}'$, and finally reduce the spherical harmonics using a product relation,

$$Y^*_{lm}(\hat{r}) Y^*_{l'm'}(\hat{r}) = \sum_{LM} \sqrt{\frac{(2l+1)(2l'+1)}{4\pi(2L+1)}} (lml'm'|LM)(l0l'0|L0) Y^*_{LM}(\hat{r}) \ . \tag{A.41}$$

This process leads to the general form for each term in the kinetic density sum,

$$\begin{aligned}\nabla_u \nabla'_{-u} \rho(\vec{r}, \vec{r}')|_{\vec{r}=\vec{r}'} = &\sum_{nln'l'Kkm_l m_{l'}} \alpha^{K,i,f}_{nln'l'} (lm_l l' m_{l'}|LM) \\ &\times \Bigg[c_{u0} \left(\frac{dR_{nl}(r)}{dr} - \frac{l}{r} R_{nl}(r) \right) \left(\frac{dR_{n'l'}(r)}{dr} - \frac{l'}{r} R_{n'l'}(r) \right) \\ &+ c_{u1} \left(\frac{dR_{nl}(r)}{dr} - \frac{l}{r} R_{nl}(r) \right) \left(\frac{dR_{n'l'}(r)}{dr} + \frac{l'+1}{r} R_{n'l'}(r) \right) \\ &+ c_{u2} \left(\frac{dR_{nl}(r)}{dr} + \frac{l+1}{r} R_{nl}(r) \right) \left(\frac{dR_{n'l'}(r)}{dr} - \frac{l'}{r} R_{n'l'}(r) \right) \\ &+ c_{u3} \left(\frac{dR_{nl}(r)}{dr} + \frac{l+1}{r} R_{nl}(r) \right) \left(\frac{dR_{n'l'}(r)}{dr} + \frac{l'+1}{r} R_{n'l'}(r) \right) \Bigg] Y^*_{LM}(\hat{r}) \ .\end{aligned} \tag{A.42}$$

Note that we group all spherical harmonics under the collective index L and projection M. The angular momentum coefficients are provided in Appendix A.3.1. With the angular momentum algebra complete, we only must evaluate the derivatives of the RHO functions. To begin, we introduce existing derivative and recurrence relations for Laguerre polynomials:

$$\frac{d}{dr} L^l_n(r) = -L^{l+1}_{n-1}(r) \tag{A.43}$$

$$L^l_n(r) + L^{l+1}_{n-1}(r) = L^{l+1}_n(r) \tag{A.44}$$

Recall that the radial harmonic oscillator (RHO) function is given by

$$R_{n,l}(r) = \sqrt{\frac{2\Gamma(n+1)}{(b^2)^{l+\frac{3}{2}} \Gamma(n+l+\frac{3}{2})}} \, r^l \exp\Big(-\frac{r^2}{2b^2} \Big) L^{l+\frac{1}{2}}_n \left(\frac{r^2}{b^2} \right) , \tag{A.45}$$

where b is the harmonic oscillator length and Γ is the gamma function. We now define

$$\gamma_{n,l,b} = \sqrt{\frac{2\Gamma(n+1)}{(b^2)^{l+\frac{3}{2}}\Gamma(n+l+\frac{3}{2})}} \tag{A.46}$$

for simplicity. Taking the radial derivative and using (A.43), we have

$$\begin{aligned}\frac{dR_{n,l}}{dr} = \gamma_{n,l,b}\Big[& lr^{l-1}\exp\Big(-\frac{r^2}{2b^2}\Big)L_n^{l+\frac{1}{2}}\Big(\frac{r^2}{b^2}\Big) - \frac{r^{l+1}}{b^2}\exp\Big(-\frac{r^2}{2b^2}\Big)L_n^{l+\frac{1}{2}}\Big(\frac{r^2}{b^2}\Big) \\ & - \frac{2r^{l+1}}{b^2}\exp\Big(-\frac{r^2}{2b^2}\Big)L_{n-1}^{l+\frac{3}{2}}\Big(\frac{r^2}{b^2}\Big)\Big].\end{aligned} \tag{A.47}$$

Now making use of (A.44) and rewriting in terms of RHO functions,

$$\begin{aligned}\frac{dR_{n,l}}{dr} &= \frac{l}{r}R_{n,l}(r) - \gamma_{n,l,b}\frac{r^{l+1}}{b^2}\exp\Big(-\frac{r^2}{2b^2}\Big)\Big[L_n^{l+\frac{1}{2}}\Big(\frac{r^2}{b^2}\Big) + 2L_{n-1}^{l+\frac{3}{2}}\Big(\frac{r^2}{b^2}\Big)\Big] \\ \frac{dR_{n,l}}{dr} &= \frac{l}{r}R_{n,l}(r) - \gamma_{n,l,b}\frac{r^{l+1}}{b^2}\exp\Big(-\frac{r^2}{2b^2}\Big)\Big[L_n^{l+\frac{3}{2}}\Big(\frac{r^2}{b^2}\Big) + L_{n-1}^{l+\frac{3}{2}}\Big(\frac{r^2}{b^2}\Big)\Big] \\ \frac{dR_{n,l}}{dr} &= \frac{l}{r}R_{n,l}(r) - \frac{1}{b^2}\gamma_{n,l,b}\left[\frac{R_n^{l+1}(r)}{\gamma_{n,l+1,b}} + \frac{R_{n-1}^{l+1}(r)}{\gamma_{n-1,l+1,b}}\right]\end{aligned} \tag{A.48}$$

we can derive our final result,

$$\frac{dR_{n,l}}{dr} = \frac{l}{r}R_{n,l} - \frac{1}{b}\left[\sqrt{n+l+\frac{3}{2}}\,R_{n,l+1}(r) + \sqrt{n}\,R_{n-1,l+1}(r)\right]. \tag{A.49}$$

Note that when computing the derivative of the RHO in the case of the translationally invariant nonlocal density, one must take the derivative with respect to the Jacobi coordinates, not the Cartesian coordinate.

Then, the kinetic density may be computed from *ab initio* nonlocal densities. Both the **c.m. contaminated kinetic density** and **translationally invariant kinetic density** are implemented in the *trdens_kernels_Oeff.f* code of Petr Navrátil, in the subroutine *kinetic_density(version)* which takes a parameter identifying translational invariance or c.m. contamination in the density. For analysis on the effects of translational invariance in the nuclear kinetic density, see Ref. [**?**].

From the nuclear kinetic densities, it is possible to exactly recover the mean value intrinsic kinetic energy of the nucleus, which is independently calculated from the two-body density matrix elements introduced in second quantization,

$$\begin{aligned}\langle T_{int}\rangle &= \frac{1}{4}\sum_{abcd}\langle ab|\,T_{int}\,|cd\rangle_{\,SD}\,\langle A\lambda JT|\,a_a^\dagger a_b^\dagger a_d a_c\,|A\lambda JT\rangle_{\,SD} \\ &= {}_{SD}\,\langle A\lambda JT|\left(\frac{\hbar^2}{2m}\tau_0^{trinv}\right)|A\lambda JT\rangle_{\,SD} \\ &= \frac{\hbar^2}{2m}\int_0^\infty dr\,r^2\tau_0^{trinv}(r)\end{aligned} \tag{A.50}$$

In particular, it is possible to verify that we have precisely removed the c.m. contamination present in

the NCSM eigenstates as we know the c.m. contribution to the kinetic energy of the nucleus:

$$\begin{aligned}\langle T_{wiCOM}\rangle &= {}_{SD}\langle A\lambda JT|\left(\frac{\hbar^2}{2m}\tau_0^{wiCOM}\right)|A\lambda JT\rangle_{SD}\\ &= \frac{\hbar^2}{2m}\int_0^\infty r^2\tau_0^{wiCOM}(r)\,dr\\ &= {}_{SD}\langle A\lambda JT|\frac{\hbar^2}{2m}\left(\tau_0^{int}+\tau_0^{COM}\right)|A\lambda JT\rangle_{SD}\\ &= \langle T_{int}\rangle + \frac{3}{4}\hbar\Omega\ .\end{aligned} \tag{A.51}$$

This is confirmed in Tbl. 3.1.

A.3.1 Angular momentum coefficients

The c_{uj} coefficients are complicated angular momentum factors provided here,

$$\begin{aligned}&\times(l-1,m_l,l'-1,m_{l'}|LM)\,(l-1,0,l'-1,0|L0)\\ c_{\pm10} &= \sqrt{\frac{(l+m_l+1)(l+m_l+2)}{2(2l+1)(2l+3)}}\sqrt{\frac{(l'-m_{l'}+1)(l'-m_{l'}+2)}{2(2l'+1)(2l'+3)}}\sqrt{\frac{(2l+3)(2l'+3)}{4\pi(2L+1)}}\\ &\times(l+1,m_l+1,l'+1,m_{l'}-1|LM)\,(l+1,0,l'+1,0|L0)\\ c_{\pm11} &= -\sqrt{\frac{(l+m_l+1)(l+m_l+2)}{2(2l+1)(2l+3)}}\sqrt{\frac{(l'+m_{l'}-1)(l'+m_{l'})}{2(2l'-1)(2l'+1)}}\sqrt{\frac{(2l+3)(2l'-1)}{4\pi(2L+1)}}\\ &\times(l+1,m_l+1,l'-1,m_{l'}-1|LM)\,(l+1,0,l'-1,0|L0)\\ c_{\pm12} &= -\sqrt{\frac{(l-m_l-1)(l-m_l)}{2(2l-1)(2l+1)}}\sqrt{\frac{(l'-m_{l'}+1)(l'-m_{l'}+2)}{2(2l'+1)(2l'+3)}}\sqrt{\frac{(2l-1)(2l'+3)}{4\pi(2L+1)}}\\ &\times(l-1,m_l+1,l'+1,m_{l'}-1|LM)\,(l-1,0,l'+1,0|L0)\\ c_{\pm13} &= \sqrt{\frac{(l-m_l-1)(l-m_l)}{2(2l-1)(2l+1)}}\sqrt{\frac{(l'+m_{l'}-1)(l'+m_{l'})}{2(2l'-1)(2l'+1)}}\sqrt{\frac{(2l-1)(2l'-1)}{4\pi(2L+1)}}\\ &\times(l-1,m_l+1,l'-1,m_{l'}-1|LM)\,(l-1,0,l'-1,0|L0)\\ c_{\mp10} &= \sqrt{\frac{(l-m_l+1)(l-m_l+2)}{2(2l+1)(2l+3)}}\sqrt{\frac{(l'+m_{l'}+1)(l'+m_{l'}+2)}{2(2l'+1)(2l'+3)}}\sqrt{\frac{(2l+3)(2l'+3)}{4\pi(2L+1)}}\\ &\times(l+1,m_l-1,l'+1,m_{l'}+1|LM)\,(l+1,0,l'+1,0|L0)\\ c_{\mp11} &= -\sqrt{\frac{(l-m_l+1)(l-m_l+2)}{2(2l+1)(2l+3)}}\sqrt{\frac{(l'-m_{l'}-1)(l'-m_{l'})}{2(2l'-1)(2l'+1)}}\sqrt{\frac{(2l+3)(2l'-1)}{4\pi(2L+1)}}\\ &\times(l+1,m_l-1,l'-1,m_{l'}+1|LM)\,(l+1,0,l'-1,0|L0)\\ c_{\mp12} &= -\sqrt{\frac{(l+m_l-1)(l+m_l)}{2(2l-1)(2l+1)}}\sqrt{\frac{(l'+m_{l'}+1)(l'+m_{l'}+2)}{2(2l'+1)(2l'+3)}}\sqrt{\frac{(2l-1)(2l'+3)}{4\pi(2L+1)}}\\ &\times(l-1,m_l-1,l'+1,m_{l'}+1|LM)\,(l-1,0,l'+1,0|L0)\\ c_{\mp13} &= \sqrt{\frac{(l+m_l-1)(l+m_l)}{2(2l-1)(2l+1)}}\sqrt{\frac{(l'-m_{l'}-1)(l'-m_{l'})}{2(2l'-1)(2l'+1)}}\sqrt{\frac{(2l-1)(2l'-1)}{4\pi(2L+1)}}\\ &\times(l-1,m_l-1,l'-1,m_{l'}+1|LM)\,(l-1,0,l'-1,0|L0)\end{aligned} \tag{A.52}$$

$$
\begin{aligned}
c_{00} &= \sqrt{\frac{(l+1)^2 - m_l^2}{(2l+1)(2l+3)}}\sqrt{\frac{(l'+1)^2 - m_{l'}^2}{(2l'+1)(2l'+3)}}\sqrt{\frac{(2l+3)(2l'+3)}{4\pi(2L+1)}} \\
&\quad \times (l+1, m_l, l'+1, m_{l'}|LM)\,(l+1, 0, l'+1, 0|L0) \\
c_{01} &= \sqrt{\frac{(l+1)^2 - m_l^2}{(2l+1)(2l+3)}}\sqrt{\frac{l'^2 - m_{l'}^2}{(2l'-1)(2l'+1)}}\sqrt{\frac{(2l+3)(2l'-1)}{4\pi(2L+1)}} \\
&\quad \times (l+1, m_l, l'-1, m_{l'}|LM)\,(l+1, 0, l'-1, 0|L0) \\
c_{02} &= \sqrt{\frac{l^2 - m_l^2}{(2l-1)(2l+1)}}\sqrt{\frac{(l'+1)^2 - m_{l'}^2}{(2l'+1)(2l'+3)}}\sqrt{\frac{(2l-1)(2l'+3)}{4\pi(2L+1)}} \\
&\quad \times (l-1, m_l, l'+1, m_{l'}|LM)\,(l-1, 0, l'+1, 0|L0) \\
c_{03} &= \sqrt{\frac{l^2 - m_l^2}{(2l-1)(2l+1)}}\sqrt{\frac{l'^2 - m_{l'}^2}{(2l'-1)(2l'+1)}}\sqrt{\frac{(2l-1)(2l'-1)}{4\pi(2L+1)}}
\end{aligned}
\tag{A.53}
$$

where $\pm$ indicates the order of gradient application.